



HAL
open science

Adaptive Optics for LEO-to-Ground Optical Communication: Modeling, Optimization, and Experiment

Pablo Rodríguez Robles

► **To cite this version:**

Pablo Rodríguez Robles. Adaptive Optics for LEO-to-Ground Optical Communication: Modeling, Optimization, and Experiment. Engineering Sciences [physics]. Aix-Marseille Université (AMU), 2023. English. NNT: 2020AIXM0001 . tel-04746416

HAL Id: tel-04746416

<https://hal.science/tel-04746416v1>

Submitted on 21 Oct 2024

HAL is a multi-disciplinary open access archive for the deposit and dissemination of scientific research documents, whether they are published or not. The documents may come from teaching and research institutions in France or abroad, or from public or private research centers.

L'archive ouverte pluridisciplinaire **HAL**, est destinée au dépôt et à la diffusion de documents scientifiques de niveau recherche, publiés ou non, émanant des établissements d'enseignement et de recherche français ou étrangers, des laboratoires publics ou privés.



Distributed under a Creative Commons Attribution - NonCommercial - ShareAlike 4.0 International License

THÈSE DE DOCTORAT

Soutenue à Aix-Marseille Université
le 14 décembre 2023 par

Pablo ROBLES

Optique adaptative pour la communication optique LEO-sol : Modélisation, optimisation et expérimentation

Discipline

Physique et sciences de la matière

Spécialité

Instrumentation

École doctorale

ED352 : Physique et sciences de la matière

Laboratoire et partenaires de recherche

Laboratoire d'astrophysique
de Marseille (LAM)

Office national d'études et
de recherches aérospatiales (ONERA)

Centre national d'études spatiales (CNES)

Composition du jury

Andrés GUESALAGA Rapporteur
Professeur, Pontificia Universidad Católica de Chile

Lisa A. POYNEER Rapporteuse
Senior Scientist, Lawrence Livermore National Laboratory

Tim MORRIS Examineur
Professeur, Durham University

Marc FERRARI Président du jury
Astronome, LAM

Benoit NEICHEL Directeur de thèse
Chargé de recherche, LAM

Cyril PETIT Co-directeur de thèse
Ingénieur de recherche, ONERA

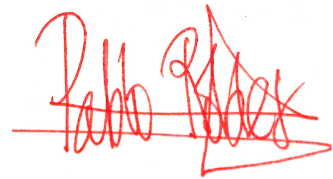
Bouchra BENAMMAR Invitée
Ingénieure de recherche, CNES

Affidavit

Je soussigné, Pablo Robles, déclare par la présente que le travail présenté dans ce manuscrit est mon propre travail, réalisé sous la direction scientifique de Benoit Neichel, dans le respect des principes d'honnêteté, d'intégrité et de responsabilité inhérents à la mission de recherche. Les travaux de recherche et la rédaction de ce manuscrit ont été réalisés dans le respect à la fois de la charte nationale de déontologie des métiers de la recherche et de la charte d'Aix-Marseille Université relative à la lutte contre le plagiat.

Ce travail n'a pas été précédemment soumis en France ou à l'étranger dans une version identique ou similaire à un organisme examinateur.

Fait à Châtillon, le 29 septembre 2023,



Cette œuvre est mise à disposition selon les termes de la [License Creative Commons Attribution - Pas d'Utilisation Commerciale - Partage dans les Mêmes Conditions 4.0 International \(CC BY-NC-SA 4.0\)](https://creativecommons.org/licenses/by-nc-sa/4.0/).

This work is published under the terms of the [Creative Commons License Attribution - Non Commercial - Share Alike 4.0 International \(CC BY-NC-SA 4.0\)](https://creativecommons.org/licenses/by-nc-sa/4.0/).

List of Publications and Conferences

Publications Produced as Part of the Thesis Project:

1. **P. Robles**, C. Petit, J.-M. Conan, B. Benammar, and B. Neichel, “Predictive adaptive optics for satellite tracking applications: optical communications and satellite observation,” in *Adaptive Optics Systems VIII*, SPIE, Aug. 2022, pp. 917–931. doi: 10.1117/12.2630217.
2. **P. Robles**, “Emulating and characterizing strong turbulence conditions for space-to-ground optical links: the PICOLO bench”, *JATIS*, 2023, submitted.

Participation in Conferences during the Thesis Period:

1. **P. Robles**, C. Petit, B. Benammar, and B. Neichel, ”Adaptive optics predictive control for low-Earth-orbit satellites: Application to telecommunication and observation”, talk, *SFO/JIROA*, July 2021, Dijon (France).
2. **P. Robles**, C. Petit, B. Benammar, and B. Neichel, ”Improving LEO downlink laser communications through predictive adaptive optics”, talk, *ICSOS Workshop*, April 202, online.
3. **P. Robles**, C. Petit, J.-M. Conan, B. Benammar, and B. Neichel, ”Predictive adaptive optics for satellite tracking applications: optical communications and satellite observation”, talk, *SPIE Astronomical Telescopes + Instrumentation*, July 2022, Montreal (Canada).
4. **P. Robles**, C. Petit, J.-M. Conan, B. Benammar, and B. Neichel, ”Laboratory validation of an adaptive optics predictive controller for LEO satellite tracking applications”, talk, *COAT*, July 2023, Durham (United Kingdom).
5. **P. Robles**, C. Petit, M.-T. Velluet, L. Le Leuch , A . Montmerle-Bonnefois, L. Paillier , J.-M. Conan, F. Cassaing, J. Montri, and N. Védrenne, ”PICOLO: Turbulence emulator for low elevation LEO links”, poster, *COAT*, July 2023, Durham (United Kingdom).
6. ZEISS European Autumn School Lithography Optics, October 2021, online.
7. International School on Space Optics, October 2021, online.

Résumé

Les liaisons optiques satellite-sol en orbite terrestre basse (LEO) permettront des communications directes à haut débit entre les satellites et les stations sol. Afin d'exploiter les réseaux de télécommunication optique existants, le faisceau optique descendant peut être injecté dans une fibre monomode. Cependant, la turbulence atmosphérique dégrade la propagation du faisceau optique, altérant le couplage dans la fibre monomode. L'optique adaptative (AO) peut fournir une correction en temps réel des effets de turbulence. L'objectif de cette thèse est d'améliorer les performances de l'optique adaptative pour les liaisons optiques LEO-sol.

Dans les applications de liens LEO-sol, le vent apparent dû au mouvement relatif entre le télescope et l'atmosphère entraîne une évolution plus rapide de la turbulence, augmentant l'erreur temporelle induite par le retard entre la mesure et la correction du front d'onde fournies par la boucle d'OA. Cette thèse s'intéresse à la limite théorique de réduction de l'erreur temporelle grâce à la prédiction de la turbulence. Cette thèse considère alors un algorithme de contrôle prédictif pour atténuer en temps réel l'impact de l'erreur temporelle. Les résultats de simulation pour le contrôleur montrent une réduction significative des évanouissements de couplage dans la fibre. Le même contrôleur est appliqué à l'imagerie au sol des satellites en orbite LEO, avec de forts gains en qualité d'image. Alternativement, le contrôleur peut être utilisé pour assouplir la fréquence d'asservissement de boucle d'OA, réduisant ainsi la complexité du système et augmentant le flux de photons disponible pour l'analyse du front d'onde.

Enfin, cette thèse présente PICOLO, un émulateur de turbulence pour les liaisons basse élévation. À basse élévation, les effets de la turbulence sont plus forts, entraînant une scintillation qui altère le fonctionnement de l'OA. Les effets de scintillation du banc ont été caractérisés et comparés à une simulation numérique, validant l'émulateur et définissant ainsi son jumeau numérique. PICOLO servira aux tests en laboratoire de nouveaux concepts d'OA pour les liaisons LEO-sol dans des conditions réalistes. Un premier test a ainsi été réalisé en couplant un système d'OA à l'émulateur ; les statistiques de couplage de la correction par OA utilisant un contrôleur classique ont été comparées avec succès aux simulations numériques. Des travaux ultérieurs mèneront à une démonstration expérimentale du contrôleur prédictif proposé dans la perspective d'une démonstration sur le ciel.

Mots clés : turbulence atmosphérique, optique adaptative, communication optique, satellite en orbite basse, command prédictif, contrôleur linéaire-quadratique-gausséen, filtre de Kalman, forte scintillation

Abstract

Low-Earth-orbit (LEO) satellite-to-ground optical downlinks will allow direct high-data-rate communications between satellites and ground stations. To benefit from the existing optical telecommunication network, the received beam can be injected into a single mode fiber. However, atmospheric turbulence degrades optical beam propagation, impairing coupling into single-mode fiber. Adaptive optics (AO) can provide real-time correction of turbulence effects. The goal of this thesis is to improve the performance of AO for LEO-to-ground optical links.

In LEO satellite tracking applications, the apparent wind due to the relative motion between the telescope and the atmosphere leads to a faster turbulence evolution, increasing the servo-lag error caused by delays between measurement and wavefront correction in the AO loop. This thesis discusses a theoretical upper bound in servo lag error reduction thanks to turbulence prediction. It then proposes a predictive control algorithm to mitigate the impact of servo-lag error. Simulation results for the controller show a significant reduction in fiber coupling fadings. The same controller is applied to ground-based imaging of satellites in LEO orbit, with strong gains in image quality. Alternatively, the predictive controller can be used to relax the loop frequency, reducing the complexity of the AO system and increasing the available photon flux for wavefront sensing.

Finally, this thesis presents PICOLO, a turbulence emulator for low-elevation links. At low elevations, turbulence distortions are stronger, resulting in scintillation that impairs AO. The scintillation characteristics of the bench were characterized and compared with numerical wave propagation simulations, validating the emulator's design and obtaining its digital twin. PICOLO will serve for the laboratory testing of new AO techniques for LEO-to-ground links in realistic conditions. A first test was conducted by coupling an AO system to the emulator; the coupling statistics of AO correction using a classical controller were successfully compared to numerical simulations. Further work will lead to an experimental demonstration of the proposed predictive controller in the prospect of on sky demonstration.

Keywords: atmospheric turbulence, adaptive optics, optical communication, low-Earth orbit satellite, predictive control, linear-quadratic-Gaussian controller, Kalman filter, strong scintillation

Acknowledgements

I would like to start by thanking **Lisa A. Poyneer** (Lawrence Livermore National Laboratory, USA) and **Andrés Guesalaga** (Pontificia Universidad Católica de Chile, Chile) for agreeing to review this manuscript. This gratitude is extended to **Marc Ferrari** (Laboratoire d’Astrophysique de Marseille, France) for presiding the jury of my defense and **Tim Morris** (Durham University, UK) for participating as examiner. It has been a great honor to have my work reviewed by researchers whose work I admire dearly.

One cannot go very far in a PhD thesis without a supervision team and I got the best constellation to guide me. **Benoit**, you always had a solution for any problem, and you gave it wrapped with your cheerfulness. **Bouchra**, thanks for sharing with me your passion for science and technology. You have both being invaluable sources of inspiration and motivation. **Cyril**... I could never imagine a better mentor. I thank you for these three years working together; they were not always easy for me, but you always got my back. Thanks for all the patience and dedication to help me become a better scientist and engineer.

My thesis took place at the *high angular resolution* team of ONERA’s optics department. This is a place of high scientific rigor and technical expertise kept by great scientist (**Aurélie, Béatrice, Caroline, Frédéric, Jean-François, Jean-Marc, Joseph, Laurent, Laurie, Marie-Thérèse, Nicolas, Pedro, Romain, Serge, Taïssir, Thierry, and Vincent**) to whom I owe a lot.

I was never alone in this, since I was always around my journey buddies: **Alix, Émile, Mehdi, Nicolas, Perrine, and Valentina** and the other PhD students and interns (**Chloé, Laurie, Matthieu, Yann L.-T., Antoine C., Luca, Hugo, Léa, Hiyam, Daniel, Yann, Pierre, Antoine O., Thimotée, Inès, and Alberto**). Thank you all for the coffee breaks, the Among Us nights, the boardgame evenings, the conferences, the seminars, the tarot games, the secret Santa, the St. Valentine’s... You were beyond question the best part of the thesis.

Yes, **Laurie** is both in the staff and in the student list, since she was everywhere and everything in the lab; I am very proud of all the things we went through together and how they made us stronger.

Of course, I cannot forget the unconditional support of my friends. The ones I met in Paris (**Carmen, Dawid, Elena, Federico, Hashmita, Paolo, Victoria**) and the ones back at home in Spain (**Andrea, Alba, Ignacio, Manuel, David, Íñigo, Carlos, Javier, Verónica, and Silvia**).

Thanks to my girlfriend **Carla**, not only because without her motivation and time management tips, I would not have managed to ever finish this manuscript,

but especially for her love, support, and understanding. I feel very lucky to have you by my side. Now you will not need to tell me anymore that it is time to finish Chapter 4.

Thanks to my aunt **Lucy**, to my brother **Mario** and sister **Lucía**, and to the rest of my **family**. Without you at my side, not only it would not be possible to achieve all I did, but it would be meaningless.

Lastly, I would like to thank my mother **Maite**; this manuscript is, of course, dedicated to her.

Synthèse en Français

Contexte

L'expansion rapide des applications spatiales, notamment l'observation de la Terre, les communications à large bande par satellite et l'exploration spatiale, a accru la demande de liaisons de communication de plus grande capacité entre les satellites et la Terre. Cette demande est encore plus forte à l'ère des grandes constellations de satellites et des missions dans l'espace lointain avec des charges utiles à haute résolution à bord, qui génèrent des volumes massifs de données. Les systèmes traditionnels de radiofréquences approchent de leurs limites inhérentes en termes de largeur de bande et de débit de données. Les communications optiques, en raison de la fréquence plus élevée des ondes électromagnétiques optiques, peuvent offrir des largeurs de bande supérieures qui dépassent de plusieurs ordres de grandeur les liaisons par radiofréquence, avec un objectif d'un téraoctet par seconde.

Les liaisons optiques espace-sol sont également confrontées à des défis importants. Avant tout, l'atmosphère terrestre atténue, diffuse et déforme le faisceau laser en raison de l'absorption, de la couverture nuageuse, du brouillard, de la pluie et des turbulences atmosphériques. Ces effets entraînent une perte et une fluctuation de la puissance reçue, ce qui provoque des erreurs et des coupures dans la communication et limite le débit de données possible. L'absorption atmosphérique peut être atténuée en sélectionnant correctement la longueur d'onde de la porteuse optique, et les phénomènes liés aux conditions météorologiques peuvent être évités grâce à la diversité des sites. Les turbulences atmosphériques, qui provoquent des distorsions de phase et d'amplitude sur l'onde optique porteuse, peuvent être corrigées par l'optique adaptative.

L'optique adaptative est une technique de correction des effets de la turbulence optique atmosphérique. Elle a été développée pour l'astronomie et les applications militaires, mais elle est désormais utilisée dans d'autres domaines tels que l'imagerie biomédicale et les communications optiques en espace libre. L'optique adaptative mesure et corrige les distorsions de phase du faisceau au moyen d'un capteur de front d'onde et d'un miroir déformable contrôlé par un ordinateur en temps réel qui traite les mesures et calcule les commandes de miroir nécessaires à l'aide d'une boucle de contrôle. La correction de phase fournie par l'optique adaptative permet de coupler le faisceau reçu dans une fibre optique monomode, tirant ainsi parti de toutes les techniques de détection optique développées pour les communications par fibre optique, telles que les amplificateurs optiques et la détection cohérente. L'optique adaptative a été reconnue comme un élément clé des futures liaisons

optiques espace-sol. Après plusieurs démonstrations de cette technique, plusieurs stations optiques au sol équipées d'optique adaptative sont actuellement en cours de construction.

Les satellites *Low Earth orbit (LEO)* sont les plus courants. Ce type d'orbite est le plus proche de la Terre et offre donc une meilleure résolution spatiale pour les charges utiles de télédétection ainsi qu'une latence plus faible pour les communications. En outre, les satellites *LEO* restent dans le champ de vision d'une station terrestre pendant environ dix minutes, ce qui limite la durée possible des liaisons de communication. Par conséquent, les liaisons descendantes optiques *direct-to-Earth (DTE)* entre les satellites *LEO* et le sol permettront aux charges utiles d'observation de la Terre de transférer la quantité croissante de données qu'elles génèrent dans le temps limité de leurs liaisons.

Les liaisons par satellite *LEO* sont particulièrement difficiles en raison du mouvement rapide du satellite dans le ciel. Pour l'optique adaptative, cela signifie trois choses : (1) les conditions de turbulence changent au fur et à mesure que la ligne de visée du satellite change ; (2) la vitesse angulaire rapide de la ligne de visée équivaut à une évolution plus rapide de la turbulence observée ; et (3) pour prolonger la durée de la liaison, celle-ci doit fonctionner à basse altitude, où la turbulence optique est plus forte. Cette thèse est consacrée à l'amélioration des performances des systèmes d'optique adaptative pour les applications satellitaires *LEO* en relevant ces défis.

Dans cette thèse, une deuxième application est également considérée en raison de ses fortes synergies avec ce défi : l'imagerie des satellites *LEO* depuis le sol. L'observation de l'orbite *LEO* avec des télescopes au sol peut être utilisée pour la surveillance et le contrôle des engins spatiaux en orbite. La présence de turbulences optiques réduit la résolution effective des télescopes, et l'optique adaptative peut aider à corriger ces effets pour obtenir des images à la limite de diffraction. Cette application présente des problèmes similaires à ceux des liaisons optiques *LEO* vers le sol, bien que le flux de signaux et les conditions de turbulence soient différents.

La boucle d'optique adaptative présente un retard inhérent entre la mesure et la correction qui entraîne une différence entre la phase corrigée et la phase au moment de la correction et, par conséquent, une diminution des performances. L'effet de ce retard est accru dans le cas des satellites *LEO*, puisque la trajectoire du satellite implique le mouvement relatif du faisceau et des couches de l'atmosphère, ce qui provoque une évolution plus rapide des distorsions atmosphériques. Cette thèse propose un nouvel algorithme de contrôle prédictif qui modélise la turbulence pour prédire son évolution entre sa mesure et sa correction. Les gains potentiels en performance du système grâce à un tel contrôleur prédictif sont analysés pour les deux applications considérées.

Il n'est pas nécessaire de travailler à faible altitude pour les applications astronomiques traditionnelles, puisque les observations sont limitées à des altitudes plus élevées où les conditions de turbulence sont plus favorables ; cependant, l'extension du fonctionnement de l'optique adaptative à de faibles altitudes en-

traînera une augmentation significative de la durée de la liaison optique. À faible hauteur de visée, la turbulence est plus forte et les distorsions d'amplitude sur le front d'onde dues à l'effet de la turbulence deviennent plus importantes. Les distorsions d'amplitude se manifestent par des distributions d'irradiance inhomogènes de type speckle sur la pupille du télescope, également connues sous le nom de scintillation. L'optique adaptative ne peut pas corriger les distorsions d'amplitude, mais ces distorsions peuvent entraver le fonctionnement des systèmes d'optique adaptative, par exemple en affectant les mesures du front d'onde. Une bonne connaissance de ces distorsions et de leurs effets sur les systèmes d'optique adaptative est nécessaire pour développer des systèmes plus robustes. Cette thèse a travaillé sur une installation de laboratoire pour l'émulation de la turbulence dans ce scénario, avec un accent particulier sur la caractérisation de la scintillation et sa comparaison avec les simulations numériques. Un tel émulateur de turbulence sera utilisé pour étudier de nouvelles solutions de contrôle d'optique adaptative qui prennent en compte les effets de scintillation.

Objectifs et contribution de la thèse

Dans cette thèse, j'ai travaillé sur deux projets principaux. Tout d'abord, j'ai développé un nouveau contrôleur prédictif dans le but d'améliorer la performance des systèmes d'optique adaptative dans les applications satellitaires. Initialement, la principale application envisagée pour ce contrôleur était la communication optique, mais au cours de ma thèse, j'ai également évalué l'observation au sol des satellites comme deuxième application. Jean-Marc Conan et Cyril Petit avaient déjà réalisé une évaluation théorique des gains de performance maximaux que la prédiction de la turbulence pouvait apporter à l'optique adaptative ; j'ai poursuivi ce travail en développant un contrôleur prédictif, et j'ai également contribué à sa publication sous le titre [Conan et al. \(2023\)](#). Pendant le développement du contrôleur, j'ai essayé d'atteindre cette performance ultime et de comprendre les limites du système qui l'éloignent de cette performance optimale. Enfin, j'ai étudié les gains de performance dans les applications spécifiques grâce à l'utilisation de la commande prédictive.

Deuxièmement, j'ai travaillé sur l'émulateur de turbulence *PICOLO* pour les liaisons descendantes *LEO* vers le sol dans des conditions de forte turbulence. J'ai travaillé sur la caractérisation de la scintillation du banc et sa comparaison avec les simulations numériques. De plus, j'ai travaillé sur le couplage du banc à un système d'optique adaptative, ce qui permettra à l'avenir de tester le contrôleur prédictif développé durant cette thèse, ainsi que d'autres méthodes d'optique adaptative, dans des conditions de turbulences réalistes et de les comparer au jumeau numérique du banc qui est maintenant disponible grâce à ma caractérisation.

Les travaux présentés dans ce manuscrit ont porté sur l'amélioration de la correction de la turbulence atmosphérique de l'optique adaptative dans le cas des

liaisons optiques descendantes *LEO* vers le sol et de l'imagerie des satellites à partir de télescopes terrestres.

Conclusions générales

Au chapitre 1 j'ai présenté l'origine de la turbulence optique et ses effets sur un faisceau qui s'y propage. J'ai montré comment les aberrations de phase introduites par la turbulence atmosphérique se transforment également en distorsions d'amplitude au cours de la propagation, en particulier dans les cas de forte turbulence, ce qui entraîne des fluctuations d'irradiance à travers la pupille du télescope, connues sous le nom de scintillation. J'ai également présenté la description statistique de la turbulence et sa représentation en tant que projection sur une base polynomiale de Zernike, qui est au cœur de l'identification des modèles prédictifs présentés plus loin dans ce manuscrit.

Au chapitre 2 j'ai présenté le principe de l'optique adaptative et ses composants. Le chapitre a également donné une introduction au contrôle de l'optique adaptative et à l'importance du retard, un concept crucial pour cette thèse puisqu'il est à l'origine du besoin de contrôle prédictif. Enfin, j'ai introduit le concept de budget d'optique adaptative, l'outil principal pour la conception et l'évaluation des performances des systèmes d'optique adaptative.

Le chapitre 3 a décrit l'effet de la turbulence atmosphérique sur la qualité de l'imagerie des télescopes et sur le couplage des fibres et les systèmes de communication. J'ai également présenté les différents systèmes pris en compte dans les études de cas de ce manuscrit. Quatre systèmes différents ont été présentés, deux pour les communications optiques et deux pour l'observation par satellite, couvrant deux spécifications de système, l'une plus performante et complexe et l'autre plus simple et moins coûteuse.

Au chapitre 4 j'ai discuté des deux principaux éléments du contrôleur prédictif de cette thèse et de la plupart des contrôleurs de la littérature : les modèles autorégressifs et le contrôleur *LQG* en tant que contrôleur prédictif. J'ai souligné comment le contrôleur *LQG* incorpore trois tâches nécessaires que de nombreux systèmes d'optique adaptative mettent en œuvre séparément : (1) la reconstruction de la phase à partir de l'espace de pente du capteur de front d'onde vers l'espace de phase souhaité (espace zonal, modal ou *DM*), (2) l'optimisation du gain du contrôleur et (3) l'estimation de la phase future pour réduire l'effet du délai entre la mesure et la correction, c.-à-d. le contrôle prédictif.

Dans le chapitre 5 j'ai présenté la méthode de prévisibilité des turbulences initialement introduite dans [Conan et al. \(2023\)](#) et je l'ai appliquée aux systèmes étudiés. J'ai analysé à la fois la prévisibilité des systèmes et la possibilité de réduire la fréquence de la boucle *AO*. La méthode a montré des gains très prometteurs pour la plupart des systèmes. Seuls les systèmes *FEELINGS* semblent avoir déjà une très bonne performance en termes d'erreur temporelle. Parmi les autres résultats,

on peut citer la nécessité d'utiliser des modèles *VAR* d'ordre supérieur pour obtenir de meilleures performances de prédiction dans le cas des applications satellitaires *LEO* pour l'optique adaptative.

Le chapitre 6 a présenté le contrôleur prédictif développé dans cette thèse : le *high-order VAR Zernike LQG*. J'ai discuté de la manière dont le modèle est identifié et de ses similitudes avec le prédicteur utilisé au chapitre 5. J'ai également fourni une analyse des schémas possibles d'identification des données qui pourraient conduire à une identification en ligne du contrôleur et à son adaptation le long de la trajectoire *LEO*.

Le chapitre 7 présente les simulations de bout en bout du contrôleur dans différents scénarios. Une première simulation a utilisé un capteur de front d'onde simplifié et un miroir déformable pour vérifier les performances du modèle prédictif dans le *LQG* et les comparer à l'évaluation de la prévisibilité ; la comparaison a prouvé que dans les conditions simplifiées, le contrôleur peut atteindre les performances attendues par l'évaluation. Cette simulation a également été utilisée pour montrer la robustesse du contrôleur par rapport au bruit de mesure. L'introduction d'un capteur de front d'onde Shack-Hartmann dans les simulations exige que le contrôleur effectue également une reconstruction modale à partir des mesures de la pente vers les polynômes de Zernike utilisés par le modèle prédictif. Cette opération et la présence d'un repliement provoquent une erreur supplémentaire dans le contrôleur qui, si elle n'est pas gérée correctement, entraîne une erreur beaucoup plus importante que l'erreur de repliement présente dans le contrôleur à action intégrale classique. J'ai proposé une analyse de cette reconstruction en utilisant le reconstruteur *MAP* comme substitut de la reconstruction dans le filtre de Kalman. Le reconstruteur *MAP* a été utilisé pour étudier le nombre optimal de modes nécessaires pour diminuer l'erreur de reconstruction, l'influence du facteur de correction et le bruit de mesure dans cette reconstruction. Bien qu'un facteur de correction puisse être utilisé pour améliorer la performance de la reconstruction sans augmenter le nombre de modes reconstruits, la recommandation de cette thèse est de reconstruire plus de modes (à peu près les modes équivalents à deux fois la fréquence d'échantillonnage du Shack-Hartmann). Les simulations de bout en bout du contrôleur ont montré comment les contrôleurs prédictifs réduisent de manière significative l'erreur temporelle dans les systèmes d'optique adaptative. L'impact de cette réduction sur les mesures de performance spécifiques du système dépend du reste du budget *AO* et de la nature de la mesure. Pour le couplage de fibres monomodes, la commande prédictive est capable de réduire les évanouissements ; pour l'observation par satellite, la réduction de la variance résiduelle conduit à de fortes améliorations du rapport de Strehl. Dans tous les cas, les contrôleurs prédictifs peuvent être utilisés pour réduire la fréquence de la boucle d'optique adaptative à la moitié de la fréquence nominale tout en maintenant les performances d'un contrôleur intégral. Pour l'observation par satellite, cela signifie l'imagerie de cibles moins lumineuses.

Le chapitre 8 fait état de mes travaux sur la caractérisation de la scintillation

de l'émulateur de turbulence *PICOLO* pour les liaisons *LEO* vers le sol dans des conditions de forte turbulence. J'ai effectué des mesures expérimentales de la scintillation sur le banc, d'abord par écran puis pour le profil de turbulence complet, et je les ai comparées à des simulations numériques utilisant le code de simulation *TURANDOT*. La caractérisation a montré que le banc fournit les caractéristiques de scintillation attendues et le jumeau numérique qui en résulte peut maintenant être utilisé pour comparer les performances des expériences sur le banc aux simulations numériques. Cette caractérisation est essentielle pour préparer la validation expérimentale de concepts innovants en matière de détection et de contrôle du front d'onde afin de permettre à l'optique adaptative de faire face à la scintillation à faible élévation. Pour préparer ces travaux futurs, j'ai également réalisé les premières expériences avec l'émulateur en utilisant le système d'optique adaptative *LISA*, comme je l'ai indiqué au chapitre 9.

Limitations et recommandations

Cette section présente mes recommandations basées sur les résultats de cette thèse et leurs limites. Mes suggestions particulières sont décrites ci-dessous :

1. Cette thèse a défini un ensemble de quatre systèmes d'optique adaptative et leurs profils de turbulence associés en essayant de couvrir les points de fonctionnement et les situations les plus courants. Bien que la méthodologie proposée puisse être appliquée à n'importe quel système et que les tendances observées devraient être cohérentes pour d'autres points de fonctionnement, seule une étude de cas pour chaque système considéré pourrait donner des résultats définitifs.
2. La méthode d'identification de cette thèse, basée sur des expressions analytiques des covariances angulaires entre les coefficients de la phase turbulente projetés sur une base polynomiale de Zernike, a une grande valeur non seulement pour les évaluations théoriques, mais aussi pour une mise en œuvre sur le ciel et l'adaptation du contrôleur grâce à des antécédents. Néanmoins, une méthode basée sur l'identification des matrices de covariance spatio-temporelles à partir des données, suivant la discussion de la section 6.3 devrait être étudiée, en particulier une méthode basée sur l'identification récursive pour permettre l'adaptation du modèle prédictif sur toute la *LEO* trajectoire du satellite.
3. Il a été démontré que le coût de calcul du contrôleur prédictif doit augmenter pour réduire la propagation du repliement dans la reconstruction modale et le modèle prédictif du contrôleur. Dans le cas du couplage de fibres, les modèles d'ordre supérieur ont moins d'effet sur les évanouissements ; le contrôleur proposé pourrait être simplifié en réduisant le nombre de modes prédits.

4. Il a été démontré que le coût de calcul du contrôleur prédictif doit augmenter pour réduire la propagation du repliement dans la reconstruction modale et le modèle prédictif du contrôleur. Dans le cas du couplage de fibres, les modèles d'ordre supérieur ont moins d'effet sur les évanouissements ; le contrôleur proposé pourrait être simplifié en réduisant le nombre de modes prédits.
5. Les contrôleurs de l'espace de pente devraient faire l'objet d'un examen plus approfondi en raison de leur facilité d'identification et de la réduction des besoins d'étalonnage, en particulier dans les cas où le repliement dans les modes d'ordre supérieur peut ne pas être toléré.
6. Cette thèse a limité les essais du contrôleur aux distorsions du front d'onde en phase seulement et à une propagation géométrique de la phase turbulente. Les performances du contrôleur prédictif devraient être testées dans des conditions de forte turbulence. Deux points seront cruciaux : (1) Les formules analytiques pour le calcul des statistiques de phase peuvent ne pas fonctionner dans des conditions de forte turbulence et de phase fortement diffractée ; dans ce cas, l'utilisation d'une identification basée sur les données peut s'avérer nécessaire pour obtenir ces statistiques. (2) La robustesse du contrôleur aux effets de scintillation sur la détection du front d'onde doit également être étudiée.
7. Le contrôleur prédictif présenté dans cette thèse pourrait être combiné à l'approche proposée par [Lognoné et al. \(2022\)](#), qui propose un estimateur de l'angle d'avance des liaisons optiques montantes en utilisant des statistiques de phase et de scintillation.
8. L'utilisation de la commande prédictive peut servir de technique d'atténuation des effets de la scintillation sur le capteur de front d'onde Shack-Hartmann. Les mesures manquantes peuvent être remplacées par des prédictions de la phase, c'est-à-dire qu'il n'y a pas d'étape de mise à jour s'il n'y a pas de mesure, au lieu d'utiliser une mesure médiocre. Deux techniques supplémentaires peuvent être utilisées pour rendre le contrôleur plus robuste à la scintillation :
 - a) L'utilisation d'un filtre de Kalman séquentiel qui met à jour les mesures de pente indépendamment (en supposant qu'il n'y a pas de corrélation entre les bruits de mesure dans les mesures de pente, une hypothèse déjà utilisée) et qui saute l'étape de mise à jour lorsque la mesure de pente est annotée comme non valide en raison des effets de la scintillation ; dans ce cas, seule l'étape de prédiction sera utilisée.
 - b) L'utilisation d'une base zonale pour maximiser le découplage entre les points de la pupille du télescope. La présence de scintillation signifie que certaines zones de la pupille n'auront pas de flux ; la reconstruction de la phase sur la pupille peut imposer de fortes contraintes et aggraver la reconstruction des points qui n'ont pas de problèmes de scintillation. L'utilisation d'une base zonale pour le contrôle peut aider à traiter le

front d'onde lorsqu'il n'y a pas de mesures disponibles pour plusieurs points de la pupille.

9. La prochaine étape dans le développement du contrôleur prédictif devrait être sa démonstration en laboratoire en utilisant l'émulateur de turbulence *PICOLO* avant sa validation sur le ciel. Cette thèse a commencé ce travail mais n'a pas pu le terminer. Une première démonstration devrait utiliser un seul écran de phase à la pupille du télescope pour éviter tout effet de scintillation. Par la suite, le banc peut également être utilisé pour tester le contrôleur dans des conditions de forte turbulence et de scintillation. Différentes méthodes d'identification peuvent également être testées sur le banc.

To my mother, of course.

*The greatest remedy for
anger is delay.*

— Lucius Annaeus Seneca

Contents

Affidavit	ii
List of Publications and Conferences	iii
Résumé	iv
Abstract	v
Acknowledgements	vi
Synthèse en Français	viii
Contents	xviii
List of Figures	xxiii
List of Tables	xxvi
Lists of Acronyms	xxvii
Introduction	1
I. Adaptive Optics for Satellite-to-Ground Links	5
1. Propagation of Light across Atmospheric Turbulence	6
1.1. Atmospheric Optical Turbulence	7
1.1.1. Physical Origin	7
1.1.2. Index of Refraction Fluctuations	8
1.1.3. Frozen Flow Hypothesis	9
1.2. Optical Propagation in Turbulent Media	10
1.2.1. Helmholtz Equation	11
1.2.2. Phase Screen Propagation Model	13
1.2.3. Weak Perturbations Regime	14
1.2.4. Geometric Propagation of Phase	17
1.2.5. Integrated Parameters	17
1.2.6. Strong Perturbations Regime	18

1.3.	Modal Decomposition of the Phase	20
1.3.1.	Zonal Basis	21
1.3.2.	Zernike Polynomials	21
2.	Adaptive Optics	27
2.1.	Adaptive Optics Principle	28
2.2.	Wavefront Sensing	29
2.3.	Wavefront Correction	31
2.4.	Adaptive Optics Control	32
2.4.1.	Adaptive Optics Loop	33
2.4.2.	Interaction and Control Matrices	34
2.4.3.	Integral Action Control	36
2.4.4.	Modal Control	36
2.4.5.	Phase Reconstruction	37
2.4.6.	Linear Quadratic Gaussian Control	39
2.5.	Error Budget	39
2.5.1.	Turbulence Induced Errors	39
2.5.2.	Adaptive Optics System Errors	41
2.5.3.	Other Errors	43
3.	Adaptive Optics for <i>LEO</i> Satellite Tracking	45
3.1.	Low-Earth-Orbit Satellite Tracking	46
3.1.1.	Challenges of <i>AO LEO</i> Applications	48
3.1.2.	Satellite Orbits Considered	49
3.2.	Turbulence Conditions	50
3.2.1.	Atmospheric Turbulence Profiles	50
3.2.2.	Wind Profile	53
3.2.3.	Variation of Integrated Parameters with Elevation	54
3.3.	System Performance Metrics	56
3.3.1.	Image Formation in Presence of Atmospheric Turbulence	56
3.3.2.	Communication Channel Impairments Induced by the Atmosphere	59
3.4.	Adaptive Optics Systems: Case Studies	63
3.4.1.	Wavefront Sensing Noise Levels	63
3.4.2.	Error Budgets	65
4.	Atmospheric Turbulence Prediction	70
4.1.	Temporal Prediction Problem	71
4.1.1.	Mathematical Formulation	71
4.1.2.	Predictive Control for Adaptive Optics	72
4.2.	Autoregressive Predictive Models	74
4.2.1.	VAR(p) Processes	74
4.2.2.	Important Properties	75

4.2.3.	Autoregressive Model Identification	78
4.2.4.	Yule-Walker Estimator	79
4.2.5.	Computation of Spatio-Temporal Covariance Matrices	82
4.3.	Linear-Quadratic-Gaussian Controller as Predictive Controller	86
4.3.1.	State-Space Representation for a Linear Stochastic System	87
4.3.2.	Optimal Linear-Quadratic-Regulator (<i>LQR</i>)	88
4.3.3.	Kalman Filter	90
4.3.4.	Synthesis of the <i>LQG</i> Controller	94
4.3.5.	Use of the <i>LQG</i> in Adaptive Optics	94
4.3.6.	Summary of the <i>LQG</i> Predictive Controller	95

II. Predictive Controller 97

5. Assessment of Turbulence Predictability 98

5.1.	<i>MMSE</i> Temporal Prediction	99
5.1.1.	State of the Art	99
5.1.2.	Linear <i>MMSE</i> Estimator	100
5.1.3.	Temporal Prediction as a Linear Estimation Problem	101
5.1.4.	Phase Representation	102
5.1.5.	Prediction Error	102
5.1.6.	No Prediction Error	104
5.1.7.	Adaptive Optics Performance Assessment	104
5.1.8.	<i>MMSE</i> vs. <i>VAR</i> Predictors	105
5.1.9.	Data-based Version of the <i>MMSE</i> Predictor	106
5.2.	Predictability of <i>LEO</i> Satellite <i>AO</i> Applications	106
5.2.1.	Prediction Gain	107
5.2.2.	Predictability	108
5.2.3.	Effect of the Model Order	111
5.2.4.	Results per Mode	113
5.2.5.	Reduction of Loop Frequency	116
5.2.6.	Performance on a Time Series	117
5.2.7.	Effect of Unknown Natural Wind	119

6. Higher-Order *VAR* Zernike *LQG* 124

6.1.	Controller Description	125
6.1.1.	State-Space Representation	126
6.1.2.	Stability	129
6.1.3.	Predictive Model	130
6.2.	Comparison to Other Methods	131
6.2.1.	Covariance-Based Translation	132
6.2.2.	Explicit Zonal Representation Translation	135
6.2.3.	Explicit Fourier Domain Translation	136

6.3.	Data-Based Identification	137
6.3.1.	Identification of Spatio-Temporal Covariance Matrices	137
6.3.2.	Learn & Apply Method	141
6.3.3.	Other Identification Methods	144
6.4.	Model Update and Adaptation	145
6.4.1.	Analytical Model Update	145
6.4.2.	Data-Based Recursive Model Update	145
7.	Predictive Controller Results	147
7.1.	Simulation Methodology	148
7.1.1.	Simulation Strategy	148
7.1.2.	Simulations Implementation	149
7.2.	Ideal Wavefront Sensor and Deformable Mirror	151
7.2.1.	Comparison with the <i>MMSE</i> Predictability Assessment	152
7.2.2.	Behavior in the Presence of Measurement Noise	154
7.2.3.	Conclusions	154
7.3.	Effect of Aliasing and Modal Reconstruction	156
7.3.1.	Problem Statement	156
7.3.2.	Aliasing in Predictive Controllers	156
7.3.3.	Analytical Study of Modal Reconstruction with <i>MAP</i>	157
7.3.4.	Methodology	157
7.3.5.	Case 1: 8×8 <i>SH</i> and $n_{\text{cor}} = 10$ <i>DM</i>	161
7.3.6.	Case 2: 16×16 <i>SH</i> and $n_{\text{cor}} = 20$ <i>DM</i>	164
7.3.7.	Case 3: <i>LISA</i> and <i>FEELINGS</i>	165
7.3.8.	Case 4: Oversampled 16×16 <i>SH</i> and $n_{\text{cor}} = 10$ <i>DM</i>	166
7.3.9.	Case 5: Effect of Telescope Aperture Obscuration	167
7.3.10.	Conclusions	167
7.4.	End-to-End Simulations	170
7.5.	Reduction of the Loop Sampling Frequency	172
7.6.	Effect of Fadings	173
7.7.	Strehl Ratio	175
III.	Experimental Validation	180
8.	<i>PICOLO</i> Turbulence Emulator	181
8.1.	Context	184
8.2.	Optical Turbulence Emulation	185
8.3.	Bench Definition	188
8.3.1.	Turbulence Profile Compression	188
8.3.2.	Propagation Path Geometrical Scaling	190
8.3.3.	Phase Screen Specification	192
8.3.4.	Opto-mechanical Design	193

8.4.	Characterization	195
8.4.1.	Phase Characterization	195
8.4.2.	Scintillation Characterization	198
8.5.	Operating Conditions	206
8.6.	Conclusion	206
9.	Experimental Validation	210
9.1.	Towards a Predictive Controller Demonstration	211
9.2.	<i>LISA</i> Adaptive Optics System	212
9.3.	Coupling to the <i>PICOLO</i> Turbulence Emulator	214
9.4.	Coupling Optimization	216
9.5.	Coupling Measurements	217
9.6.	Integrator Validation	218
9.6.1.	<i>RTC</i> Implementation	219
9.6.2.	Temporal Characterization	219
9.6.3.	Results	221
	Conclusion	223
	Bibliography	227
	Appendices	256
A.	Mathematical Notation	256
A.1.	Covariance and Cross-covariance Matrices	256
A.2.	Auto-covariance Matrix	256
B.	Derivation of the Minimum Mean Square Error Estimator	258
B.1.	Derivation of the MMSE Estimator without Measurement Noise	258
B.2.	Derivation of the MMSE Estimator with Measurement Noise	259
C.	Frequency Coverage of Zernike Polynomials vs. Zonal Basis	262
D.	Turbulence temporal prediction performance assessment for adaptive optics: application to LEO satellite observation and communication links	265

List of Figures

1.1. Saturation of the scintillation with the increase of the turbulence strength.	20
1.2. Intensity <i>PSD</i> for a plane wave after a phase screen.	20
1.3. Covariance matrix of Zernike modes assuming Kolmogorov turbulence.	24
2.1. Adaptive optics system diagram. (Credit: C. Max.)	29
2.2. Architecture diagram of a closed-loop adaptive optics system.	34
2.3. Chronogram of the adaptive optics control loop.	34
3.1. Evolution of elevation of the line of sight and distance to the satellite with time for a 750 km altitude orbit with culmination at 90°.	47
3.2. Satellites launched per year and orbit type since the year 2000. (Source: USC (2023)).	48
3.3. Example of changing turbulence conditions with elevation.	50
3.4. Atmospheric turbulence profiles used for the different operating points.	53
3.5. Wind profiles considered for the case studies. The natural wind profile is given by a Bufton profile with a ground layer speed of 3 m/s and an upper layer speed of 20 m/s. The apparent wind speed is given by the product between the angular speed of the tracking and the distance to the corresponding layer of turbulence. The profiles are plotted for two different layers to illustrate their variation with elevation.	54
3.6. Evolution of integrated parameters with elevation for the <i>MOSPAR-90/90</i> day-time profile used for the optical communication case studies.	55
3.7. Evolution of integrated parameters with elevation for the <i>MOSPAR-75/75</i> night-time profile used for the satellite observation case studies.	55
3.8. Illustration of the effect of turbulence on the <i>PSF</i>	58
3.9. Computation of the Strehl ratio.	58
3.10. Noise ranges covered by the <i>SNR</i> scale.	65
3.11. <i>AO</i> budget for the four system configurations considered.	69
4.1. Illustration of the use of frozen flow assumption to compute temporal phase covariances from spatial statistics.	83
4.2. Geometry for the computation of temporal cross-covariances of turbulence projected on Zernike polynomials using spatial statistics.	85

5.1.	Predictability for different <i>AO</i> system parameters that influence the temporal correlation of turbulence.	110
5.2.	Prediction performance vs. model order for different predictors.	112
5.3.	Residual phase modal variance for the <i>LISA</i> case with and without <i>MMSE</i> temporal prediction.	114
5.4.	Residual phase modal variance for the <i>ODISSEE</i> case with and without <i>MMSE</i> temporal prediction.	114
5.5.	Residual phase modal variance for the <i>ODISSEE</i> case with and without <i>MMSE</i> temporal prediction.	115
5.6.	Residual phase variance after prediction for a different number of predicted modes for the <i>ODISSEE</i> system.	116
5.7.	Autocovariance matrices for the <i>LISA</i> case.	116
5.8.	Residual phase variance after prediction for a different number of predicted modes for the <i>ODISSEE</i> system.	117
5.9.	Prediction of a time series using a predictor computed from theoretical covariance data and from the sample covariance data.	119
5.10.	Comparison of <i>MMSE</i> prediction performance in the case of known and unknown natural wind.	120
7.1.	Analytical <i>MAP</i> reconstruction performance, <i>ODISSEE</i> , 8×8 SH, $n_{\text{cor}} = 10$, several <i>SNRs</i>	161
7.2.	Analytical <i>MAP</i> reconstruction performance, <i>ODISSEE</i> , 8×8 SH, $n_{\text{cor}} = 10$, $\text{SNR} = 100$, several fudge factors.	163
7.3.	Numerical verification of the <i>MAP</i> reconstruction performance for <i>ODISSEE</i> , 8×8 SH, $n_{\text{cor}} = 10$, $\text{SNR} = 100$	164
7.4.	Analytical <i>MAP</i> reconstruction performance, <i>ODISSEE++</i> , 16×16 SH, $n_{\text{cor}} = 20$, several <i>SNRs</i>	165
7.5.	Numerical verification of the <i>MAP</i> reconstruction performance for <i>ODISSEE++</i> , 16×16 SH, $n_{\text{cor}} = 20$, $\text{SNR} = 100$, no fudge factor.	165
7.6.	Numerical verification of the <i>MAP</i> reconstruction performance for the communication systems.	166
7.7.	Analytical <i>MAP</i> reconstruction performance, <i>ODISSEE</i> , 16×16 SH, $n_{\text{cor}} = 10$, several <i>SNRs</i>	167
7.8.	Analytical <i>MAP</i> reconstruction performance, <i>ODISSEE</i> , 16×16 SH, $n_{\text{cor}} = 10$, $\text{SNR} = 100$, several fudge factors.	168
7.9.	Numerical verification of the <i>MAP</i> reconstruction performance in the presence of a 25% obscuration, $\text{SNR} = 100$, no fudge factor.	168
7.10.	Coupled flux time series for different controller simulations.	174
7.11.	Coupled flux <i>CDF</i> for different controller simulations.	175
7.12.	Coupled flux <i>CDF</i> for different controller simulations with perfect tip-tilt correction.	176
7.13.	End-to-end simulation Strehl ratio time series for the <i>ODISSEE</i> system.	176

7.14. End-to-end simulation Strehl ratio time series for the <i>ODISSEE++</i> system.	177
8.1. Opto-mechanical design of the <i>PICOLO</i> turbulence emulator.	194
8.2. Image of the implementation of the <i>PICOLO</i> bench.	194
8.3. Exemplary experimental acquisitions of short-exposure <i>PSF</i> and pupil images for the different phase screen configurations.	195
8.4. Reconstructed Zernike mode variances vs. their fit to a von Kármán spectrum for <i>PS2</i>	198
8.5. Spatial and temporal one-dimensional power spectral densities of the normalized irradiance distributions produced by the phase screens.	203
8.6. Cumulative sum of spatial and temporal one-dimensional power spectral densities of the normalized irradiance distributions produced by the phase screens.	204
8.7. Zoom in on the time series of the pupil averaged flux.	207
8.8. Power spectral density of the time series of the pupil averaged flux.	207
8.9. Histogram of the time series of the pupil averaged flux.	207
9.1. Strategy for the demonstration of the predictive controller using the <i>PICOLO</i> bench.	212
9.2. <i>LISA</i> adaptive optics system.	214
9.3. Coupling between the <i>PICOLO</i> turbulence emulator and the <i>LISA</i> adaptive optics bench.	215
9.4. Zoom in the coupling path of the <i>LISA</i> system.	216
9.5. Comparison of the integrator rejection transfer function measured on the laboratory vs. its theoretical model.	220
9.6. Coupling efficiency results, comparison between the experiment (integral action controller) and the numerical simulations (integral action controller and predictive controller).	221
C.1. Comparison of the spatial frequency coverage vs. the number of required variables for a zonal and a Zernike polynomial basis. The zonal basis is oversampled as a multiple of the number of subpupils in the system, N_{sp} , or an equivalent number of radial orders, n_{max}	263

List of Tables

3.1.	Adaptive optics system parameters for the four <i>AO</i> configurations.	64
3.2.	<i>AO</i> error budget for different elevations.	68
5.1.	Prediction gains for all <i>AO</i> configurations vs. elevation. Residual phase variance (in rad ²) over the corrected modes.	109
5.2.	Performance of the $\mathbf{R}_{\text{MMSE}}^{(s=2,p)}$ predictor for different model orders.	113
5.3.	<i>AO</i> residual wavefront variance (in rad ²) budget for <i>ODISSEE</i> configuration.	118
7.1.	Results for the simplified <i>E2E</i> controller simulation and comparison with respect to the predictability assessment.	153
7.2.	Performance of the controller as a function of <i>SNR</i> , <i>ODISSEE</i> case at 30° elevation.	155
7.3.	Results for the controller simulations using an increased number of modes.	171
7.4.	Results for the controller simulations reducing the <i>AO</i> loop frequency by a factor of two.	173
7.5.	End-to-end simulation Strehl ratio results, units of %.	177
8.1.	Integrated turbulence parameters for the 50-layer profile and the compressed three-layer profile.	189
8.2.	Resulting geometric down-scaling for the different phase screens.	192
8.3.	Summary of the different three-layer profiles considered in this work.	193
8.4.	Reconstructed Zernike mode variances fitting results to von Kármán spectrum.	198
8.5.	Spatial scintillation index comparison between numerical simulation and experiment.	202
8.6.	Temporal scintillation index comparison between numerical simulation and experiment.	205
8.7.	Operating conditions of the turbulence delivered by the emulator.	208
9.1.	Coupling calibrations for the 13/03/2023 experiment.	218

Lists of Acronyms

- AO** adaptive optics. , 28, 36, 95, 96, 184
- AR** autoregressive. , 72, 74
- BTTB** block Toeplitz with Toeplitz block. , 136
- DKF** discrete Kalman filter. , 135
- DM** deformable mirror. , 28, 31, 96
- DMD** dynamic mode decomposition. , 144
- DTE** direct-to-Earth. ix, , 2, 184
- EOF** empirical orthogonal functions. , 134, 144
- ESO** European Southern Observatory. , 186
- FECC** forward error correction coding.
- FIM** fiber injection module. , 213
- FPGA** field programmable gate array. , 43
- GEO** geosynchronous equatorial orbit. , 46
- GPU** graphics processing unit. , 43
- KL** Karhunen-Loève.
- L&A** learn & apply. , 133, 141
- LC** liquid crystal. , 186
- LEO** low Earth orbit. ix, , 1, 46, 184
- LISA** Light and Small Adaptive optics. , 212
- LQG** linear-quadratic-Gaussian. , 4, 39, 71, 72, 86, 95

LQR linear-quadratic regulator. , 86, 88

LTAO laser tomography adaptive optics.

MAP maximum a posteriori. , 38, 261, 263

MCAO multi conjugated adaptive optics. , 133

MEO Metrology and Optics. , 212

MIMO multiple-input multiple-output. , 32

MMF multi-mode fiber. , 217

MMSE minimum mean square error. , 99, 261

MOAO multi object adaptive optics. , 133

MOS Monin-Obukhov similarity. , 52

MSE mean square error. , 77, 90, 100

NP no prediction. , 104

OCA Observatoire de la Côte d’Azur. , 212

OMGI optimal modal gain integrator. , 36

OPD optical path difference. , 186

OTF optical transfer function. , 56

PCA principal component analysis. , 144

PFC predictive Fourier control. , 137

PIC photonic integrated circuit. , 209

POL pseudo open-loop.

POLC pseudo open-loop control.

PSD power spectral density. , 8

PSF point spread function. , 56, 195

pyGAOS Python geometric adaptive optics simulator. , 150

RTC real-time computer. , 28

- SAOST** simplified adaptive optics simulation tool. , 66
- SH** Shack-Hartmann. , 29, 261
- SLM** spatial light modulator. , 186
- SLODAR** slope detection and ranging. , 143
- SMF** single-mode fiber. , 59
- SNR** signal-to-noise ratio. , 36, 64
- SR** Strehl ratio. , 57
- SVD** singular value decomposition. , 35
- USC** Union of Concerned Scientists. , 47
- VAR** vector autoregressive. , 74
- WFS** wavefront sensor. , 28

Introduction

Context

The rapid expansion of space-based applications, including Earth observation, satellite broadband communications, and space exploration, has increased the demand for higher-capacity communication links between satellites and Earth. This demand becomes even more pronounced in the era of large satellite constellations and deep space missions with high-resolution payloads onboard, which generate massive volumes of data. Traditional radio frequency systems are approaching their inherent limits in terms of bandwidth and data throughput. Optical communications, because of the higher frequency of optical electromagnetic waves, can offer higher bandwidths that exceed radio frequency links by orders of magnitude, aiming at one terabit per second.

Space-to-ground optical links also face significant challenges. Above all, Earth's atmosphere attenuates, scatters, and distorts the laser beam due to absorption, cloud coverage, fog, rain, and atmospheric turbulence. These effects cause the loss and fluctuation of the received power, causing errors and outages in communication and limiting the possible data rate. Atmospheric absorption can be mitigated with the proper selection of optical carrier wavelength, and weather-related phenomena can be avoided by means of site diversity. Atmospheric turbulence, which causes phase and amplitude distortions on the carrier optical wave, can be corrected by adaptive optics.

Adaptive optics is a technique for correction of the effects of atmospheric optical turbulence. It has been developed for astronomy and military applications, but it is now used in other fields such as biomedical imaging and free-space optical communications. Adaptive optics measures and corrects the phase distortions of the beam by means of a wavefront sensor and a deformable mirror controlled by a real-time computer that processes the measurements and computes the necessary mirror commands using a control loop. The phase correction provided by adaptive optics enables coupling the received beam into a single-mode optical fiber, thus leveraging all the optical detection techniques developed for fiber optics communications, such as optical amplifiers and coherent detection. Adaptive optics has been acknowledged as a key enabler of future space-to-ground optical links, after several demonstrations of this technique, several optical ground stations equipped with adaptive optics are being built at the moment.

Low Earth orbit (LEO) satellites are the most common kind of satellite, this kind of orbit is the closest to Earth and therefore offers higher spatial resolution for

remote sensing payloads as well as lower latency for communications. Additionally, *LEO* satellites stay in the view of a ground station for about ten minutes, limiting the possible duration of communication links. As a result, optical *direct-to-Earth* (*DTE*) downlinks between *LEO* satellites and the ground will allow Earth observation payloads to transfer the growing amount of data they generate within the limited time of their links.

LEO satellite links are especially challenging due to the fast movement of the satellite across the sky. For adaptive optics, this means three things: (1) the turbulence conditions change as the satellite line of sight changes; (2) the fast angular rate of the line of sight is equivalent to a faster evolution of the turbulence observed; and (3) to extend the link duration, the link needs to operate at low elevations, where optical turbulence is stronger. This thesis is devoted to improving the performance of adaptive optics systems for *LEO* satellite applications by tackling these challenges.

In this thesis a second application is also considered due to its strong synergies with this challenge: the imaging of *LEO* satellites from the ground. The observation of the *LEO* orbit with ground telescopes can be used for surveillance and monitoring of spacecraft in orbit. The presence of optical turbulence reduces the effective resolution of the telescopes, and adaptive optics can help correct for these effects to image them at the diffraction limit. This application shares similar problems as *LEO*-to-ground optical links, though signal flux and turbulence conditions differ.

The adaptive optics loop has an inherent delay between the measurement and the correction that causes a difference between the corrected phase and the phase at the time of correction and, therefore, a decrease in performance. The effect of this delay is increased in the case of *LEO* satellites, since the trajectory of the satellite implies the relative movement of the beam and the layers of the atmosphere, which causes a faster evolution of the atmospheric distortions. This thesis proposes a new predictive control algorithm that models turbulence to predict its evolution between its measurement and correction. The potential gains in system performance due to such a predictive controller are analyzed for the two applications considered.

Working at low elevation is not necessary for traditional astronomy applications, since the observations are limited to higher elevations where turbulence conditions are more favorable; however, extending adaptive optics operation to low elevations will lead to a significant increase in optical link duration. At low line-of-sight elevations, the turbulence is stronger, and the amplitude distortions on the wavefront due to the effect of turbulence become more important. Amplitude distortions manifest as inhomogeneous speckle-like irradiance distributions over the pupil of the telescope, also known as scintillation. Adaptive optics cannot correct for amplitude distortions, but these distortions can impair the work of adaptive optics systems, for example, by affecting the wavefront measurements. Proper knowledge of these and their effect on adaptive optics systems is necessary to develop more robust systems. This thesis worked on a laboratory setup for the emulation of turbulence in this scenario, with a particular emphasis on the characterization of the scintillation

and its comparison to numerical simulations. Such a turbulence emulator will be used for investigating new adaptive optics control solution that under scintillation effects.

Thesis Objectives and Contribution

In this thesis I worked on two main projects. First, I developed a new predictive controller with the aim of improving the performance of adaptive optics systems in *LEO* satellite applications. Initially, the main application considered for this controller was optical communication, but during my PhD I also assessed the ground-based observation of satellites as a second application. A previous seminal work by Jean-Marc Conan and Cyril Petit had provided a theoretical assessment of the maximum performance gains that turbulence prediction could bring to adaptive optics; I continued this work with the development of a predictive controller, while I also contributed to its publication as Conan et al. (2023). During the development of the controller, I tried to achieve this ultimate performance and to understand the limitations within the system that separate it from this optimal performance. Finally, I studied the performance gains in application specific performance thanks to the use of predictive control.

Secondly, I worked on the *PICOLO* turbulence emulator for *LEO*-to-ground downlinks under strong turbulence conditions. I worked on the scintillation characterization of the bench and its comparison with numerical simulations. Additionally, I worked on the coupling of the bench to an adaptive optics system, which will allow in the future to test the predictive controller developed during this thesis, as well as other adaptive optics methods, in realistic turbulent conditions and compare them to the numerical twin of the bench that it is now available thanks to my characterization.

Thesis Outline

This manuscript is divided into three parts:

- “*Part I: Adaptive Optics for LEO Satellite Applications*” provides the theoretical basis of this work; it contains the following chapters:
 - Chapter 1 describes the properties of atmospheric optical turbulence and its effect on optical waves when they propagate across it.
 - Chapter 2 introduces the principle of adaptive optics and its components. The chapter also discusses the control problem in the case of adaptive optics and some of the common tools for adaptive optics control. Finally, the concept of *AO* error budgets is introduced as a methodology to assess and validate the performance of an adaptive optics loop.

- Chapter 3 discusses the relevant performance metrics for the two applications considered and the effect that atmospheric optical turbulence has on them. The chapter also provides the description of the *AO* systems and turbulence conditions used in the case studies in this manuscript.
- Chapter 4 introduces the prediction of atmospheric turbulence for control applications. This includes the theory of autoregressive processes as the standard model for the evolution of turbulence and the use of the *linear-quadratic-Gaussian (LQG)* as a predictive controller.
- “*Part II: Predictive Controller*” discusses the proposed predictive controller to improve adaptive optics performance for *LEO* satellite applications; it contains the following chapters:
 - Chapter 5 discusses and applies a method for assessing the predictability of turbulence originally presented in Conan et al. (2023). The assessment method provides expected performances for turbulence phase evolution predictive models in the frame of *AO* controllers. The method is applied to the cases under study in this thesis and these results serve as performance expectations for the predictive controller proposed in this thesis.
 - Chapter 6 introduces the predictive controller proposed in this thesis.
 - Chapter 7 analyzes the performance of the proposed predictive controller for the cases defined in Chapter 3 using numerical simulations.
- “*Part III: Experimental Validation*” contains the experimental part of this thesis; it contains two chapters:
 - Chapter 8 reports the characterization and validation of a turbulence emulator for *LEO*-to-ground links under strong scintillation conditions. This chapter corresponds to the publication Robles et al. (2023).
 - Chapter 9 discusses the first steps towards the experimental validation of the predictive controller developed in this thesis using the *PICOLO* turbulence emulator.

Part I.

Adaptive Optics for Satellite-to-Ground Links

1. Propagation of Light across Atmospheric Turbulence

Contents

1.1. Atmospheric Optical Turbulence	7
1.1.1. Physical Origin	7
1.1.2. Index of Refraction Fluctuations	8
1.1.2.1. Structure Function	8
1.1.2.2. Inertial Domain	8
1.1.2.3. Power Spectral Density	8
1.1.2.4. Vertical Structure of C_n^2	9
1.1.3. Frozen Flow Hypothesis	9
1.2. Optical Propagation in Turbulent Media	10
1.2.1. Helmholtz Equation	11
1.2.2. Phase Screen Propagation Model	13
1.2.3. Weak Perturbations Regime	14
1.2.3.1. Rytov Approximation	14
1.2.3.2. Effect on Phase and Amplitude	16
1.2.4. Geometric Propagation of Phase	17
1.2.5. Integrated Parameters	17
1.2.6. Strong Perturbations Regime	18
1.2.6.1. Intensity Fluctuations	19
1.2.6.2. Scintillation Saturation	19
1.2.6.3. Scintillation Power Spectrum	19
1.3. Modal Decomposition of the Phase	20
1.3.1. Zonal Basis	21
1.3.1.1. Covariance	21
1.3.2. Zernike Polynomials	21
1.3.2.1. Advantages	22
1.3.2.2. Variance	23
1.3.2.3. Spatial Covariance	23
1.3.2.4. Temporal Characteristics	23
1.3.2.5. Angular Covariance	24

Introduction

This chapter introduces the origin of the phase and amplitude distortions of an electromagnetic field when it propagates across a turbulent medium.

First, Section 1.1 introduces the origin of atmospheric optical turbulence and provides a statistical description of the index of refraction fluctuations.

Section 1.2 presents the theory of optical propagation in turbulent media and shows how the phase distortions caused by the index of refraction fluctuations within a layer generate both phase and amplitude distortions in the propagated field. A statistical description of the resulting intensity fluctuations, also known as scintillation, is also given; first analytically thanks to the Rytov approximation in the weak perturbation regime and later computationally for the strong perturbation regime.

Section 1.2.5 defines some integrated parameters that capture the accumulated influence of turbulence across its propagation path.

Finally, Section 1.3 discusses the modal representation of the turbulent phase, with a special emphasis on the Zernike polynomial basis and the analytical computation of the statistics of turbulence projected on this basis.

1.1. Atmospheric Optical Turbulence

1.1.1. Physical Origin

Earth's atmosphere is a mixture of masses of air in continuous movement due to solar radiation and the heat transfer within itself and with the ground. The variations in temperature within the atmosphere cause local variations in the air density that result in local variations in the index of refraction. The index of refraction of a medium affects the propagation of electromagnetic waves across this medium; the resulting difference in propagation speed for each point of the wavefront leads to optical path differences, which create a difference in phase across the wavefront.

The theory describing atmospheric turbulence and the index of refraction fluctuations within it is based on the concept of energy cascades proposed by Kolmogorov (Kolmogorov 1941). This theory models the transfer of kinetic energy within the atmosphere as a cascade of eddies, where energy flows from bigger to smaller scale eddies until it is consumed by the dissipation caused due to the viscous friction between air molecules. The large scales of turbulence are initiated by some external macroscopic phenomena that start the movement of air masses (e.g. wind shear, thermal convection, topography, etc.). The larger-scale eddies break into smaller-scale eddies causing a transfer of energy; this stops when the eddies are small enough for viscous friction to become relevant and dissipate the energy as heat. As a result, two typical sizes, i.e. scales, are defined: (1) the outer scale, L_0 , which is conditioned by the external causes of turbulence, typically between tenths

1. Propagation of Light across Atmospheric Turbulence
1.1. Atmospheric Optical Turbulence

and hundreds of meters; and (2) the inner scale, l_0 , which is the size of the smallest turbulent structures, typically some millimeters.

1.1.2. Index of Refraction Fluctuations

The index of refraction fluctuations caused by atmospheric turbulence is stochastic in nature and, therefore, requires a statistical analysis. This section introduces the statistical description of the index of refraction fluctuations.

In general in all this analysis turbulence is considered isotropic, which means that the statistical parameters of turbulence do not vary with direction, and stationary, which means that they do not change with time. Although these assumptions are not true in reality, they are helpful for the development of statistical descriptions and will be close to reality for sufficiently small distances and periods of time.

1.1.2.1. Structure Function

We start by considering the spatial variation of the index of refraction, $n(\mathbf{r})$, where \mathbf{r} is a vector in a three-dimensional Cartesian space.

The index of refraction structure function is the variance of the difference in the index of refraction between two points in space separated by a given distance; it has been shown to be described by (Obukhov 1949; Yaglom 1949):

$$D_n(\boldsymbol{\rho}) = \langle n(\mathbf{r}) - n(\mathbf{r} + \boldsymbol{\rho})^2 \rangle = C_n^2 \rho^{2/3}, \quad (1.1)$$

where $\langle \cdot \rangle$ represents the ensemble average, $\rho = |\boldsymbol{\rho}|$, and C_n^2 is the index of refraction structure constant of the turbulence with units of $\text{m}^{-2/3}$.

1.1.2.2. Inertial Domain

The inertial domain is the range of scales within which turbulence is fully developed, meaning that neither there is energy being injected nor dissipated as heat, but is instead only cascading down from larger to smaller scales. As a result, the inertial domain is limited within the external scale and internal scale. For values outside of this range, $l_0 < \rho < L_0$, the fluctuations of the index of refraction are independent of each other and the structure function is not defined.

1.1.2.3. Power Spectral Density

The *power spectral density* (*PSD*) of the index of refraction fluctuations can be computed from their structure functions. Since it is a variance, the Wiener-Khinchine theorem can be used to compute the *PSD* as a Fourier transform of the structure function, known as the Kolmogorov spectrum (Tatarskii 1961):

$$W_n^{\text{Kol}}(f) \approx 0.033(2\pi)^{-2/3} C_n^2 f^{-11/3}, \quad (1.2)$$

1. Propagation of Light across Atmospheric Turbulence

1.1. Atmospheric Optical Turbulence

where f corresponds to the spatial frequency in units of m^{-1} . The Kolmogorov spectrum is only valid within the inertial domain, $1/L_0 < f < 1/l_0$, and it assumes that the external and internal scales are infinite and zero, respectively.

This model was completed by von Kármán, so it accounts for the effect of the internal scale and the external scales of the turbulence (Tatarskii 1961):

$$W_n^{\text{Kar}}(f) \approx 0.033(2\pi)^{-2/3} C_n^2 \left(f^2 + \left(\frac{1}{L_0} \right)^2 \right)^{-11/6} e^{-\left(\frac{2\pi l_0 f}{5.91} \right)^2}. \quad (1.3)$$

1.1.2.4. Vertical Structure of C_n^2

The strength of the index of refraction fluctuations, represented by the index of refraction structure constant, C_n^2 , will vary with the meteorological dynamics and the surrounding topography. As a result, the value of C_n^2 varies in time and space. The analysis of the propagation of light across atmospheric turbulence requires therefore the knowledge of the distribution of C_n^2 along its propagation path. The common assumption is that this distribution varies vertically, while horizontal variations around the observation location are negligible. The atmosphere is therefore modeled as a stratified distribution that can be understood as a sequence of independent layers with different turbulence strengths and statistics. The vertical stratification of turbulence depends on a mixture of different physical factors, such as thermal gradients between the Earth's surface and the atmosphere, wind shear (e.g. jet stream), the stability of the air masses (e.g. inversion layers), meteorological phenomena, or the decrease of air density with altitude.

There exist various models and metrology techniques for the description of the C_n^2 vertical profile; Section 3.2.1 discusses briefly some of them. This thesis uses a family of profiles developed at *ONERA*, the *MOSPAR* profiles; the structure and construction of *MOSPAR* profiles is detailed in Section 3.2.1.1.

1.1.3. Frozen Flow Hypothesis

So far, the statistical description of the index of refraction fluctuations has been limited to its spatial variation; now a description of their temporal evolution is introduced.

In general, there exist two different transport mechanisms for a field within a fluid (such as temperature and density) that lead to its temporal variation: advection and diffusion. Advection refers to the transport of a field by the fluid's flow, while diffusion refers to the transport due to the gradients within the field. Those two phenomena are coupled and lead to complex interactions; however, for most conditions, and within a small enough time scale, it is possible to consider only one of them.

The long-term temporal evolution of turbulence depends on the dynamics of the atmosphere; however, at short time scales, the turbulence can be considered

1. Propagation of Light across Atmospheric Turbulence
1.2. Optical Propagation in Turbulent Media

steady, and its evolution driven by the translation of wind (i.e. advection). This simplification is the so-called Taylor frozen flow hypothesis, which states that in the time scales relevant to adaptive optics the turbulence phase does not change its shape in space, i.e. it is frozen, but it is driven by a shift of the frozen phase screen related to the layer with the wind speed, \mathbf{V} . For a given layer, the Taylor frozen flow hypothesis assumes that:

$$n(\mathbf{r}, t + \tau) = n(\mathbf{r} - \tau\mathbf{V}, t), \quad (1.4)$$

where τ is a time interval.

This hypothesis will be very important for the analytical computation of temporal turbulence statistics, since it allows to compute them from the spatial statistics and the translation of each layer of the atmosphere.

The frozen flow hypothesis has been experimentally validated in different published works (Schöck and Spillar 2000; Poyneer et al. 2009; Guesalaga et al. 2014). Note that in the case of *LEO* satellite tracking applications, the validity of the frozen flow hypothesis becomes stronger due to the presence of apparent wind.

In some cases, the turbulence flow does not follow a frozen flow and diffusion effects become predominant. This is the case when there exist strong gradients, typically at the ground layer (temperature gradient between the Earth's surface and the atmosphere) or between the dome of the telescope and the atmosphere. The diffusive transport of index of refraction fluctuations is known as boiling turbulence in the adaptive optics literature.

1.2. Optical Propagation in Turbulent Media

This section discusses how fluctuations in the index of refraction produce phase and amplitude distortions on a wave propagated across a turbulent medium. For this, the numerical and analytical computation of the wave propagation is introduced. The goal is to describe the rigorous description of the propagation necessary to study the statistics and characteristics of scintillation (i.e. intensity fluctuations within the optical wavefront) and to present some of these results. The phase distortion statistics are introduced in later sections, usually neglecting propagation effects and focusing on the statistics of the phase introduced by every layer and assuming their geometrical propagation.

Section 1.2.1 discusses the Helmholtz equation as the main wave propagation equation within turbulent media; the equation is simplified using certain assumptions for the optical regime. This propagation is further simplified by the phase screen propagation model introduced in Section 1.2.2, which models the atmosphere as a sequence of layers that act as phase screens and divides the effects of propagation into two steps: (1) a phase disturbance due to the index of refraction fluctuations within the phase screen, (2) and a numerically inexpensive propagation using Fresnel propagation (the solution of the Helmholtz equation for

a homogeneous medium) that leads to amplitude distortions and further phase distortions.

The phase screen model and the Fresnel propagator are used for the implementation of numerical simulations of optical propagation; however, the analytical study of the effects of propagation requires further simplifications. Section 1.2.3 introduces the Rytov approximation, which allows for an analytical description of the statistics of the phase and amplitude distortions. Section 1.2.4 briefly introduces the case where no diffractive effect is considered and only phase distortions are taken into account; this is a common assumption in adaptive optics simulations to reduce their computational cost, as well as in some analytical derivations.

Finally, Section 1.2.6 discusses the strong turbulence regime, the regime in which the turbulence strength is too strong and the Rytov approximation is not valid any more, requiring the help of computational simulations. More interestingly, the strong perturbations regime will show different physical characteristics, such as the saturation of the variance of the intensity fluctuations and a different shape in their spectrum.

1.2.1. Helmholtz Equation

The propagation of an electromagnetic wave in a dielectric medium, such as air, is described by the Maxwell equations. Under the assumption that the temporal evolution of the refractive index fluctuations is very low with respect to the oscillation period of the electromagnetic wave, $2\pi/\omega$, it is possible to simplify the Maxwell equations to describe the spatio-temporal evolution of the vectorial electrical field amplitude, $\mathbf{E}(\mathbf{r})$, (Tatarskii 1961); the resulting equation is the Helmholtz equation:

$$\nabla^2 \mathbf{E}(\mathbf{r}) + k_0^2 n^2(\mathbf{r}) \mathbf{E}(\mathbf{r}) + 2\nabla(\mathbf{E}(\mathbf{r}) \nabla \cdot (\log(n(\mathbf{r})))) = 0, \quad (1.5)$$

where $\mathbf{r} = (x, y, z)$ represents a point in space, $k_0 = 2\pi/\lambda$ is the wave number of the field propagating through vacuum, and $\nabla = [\partial/\partial x, \partial/\partial y, \partial/\partial z]^\top$ is the nabla differential operator of vector calculus.

Scalar Helmholtz equation: The term $\nabla(\mathbf{E}(\mathbf{r}) \nabla \cdot (\log(n(\mathbf{r}))))$ represents the change in the wave polarization across its propagation, since the wavelength, λ , is much smaller than the inner scale of the spatial fluctuations of the index of refraction, l_0 , this term can be neglected (Strohbehn et al. 1978). This allows to further simplify the Helmholtz equation as:

$$\nabla^2 \mathbf{E}(\mathbf{r}) + k_0^2 n^2(\mathbf{r}) \mathbf{E}(\mathbf{r}) = 0. \quad (1.6)$$

This equation can be decomposed into three equations for the three scalar Cartesian components of \mathbf{E} .

1. Propagation of Light across Atmospheric Turbulence
 1.2. Optical Propagation in Turbulent Media

Complex amplitude Helmholtz equation: Consider a monochromatic wave that can be decomposed on a spectrum of plane waves (Goodman 2017) that propagates in space along a direction \mathbf{e}_z ; as a result, only the component of Equation 1.6 in this direction is of interest. The scalar amplitude of the electromagnetic field, E , can be decomposed as:

$$E(\mathbf{r}) = A_0\Psi(\mathbf{r})e^{ikz}, \quad (1.7)$$

where A_0 represents the complex amplitude of the wave before propagation and $\Psi(\mathbf{r})$ is a complex amplitude that represents the deviation from a plane wave e^{ikz} due to propagation. The wave propagates across a medium with an average index of refraction $\bar{n}(\mathbf{r}) = \langle n(\mathbf{r}) \rangle$, where $\langle \cdot \rangle$ is the temporal average operator; the wavenumber is given by $k = \bar{n}k_0$. Considering $\Psi(\mathbf{r})$ as the solution of the Helmholtz equation, Equation 1.6 can be rewritten as:

$$\nabla^2\Psi(\mathbf{r}) + 2ik\frac{\partial\Psi(\mathbf{r})}{\partial z} + k_0(n^2(\mathbf{r}) - \bar{n}^2(\mathbf{r}))\Psi(\mathbf{r}) = 0. \quad (1.8)$$

Paraxial approximation: The paraxial approximation implies that the variation of the field along the propagation direction due to diffraction is negligible compared to the transversal directions:

$$\left| \frac{\partial^2\Psi}{\partial z^2} \right| \ll \left| \frac{\partial^2\Psi}{\partial x^2} + \frac{\partial^2\Psi}{\partial y^2} \right|, \quad (1.9)$$

where the transverse Laplacian can be written as $\nabla_{\perp}^2\Psi = (\partial^2\Psi/\partial x^2 + \partial^2\Psi/\partial y^2)$. The paraxial approximation is usually valid for the propagation of plane waves with wavelengths in the optical domain.

Weak fluctuations approximation: Additionally, the index of refraction fluctuations, $n(\mathbf{r}) = \bar{n}(\mathbf{r}) + N(\mathbf{r})$, are approximated assuming weak fluctuations (Rytov et al. 1989), i.e. $N \ll 1$, so that the following first-order approximation is possible:

$$n^2 \approx \bar{n}^2 + 2N\bar{n}. \quad (1.10)$$

This approximation is less strict than the approximation introduced in Section 1.2.3 and is generally valid for optical wavelengths under all turbulence conditions within the atmosphere.

Final Helmholtz equation: Applying the paraxial approximation and the approximation of weak the index of refraction fluctuations, Equation 1.8 becomes:

$$\nabla_{\perp}^2\Psi(\mathbf{r}) + 2ik\frac{\partial\Psi(\mathbf{r})}{\partial z} + 2k_0^2N(\mathbf{r})\bar{n}(\mathbf{r})\Psi(\mathbf{r}) = 0. \quad (1.11)$$

1.2.2. Phase Screen Propagation Model

The Helmholtz equation presented so far until Equation 1.11 cannot be solved analytically, and its numerical computation is very costly. Nevertheless, assuming that the perturbations occur only at certain locations and that the wave propagation happens in a homogeneous medium allows the simplification of this computation.

The suggested approximation is therefore equivalent to the decomposition of the turbulence volume into a series of layers whose thickness, δz , is small enough to neglect the propagation effects within each layer. Therefore, the propagation is divided into two steps:

1. The complex amplitude is first propagated between two phase screens in a homogeneous media using the Fresnel approximation.
2. The complex amplitude is perturbed in phase only by the phase screen.

This model can be used as a simplification of the actual propagation of the optical wave across a continuous volume of inhomogeneous media. Such an approximation enables the analytical treatment of propagation and an efficient computational solution of the initial Helmholtz equation used for optical propagation simulations.

Propagation in vacuum: The Helmholtz equation can be solved for homogeneous media, i.e. $N = 0$, between layers with propagation in the z -direction by convolution with the Fresnel propagation:

$$\Psi(\boldsymbol{\rho}, z + d) = \Psi(\boldsymbol{\rho}, z) * \mathcal{F}_d(\boldsymbol{\rho}), \quad (1.12)$$

where $\boldsymbol{\rho} = (x, y)$ are the Cartesian coordinates in a plane perpendicular to the z -direction and d is the distance between the two phase screens. The operator $\mathcal{F}_d(\boldsymbol{\rho})$ corresponds to the Fresnel propagator across a distance d and is defined as:

$$\mathcal{F}_d(\boldsymbol{\rho}) = \frac{e^{ikd}}{i2\pi d} e^{\frac{ik\boldsymbol{\rho}}{2d}}. \quad (1.13)$$

Phase disturbance due to phase screen: The influence of fluctuations of the index of refraction is limited to the propagation within the phase screen and only affect the phase of the complex amplitude:

$$\varphi(\boldsymbol{\rho}, z + \delta z) = k_0 \int_z^{z+\delta z} N(\boldsymbol{\rho}, z) dz. \quad (1.14)$$

Thus, the effect of the propagation across the phase screen is equal to a phase shift of the complex amplitude:

$$\Psi(\boldsymbol{\rho}, z + \delta z) = \Psi(\boldsymbol{\rho}, z) e^{i\varphi(\boldsymbol{\rho}, z + \delta z)}. \quad (1.15)$$

1. Propagation of Light across Atmospheric Turbulence
 1.2. Optical Propagation in Turbulent Media

Simulation tool: A simulation tool can iteratively apply these two steps between phase screens to compute the numerical propagation across a sequence of phase screens. The propagation adheres to the subsequent scheme:

$$\begin{aligned}
 \Psi(\boldsymbol{\rho}, z) &= A_0(\boldsymbol{\rho}), \\
 \Psi(\boldsymbol{\rho}, z + \delta z) &= \Psi(\boldsymbol{\rho}, z) \cdot e^{i\varphi_1(\boldsymbol{\rho})}, \\
 \Psi(\boldsymbol{\rho}, z + d) &= \Psi(\boldsymbol{\rho}, z + \delta z) * \mathcal{F}_d(\boldsymbol{\rho}), \\
 \Psi(\boldsymbol{\rho}, z + d + \delta z) &= \Psi(\boldsymbol{\rho}, z + d) \cdot e^{i\varphi_2(\boldsymbol{\rho})}, \\
 \Psi(\boldsymbol{\rho}, z + 2d) &= \Psi(\boldsymbol{\rho}, z + d + \delta z) * \mathcal{F}_d(\boldsymbol{\rho}), \\
 &\dots = \dots
 \end{aligned}$$

A numerical tool of this nature must consider various dimensioning rules to ensure accurate propagation. The strength of each of the phase screens can be set to represent an atmospheric profile.

The *TURANOT* optical propagation tool (Vedrenne et al. 2012), developed by ONERA, is implemented in accordance with these guidelines. During this thesis, it will serve as the primary tool for conducting end-to-end simulations of optical propagation, including diffractive effects, under conditions of strong turbulence.

Temporal evolution of the disturbances: The temporal evolution of turbulence is modeled under the frozen flow assumption (see Section 1.1.3) by shifting the phase screen with a speed corresponding to the speed of the layer in the orthogonal direction to the line of sight, \mathbf{V}_\perp . The phase of each layer is shifted so that $\varphi(\mathbf{r}, t) \approx \varphi(\mathbf{r} - \mathbf{V}_\perp(\mathbf{r})t)$.

1.2.3. Weak Perturbations Regime

Although it is not possible to compute an analytical solution of the Helmholtz equation as given in Equation 1.6, establishing certain hypotheses about the strength of the perturbations allows to simplify the equation thanks to the linearization of the wave equation. The Rytov approximation (Tatarskii 1961) is such an approximation. The subsequent analytical solution of the propagation equations for phase and amplitude allows us to compute the statistics of phase and amplitude distortions.

1.2.3.1. Rytov Approximation

Consider a wave with an electrical field amplitude $E_0(\mathbf{r}) = e^{\psi_0(\mathbf{r})}$, where $\psi_0(\mathbf{r})$ is the logarithm of the complex amplitude of the field. Throughout its propagation across the atmosphere, this complex amplitude will suffer the effect of the fluctuations of

1. Propagation of Light across Atmospheric Turbulence
1.2. Optical Propagation in Turbulent Media

the index of refraction, as described by Equation 1.6. The Rytov approximation describes this perturbation as:

$$E(\mathbf{r}) = e^{\psi_0(\mathbf{r}) + \psi(\mathbf{r})}, \quad (1.16)$$

where $\psi(\mathbf{r})$ is the logarithm of the complex amplitude due to the effect of propagation. Equation 1.6 can be rewritten as:

$$(\nabla^2(\psi_0 + \psi) + (\nabla(\psi_0 + \psi))^2 + k_0 n^2) e^{\psi_0 + \psi} = 0. \quad (1.17)$$

Solving this equation for a non-zero E_0 requires:

$$\nabla^2(\psi_0 + \psi) + (\nabla(\psi_0 + \psi))^2 + k_0^2 n^2 = 0. \quad (1.18)$$

Which means that the unperturbed field satisfies Equation 1.6 as:

$$\nabla^2 \psi_0 + (\nabla \psi_0)^2 + k_0^2 \bar{n}^2 = 0. \quad (1.19)$$

The fluctuation of the index of refraction can be developed as:

$$n^2 = \bar{n}^2(1 + 2\delta n + \delta n^2), \quad (1.20)$$

where $\delta n(\mathbf{r}) = N(\mathbf{r})/\bar{n}(\mathbf{r})$ corresponds to the fluctuation of $n(\mathbf{r})$ with respect to its temporal average. Injecting this development and Equation 1.19 into Equation 1.18:

$$\nabla^2 \psi + \nabla \psi \cdot (\nabla \psi + 2\nabla \psi_0) + k_0^2 \delta n^2 + 2k_0^2 \bar{n} \delta n = 0. \quad (1.21)$$

The equation above can be solved analytically if the terms $(\nabla \psi)^2$ and $k_0^2 \delta n^2$ can be neglected. The Rytov approximation assumes that this is true if ([Tatarskii 1961](#)):

- $\delta n(\mathbf{r}) \ll 1$ and
- $|\nabla \psi| \ll |\nabla \psi_0| = k_0$ (meaning that the complex amplitude does not change much over a distance of λ).

While the first condition is always true for atmospheric perturbations, the second one limits the strength of the perturbations that can be properly modeled and limits the Rytov approximation to a regime known as the weak perturbation regime [Fante \(1975\)](#). If the two conditions are satisfied, Equation 1.21 can be simplified to:

$$\nabla^2 \psi + 2\nabla \psi \cdot \nabla \psi_0 + 2k_0^2 \bar{n} \delta n = 0. \quad (1.22)$$

Such an equation has the form of a Ricatti equation and can be solved as:

1. Propagation of Light across Atmospheric Turbulence
 1.2. Optical Propagation in Turbulent Media

$$\psi(\mathbf{r}) = \frac{k^2}{2\pi E_0(\mathbf{r})} \int_{\mathcal{V}} \delta n(\mathbf{r}') E_0(\mathbf{r}') \frac{e^{ik|\mathbf{r}-\mathbf{r}'|}}{|\mathbf{r}-\mathbf{r}'|} d\mathbf{r}', \quad (1.23)$$

where \mathcal{V} is the considered propagation volume.

1.2.3.2. Effect on Phase and Amplitude

The Rytov approximation allows to analyze the perturbations of the field as a complex argument of the exponential function that can be decomposed in real and imaginary parts:

$$\psi = \chi + i\varphi, \quad (1.24)$$

where χ corresponds to the log-amplitude and φ phase of the wavefront distortion.

Propagation: The solution of the field propagation given in Equation 1.23 can be applied to this decomposition to obtain (Tatarskii 1961; Sasiela 1994):

$$\chi = \frac{k_0^2}{2\pi} \int_0^L \frac{1}{L-z} \int_{-\infty}^{+\infty} N(\boldsymbol{\rho}', z) \cos\left(\frac{k}{2} \frac{|\boldsymbol{\rho}-\boldsymbol{\rho}'|^2}{L-z}\right) d\boldsymbol{\rho}' dz, \quad (1.25)$$

$$\varphi = \frac{k_0^2}{2\pi} \int_0^L \frac{1}{L-z} \int_{-\infty}^{+\infty} N(\boldsymbol{\rho}', z) \sin\left(\frac{k}{2} \frac{|\boldsymbol{\rho}-\boldsymbol{\rho}'|^2}{L-z}\right) d\boldsymbol{\rho}' dz, \quad (1.26)$$

where L is the total propagation distance.

Notice how the log-amplitude is a phase distortion that becomes an amplitude distortion thanks to its propagation.

Power spectral densities: The statistical description of the spatial distribution of phase and log-amplitude can be given by the computation of their power spectral densities. It is assumed that the atmosphere is divided into several layers that act as phase screens, meaning that the contribution of each layer is uncorrelated with the other layers and that the layers are thin enough so that there are diffractive effects due to the propagation across the layer. The power spectral densities of the log-amplitude and the phase are thus given by:

$$W_\chi(f) = k^2 \int_0^L W_n(f) \sin^2(\pi z \lambda f^2) dz \quad (1.27)$$

$$W_\varphi(f) = k^2 \int_0^L W_n(f) \cos^2(\pi z \lambda f^2) dz \quad (1.28)$$

Variations: The expression for the variances of the log-amplitude and the phase fluctuations can be obtained by integration of their power spectral densities:

1. Propagation of Light across Atmospheric Turbulence
 1.2. Optical Propagation in Turbulent Media

$$\sigma_{\chi}^2 = k_0^2 \int_0^L \int_0^{\text{inf}} 2\pi f W_n(f) \sin^2(\pi z \lambda f^2) df dz, \quad (1.29)$$

$$\sigma_{\varphi}^2 = k_0^2 \int_0^L \int_0^{\text{inf}} 2\pi f W_n(f) \cos^2(\pi z \lambda f^2) df dz. \quad (1.30)$$

The variance for the log-amplitude can be computed assuming a Kolmogorov spectrum within Equation 1.29 as:

$$\sigma_{\chi_R}^2 = 0.5631 k_0^{7/6} \int_0^L C_n^2(z) z^{5/6} dz. \quad (1.31)$$

This expression is a simplified expression of the log-amplitude computation that is called the Rytov variance. Its validity is limited to a certain regime for which this variance does not approximate the log-amplitude any more. The expression can be used as a simple way of evaluating the strength of the scintillation effects for a given turbulence profile and decide whether those are strong enough to consider a more rigorous treatment of propagation.

1.2.4. Geometric Propagation of Phase

Roddiar (1981) showed that for weak turbulence regimes the effects of diffraction in the phase and amplitude of the wavefront are negligible. In this case, the propagation of the field results in no effect on its amplitude and in a phase that is given by the sum of the phases by each layer:

$$\phi(\mathbf{r}) = \sum_{i=1}^{n_l} \varphi(\mathbf{r}, h_i), \quad (1.32)$$

where n_l is the number of layers and $\phi(\mathbf{r})$ is the phase at the telescope pupil.

1.2.5. Integrated Parameters

The integrated turbulence parameters are a set of quantities that describe the overall effect of atmospheric turbulence along a certain propagation path defined by its C_n^2 profile. Their computation is based on the same phase screen assumption presented above.

The first of those parameters is the Fried parameter Fried (1982):

$$r_0 = \left[0.423 k^2 \int_{\text{path}} C_n^2(z) dz \right]^{-3/5}, \quad (1.33)$$

It describes the integrated coherence length of the turbulence phase distortion along the propagation path. In particular, it is defined so that a telescope of diameter r_0 will have a phase variance of 1 rad^2 across its pupil, assuming a

1. Propagation of Light across Atmospheric Turbulence
1.2. Optical Propagation in Turbulent Media

Kolmogorov spectrum. Notice how it depends on the reference wavelength through the wavenumber k .

In a similar way, it is possible to define an integrated coherence time so that $\langle(\varphi(t) - \varphi(t + \tau))^2\rangle = 1 \text{ rad}^2$. This parameter can be computed as (Roddier 1981):

$$\tau_0 = 0.314 \frac{r_0}{\bar{V}}. \quad (1.34)$$

\bar{V} is a weighted turbulence layer speed given by:

$$\bar{V} = \left[\frac{\int_{path} C_n^2(z) V_{\perp}^{5/3} dz}{\int_{path} C_n^2(z) dz} \right]^{3/5}, \quad (1.35)$$

where V_{\perp} is the transverse velocity of the layer. The integrated coherence time and its reciprocal, the Greenwood frequency (Fried 1990), are commonly used to define the correction bandwidth necessary for an adaptive optics system.

Finally, the anisoplanatic angle (Fried 1982):

$$\theta_0 = \left[2.05 k^2 \int_{path} C_n^2(z) z^{5/3} dz \right]^{-3/5}. \quad (1.36)$$

The anisoplanatic angle is defined as the angular distance between two lines of sight for which an angular separation of θ_0 leads to $\langle(\varphi(0) - \varphi(\theta_0))^2\rangle = 1 \text{ rad}^2$.

These terms are used for the analytical evaluation of the phase effects of turbulence for a given atmospheric profile and are part of the formulas used to assess adaptive optics performance within error budgets (see 2.5).

1.2.6. Strong Perturbations Regime

When the fluctuations of the index of refraction become sufficiently large, the scattering due to propagation becomes strong enough for multiple path effects to occur, where the optical wavefront gets broken into multiple beams that interfere with each other. As a result, the intensity fluctuations at the receiver plane are not linear anymore with respect to the phase perturbation by a layer. The main result of this non-linearity is the emergence of the phenomenon of saturation Gracheva and Gurvich (1965), which is not represented by the Rytov approximation.

Given that the analytical solutions of the Helmholtz equation are not valid for the strong perturbations regime, the use of numerical simulations is necessary for the study of scintillation in the strong regime. This section presents two of the phenomena characteristic of scintillation in the strong perturbations regime:

- The saturation of the intensity fluctuations: The non-linear effects of propagation lead to the saturation of the scintillation, at some point stronger turbulence does not lead to stronger scintillation conditions.

1. Propagation of Light across Atmospheric Turbulence
 1.2. Optical Propagation in Turbulent Media

- Appearance of a second cut-off frequency in the scintillation spectrum: The spatial distribution of the scintillation shows a different signature in the strong perturbations regime (described by its power spectral density).

1.2.6.1. Intensity Fluctuations

The use of the log-amplitude is convenient for the weak perturbations regime since it allows the analytical computation of the amplitude fluctuation statistics. However, from an instrumental point of view, it is the intensity fluctuations that are of interest. We define the normalized intensity fluctuations as follows:

$$\bar{I} = \frac{I - \langle I \rangle}{\langle I \rangle}, \quad (1.37)$$

where $I = \Psi\Psi^* = I_0e^{2\chi}$. Under the assumption of weak perturbations, it is possible to find a relationship between the log-amplitude and the intensity fluctuations and compute analytical expression for the latter: $e^{2\chi} \approx 1 + 2\chi$, by Taylor expansion, and $\bar{I} \approx 2\chi$ with $\sigma_{\bar{I}}^2 \approx 4\sigma_{\chi}^2$.

1.2.6.2. Scintillation Saturation

Figure 1.1 shows an example of the evolution of the intensity fluctuations, $\sigma_{\bar{I}}^2$, as well for the log-amplitude, σ_{χ}^2 , with an increase in turbulence strength. The strength of the turbulence is measured using the Rytov variance, $\sigma_{\chi_R}^2$ (Equation 1.31); a constant C_n^2 profile was used, with the value computed from the Rytov variance. The experiment corresponds to a propagation of $L = 20$ km with $L_0 = 2$ m and $l_0 = 5$ mm.

Two different regimes are observed: (1) For $\sigma_{\chi_R}^2 < 0.15$ the approximation $\bar{I} \approx 2\chi$ is valid and (2) for $\sigma_{\chi_R}^2 < 0.4$ the log-amplitude variance, σ_{χ}^2 , is well represented by the Rytov variance, $\sigma_{\chi_R}^2$. The former limit is generally defined as $\sigma_{\chi_R}^2 < 0.3$ (Fante 1975). For stronger turbulence, the intensity fluctuations saturate or even decrease.

1.2.6.3. Scintillation Power Spectrum

Figure 1.2 shows an example of the power spectral density of the intensity fluctuations in a propagation case with weak and strong perturbations, respectively. Depending on the turbulence strength regime, the spectra have a different shape, defined by their cutoff frequencies Sechaud et al. (1999); Andrews et al. (1999). The spectra of scintillation under weak turbulence show a peak around $\frac{1}{\sqrt{\lambda L}}$. The spectra of scintillation under strong turbulence have been observed to have a spectrum divided that shows two different cutoff frequencies:

- At low frequencies $\frac{r_0}{\lambda L}$ related to multiple scattering.
- At high frequencies $\frac{1}{r_0}$, due to single scattering.

1. Propagation of Light across Atmospheric Turbulence
 1.3. Modal Decomposition of the Phase

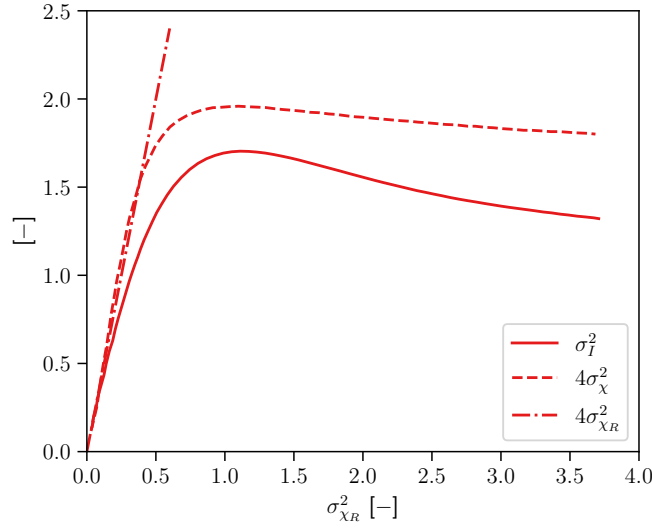
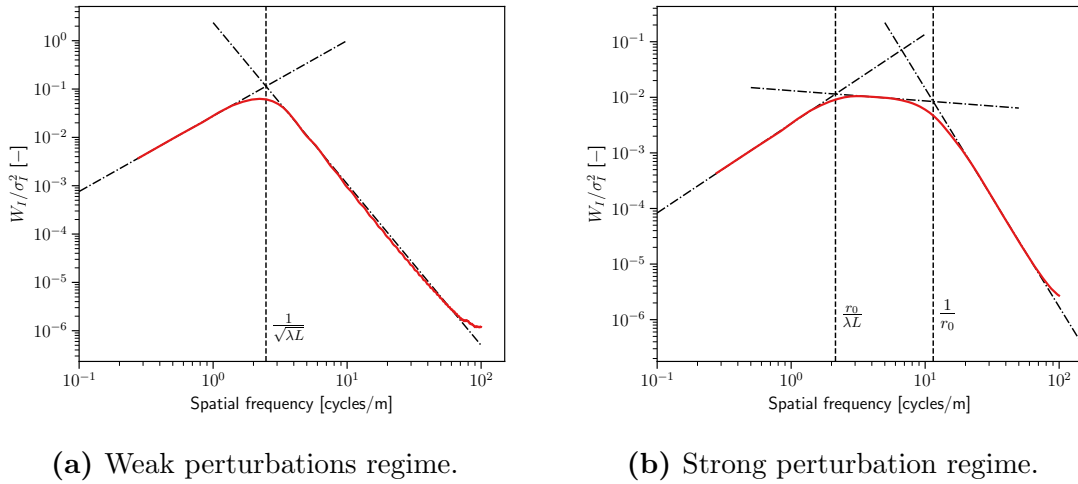


Figure 1.1.: Saturation of the scintillation with the increase of the turbulence strength. (Credit: Védrenne (2008)).



(a) Weak perturbations regime.

(b) Strong perturbation regime.

Figure 1.2.: Intensity *PSD* for a plane wave after a phase screen.

1.3. Modal Decomposition of the Phase

Adaptive optics corrects for the phase of the complex amplitude distortions on the incoming optical electromagnetic field. We search a vector space to describe the phase φ and its variation in space. Such a phase representation will be needed for the formulation of adaptive optics controllers that use a mathematical model of the phase in such a space. Different bases are possible to form such a vector space. The selected basis should be orthonormal with respect to their geometrical scalar product to allow a projection of the phase in such a basis.

We define ϕ^{tur} , the vectorial representation of the turbulent phase in the telescope

pupil, and use φ as the vectorial representation of the phase distortion induced by a given atmospheric layer. This vector corresponds to a projection of phase onto a given basis:

- Zonal basis.
- Zernike polynomial modal basis.
- Karuhen-Loève modal basis.
- Fourier modal basis.

Only the zonal basis and the Zernike polynomial basis are discussed here; the phase statistics of the turbulent phase projected on this base that are relevant for this thesis are given as well.

1.3.1. Zonal Basis

The zonal basis representation of the turbulent phase corresponds to a discrete spatial sampling of the continuous phase that has been presented so far; the statistical properties of this basis can be computed using the formulas given above. The spatial resolution of the sampling grid determines the frequency content of the representation following the Nyquist–Shannon sampling theorem.

1.3.1.1. Covariance

The covariance function between two points of the phase distribution can be computed from the structure function. In the case of von Kármán turbulence its analytical expression is given as ([Assémat et al. 2006](#)):

$$\begin{aligned} C(\rho) &= \langle (\varphi(\mathbf{r}) - \varphi(\mathbf{r} + \boldsymbol{\rho}))^2 \rangle \\ &= \left(\frac{L_0}{r_0} \right)^{5/3} \frac{\Gamma(11/6)}{2^{5/6} \pi^{8/3}} \left[\frac{24}{5} \Gamma\left(\frac{6}{5}\right) \right]^{5/6} \left(\frac{2\pi\rho}{L_0} \right)^{5/6} K_{5/6}\left(\frac{2\pi\rho}{L_0}\right), \end{aligned} \quad (1.38)$$

where $K_{5/6}(x)$ is the modified Bessel function of the third kind and $\Gamma(x)$ is the gamma function.

1.3.2. Zernike Polynomials

The Zernike polynomials are a basis of modes that are orthogonal over a circular support ([Noll 1976](#)):

$$\frac{1}{S} \int_S Z_i(\mathbf{r}) Z_j(\mathbf{r}) d\mathbf{r} = \delta_{ij}, \quad (1.39)$$

1. Propagation of Light across Atmospheric Turbulence
1.3. Modal Decomposition of the Phase

where δ_{ij} represents the Kronecker delta function. Each polynomial is described by an analytical expression that is the product of a radial function $R_n^m(\mathbf{r})$ and an azimuthal function $\Theta_n^m(\theta)$:

$$Z_j(\mathbf{r}) = R_n^m(\mathbf{r})\Theta_n^m(\theta), \quad (1.40)$$

where the parameters m and n correspond to the azimuthal and radial orders, respectively. The index j is a function of m and n that serves to order the basis, several conventions are possible, here the one of Noll (1976) is used. The radial component is given by:

$$R_n^m(\mathbf{r}) = \sum_{s=0}^{(n-m)/2} \frac{(-1)^s (n-s)!}{s! (n+m)/2 - s)! ((n-m)/2 - s)!} \mathbf{r}^{n-2s}. \quad (1.41)$$

The azimuthal component is given by:

$$\Theta_n^m(\theta) = \begin{cases} \sqrt{n+1} & \text{if } m = 0, \\ \sqrt{2(n+1)} \cos(m\theta) & \text{if } m \neq 0 \text{ and } m \text{ even} . \\ \sqrt{2(n+1)} \sin(m\theta) & \text{if } m \neq 0 \text{ and } m \text{ odd} \end{cases} \quad (1.42)$$

The turbulent phase can be projected into the Zernike polynomials to form a modal basis so that:

$$\varphi(\mathbf{r}) = \sum_{j=1}^{\infty} a_j Z_j(\mathbf{r}), \quad (1.43)$$

where a_j is the coefficient associated to the mode $Z_j(\mathbf{r})$ and is given by:

$$a_i = \frac{1}{\mathcal{S}} \int_{\mathcal{S}} \varphi(\mathbf{r}) Z_j(\mathbf{r}) d\mathbf{r}. \quad (1.44)$$

For practical applications the basis is truncated to a given number of modes, usually considering the modes up to a certain radial order. Since the constant phase offset within the pupil has no effect on the imaging quality (or fiber coupling) it is often removed from the basis.

1.3.2.1. Advantages

The Zernike polynomials offer several advantages for their use as modal description of turbulence; the following advantages are highlighted:

- Their orthogonality over a circular pupil allows them to be used as a modal basis.
- The low order polynomials have a physical meaning in terms of optical aberrations: piston (constant phase offset), tip and tilt, defocus, and other

1. Propagation of Light across Atmospheric Turbulence
 1.3. Modal Decomposition of the Phase

aberrations such as astigmatism, coma, and spherical aberration. This allows an intuitive understanding of the impact of each mode in terms of the resulting imaging performance.

- The energy of the turbulence is ordered by radial order.
- The polynomials can be computed analytically and so can also the statistics of turbulence projected on them, see the following sections.
- Each radial order has a characteristic spatial frequency given by (Conan et al. 1995): $\kappa \approx 0.37(n + 1)/D$.

1.3.2.2. Variance

Thanks to the fact that the Zernike polynomial basis is orthonormalized, the temporal variance of the turbulent phase is equal to the sum of the variances of each coefficient:

$$\sigma_\varphi^2 = \frac{1}{S} \int_S \langle \varphi(\mathbf{r})^2 \rangle d\mathbf{r} = \sum_{j=1}^{\infty} \langle a_j^2 \rangle. \quad (1.45)$$

1.3.2.3. Spatial Covariance

Noll (1976) developed the analytical computation of the covariance between two turbulent modes of Kolmogorov turbulence projected on the Zernike polynomials. Figure 1.3 shows an example of such a covariance matrix.

First, it can be observed how the diagonal of the matrix, corresponding to the variance of each of the modes, is ordered from more to less energy. Second, it can be observed that the covariance matrix is not diagonal, which means that the modes are not statistically independent of each other. Although the Zernike polynomials are orthogonal over the unit circle, the turbulent phase projected on them are not statistically independent. This fact is a disadvantage since it makes necessary to consider the cross-correlations between modes when analyzing the statistics of the turbulence, for example the measurement noise propagation or the statistical estimation of the coefficients. Similar results are obtained for von Kármán spectrum turbulence.

1.3.2.4. Temporal Characteristics

The temporal characteristics of the turbulence projected on a Zernike polynomial basis can be obtained by considering the frozen flow assumption and computing them from the spatial statistics for a distance that is equivalent to the displacement due to the translation of the turbulence layer, see Section 4.2.5.

Conan et al. (1995) studied the temporal spectra of turbulence projected onto a Zernike polynomial basis. The work considers that the layers evolve under the

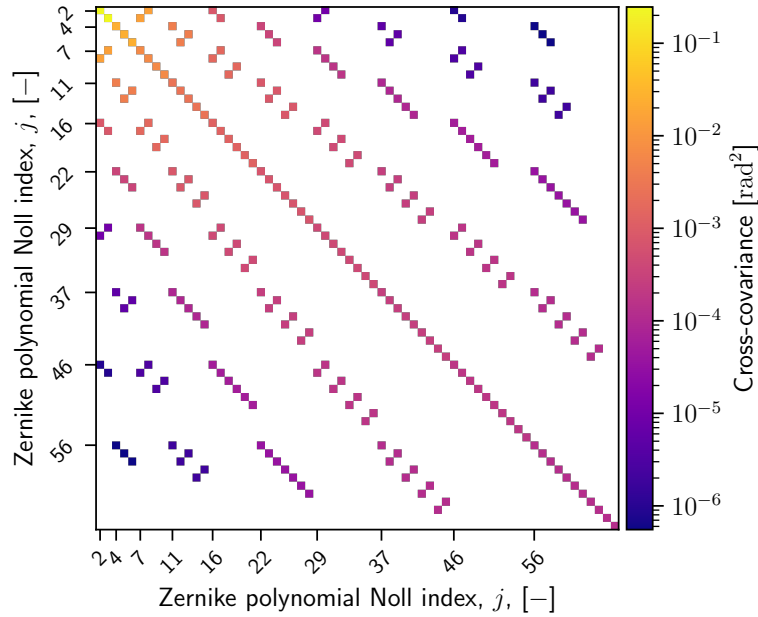


Figure 1.3.: Covariance matrix of Zernike modes assuming Kolmogorov turbulence.

frozen flow assumption and provides the calculation of the temporal spectrum of turbulence projected on each of the Zernike polynomials. One of the main results presented is that the cutoff frequency of each spectral is proportional to:

$$\nu_c \propto 0.3(n + 1) \frac{V}{D}, \quad (1.46)$$

where V is the layer speed, D is the diameter of the telescope, and n is the Zernike polynomial radial order. This means that the temporal evolution of higher-order modes is faster. However, since most of the energy is concentrated on the high-order modes, the temporal filtering of turbulence is driven by both the cutoff frequency of each mode but weighted by the energy of each mode.

1.3.2.5. Angular Covariance

This thesis relies on the computation of the angular covariances between Zernike coefficients to compute the spatio-temporal covariance matrices of turbulence projected on a Zernike modal basis; see Section 4.2.5.2.

The angular covariances between Zernike coefficients, $C(\Delta\alpha)$, for a given angular distance $\Delta\alpha$ are given by [Chassat et al. \(1989\)](#), assuming a von Kármán spectrum and a weak turbulence regime:

1. Propagation of Light across Atmospheric Turbulence
1.3. Modal Decomposition of the Phase

$$\begin{aligned}
C(\Delta\alpha) = & \langle (a_i(0) - a_j(\Delta\alpha))^2 \rangle = \\
& 5.20 K_{ij} \int_0^L C_n^2(z) \int_0^{+\infty} k^{-\frac{14}{3}} \\
& \times J_{n_i+1}(k) J_{n_j+1}(k) \cos^2\left(\frac{zk^2}{2k_0 R_{\text{tel}}^2}\right) \left(1 + \frac{2\pi R_{\text{tel}}^2}{L_0 k}\right)^{-\frac{11}{6}} \\
& \times \left(S_1 J_{m_1+m_2}\left(\frac{k d(z, \Delta\alpha)}{R_{\text{tel}}}\right) + S_2 J_{|m_1-m_2|}\left(\frac{k d(z, \Delta\alpha)}{R_{\text{tel}}}\right)\right) \\
& \times dz dk,
\end{aligned} \tag{1.47}$$

where:

- $k = 2\pi f$ is the angular spatial frequency of the domain in which the polynomials are defined,
- (n_i, m_i) and (n_j, m_j) are the radial and azimuthal degrees of the i th and j th Zernike polynomials respectively,
- z is the distance to the telescope pupil on the line of sight,
- R_{tel} is the telescope pupil radius,
- $k_0 = \frac{2\pi}{\lambda}$ is the wavenumber,
- K_{ij} is defined as $K_{ij} = \sqrt{(n_i + 1)(n_j + 1)} \cdot (-1)^{\frac{n_i+n_j-m_i-m_j}{2}} \cdot R_{\text{tel}}^{\frac{5}{3}} \cdot k_0^2$,
- $C_n^2(z)$ is the turbulence refractive index structure function at a distance to the pupil z ,
- $J_n(k)$ are the Bessel functions of the first kind of order n ,
- $\cos^2\left(\frac{zk^2}{2k_0 R_{\text{tel}}^2}\right)$ corresponds to the Fresnel term to account for the diffractive effects on phase due to propagation (Lognoné et al. 2022),
- $\left(1 + \frac{2\pi R_{\text{tel}}^2}{L_0 k}\right)^{-\frac{11}{6}}$ is the von Kármán term accounting for the influence of the turbulence outer scale L_0 ,
- $d(z, \Delta\alpha)$ is the distance between the two beam footprints separated by an angular distance $\Delta\alpha$ at a distance z ,
- S_1 and S_2 are geometrical coefficients that capture the relative angular clocking rotation of the beam footprints as described in Chassat (1992).

* * *

Summary

This chapter discussed the phase and amplitude distortions of an optical wave propagating across atmospheric turbulence.

First, the origin and statistics of the index of refraction fluctuation were discussed. The frozen flow assumption was presented as a fundamental hypothesis in this thesis, since it allows one to describe the temporal evolution of turbulence from its spatial statistics.

The numerical and analytical treatment of the propagation of an optical wavefront in atmospheric turbulence was discussed. This allowed the introduction of the origin of the phase and the amplitude distortions on the beam. The method for the numerical simulation of optical propagation used in the *TURANDOT* simulation tool was also introduced. These methods and tools will be used to study the scintillation characteristics of the strong turbulence emulator presented in Chapter 8.

Finally, the representation of turbulent phase on a modal basis and the statistics of each mode were introduced. This tool will be used for the analytical computation of phase correction and for the formulation of phase evolution models to be incorporated into the predictive controller developed in this thesis.

2. Adaptive Optics

Contents

2.1. Adaptive Optics Principle	28
2.2. Wavefront Sensing	29
2.3. Wavefront Correction	31
2.4. Adaptive Optics Control	32
2.4.1. Adaptive Optics Loop	33
2.4.2. Interaction and Control Matrices	34
2.4.3. Integral Action Control	36
2.4.4. Modal Control	36
2.4.5. Phase Reconstruction	37
2.4.6. Linear Quadratic Gaussian Control	39
2.5. Error Budget	39
2.5.1. Turbulence Induced Errors	39
2.5.1.1. Scintillation Error, σ_{scint}^2	40
2.5.1.2. Anisoplanatism Error, σ_{aniso}^2	40
2.5.2. Adaptive Optics System Errors	41
2.5.2.1. Fitting Error, $\sigma_{\text{fitting}}^2$	41
2.5.2.2. Aliasing Error, σ_{alias}^2	42
2.5.2.3. Wavefront Sensor Noise Error, σ_{meas}^2	42
2.5.2.4. Temporal Error, σ_{temp}^2	42
2.5.3. Other Errors	43
2.5.3.1. Calibration Error, σ_{cal}^2	43
2.5.3.2. Non-Common Path Aberration Error, σ_{NCPA}^2	43
2.5.3.3. Mechanical Vibrations, σ_{vib}^2	44
2.5.3.4. Modeling Errors	44

Introduction

This chapter presents the basics of adaptive optics systems and their components.

The chapter will also discuss adaptive optics as a control problem. This includes two different aspects, the shaping of a stable control loop with the best performance possible and the necessary phase reconstruction to optimize necessary for certain kinds of advanced adaptive optics controllers. Finally, the concept of adaptive optics error budget is introduced; this can be seen as a methodology for the analysis of adaptive optics performance based on the analytical modeling of an adaptive optics loop. The use of error budgets and other modeling tools is at the heart of the methodology followed in this thesis.

2.1. Adaptive Optics Principle

An *adaptive optics* (*AO*) system is an optomechanical system used to correct in real-time the distortions on an optical wavefront. Figure 2.1 depicts such a system. The distorted wavefront enters the telescope, a *wavefront sensor* (*WFS*) is used to measure it. The measurement is processed by a *real-time computer* (*RTC*) that computes and sends commands to a *deformable mirror* (*DM*). The mirror is controlled to impose the same but opposite in sign wavefront distortion as the one measured on the beam. The resulting (partially) corrected wavefront provides (close to) diffraction-limited focusing of the beam, improving the performance of the instrument using the beam, for example, imaging or fiber coupling.

Most adaptive optics systems work in closed-loop, where the wavefront sensor is placed after the deformable mirror so that the measurement wavefront corresponds to the residual one. Typically, the corrected distortions will come from atmospheric turbulence; however, adaptive optics can also correct other aberrations present in the system.

The remainder of this chapter details the working principle and mathematical modeling of adaptive optics systems. The discussion is focused on the architecture used for the application covered in this thesis. These are relatively small telescopes and, therefore, relatively small *AO* systems when compared to the modern 40 m-class telescopes under construction Bonnet et al. (2018). First, the two main physical elements of *AO* systems are discussed: Section 2.2 introduces the Shack-Hartmann wavefront sensor, while Section 2.3 discusses the use of a deformable mirror as wavefront corrector. Nevertheless, due to the presence of measurement noise and the delay between the measurement and correction, it is not possible to directly apply the wavefront correction as it is measured. Instead, the correction needs to be temporally filtered by a control system to achieve a stable closed-loop control. Section 2.4 discusses the control algorithms and techniques used in *AO*. Finally, in truth, adaptive optics suffers physical and instrumental limitations that

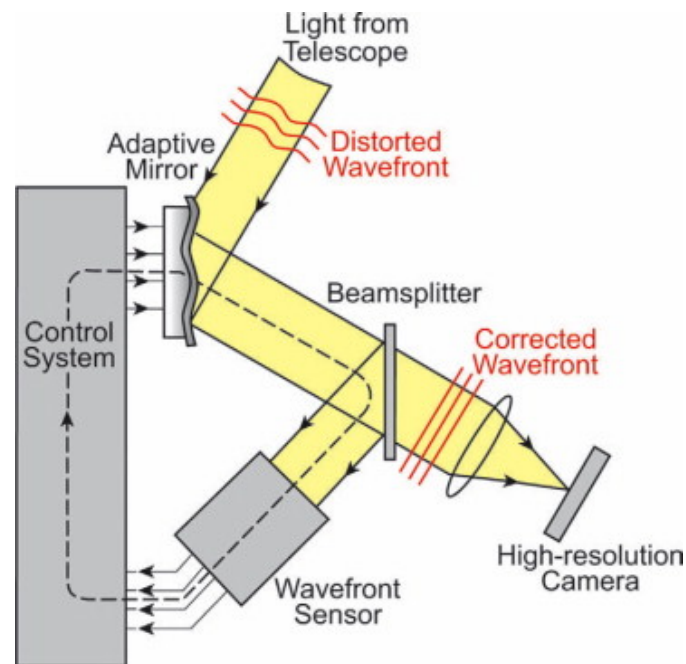


Figure 2.1.: Adaptive optics system diagram. (Credit: C. Max.)

make its correction only partial. Section 2.5 introduces the adaptive optics error budget as the breakdown of the various contributions to the residual wavefront error after adaptive optics correction.

2.2. Wavefront Sensing

This thesis limits its discussion to the *Shack-Hartmann* (*SH*) as *AO* wavefront sensor. The *SH* is used in most of the *AO* systems in operation at the moment and accumulates a strong heritage; as a sensor, it is linear over a high dynamic range, has a simple design, has a robust operation and it is achromatic. As an alternative, the use of a pyramid wavefront sensor [Ragazzoni \(1996\)](#) is being studied, especially for satellite imaging applications, as it can offer an increase in sensitivity ([Ragazzoni and Farinato 1999](#)) and a reduction in the effect of aliasing. Nevertheless, the pyramid sensor has a low range over which it is linear and requires the use of a set of gains (known as optical gains) that change with the turbulence conditions; while some solutions have been suggested to adjust these gains, changing turbulence conditions during the tracking of *LEO* satellites increase the difficulty of the pyramid sensor operation for this application.

The Shack-Hartmann measures the local slopes of the wavefront. It does so by placing a microlens array on the pupil plane of the telescope that split the wavefront in a grid of subpupils and images the light within each of them at a different location on a detector. The image within each subpupil will be a spot

on the detector (when using a point source); the position and shape of the spot are a result of the local wavefront within the subpupil. The local wavefront slopes will influence the position of the spot, i.e. its centroid, on the detector, while higher-order aberrations are responsible for the shape of the spot (the diffraction pattern of the pupil when diffraction-limited, which is distorted in the presence of turbulence). Since the effect of turbulence distortion on the spots affects the measurements, the Shack-Hartmann is usually dimensioned to be near-diffraction-limited within each subpupil. The displacement of the centroid of the spot of each microlens, (x_c, y_c) , also known as wavefront slopes, is related to the local slope of the corresponding sub-aperture by the following expressions:

$$\frac{x_c}{f_{\text{ml}}} = \frac{\lambda}{2\pi S} \iint_{\text{spup}} \frac{\partial \phi}{\partial x} dx dy, \quad (2.1)$$

$$\frac{y_c}{f_{\text{ml}}} = \frac{\lambda}{2\pi S} \iint_{\text{spup}} \frac{\partial \phi}{\partial y} dx dy, \quad (2.2)$$

where f_{ml} corresponds to the focal length of the microlenses and S to the surface of each subpupil. These equations neglect the effect of scintillation [Mahe et al. \(2000\)](#).

Within the Shack-Hartmann post-processing chain, the slopes are computed as using a centroid computation algorithm, generally a variation of center of gravity computation, on the intensity distribution measured by the detector [Thomas et al. \(2006\)](#). The measurement is compared to a reference position previously calibrated in absence of turbulence to compute the slope error.

The Shack-Hartman measurements are linear, apart from some measurement and post-processing artifacts at the end of its dynamic range. Thus they can be modeled by the following equation:

$$\boxed{\mathbf{y} = \mathbf{D}\phi + \mathbf{w}}, \quad (2.3)$$

where \mathbf{y} are the measured slopes, ϕ is a vectorial representation of the phase in front of the wavefront sensor, and \mathbf{D} is the model of the wavefront sensor measurement. Finally, \mathbf{w} is an additive measurement noise component.

There are two sources of noise within the Shack-Hartmann: (1) the photon noise and (2) the detector read-out noise. Both noises appear at a pixel level adding uncertainty to the measurement of centroid of the spot; this propagates further to the slope measurement. Photon noise derives from the arrival statistics of individual photons at each pixel and therefore it follows a Poisson distribution. The detector read-out noise is due to the variation in the electrical signal produced at each pixel due to the analog to digital conversion, amplification, and other processing steps; it follows a Gaussian distribution. The propagation of these errors within the slopes computation depends on the method used to compute them ([Nicolle et al. 2004](#); [Thomas et al. 2006](#)).

Remark

The estimation algorithms in this thesis assume that the noise terms are Gaussian and white. Photon noise instead follows a Poisson distribution (but still white). Nevertheless, it is often, but not always (Gratadour et al. 2005), approximated as Gaussian when deriving estimators; this is the case in this thesis.

In the case of the center of gravity method, variance slope measurement noise (in radians squared of phase across a subpupil) due to photon noise is given by:

$$\sigma_{\text{ph}}^2 = \frac{\pi^2}{2} \frac{1}{N_{\text{ph}}} \frac{N_T^2}{N_D^2} \text{ (rad}^2\text{)} , \quad (2.4)$$

where N_{ph} is the average number of photons per subpupil, N_T the full width at half maximum of the lenslet spot under the influence of turbulence, and N_D the full width at half maximum of the diffraction-limited spot. Both widths are usually given in pixels.

For detector read-out noise we have (in the same units):

$$\sigma_{\text{RON}}^2 = \frac{\pi^2}{3} \frac{\sigma_{\text{RON}}^2}{N_{\text{ph}}^2} \frac{N_S^4}{N_D^2} \text{ (rad}^2\text{)} , \quad (2.5)$$

where $\sigma_{\phi, \text{RON}}$ corresponds to the standard deviation of the read-out noise per pixel in photo-electrons and N_S the number of pixels used for the computation of the center of gravity (in general $N_S \approx 2N_T$).

The previous expressions express the centroid computation errors in units of phase difference across the subpupils (in radians). In some occasions, it is necessary to express these noises in pixels since these are the units in which the calibrations (i.e. interaction matrix) are measured. The slope error variance in radians squared can be translated to pixel squared by multiplying by $(N_{\text{samp}}/2\pi)^2$, where N_{samp} is the sampling parameter of the lenslet spot (Thomas et al. 2006). Rigaut and Gendron (1992) provides formulas for the propagation of the slope measurement error to the reconstruction of Zernike coefficients using the least-square method.

2.3. Wavefront Correction

In an adaptive optics system, a *deformable mirror* (*DM*) is used to introduce an additional phase distortion on the beam that should (at least partially) cancel the distortions originated by atmospheric turbulence. The typical *DM* is composed of a continuous flexible mirror substrate and coating that can be deformed thanks to a set of actuators that receive commands to control their stroke. As a result, the mirror is able of changing shape to correct the turbulence distorted wavefront in

real time. For an overview of the different *DM* technologies available see [Madec \(2012\)](#).

The correction phase ϕ^{cor} generated by the *DM* for a given command vector \mathbf{u} can be modeled as a sum of the responses of the surface to each individual actuator command, denominated influence function of the actuator, $f_i(\mathbf{r})$, times the commanded amplitude for the actuator:

$$\phi^{\text{cor}}(t) = \sum_{i=1}^{N_{\text{act}}} f_i(\mathbf{r})u_i = \mathbf{M}_{\text{inf}}\mathbf{u}(t), \quad (2.6)$$

where N_{act} is the number of actuators of the *DM* and \mathbf{M}_{inf} is a matrix that concatenates the influence functions for each actuator, denominated influence matrix, and \mathbf{u} is a vector concatenating the commands for each actuator.

2.4. Adaptive Optics Control

The presence of measurement noise and a delay between measurement and correction prevents a direct application of the measured phase from leading to a stable closed-loop behavior. Instead, the phase measurements need to be filtered in time using a control system that guarantees stability while maximizing the correction performance.

Remark

While the measurement vector \mathbf{y} is in the slopes space, the (classical) *AO* controller is in the *DM* space. As a result, an intermediate phase reconstruction is necessary, see Section 2.4.5.

From a control system theory point of view, adaptive optics control is a *multiple-input multiple-output (MIMO)* regulation problem: (1) a *MIMO* problem since it computes several commands (i.e. inputs) that will affect several measurements (i.e. outputs) and (2) a regulation problem since the goal of the control system is to reject the disturbances on the system (the atmospheric turbulence evolution) that cause it to deviate from its reference state (the reference slopes that lead to the desired wavefront, usually flat).

With respect to other aerospace control problems, adaptive optics comes with particular challenges:

1. Its plant, i.e. the atmospheric turbulence phase distortions, is stochastic and difficult to model. Chapter 1 introduced the statistical description of turbulence, the statistical models of turbulence allow analyzing the performance of adaptive optics systems and also designing predictive controllers, as will be discussed in Chapter 4. However, these models do not capture all the possible

problems (Petit et al. 2006; Sauvage et al. 2015; Lai et al. 2019) that impact the performance of adaptive optics systems.

2. The states of its plant (electromagnetic optical phase) are not easily measurable, since no optical phase can be measured directly and requires instead indirect measurements such as wavefront slopes and a phase reconstruction step.
3. The measurements are noisy because of the use of faint sources for wavefront sensing.
4. There exists an important delay between the measurement and the correction.
5. It involves a large number of measurements and actuators, in the order of the hundreds for medium-size systems like the ones discussed in this thesis, but up to thousands in the case of bigger telescopes. This increases the computational complexity and cost of its control laws.
6. It needs to run at high loop frequency. The evolution of the atmospheric disturbance is so fast that it requires loop frequencies of the order of thousands of Hz. This limits the computation time for its control laws, reduces the time available for wavefront sensing (limiting the flux further), and increases the complexity and cost of the system components.

The remainder of this section is an introduction to the control aspects of adaptive optics. Section 2.4.1 introduces the *AO* loop and its notation. Section 2.4.2 deals with the computation of *DM* commands from slopes. The classical *AO* controller, the integral action controller, is introduced in Section 2.4.3; this is followed by two refinements: (1) modal control in Section 2.4.4 and (2) phase reconstruction in Section 2.4.5.

2.4.1. Adaptive Optics Loop

The use of a chronogram allows to illustrate the working principle of the adaptive optics loop. Figure 2.3 depicts such a chronogram and introduces the related notation. The loop is divided into time intervals of a period T defined by the frequency of the loop $T = 1/f_{\text{samp}}$. The *WFS* detector uses an exposure time of T of enough duration to have enough photons. The exposure results in an integration of the phase during this time:

$$\phi_k^{\text{res}} = \frac{1}{T} \int_{(k-1)T}^{kT} \phi^{\text{res}}(t) dt. \quad (2.7)$$

The *WFS* image is read-out and post-processed, which produces a measurement y_k that corresponds to the wavefront ϕ_{k-1}^{res} . Using the new measurement, the next

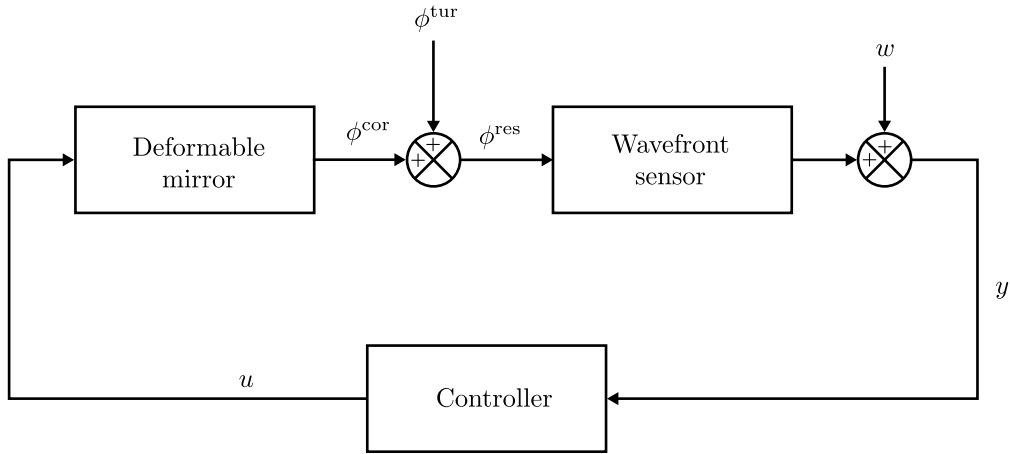


Figure 2.2.: Architecture diagram of a closed-loop adaptive optics system.

DM command \mathbf{u}_{k+1} is computed and applied during a complete interval as a zero-order hold:

$$\mathbf{u}_{k+1} = \mathbf{u}(t), \quad t \in [kT, (k+1)T[. \quad (2.8)$$

Note that by the time the command u_{k+1} is applied, it will act on the wavefront ϕ_{k+1}^{res} while it is based on the measurement y_k and therefore on the wavefront ϕ_{k-1}^{res} , thus the two frame delay. The difference between these two phases is responsible for the temporal error (see Section 2.5.2.4).

Figure 2.3 illustrates the case of the typical two-frame delay considered for most adaptive optics systems. In practice, this delay can be non-integer and arbitrarily long depending on the time required to post-process the *WFS* measurement and compute the new command.

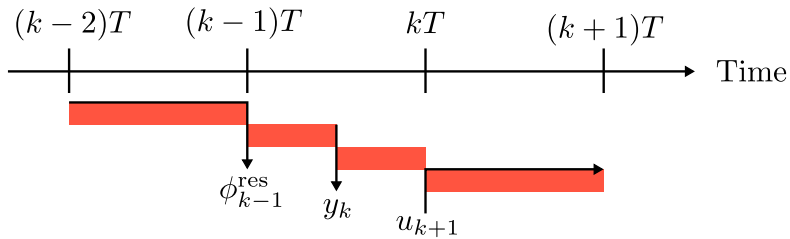


Figure 2.3.: Chronogram of the adaptive optics control loop.

2.4.2. Interaction and Control Matrices

Before defining a control strategy, it is necessary to define a link between the controller quantity, the measurement of the *WFS*, \mathbf{y} and the control commands, \mathbf{u} . This relationship is linear and is given by the following expression:

$$\mathbf{y} = \mathbf{M}_{\text{int}} \cdot \mathbf{u}, \quad (2.9)$$

where \mathbf{M}_{int} is the matrix called interaction matrix.

The control matrix \mathbf{M}_{ctrl} is defined as the matrix that provides the control commands that will cancel the input *WFS* measurement:

$$\mathbf{u} = -\mathbf{M}_{\text{ctrl}} \cdot \mathbf{y}. \quad (2.10)$$

This matrix can be computed as the pseudo-inverse of the interaction matrix: $\mathbf{M}_{\text{ctrl}} = (\mathbf{M}_{\text{int}})^\dagger$. This pseudo-inverse is computed by means of *singular value decomposition* (*SVD*) decomposition:

$$\mathbf{M}_{\text{int}} = \begin{bmatrix} \mathbf{U}^\parallel & \mathbf{U}^\perp \end{bmatrix} \cdot \text{diag}(\mathbf{s}) \begin{bmatrix} \mathbf{V}^\parallel \\ \mathbf{V}^\perp \end{bmatrix}^\top, \quad (2.11)$$

where \mathbf{s} is the vector of singular values ordered in descending order. The \mathbf{U}^\parallel vectors span a base of orthogonal modes that can be measured and controlled, while in the case of \mathbf{U}^\perp the vectors are the modes that cannot be measured since they have very low (poorly seen modes since sensitive to noise) or zero (unseen modes) singular values. The \mathbf{V}^\perp vectors correspond to the *DM* commands that generate a poorly seen or unseen measurement.

A simple thresholding of the lowest singular values may not be enough due to the presence of waffle mode. See Appendix B of [Petit \(2006\)](#) for how to filter the waffle mode and other details on the computation of the control matrix.

Once the modes have been filtered, the pseudo-inverse of the interaction matrix can be computed as:

$$\mathbf{M}_{\text{ctrl}} = (\mathbf{M}_{\text{int}})^\dagger = \mathbf{V}^\parallel \cdot \text{diag}(\mathbf{s}')^{-1} \cdot (\mathbf{U}^\parallel)^\top, \quad (2.12)$$

where \mathbf{s}' is the vector that contains the singular values associated with the modes kept as part of \mathbf{U}^\parallel and \mathbf{V}^\perp .

So far it has been assumed that the interaction matrix is known; however, it needs to be computed. The interaction matrix can be experimentally computed as a calibration procedure. The interaction matrix can be calculated as a sensitivity matrix of the response of the *WFS* to each of the *DM* actuators. This matrix is computed by applying and measuring the response of the *WFS* to a positive and negative (small) command amplitudes, computing their difference and dividing by two. This calibration needs access to a point source to provide a flat wavefront to illuminate the system. In the absence of a stable wavefront, a point source subject to atmospheric turbulence (typically a guide star) can be used if the *WFS* measurements are averaged for a long enough time, assuming that turbulence has zero mean. Other methods of obtaining the interaction matrix rely on mathematical models ([Oberti et al. 2006](#)).

2.4.3. Integral Action Control

The traditional adaptive optics controller is the integral action or integrator. The formulation of the integral action controller is a self-recurrent expression:

$$\mathbf{u}_{k+1} = \mathbf{u}_k + \mathbf{G} \cdot \mathbf{y}_k \quad (2.13)$$

where \mathbf{G} is typically $g \cdot \mathbf{M}_{ctrl}$, a scalar gain and the control matrix of the *adaptive optics (AO)* system. Setting the gain is a trade-off between noise propagation, loop stability, and performance. Since the turbulence disturbance dynamics (Conan et al. 1995) and the propagation of noise (Rigaut and Gendron 1992) are not the same for different modes of turbulence, the *optimal modal gain integrator (OMGI)* method (Gendron and Lena 1994; Dessenne et al. 1998) was developed to provide a different optimal gain for each of the controller modes in the AO system.

An additional improvement to the integral action is the use of a coefficient in the integral term of the controller as a forgetting factor. The resulting controller is the leaky integrator:

$$\mathbf{u}_{k+1} = f \cdot \mathbf{u}_k + \mathbf{G} \cdot \mathbf{y}_k \quad (2.14)$$

The leaky integrator has been reported to reduce noise and aliasing propagation (Agapito et al. 2019), in particular for high-order modes. This kind of control structure is widely used in current adaptive optics systems (Banet and Spencer 2020; Agapito et al. 2021; van Kooten et al. 2022).

2.4.4. Modal Control

Since the optical wavefront phase is not directly measured, it has to be reconstructed (i.e. estimated) from the slope measurements provided by the Shack-Hartmann wavefront sensor. Two kinds of approaches are possible for phase reconstruction: (1) zonal if the phase is estimated at a local point or (2) modal if the phase is estimated as the coefficients of a modal basis defined across the telescope aperture. Once the phase has been reconstructed, a projection matrix is used to create the shape of the sum of the estimated modes with the *DM*.

The early results in adaptive optics theory highlighted the advantages of the use of modal phase representations for wavefront correction. These early phase reconstruction methods (zonal or modal) start with Rimmer (1974), followed by several publications (Fried 1977; Hudgin 1977; Noll 1978; Fried 1978; Hunt 1979; Cubalchini 1979; Herrmann 1980), and finish with Southwell (1980). All these methods are based on the least squares estimator (see Section 2.4.5) while they study the comparison between different zonal and modal reconstruction bases in terms of noise propagation and computational complexity. Southwell (1980) compares zonal and modal reconstruction and shows that noise propagation is lower in the case of modal reconstruction compared to several zonal reconstruction methods. Additionally, the modes with lower *signal-to-noise ratio (SNR)* can be

filtered out, so they are not used in the correction (known as modal truncation) since they will add more noise than signal to it.

The Zernike polynomials can be used for modal control; their main advantage is their analytical tractability, which allows one to compute formulas for turbulence statistics and performance metrics. The Karhunen–Loève (Fried 1978) basis has the advantage of being optimal in the sense that it is the basis that better fits the turbulence for a given number of modes; using fewer modes allows to relax the computational cost of the correction. Unfortunately, the KL cannot be easily computed analytically (Dai 1995).

As introduced in Section 2.4.3 in the context of the *OMGI* controller, the use of modes allows to take advantage of the different dynamics and noise propagation of each mode to optimize their gain to optimize the rejection performance.

The greater desirability of one reconstruction basis over another is not a closed question in the literature. A complete evaluation of this problem would require considering not only the noise propagation and reconstruction error, but also factors such as the instrumental implementation of the calibration for each basis or the sensitivity to model errors. Some additional observations on the comparison of zonal and modal reconstruction bases are given in Section 6.2 in the context of prediction of turbulence.

Section 2.4.5 details the methods used in phase reconstruction. Note, not only modal methods, but also zonal methods benefit of phase reconstruction.

2.4.5. Phase Reconstruction

Historically (see Flicker et al. (2000) and Ellerbroek (2002) for an overview, comparison, and historical context of phase reconstruction methods), phase reconstruction was carried out using the pseudo-inverse of the influence matrix. This is the least squares estimator that finds the best fit of the slopes to the DM . This was not enough for tomographic reconstructors since there exist many poorly seen modes. A solution to this problem is to regularize this inversion; two main groups of options are available regarding the regularization of inversion problems: (1) *SVD* and truncation of the lower singular values (i.e., the poorly seen modes) as discussed in Section 2.4.2; (2) using a regularization term in the reconstructor. The second category is discussed below.

We start by considering the following measurement equation:

$$\mathbf{y} = \mathbf{D}\boldsymbol{\phi} + \mathbf{w}, \quad (2.15)$$

where \mathbf{y} are the measured slopes, $\boldsymbol{\phi}$ is a vectorial representation (in an arbitrary space) of the phase in front of the wavefront sensor, and \mathbf{D} is the model of the measurement of the wavefront sensor. Finally, \mathbf{w} is an additive measurement noise component of the covariance matrix $\boldsymbol{\Sigma}_w$.

The goal is to find the phase reconstructor \mathbf{R} so that:

$$\hat{\phi} = \mathbf{R}\mathbf{y} = \mathbf{D}^\dagger \mathbf{y}, \quad (2.16)$$

where $\hat{\phi}$ is the estimated phase and $\mathbf{R} = \mathbf{D}^\dagger$ is a pseudo-inverse of the measurement equation.

The classical least-squares pseudo-inverse solution is given by:

$$\mathbf{D}^\dagger = (\mathbf{D}^\top \mathbf{D})^{-1} \mathbf{D}^\top. \quad (2.17)$$

Remark

Here, $\mathbf{D}^\top \mathbf{D}$ is, in general, not guaranteed to be invertible due to unseen or poorly-seen modes whose eigenvalues are close to zero. Thus, this solution requires a regularization that at least will filter out these modes.

The least-squares solution can be regularized by using the noise-weighted case:

$$\mathbf{D}^\dagger = (\mathbf{D}^\top \Sigma_w^{-1} \mathbf{D})^{-1} \mathbf{D}^\top \Sigma_w^{-1}. \quad (2.18)$$

As an alternative, Tikhonov regularization will introduce a regularization parameter $\alpha > 0$ so that:

$$\mathbf{D}^\dagger = (\mathbf{D}^\top \mathbf{D} + \alpha \mathbf{I})^{-1} \mathbf{D}^\top. \quad (2.19)$$

A classical result is that Tikhonov regularization is equivalent to the *SVD* truncation, where the regularization parameter tunes the number of singular values that are truncated. Singular value truncation removes information from the truncated modes under the assumption that their *SNR* is too low to be useful. Instead, the *maximum a posteriori* (*MAP*) estimator (Wallner 1983) can be used:

$$\mathbf{D}^\dagger = (\mathbf{D}^\top \Sigma_w^{-1} \mathbf{D} + \Sigma_\phi^{-1})^{-1} \mathbf{D}^\top \Sigma_w^{-1}, \quad (2.20)$$

where Σ_ϕ is the covariance of the phase. Note how this is a mixture of the noise weighted least squares solution with a regularization similar to the Tikhonov regularization, but in this case using a weighting that depends on the turbulence variance with respect to the measurement noise; in fact, the *MAP* reconstructor can be seen as a Tikhonov regularization but with the optimal parameter found thanks to the statistic priors (Foster 1961).

Fusco et al. (2001) adapted the method for tomographic approaches, while Thiébaud and Tallon (2010) introduced a method to solve the reconstruction using iterative methods that are more computationally affordable.

Remark

The phase covariance statistics required for the *MAP* based regularization are only available for open-loop turbulence. As a result, a pseudo open-loop controller needs to be used for these methods.

2.4.6. Linear Quadratic Gaussian Control

The *linear-quadratic-Gaussian* (*LQG*) controller is explained in detail in Section 4.3.

2.5. Error Budget

The wavefront correction provided by adaptive optics will be only partial, resulting in a residual wavefront error. The adaptive optics error budget is the breakdown of the different contributors to the residual wavefront error. The adaptive optics budget is expressed in terms of the variance of the residual phase; under the assumption that all error terms are statistically uncorrelated, the variance for an element can be summed to compute the total residual variance.

The elements causing errors in *AO* systems can be grouped into three categories:

1. Turbulence induced errors,
2. adaptive optics system errors, and
3. other errors.

Some of those are detailed below, although this list is not exhaustive. Depending on the adaptive optics system, application, and operating point, some terms will become more relevant than others, while others can be neglected.

Remark

Understanding and tracking the error budget is crucial to analyze and verify the performance of an adaptive optics system during its design and implementation.

2.5.1. Turbulence Induced Errors

Those are errors related to the nature of optical propagation in turbulent media, such as the anisoplanatism of turbulence or the amplitude distortions across atmospheric propagation that cannot be corrected by adaptive optics. Other errors such as the atmospheric chromatism error are of importance in some cases, but are not considered in this manuscript.

2.5.1.1. Scintillation Error, σ_{scint}^2

Scintillation is the variation in the irradiance distribution over the pupil of a telescope (or its focal plane) caused by amplitude distortions of the wavefront resulting from the propagation of phase distortions along its path. Two factors drive the strength of this effect: (1) long propagation distances, so the upper layers of the atmosphere are its biggest contributor; and (2) strong turbulence. Since adaptive optics only corrects the phase of the electromagnetic wave, its performance, measured as the variance of the residual phase, is not directly linked to scintillation. However, scintillation contributes to the residual phase budget since the inhomogeneous irradiance distribution produces measurement errors in the wavefront sensors (Mahe et al. 2000) and in stronger regimes can impair wavefront sensing.

For astronomical observations and ground-based imaging of satellites, the effect of scintillation is often neglected, since these observations happen at higher line of sight elevations and during night, when turbulence strength is weaker. Scintillation becomes more important in the case of free-space optical communication, since they take place in less favorable locations during night-time and day-time (when turbulence is stronger) and ground-to-*LEO* links need to be extended to lower elevations to increase the duration of the link. Additionally, although not affecting phase correction directly, scintillation affects other performance metrics such as fiber coupling; see Section 3.3.2.1.

2.5.1.2. Anisoplanatism Error, σ_{aniso}^2

Most adaptive optics applications aim to correct in an angular direction different to the direction of the source used for wavefront sensing, for example the use of a natural guide star to image a galaxy. This is because most targets in astronomy are not bright enough to be used for wavefront sensing. Although the integration time of the imaging cameras can be long enough to image faint targets, the integration time of the wavefront sensor is limited by the *AO* loop rate, which limits the possible sources for wavefront sensing.

The anisoplanatism error is defined as the difference between the turbulence phase in the direction of correction and the phase in the direction at which wavefront sensing is performed:

$$\sigma_{\text{aniso}}^2 = \langle (\phi(\alpha) - \phi(0))^2 \rangle, \quad (2.21)$$

where α is the angle between both directions. Anisoplanatism phase variance can be computed using the spatial angular decorrelation of turbulence (Fried 1982).

The anisoplanatic error becomes bigger with bigger angular distance between the source and the target, which limits the guide stars available for a given target. This lack of natural guide stars is what motivated the development of laser guide stars. For ground-based imaging of satellites, it is often possible to use the reflection

of sunlight on the satellite as a wavefront source, although laser guide stars are also common (Fugate et al. 1994). Anisoplanatism is not a problem in the case of optical communication downlinks, since in this case the satellite is used as a beacon. For precompensated uplinks (Shapiro 1975; Tyson 1996) it is possible to use the satellite downlink beam as a beacon; however, the angular distance between the downlink and uplink beams (i.e. the point ahead angle (Lognone et al. 2022; Lognoné et al. 2022)) introduces anisoplanatism error in the *AO* correction.

2.5.2. Adaptive Optics System Errors

Those are wavefront errors caused by the design and characteristics of the adaptive optics systems and their components. All these errors are driven by the adaptive optics system design, therefore, the different parameters of the system elements such as the wavefront sensor, deformable mirror, or control loop can be traded off to balance them.

2.5.2.1. Fitting Error, $\sigma_{\text{fitting}}^2$

This error corresponds to the difference between the shape of the wavefront and the shape that the deformable mirror can fit. In the spatial frequency domain, this corresponds to the limited bandwidth covered by the deformable mirror influence functions. As a result, the high spatial frequencies that are not covered by the *DM* are not corrected (even if the phase is perfectly measured) and contribute to the residual wavefront.

The fitting error variance can be computed as:

$$\sigma_{\text{fitting}}^2 = 0.458(n_{\text{max}} + 1)^{-5/3} \left(\frac{D}{r_0}\right)^{5/3}, \quad (2.22)$$

where n_{max} is the maximum corrected Zernike radial order in the system, r_0 is the Fried parameter, and D is the diameter of the telescope entrance aperture.

A deformable mirror with more actuators is able to cover a broader spatial frequency and, therefore, fits more turbulence and reduces fitting error. Nevertheless, the cost of the *DM* increases with the number of actuators, and so does the computational complexity of the control algorithm, which limits the maximum temporal sampling frequency of the loop (see temporal error). Correcting for more spatial frequencies requires the reconstruction of those frequencies. Reconstructing more spatial frequencies requires a finer sampling of the phase; for a fixed number of photons over the telescope pupil, this implies fewer photons per measurement point. For example, for the Shack-Hartmann *WFS*, a finer sampling requires the use of more subpupils, which reduces the number of photons available per subpupil.

2.5.2.2. Aliasing Error, σ_{alias}^2

This error is related to the finite spatial sampling of the wavefront by the wavefront sensor. For the Shack-Hartmann *WFS* the sampling is defined by the number of microlenses that sample the telescope pupil. The Shack-Hartmann samples the phase of the wavefront at a spatial frequency of $f_{\text{samp}}^{\text{WFS}} = 1/d$, where d is the pitch between two subpupils. The spatial frequencies of the wavefront that are higher than the Nyquist-Shannon sampling criterion of $f_{\text{max}} = f_{\text{samp}}/2 = 1/(2d)$ are not properly sampled by the *SH*. The resulting sampled spectrum is symmetric around f_{max} , also known as spectrum folding, and therefore there is no way to distinguish the energy allocated to a frequency from its symmetric. This wavefront measurement error propagates to the correction causing the aliasing error.

The aliasing error can be computed as a fraction of the fitting error (Rigaut et al. 1998; Neichel 2008):

$$\sigma_{\text{aliasing}}^2 = \alpha \sigma_{\text{fitting}}^2, \quad (2.23)$$

where α is a constant that varies from 0.3 to 0.4. A value of $\alpha = 0.35$ is assumed throughout this thesis.

Spatial filtering techniques (Poyneer and Macintosh 2004; Fusco et al. 2005) reduce the aliasing error by removing the high frequencies of the wavefront so that the wavefront sensor does not see them and therefore cannot be folded into lower frequencies. However, spatial filtering requires partially corrected wavefronts to operate, limiting its use to high-performance systems such as the extreme *AO* systems (Fusco et al. 2006; Poyneer et al. 2016).

2.5.2.3. Wavefront Sensor Noise Error, σ_{meas}^2

The measurement noise in the wavefront sensor propagates to the wavefront reconstruction. For the case of the Shack-Hartmann *WFS*, the measurement of the slopes is impacted by the photon noise and the detector read-out noise (see Section 2.2). This error in the wavefront measurement propagates across the loop and adds up to the residual wavefront error.

The dimensioning of a Shack-Hartmann wavefront sensor depends on many variables such as the flux level available for wavefront sensing, the detector noise, the turbulence level expected and its impact on the shape of the lenslet spots, the sampling of the spots, and the centroid computation algorithm used. A detailed study of the dimensioning for this sensor is reported in Nicolle (2006).

2.5.2.4. Temporal Error, σ_{temp}^2

This error, of great importance for this thesis, is caused by the delay present in the adaptive optics loop between the measurement of the wavefront and its correction. The origin of this delay was detailed in Section 2.4.1. The temporal error increases

with a faster evolution of the turbulence and with slower temporal sampling of the loop.

The most obvious way to decrease the temporal error is to run the loop at a faster frequency. Unfortunately, this strategy faces technological limitations, such as the *DM* response time, the *DM* mechanical resonance frequencies, or the lack of enough computational power. Additionally, running the loop at a faster temporal frequency entails using a shorter integration time for wavefront sensing, which increases the measurement noise error in cases where the flux budget is already tight, such as astronomical targets and ground-based imaging of satellites.

The delay in the loop increases with the complexity of the control algorithm, since more time is necessary for the computations. To avoid increasing the loop delay while using more complex control algorithms such as tomographic reconstructions or extremely-large telescopes with thousands of actuators, different custom *RTC* architectures (Fedrigo et al. 2006) have been proposed that make use of technologies such as *field programmable gate array (FPGA)* or *graphics processing unit (GPU)* for faster computations (Perret et al. 2016). Finally, and in line with the goal of this thesis, predictive control can be used to reduce temporal error.

2.5.3. Other Errors

2.5.3.1. Calibration Error, σ_{cal}^2

This error is related to the different calibrations that are needed to run the adaptive optics loop, such as the interaction matrix or the reference slopes. To compute the commands for the deformable mirror, it is necessary to compute the interaction matrix. Some *AO* systems do not offer access to an internal source to acquire the interaction matrix. Moreover, the interaction matrix changes during operation due to the effect of the environment on the optomechanics of the system (Oberti et al. 2006). The deviations between the interaction matrix and the actual system, also known as misregistration, will cause an error when computing the commands sent to the *DM* and contribute to an additional residual wavefront.

2.5.3.2. Non-Common Path Aberration Error, σ_{NCPA}^2

Once the wavefront sensing beam is split from the main optical path, both beams will undergo different aberrations due to the remaining optical elements. Adaptive optics corrects the aberrations that are measured at the wavefront sensing beam. As a result, it will correct the aberrations in this path and will not correct the aberrations present in the imaging path. These aberrations can be calibrated (Sauvage et al. 2010) and incorporated into the *AO* loop, otherwise they will be part of the residual wavefront error.

2.5.3.3. Mechanical Vibrations, σ_{vib}^2

Mechanical vibrations coming from the telescope structure or from instrument components such as cryo-coolers will cause additional wavefront aberrations. Predictive controllers can be used as vibration filters (Petit et al. 2008; Poyneer and Véran 2010; Guesalaga et al. 2012).

2.5.3.4. Modeling Errors

There are errors in the models used within the *AO* loop. This is the case for the predictive models used in predictive controllers, for example, due to errors in the identification of the model or the turbulence profile.

* * *

Summary

This chapter introduced the basics of adaptive optics. The correction principle of adaptive optics was presented together with its two main components: the Shack-Hartmann as a wavefront sensor and the deformable mirror as a phase corrector.

Different aspects of adaptive optics control were presented. The adaptive optics chronogram was used to introduce the time delay between wavefront measurement and correction in the adaptive optics loop, which will condition adaptive optics control and that can be partially remedied by predictive control. The interaction and control matrices are the main connection between the slopes measurements and the *DM* commands, while the integral action controller is the classical adaptive optics controller that will be used as a benchmark for the predictive controller developed in this thesis. Modal control expresses the phase measurements on a modal basis, by means of phase reconstruction, and allows the controller to be expressed in a different space. This can have advantages related to the noise propagation and filtering in the controller, as well as the modeling of the disturbances to be controlled for the design of more complex control laws such as predictive controllers.

Finally, the error budget was introduced. The error budget is an assessment of the contribution of each aspect of an adaptive optics system to the final residual wavefront phase variance. The error budget allocates and tracks the performance of the system during its design and verification. Thus, it is a crucial tool for the development of adaptive optics controllers.

3. Adaptive Optics for *LEO* Satellite Tracking

Contents

3.1. Low-Earth-Orbit Satellite Tracking	46
3.1.1. Challenges of <i>AO LEO</i> Applications	48
3.1.2. Satellite Orbits Considered	49
3.2. Turbulence Conditions	50
3.2.1. Atmospheric Turbulence Profiles	50
3.2.1.1. <i>MOSPAR</i> Atmospheric Profiles	51
3.2.1.2. Reference Profiles	52
3.2.2. Wind Profile	53
3.2.3. Variation of Integrated Parameters with Elevation	54
3.3. System Performance Metrics	56
3.3.1. Image Formation in Presence of Atmospheric Turbulence	56
3.3.1.1. Effect of Turbulence on the <i>PSF</i>	57
3.3.1.2. Strehl Ratio	57
3.3.2. Communication Channel Impairments Induced by the Atmosphere	59
3.3.2.1. Effect of Turbulence Distortions on Single Mode Fiber Coupling	59
3.3.2.2. Fading Mitigation Techniques	61
3.3.2.3. Link Budget and Link Margin	62
3.4. Adaptive Optics Systems: Case Studies	63
3.4.1. Wavefront Sensing Noise Levels	63
3.4.2. Error Budgets	65

Introduction

This chapter provides a description of the adaptive optics challenges considered in this thesis. These challenges deviate from the ones found in the development of adaptive optics systems for astronomy, since they are specific for *LEO* satellite applications.

This chapter will also provide a definition of the four *AO* systems that will be used as case studies during this thesis: two for optical communications and two for satellite observation.

The chapter will provide the error budgets previously introduced to these four systems. In addition to the residual phase variance used by the *AO* error budgets the Strehl ratio and fiber coupling efficiency will be introduced as application specific metrics.

3.1. Low-Earth-Orbit Satellite Tracking

This thesis focuses on *low Earth orbit (LEO)* satellite applications. *LEO* satellites, the satellites with the lowest orbits, typically with altitudes between 300 km of 2000 km. In contrast to *geosynchronous equatorial orbit (GEO)* satellites, *LEO* satellites present a relative movement with respect to Earth's surface, which implies that they need to be tracked across their trajectory.

LEO orbits present several advantages, mainly related to their closer distance to Earth. For Earth observation payloads, this means higher resolution imaging; conversely, it means that *LEO* satellites can also be imaged with higher resolution by ground-based telescopes. For communications payloads, they allow lower latency, since the electromagnetic signals need to travel less distance, and lower geometric losses, which lead to power savings or higher bandwidths.

The main disadvantage of *LEO* satellites is related to their relative movement with respect to the Earth's surface, since they need to hand over communications between several ground stations. As a result, the duration of the link between the satellite and the ground station is limited and will condition the volume of data that can be exchanged; this volume can be improved with higher data rates, e.g. thanks to optical links.

Figure 3.1 shows the evolution of the elevation and distance of a typical *LEO* satellite with respect to a ground station. It can be observed that the satellite is only observed during a maximum of less than 13 min, while half of this time is spent at an elevation below 20° . Therefore, extended satellite link performance at low elevations can significantly increase link duration. For satellite observation, there is limited interest in imaging below 30° , since the greater distance to the satellite will imply lower received flux, limited resolution, and stronger turbulence.

Due to the advantages mentioned, the majority of satellites are in *LEO* orbits. Traditional space-based communications have privileged architectures based on high-performance payloads in the *GEO* belt, since they do not require tracking by

3. Adaptive Optics for LEO Satellite Tracking

3.1. Low-Earth-Orbit Satellite Tracking

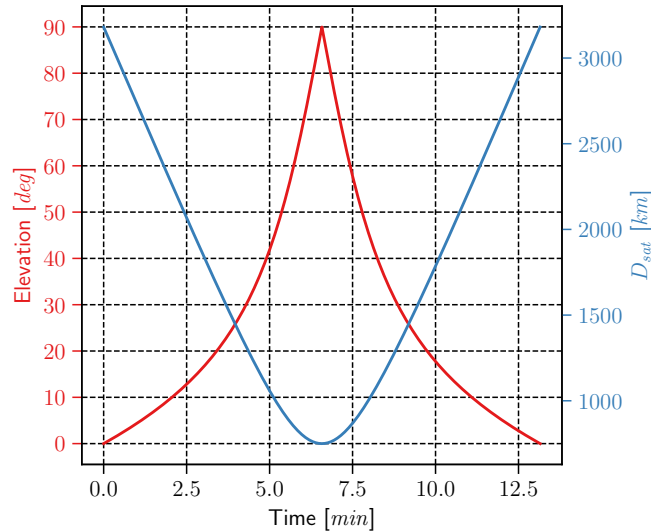


Figure 3.1.: Evolution of elevation of the line of sight and distance to the satellite with time for a 750 km altitude orbit with culmination at 90° .

the receiver, and a unique satellite can cover and service a large area. However, in the last years, a new generation of mega-constellations, e.g. Starlink and OneWeb, for communications have started operation. Figure 3.2 plots the number of satellites launched per year and per orbit type. The data is sourced from the satellite database published by the *Union of Concerned Scientists (USC)* (USC 2023), which, at the time this analysis was conducted, contains all satellites launched until January 2023. A clear trend can be observed: the number of satellites launched per year has increased exponentially in recent years, and the main share of this growth is due to *LEO* satellites.

Such an increase in the use of the *LEO* orbit will drive the interest of new technologies targeting this application. The use of *LEO*-to-ground optical links will be able to support both Earth observation and telecommunications constellations. For Earth observation, optical links will provide higher data rates to download the high-resolution data, for example, the satellites of the *CO3D* constellation by *CNES* will have optical terminals for downloading their data to optical ground stations (Lochard et al. 2023). For telecommunications constellations, optical links will bring higher-data rates, as well as the possibility of using quantum encryption in the links (Acosta et al. 2023). At the same time, the increase in occupation of *LEO* orbits will increase the need to monitor debris and other activities. Since the distance of *LEO* to the satellites is close enough, they can be imaged from ground-based telescopes using adaptive optics. The deterioration of image quality due to atmospheric turbulence means that resolved imaging of *LEO* objects is only possible with the aid of adaptive optics (Petit et al. 2020).

3. Adaptive Optics for LEO Satellite Tracking

3.1. Low-Earth-Orbit Satellite Tracking

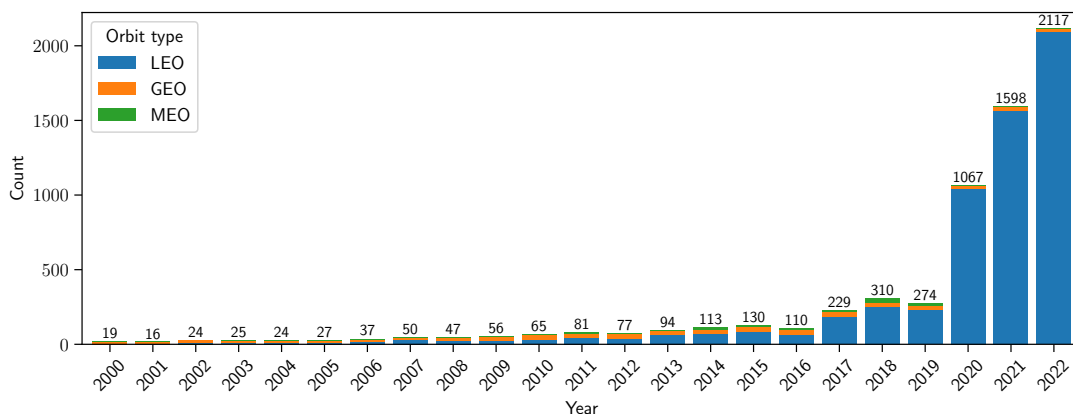


Figure 3.2.: Satellites launched per year and orbit type since the year 2000. (Source: USC (2023)).

3.1.1. Challenges of AO LEO Applications

From an adaptive optics perspective, there are three main challenges when using *LEO* satellites as targets:

1. *Faster temporal evolution of turbulence:* As discussed in Section 1.1.3, the evolution of turbulence in the time scale of adaptive optics correction (i.e. milliseconds) is driven by frozen flow. This evolution depends on the wind layer speeds of each of the layers that form the turbulence profile along the observation line of sight. The faster these wind speeds are, the faster the evolution of turbulence.

In the case of *LEO* satellite tracking, there is a second component to this evolution: the relative motion of the telescope with respect to the atmospheric layers due to the tracking of the satellite. This relative motion is equivalent to the adaptive optics line of sight staying steady and the different layers moving in a direction orthogonal to it with a speed that is the product of the tracking speed of the telescope and the distance from the telescope to the layer. Due to its similarity to the translation of the atmospheric layers caused by wind, this component is called apparent wind, while the wind effect is often called natural wind.

For *LEO* satellites, apparent wind speeds are one order of magnitude higher than natural wind; see Figure 3.5 for an example. As a result, the presence of apparent wind will significantly increase the speed with which turbulence evolves, increasing also the temporal error in the adaptive optics correction. Reducing temporal error requires increasing the adaptive optics loop frequency, which affects the complexity, cost, and possible targets for the adaptive optics system.

3. Adaptive Optics for LEO Satellite Tracking

3.1. Low-Earth-Orbit Satellite Tracking

An alternative to increasing the adaptive optics loop frequency is using predictive control. Predictive control uses a predictive model of the turbulence evolution to compensate for the delay between the measurement of turbulence and its correction by predicting the evolution of turbulence from the moment that was measured to the moment that is corrected. This thesis proposes a predictive controller that incorporates apparent wind information to be used with *LEO* satellites, see Chapter 6.

2. *Changing turbulence conditions:* In traditional astronomical applications, turbulence conditions are stable for several minutes [Poyneer et al. \(2009\)](#); [Shepherd et al. \(2014\)](#), which reduces the updates necessary for adaptive optics controllers. This is not the case for *LEO* satellites, since the line of sight elevation changes rapidly with satellite tracking; see Figure 3.1. The change in elevation will imply a change in the turbulence conditions faced by the adaptive optics system. Figure 3.3 shows an example of the change in turbulence conditions with elevation, in particular, the evolution of the Fried parameter, r_0 , which represents the turbulence strength. It can be observed that r_0 decreases by a factor of three (i.e. the turbulence strength increases) between an observation at the zenith and an observation at 10° .

In order to maintain consistent performance across all the satellite trajectory, the adaptive optics controllers need to be updated according to the change in turbulence conditions. Section 6.4 discusses how this can be done for predictive controllers.

3. *Strong scintillation conditions:* To increase the duration of the link, adaptive optics needs to extend its operation to the lowest possible elevations. At low elevations, the path of the beam across turbulence and therefore the effects of turbulence are stronger. The increase of the strength of turbulence leads to the appearance of scintillation effects, which become more important. These effects impair wavefront sensing and decrease coupling efficiency; therefore, they challenge the use of adaptive optics in this regime. Figure 3.3 plots the evolution of the Rytov variance with elevation; it can be observed how it approaches the strong perturbation regime, $\sigma_{\chi,R}^2 > 0.3$, for low elevations.

This thesis works on the development of the *PICOLO*, a turbulence emulator for low elevation *LEO*-to-ground links, see Chapter 8. This bench will be used in the future to test new adaptive optics techniques for the mitigation of the effects of turbulence.

3.1.2. Satellite Orbits Considered

A unique orbit of 750 km altitude and culmination at 90° elevation is considered for all cases. Depending on the inclination of the orbit with respect to the telescope

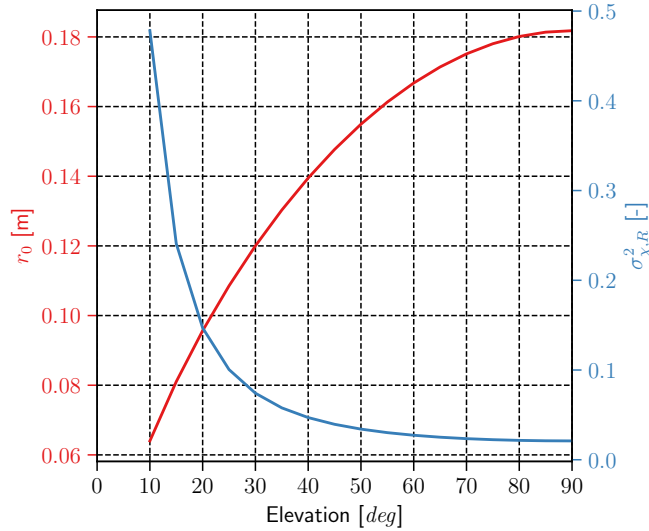


Figure 3.3.: Example of changing turbulence conditions with elevation.

location, the culmination can be different, and therefore the time spent at every elevation will also change. This kind of system study is not the aim of this thesis; therefore, the most general orbit was chosen. Although this is not the most statistically probable case, the culmination at 90° is the most general, since in this case the satellite is observed from all possible elevations.

3.2. Turbulence Conditions

This section discusses the turbulence conditions faced by adaptive optics *LEO* tracking applications, both in terms of C_n^2 and in terms of natural and apparent wind profiles. Two reference profiles are defined for the case studies in this thesis: (1) a night-time weaker turbulence profile for satellite observation applications, and (2) a day-time stronger turbulence profile for optical communication applications.

3.2.1. Atmospheric Turbulence Profiles

The design of adaptive optics systems requires the evaluation of their performance; this performance is mostly driven by the atmospheric turbulence profile under which the system operates. The turbulence profile represents the refractive index structure constant, $C_n^2(z)$, distribution across the propagation distance z ; this distribution, and not only the total turbulence strength, will affect the statistics of the turbulence seen at the telescope pupil, as discussed in Chapter 1. As a result, using an adequate atmospheric profile for the evaluation of adaptive optics performance is crucial to achieving meaningful results.

The atmospheric turbulence profile depends on the current atmospheric conditions

and the dynamics of the atmosphere. As a result, its structure evolves on a minute time scale, while diurnal and seasonal trends are also observed. Since it is not always possible to evaluate the system performance over all possible profiles, especially when conducting end-to-end simulations, the set of possible profiles needs to be reduced to one or more profiles that are representative enough of the typical turbulence that will be faced by the system. Such a typical profile can be produced by using turbulence profiling instruments (Haguenauer et al. 2020; Giordano et al. 2021) to collect measurements of the local turbulence across long periods and conduct statistical studies to derive typical profiles for a given site (Osborn et al. 2018; Giordano et al. 2022). This kind of data should be sampled at the scale of minutes and span one or several years to capture the different time scales present in the evolution of the profile. The resulting averaging from the statistical reduction of profiles will also remove some features present in some of the profiles, so this reduction needs to consider the different scenarios such as the correlation to meteorological seasons observed in the data. In order to do this, Farley et al. (2018) suggested a methodology to cluster features and generate a set of typical profiles from databases of long-term profile measurements.

The nature of the atmospheric turbulence profile varies heavily with the line of sight, and more generally with telescope location. Turbulence profiling studies are a key factor for the decision on the ideal location of an observatory (Schöck et al. 2009). To characterize the geographical variability of the turbulence profiles, Osborn and Sarazin (2018) proposed a method to derive turbulence profiles from general circulation models based on weather forecast data.

When local measurements are not available or for preliminary studies, it is possible to use analytical models published in the literature. A common choice is to use a modified Hufnagel-Valley 5/7 model Valley (1980) to define the profile, which is the recommendation of the *ITU-R P.1621-2* standard for free-space optical communications.

The choice among all the alternatives presented depends on the maturity of the study and the availability of data. In this thesis, the *MOSPAR* atmospheric profiles developed at *ONERA Védrenne* et al. (2021); Bonnefois et al. (2022) will be used.

3.2.1.1. *MOSPAR* Atmospheric Profiles

In this work, the *MOSPAR* profiles developed at *ONERA* are used as reference profiles. The *MOSPAR* profiles are computed from a profile database constructed with data available in the literature, which are combined to adequately represent a general turbulence profile for adaptive optics systems in night-time and day-time conditions. The database uses two different sources: (1) vertical turbulence profiles from Cerro Paranal (in Chile) (Osborn et al. 2018) and (2) ground C_n^2 measurements collected at Mount Teide Observatory in Tenerife (in Spain) for night-time (Ramió et al. 2012) and day-time (Sprung and Sucher 2013). The former provides high-altitude layer conditions in the free atmosphere that will

drive the anisoplanatism, while the latter provides variability in ground turbulence strength. Since the turbulence conditions vary strongly between day and night due to the thermal interaction of the ground and the atmosphere, the ground measurements data contain measurements for both night and day-time conditions. The link between the ground layer and the free atmosphere is described thanks to the *Monin-Obukhov similarity (MOS)* theory assuming a h^{-p} decrease of the C_n^2 with $p = 2/3$ for stable conditions (the case of night-time ground) and with $p = 4/3$ for unstable conditions (the case of day-time ground turbulence). The *MOSPAR* (for MOS-Paranal) profile database contains 10 000 profiles with their corresponding integrated parameters.

The construction of the *MOSPAR* profiles is detailed in [Védrenne et al. \(2021\)](#) and [Bonnefois et al. \(2022\)](#). A reference profile can be generated from the *MOSPAR* database by stitching two profiles from the two databases corresponding to the free atmosphere and the ground layer. The profiles are chosen based on the two main integrated turbulence parameters that drive *AO* performance: (1) the Fried parameter, r_0 , and (2) the anisoplanatic angle, θ_0 . The Fried parameter drives the fitting, temporal, and aliasing errors, and the anisoplanatic angle drives the anisoplanatism error. The aim is to select as a typical profile a worst-case profile that will have stronger turbulence than a given percentile across the databases. The following nomenclature *MOSPAR-A/B* is used to name the worst-case profiles, where A means that the $A\%$ of the profiles has a weaker turbulence (i.e. higher r_0) and B means that the $B\%$ of the profiles has a weaker anisoplanatism (i.e. smaller θ_0). First, the threshold on θ_0 is used to select the free atmosphere part of the profile from the Paranal database. Later, an intermediate database of profiles is generated that has the same free atmosphere for all the profiles, the one chosen by the threshold on θ_0 , and a ground layer from each of the profiles within one of the two ground-layer databases, depending of whether the desired profile is a night-time or day-time profile. The threshold in r_0 is used to select a profile from this intermediate database.

Remark

Even if for the *LEO* downlink case there is no anisoplanatic error involved, the anisoplanatic angle also drives the temporal error. Due to the presence of frozen flow turbulence, the presence of fast angular decorrelation is equivalent to a fast temporal decorrelation.

3.2.1.2. Reference Profiles

This work considers two reference profiles: one for satellite imaging and the other for optical telecommunication scenarios. For satellite imaging, the profile chosen is a *MOSPAR-75/75* night-time. The aim is to represent a scenario of favorable turbulence conditions, since these systems are located in astronomical sites and are only possible during the night. For optical communication systems, the profile

chosen is a *MOSPAR-90/90* day-time. The reference profile is a day-time profile with a strong threshold to correspond to the worst case in terms of turbulence strength. Since the optical ground stations will be located closer to the rest of the network infrastructure, they will not benefit from the favorable seeing conditions of astronomical observatories. Figure 3.4 plots the two selected profiles. The profiles are plotted with a zenithal line of sight. The main difference between their structure is the presence of a stronger ground layer in the case of the *MOSPAR-90/90* day-time due to the thermal exchange between the ground and the atmosphere during the day. The integrated parameters for the profiles are plotted in Section 3.4.2 for each of the systems considered.

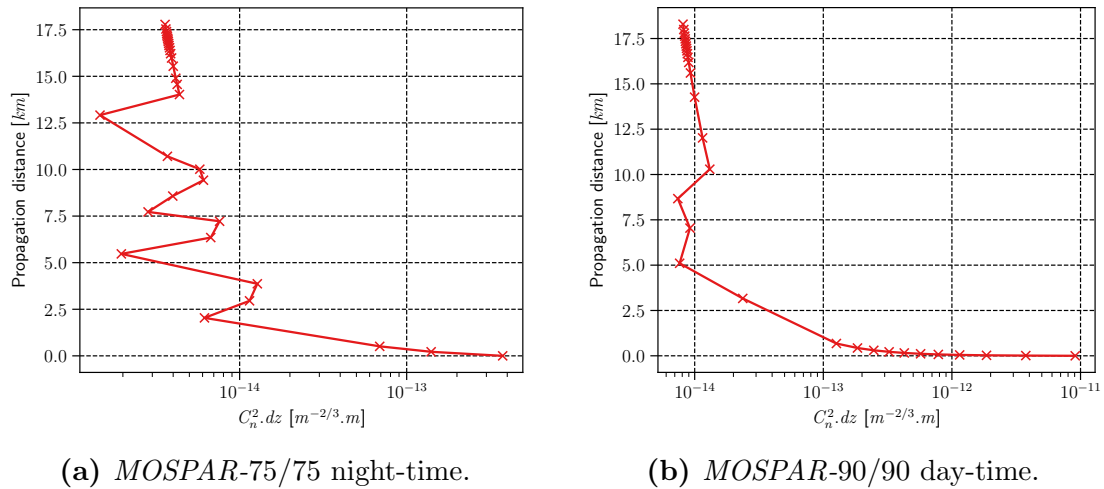


Figure 3.4.: Atmospheric turbulence profiles used for the different operating points.

3.2.2. Wind Profile

The wind profile is the same for all the simulations, but it changes with elevation. The total wind has two components: (1) the natural wind and (2) the apparent wind due to the satellite tracking. Natural wind depends on the height of the layer and here it is modeled as a Bufton profile with a ground layer speed of 3 m/s and an upper layer speed of 20 m/s. The apparent wind depends on the distance to the layer (equivalent to the propagation distance from the layer) and the angular tracking speed of the telescope (equivalent to the satellite slew rate).

Figure 3.5 depicts the wind profile used in the simulations at two different elevations. The plot uses propagation distance instead of height of the layer which causes the natural wind profiles to look different; this is normal since the line of sight is longer for lower elevations. The maximum apparent wind speed is a factor of the maximum layer distance and the slew rate at this elevation.

Remark

The temporal error is driven by the distribution along the line of sight of both the turbulence C_n^2 and the layer speeds, and not only by the wind profile. The same wind profile and the same r_0 can lead to very different temporal error.

Natural wind is assumed to have the same orientation as the apparent wind. If the two wind components have different orientations, the argument of the wind vector for a given layer may increase or decrease and with it the contribution of the layer to temporal error. Nevertheless, this effect does only slightly change the absolute results of the case under study and neglecting it does not invalidate any of the general observations presented in this work.

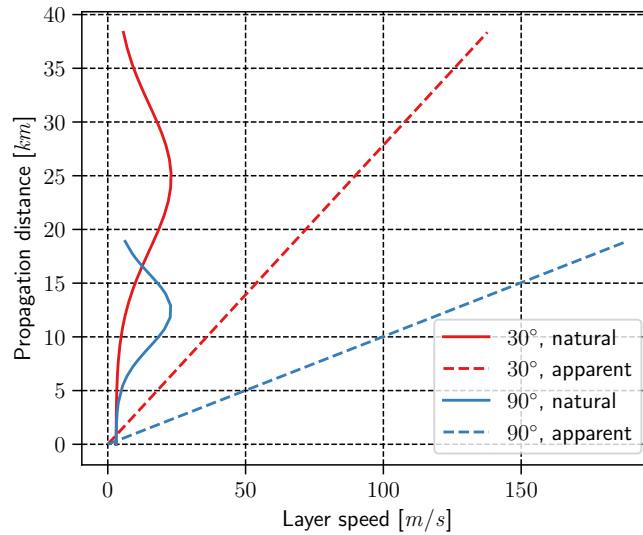


Figure 3.5.: Wind profiles considered for the case studies. The natural wind profile is given by a Bufton profile with a ground layer speed of 3 m/s and an upper layer speed of 20 m/s. The apparent wind speed is given by the product between the angular speed of the tracking and the distance to the corresponding layer of turbulence. The profiles are plotted for two different layers to illustrate their variation with elevation.

3.2.3. Variation of Integrated Parameters with Elevation

The variation of the line of sight elevation along the satellite trajectory tracking will lead to an evolution of the turbulence integrated parameters. Figure 3.6 and Figure 3.7 plot the evolution of these parameters, as presented in Chapter 1.

The evolution of these parameters will drive the performance of adaptive optics correction, which will change depending on the elevation as shown in the AO error budgets reported in Section 3.4.2. The evolution of AO performance will also lead to an evolution of the system performance metrics presented in this chapter. From

3. Adaptive Optics for LEO Satellite Tracking

3.2. Turbulence Conditions

a control system point of view, this evolution implies that the parameters of the controller (i.e. the predictive model in the case of a predictive controller) need to be updated to adapt to these changes.

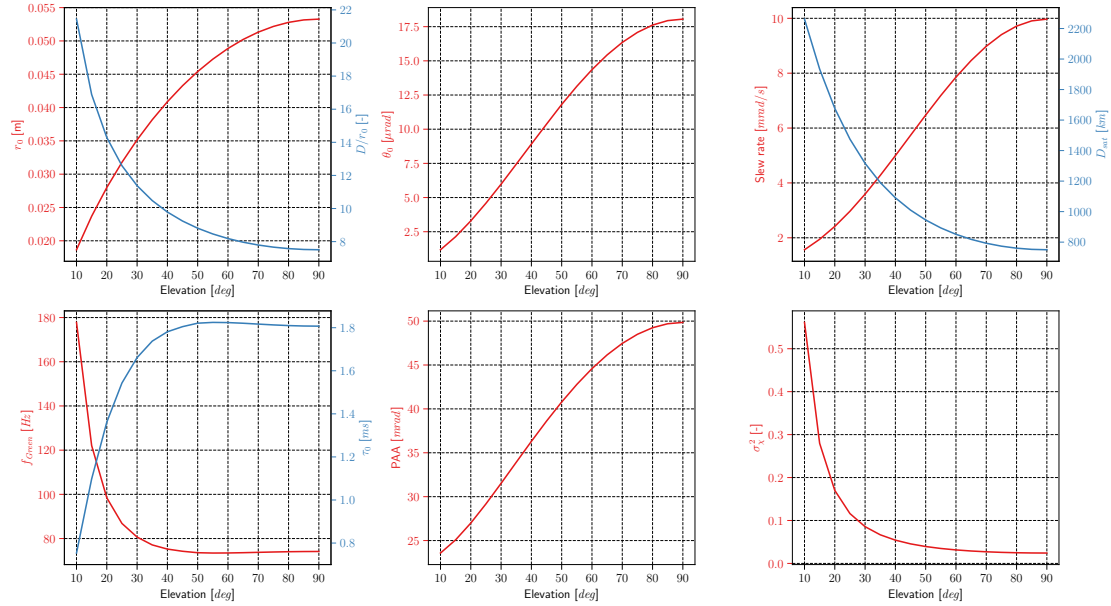


Figure 3.6.: Evolution of integrated parameters with elevation for the *MOSPAR-90/90* day-time profile used for the optical communication case studies.

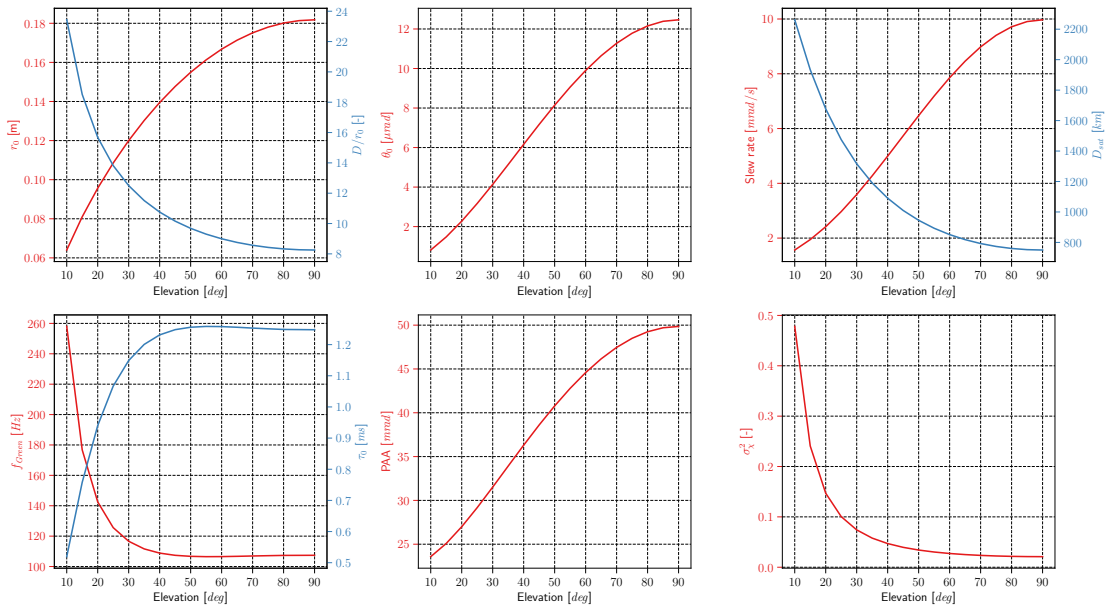


Figure 3.7.: Evolution of integrated parameters with elevation for the *MOSPAR-75/75* night-time profile used for the satellite observation case studies.

3.3. System Performance Metrics

The main performance metric for adaptive optics correction is the residual phase variance, which quantifies the remaining phase distortion after *AO* correction. This metric was discussed in Section 2.5 and will be quantified for the case studies considered in this manuscript in Section 3.4.2. The residual phase variance and its allocation to different *AO* elements is very useful for the assessment of adaptive optics system performance, and will be extensively used in this thesis as such. Nevertheless, other performance metrics are necessary to study the performance of the application under adaptive optics correction. This section will discuss the effect of turbulence distortions on the two main applications considered: image formation and single-mode fiber coupling. Image formation will be discussed first since some of these concepts are useful for the understanding of fiber coupling.

3.3.1. Image Formation in Presence of Atmospheric Turbulence

The presence of atmospheric turbulence introduces aberrations in the imaging of a telescope which result in degradation of the telescope's imaging performance. This section describes mathematically the effect of atmospheric turbulence in the image formation of a telescope and how it degrades its performance.

The image formation of an imaging system can be modeled as a convolution operation:

$$\mathbf{i} = \mathbf{h} * \mathbf{o}, \quad (3.1)$$

where \mathbf{o} represents the object imaged, \mathbf{h} is the response of the system to a point source, known as *point spread function* (*PSF*), and \mathbf{i} is the resulting image. This convolution model assumes that the system response is linear and translation invariant (i.e. the imaging performance is the same over all the field of view).

Note that the convolution operation has the effect of blurring the original; this blurring effect is stronger when the shape of the *PSF* is wider. From a Fourier optics perspective, the *PSF* and its effect on image formation can be interpreted thanks to the *optical transfer function* (*OTF*), which is the Fourier transform of the *PSF*. The *OTF* is a complex valued transfer function that represents the filtering in the Fourier domain of the object by the imaging system:

$$\text{FT}[\mathbf{i}] = \text{OTF} \cdot \text{FT}[\mathbf{o}] = \text{FT}[\mathbf{h}] \cdot \text{FT}[\mathbf{o}], \quad (3.2)$$

where $\text{FT}[\cdot]$ corresponds to the Fourier transform operator.

As a result, the spectral content of the *PSF* defines the attenuation of the spectral content of the object when it is imaged.

3.3.1.1. Effect of Turbulence on the *PSF*

The theory of Fourier optics defines the *PSF* as the squared magnitude of Fourier transform of the optical field complex amplitude at the telescope pupil (i.e. Fraunhofer diffraction pattern):

$$\mathbf{h} = |\text{FT}[\psi(\boldsymbol{\rho})\mathcal{P}(\boldsymbol{\rho})]|^2, \quad (3.3)$$

where $\psi(\boldsymbol{\rho})$ is the complex amplitude of the optical field at the telescope pupil $\mathcal{P}(\boldsymbol{\rho})$ is the pupil function, defined as:

$$\mathcal{P}(\boldsymbol{\rho}) = \begin{cases} 1 & \text{if } \frac{d}{2} \leq \|\boldsymbol{\rho}\| \leq \frac{D}{2} \\ 0 & \text{otherwise,} \end{cases} \quad (3.4)$$

where D is the diameter of the telescope pupil and d is the diameter of the central obscuration of the pupil.

Remark

The *PSF* depends therefore on the pupil shape and size with respect to the wavelength and on the complex amplitude of the optical field, that is, both its phase and its amplitude. Both phase and amplitude distortions (i.e. scintillation) contribute to the degradation of the *PSF*; here only the phase is discussed, since scintillation is negligible in most adaptive optics operation regimes in imaging applications. The effects of scintillation on the *PSF* are nevertheless considered when discussing coupling into an optical fiber.

In absence of turbulence, the optical complex field does not suffer any distortion and it has (ideally) a uniform phase and amplitude over the telescope pupil. This results in the *PSF* having the shape of the Airy disk, with a width proportional to λ/D . This case is the diffraction limited case, where the imaging resolution is limited by the diffraction of the pupil and not by the effect of the distortions of the optical field on the *PSF*. In the presence of turbulence, the short exposure *PSF* will be scattered across a broader area and broken into several speckles. For long exposure images, the speckle pattern will be averaged and the resulting pattern has a diameter that depends on the Fried parameter, r_0 .

Note how the ratio D/r_0 allows to define two regimes for the *PSF*: For $D/r_0 < 1$ the image formation is limited by the diffraction of the pupil; while for $D/r_0 > 1$ the turbulence limits the image resolution.

Figure 3.8 illustrates the effect described above for a turbulence of $D/r_0 = 12$.

3.3.1.2. Strehl Ratio

The *Strehl ratio* (*SR*) is the most common metric for optical image formation quality. It is defined as the ratio of the peak intensity of the aberrated and/or

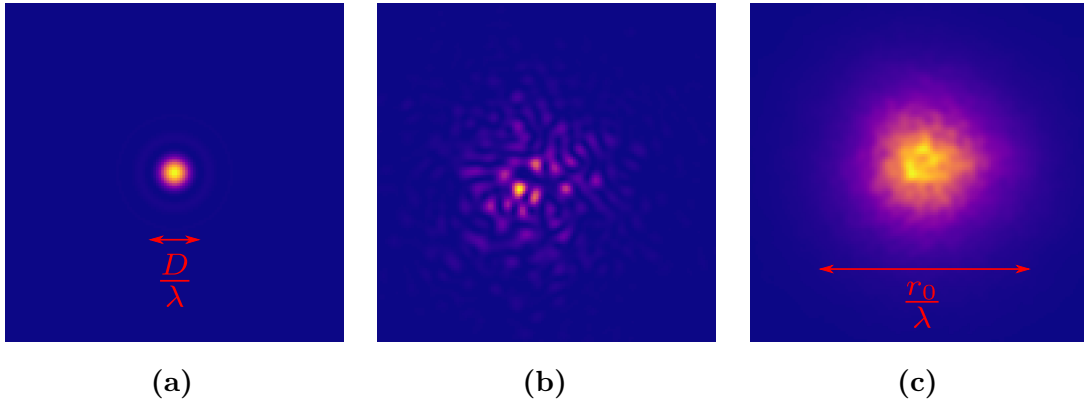


Figure 3.8.: Illustration of the effect of turbulence on the *PSF*. (a) Diffraction limited *PSF* (zoomed with 4x). (b) Short exposure *PSF* for $D/r_0 = 12$. (c) Long exposure *PSF* for $D/r_0 = 12$.

partially-corrected *PSF* to the peak intensity of the diffraction-limited *PSF* in the on axis direction:

$$\text{SR} = \frac{I_{\text{aberrated}}(0)}{I_{\text{diff.-lim.}}(0)}. \quad (3.5)$$

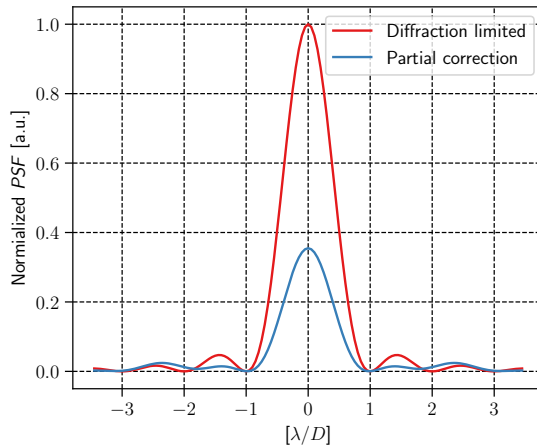


Figure 3.9.: Computation of the Strehl ratio.

The Strehl ratio represents the concentration of energy within the peak of the *PSF* with respect to the diffraction limited case; this depends mainly on the low frequencies of the optical transfer function and therefore it does not convey information about how well the high frequencies of the object are imaged. Figure 3.9 illustrates a the computation of the Strehl ratio as the ration of the peak of the diffraction limited and the partially-corrected *PSFs*.

Under the assumption of small residual phase functions, the Strehl ratio can

be approximated in terms of the residual phase variance using the definition of coherent energy (i.e. the Maréchal approximation (Ross 2009)):

$$\text{SR} \approx \exp(-\sigma_{\text{res}}^2) \quad (3.6)$$

3.3.2. Communication Channel Impairments Induced by the Atmosphere

This section discusses the effect of atmospheric optical turbulence in the communication channel, in particular in the single-mode coupling necessary for the use of different optical communication techniques such as coherent detection, erbium-doped fiber amplifiers, multiplexers, and other technologies initially developed for fibered networks. Other effects such as cloud coverage and atmospheric absorption or the Doppler effect are beyond the scope of this manuscript.

3.3.2.1. Effect of Turbulence Distortions on Single Mode Fiber Coupling

An optical receiver uses a telescope to collect the light from the satellite and to couple it into a *single-mode fiber* (*SMF*). Fiber coupling will also be affected by the distortions on the incoming wavefront (both in phase and in amplitude). The efficiency of fiber coupling depends on the mode matching between the turbulence and the optical fiber, as a result, the coupling by an overlap integral between two modes. The overlap integral can be computed in both the pupil plane or the focal plane of the telescope; the only difference between both is the Fourier transform that represents the Fraunhofer propagation of the telescope focusing the wave from the pupil to the focal plane. The two perspectives are possible to analyze the coupling of a wave into a fiber, each of them providing interesting interpretations.

We start by discussing coupling on the pupil plane since this avoids considering the Fourier transform of the wave complex field. After propagation, the complex amplitude of propagated wave received at the telescope pupil is:

$$\Psi(\mathbf{r}, t) = A_0(\mathbf{r})A_{\text{tur}}(\mathbf{r}, t)e^{i\phi^{\text{turb}}}, \quad (3.7)$$

where A_0 denotes the complex field amplitude without perturbation, A_{tur} and ϕ^{turb} represent the turbulence induced amplitude fluctuations and phase aberrations, respectively.

In the pupil plane, the coupling to a *SMF* with a mode $M_0(\mathbf{r})$ is given by the following overlap integral (Shaklan and Roddier 1988):

$$\Omega(t) = \frac{\iint P(\mathbf{r})\psi(\mathbf{r}, t)M_0^*(\mathbf{r}) dr^2}{\sqrt{\iint P(\mathbf{r})\psi(\mathbf{r}, t)\psi^*(\mathbf{r}, t) dr^2 \iint P(\mathbf{r})M_0(\mathbf{r})M_0^*(\mathbf{r}) dr^2}}, \quad (3.8)$$

where z^* denotes the complex conjugate of a complex quantity z and $P(\mathbf{r})$ is the pupil function as defined in Equation 3.4. Thanks to the Parseval theorem, a

3. Adaptive Optics for LEO Satellite Tracking
3.3. System Performance Metrics

similar relationship holds in the image plane, in this case as an overlap integral between the *PSF* and the *SMF* shape in the image plane. This second view is also interesting since all the intuitions of the *PSF*, such as angle of arrival due to aberrations, shape with respect to r_0 , can be used.

The complex coupling can be decomposed in two terms corresponding to its square modulus, the coupling efficiency, $\rho(t)$, and its argument, the phase noise, $\phi(t)$:

$$\rho(t) = |\Omega(t)|^2 \quad (3.9)$$

and

$$\phi(t) = \arg(\Omega(t)). \quad (3.10)$$

As a result, both phase and amplitude distortions will cause losses in coupling, since any mismatch between the wave complex field and the fiber mode, both in amplitude or phase, causes losses of energy in the coupling.

Even in the case of phase correction, there are two contributions related to wave amplitude, which cannot be corrected by *AO*, that will cause losses in coupling efficiency: mode mismatch in vacuum and scintillation.

The amplitude mismatch between the undisturbed beam and the fiber mode will already limit coupling. For the case of a *LEO* satellite, the unperturbed optical beam is assumed to have a constant amplitude over the pupil (the propagation length is long enough to only see a small section of the emitted beam profile due to divergence) and zero phase (by definition, since there are no perturbations). The *SMF* mode shape, $M_0(\mathbf{r})$, is approximated by a Gaussian mode shape, whose waist is optimized to provide the maximum coupling with the unperturbed optical beam. In this case, the optimal beam waist results in a maximum coupling efficiency of $\rho(t)_{\max} \approx 0.81$ (Ruilier and Cassaing 2001). This value will be lower if pupil obscuration is considered.

Scintillation will have two effects in coupling. On the one hand, the total power collected by the telescope, also known as power in the bucket, will vary as a result of scintillation. On the other hand, scintillation will also influence the overlap integral of the coupling efficiency. The computation of coupling efficiency in Equation 3.8 only accounts for the second effect. The total flux coupled into the fiber will therefore be:

$$P(t) = |\Omega(t)|^2 \times \iint_S P(\mathbf{r})\psi(\mathbf{r}, t)\psi^*(\mathbf{r}, t) dr^2, \quad (3.11)$$

where the second factor corresponds to the integral of the field flux over the pupil surface, i.e. power in the bucket. The total power coupled into the fiber depends on the power in the bucket (driven by scintillation) and the coupling efficiency (driven by *AO* correction and to a lesser extent by scintillation). This

means that the scintillation limits the stability of coupled power, also. For this reason, the design of optical ground stations may use a bigger telescope, so the effect of scintillation can be averaged to obtain a more stable signal. Nevertheless, increasing the telescope size leads to more phase effects, due to the increase in D/r_0 , and requires more complex adaptive optics systems, i.e. that correct more turbulence modes by having more actuators.

In summary, the presence of turbulence will cause a fluctuation and drops in the coupling efficiency, known as fadings. The role of adaptive optics is to correct the phase distortions on the beam so fadings can be reduced.

3.3.2.2. Fading Mitigation Techniques

Different fading mitigation techniques are available; they can be divided into physical and digital signal processing techniques. Physical techniques use the physical properties of light to reduce the power fluctuations in the received signal; digital signal processing techniques work on the way the information is encoded in the physical signal so that it is more robust to fadings.

Physical mitigation techniques can reduce the impact of atmospheric turbulence on the coupling into an optical fiber. Two main options are available: Multi-aperture receivers and adaptive optics. Multi-aperture receivers make use of several smaller telescopes; smaller telescopes are less affected by turbulence (since they have a smaller D/r_0) and are able to achieve *SMF* coupling without the use of distortion correction. The received signal is mostly limited by the collected flux and the power fluctuations due to scintillation averaged over the pupil; as a result, several telescopes are used. The optical signals of each aperture are then detected individually and recombined and postprocessed digitally. As a result, each of the elements of the detection chain (amplifiers, detectors, processing circuits) are scaled by the number of apertures and so is the system complexity and cost. In cases of strong turbulence, a multi-aperture system may need at least tip-tilt phase correction, also one per aperture, which would also increase the system complexity.

Adaptive optics provides phase correction to improve fiber coupling efficiency. Phase correction allows using a bigger and unique telescope, increasing the collected flux, and reducing the signal fluctuation due to scintillation since the effect of aperture averaging will be stronger. The principle of adaptive optics was introduced in Section 2.

Two digital signal processing techniques are the most common: forward error correction and interleaving. Forward error correction coding adds redundancy to the transmitted data, enabling the receiver to correct a certain number of errors without requiring retransmission of the data. The method operates by encoding the message into a longer block of data before transmission, such that even if some bits are altered due to channel impairments like fading, the original message can still be accurately decoded at the receiver. Interleaving rearranges the sequence of transmitted bits, such that consecutive bits in the original data sequence are spaced

apart in the transmitted sequence. Upon reception and after error correction, the bits are de-interleaved to reconstruct the original sequence. The main objective is to disperse the effects of burst errors that could result from deep fading events.

This thesis is devoted to one of those techniques, adaptive optics, which has become part of most implementations of space-to-ground optical links. In practice, the implementation of optical links rely on both kinds of techniques and requires a joint optimization of both (Canuet 2018).

3.3.2.3. Link Budget and Link Margin

The link budget is a design tool for communication systems that accounts for all the gains and losses of signal power between the emitter and a receiver in a link. The link budget allows therefore to compute the received power. The received power is then compared to the receiver sensitivity, which is the required power to achieve a given *SNR*. The receiver sensitivity depends on the modulation used by the link and ultimately on the components used within its detection chain (Anfray et al. 2019). The difference between the received power and the receiver sensitivity is the link margin, the power that can be lost during signal fadings while maintaining the desired communication performance.

The link budget can be written as:

$$P_{\text{RX}} = G_{\text{RX}}L_{\text{RX}}L_{\text{cloud}}L_{\text{abs}}L_{\text{FS}}L_{\text{TX}}G_{\text{TX}}P_{\text{TX}} , \quad (3.12)$$

where:

- P_{TX} is the transmitted power.
- P_{RX} is the received power.
- G_{TX} and G_{RX} correspond to the transmitter and receiver antenna gains, respectively; the account of the directivity of the transmission and reception.
- L_{TX} and L_{RX} correspond to the losses during transmission and reception related to telescope transmission and fixed fiber injection losses.
- L_{FS} to the free space losses due to diffraction during the optical wave propagation along its path.
- L_{cloud} represents the losses due to cloud coverage.
- L_{abs} represents the losses due to atmospheric absorption.

Other losses, such as those due to errors in pointing by the transmitter and in tracking by the receiver, may be included.

The link margin, P_{LM} (this time given in dB) is the difference between the receiver power allocated in the link budget and the sensitivity of the targeted detection system in the receiver, P_{S} :

$$P_{LM} = (G_{RX} - L_{RX} - L_{cloud} - L_{abs} - L_{FS} - L_{TX} + G_{TX} + P_{TX}) - P_S. \quad (3.13)$$

Remark

The design objective for a telecommunications system is thus to dimension a system where the instantaneous received power due to signal fadings is still below its detection threshold:

$$P_{RX}s(t) > P_S, \quad (3.14)$$

where $s(t)$ is the instantaneous signal attenuation due to fadings. In this design, different trade offs between laser source power, telescope dimensioning, optical terminal design, data-rate, modulation scheme, and fading reduction mechanism are involved. Adaptive optics, as a fading reduction mechanism, enables therefore to reduce some of those constraints to achieve higher data rates.

3.4. Adaptive Optics Systems: Case Studies

Four different systems are considered in this work, corresponding to two optical communications systems and two satellite imaging systems, with a low-performance and a high-performance variant for each. The *AO* relevant parameters for each for each of the systems are reported in Table 3.1. The systems are:

1. *LISA*: a compact adaptive optics bench for optical telecommunications developed by *ONERA* (Lim et al. 2018).
2. *FEELINGS*: the *ONERA* optical communications ground station (Petit et al. 2022).
3. *ODISSEE*: the current *ONERA* adaptive optics bench for satellite observation, installed at the Observatoire de la Côte d'Azur (Petit et al. 2020).
4. *ODISSEE++*: hypothetical high-performance version of the *ODISSEE* bench with the same sampling frequency but a doubled actuator sampling.

The reported central obscurations correspond to a circular obscuration with a diameter corresponding to the cited percentage of the telescope pupil diameter.

3.4.1. Wavefront Sensing Noise Levels

This section defines the wavefront sensing measurement noise levels that will be considered for the different applications. The noise level at which an *AO* system

3. Adaptive Optics for LEO Satellite Tracking
3.4. Adaptive Optics Systems: Case Studies

Table 3.1.: Adaptive optics system parameters for the four *AO* configurations.

Name	<i>LISA</i>	<i>FEELINGS</i>	<i>ODISSEE</i>	<i>ODISSEE++</i>	Units
Imaging wavelength, λ_{img}	1.55	1.55	0.850	0.850	μm
WFS wavelength, λ_{WFS}	1.55	1.55	0.600	0.600	μm
Telescope diameter	0.4	0.6	1.5	1.5	m
Central obscuration	0.0	25.0	25.0	25.0	%
SH subpupils	8×8	16×16	8×8	16×16	–
DM actuators	9×9	17×17	9×9	17×17	–
Loop sampling frequency	2	4.5	1.5	1.5	kHz
Loop delay	2	2	2	2	frames

operates depends on many factors, such as the flux coming from the reference source (beacon for optical communications and the light reflected from the satellite for imaging) and the detection technology used in the wavefront sensor. The aim here is not to use the exact values for a given system, but to define a range of noise values that allow covering all possible regimes at which an *AO* system and its control system may operate.

For optical telecommunication applications, wavefront sensing is conducted on a beacon on the downlink beam. As a result, the same wavelength as the telecommunication wavelength is used for wavefront sensing, i.e. $\lambda = 1.55 \mu\text{m}$. Due to the nature of the sensing source, the flux available in this application is much higher than for typical astronomical targets. For ground-based imaging of satellites wavefront sensing uses the solar radiation reflected on the target satellite. In this case, the available flux is much lower than that for optical communications. Additionally, the radiation received from the satellite is broadband in wavelength. A common strategy is to split the beam with a dichroic and use a central wavelength of $\lambda = 0.850 \mu\text{m}$ for imaging and $\lambda = 0.6 \mu\text{m}$ for wavefront sensing.

In order to provide a convenient definition of measurement noise levels the per-subpupil *signal-to-noise ratio* (*SNR*) is defined as:

$$\text{SNR} = \frac{\mu}{\sigma}, \quad (3.15)$$

where μ is the signal mean and σ is the standard deviation of the noise. Assuming that the detection is photon noise limited and neglecting the read-out noise of the detector, the signal will follow a Poisson distribution: its mean signal is the number of photons, N_{ph} , and its standard deviation is $\sqrt{N_{\text{ph}}}$, so that:

$$\text{SNR} = \frac{N_{\text{ph}}}{\sqrt{N_{\text{ph}}}} = \sqrt{N_{\text{ph}}}. \quad (3.16)$$

Plugging this into Equation 2.4 and assuming that the spot on the detector is

3. Adaptive Optics for LEO Satellite Tracking
3.4. Adaptive Optics Systems: Case Studies

close to the diffraction limit, i.e. $X_T = X_D$:

$$\sigma_{\text{meas}}^2 = \frac{\pi^2}{2} \frac{1}{\text{SNR}^2} \text{ (rad}^2\text{)} . \quad (3.17)$$

where σ_{meas}^2 is the variance of phase in radians squared over the subpupil.

The definition of SNR presented above allows for defining high and low noise scenarios in a simple manner. We will consider $\text{SNR} = 100$ as a case with low measurement error and lower values as high noise cases.

The assumption of photon noise limited is reasonable since for satellite imaging applications even if the number of photons is low the *EMCCD* detectors used have very low read-out noise. For optical communications, the number of photons is high enough so that photon noise dominates over the detector noise.

Figure 3.10 illustrates the equivalence of the defined SNR in terms of photons per frame per subpupil, phase variance over the subpupil, and slope measurement noise. It can be observed how the SNR scale used provides a good coverage of all the regimes that may be encountered.

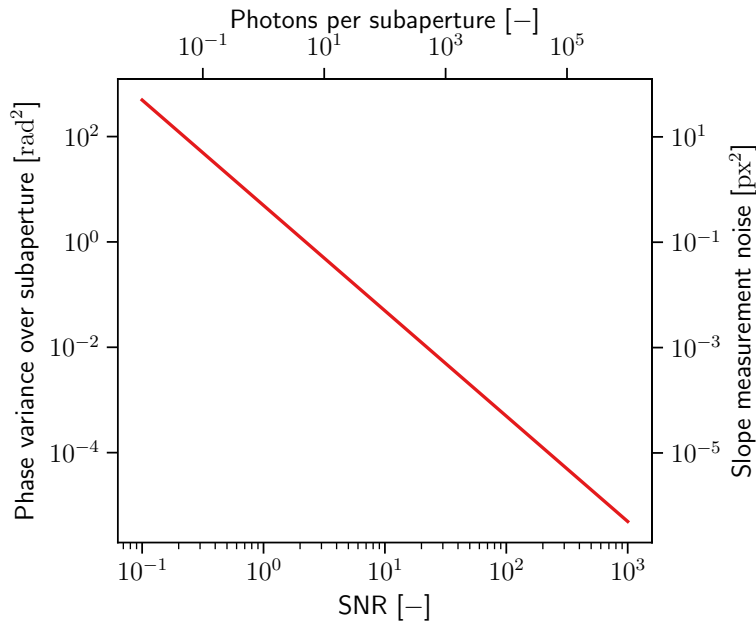


Figure 3.10.: Noise ranges covered by the SNR scale.

3.4.2. Error Budgets

This section provides and discusses the *AO* error budgets for the four systems considered.

The use of error budgets is of utmost importance for the methodology followed in this thesis. Error budgets are used for the validation of the end-to-end simulations

3. Adaptive Optics for LEO Satellite Tracking

3.4. Adaptive Optics Systems: Case Studies

and for the assessment of their results. They allow understanding the performance limits of the system and the origin of possible performance gains or losses.

The error budgets presented here use the tool *simplified adaptive optics simulation tool* (*SAOST*); a detailed description of the tool can be found in [Bonnetois et al. \(2022\)](#). *SAOST* is based on the modal decomposition of phase in Zernike polynomials; as a result, it is able to provide a residual phase variance budget per mode including fitting, aliasing, temporal, and anisoplanatic error. The calculation of temporal error is conducted using the temporal power spectral density function for each of the modes as provided by [Conan et al. \(1995\)](#) and filtered by the rejection transfer function of an integral action controller. The integrator used has a two-frame delay and a gain that is optimized for the noise level using a scalar gain optimization. This computation was modified in this thesis to also include the noise transfer function of the integrator and compute the contribution of measurement noise to the residual phase variance.

The error budgets presented use the wind profile with only apparent wind speed, since most of the simulations in this thesis will not incorporate natural wind speed. As stated in Section 3.2.2 the two optical communication systems use the *MOSPAR-90/90* day-time profile and the two satellite observation systems use the *MOSPAR-75/75* night-time profile.

The results provided here are for a scenario of $\text{SNR} = 100$, a high *SNR*; therefore, the contribution of measurement noise is negligible.

The *LISA* and the *ODISSEE* systems, both with a 9×9 *DM*, are assumed to correct the first $n_{\max} = 10$ Zernike polynomials radial orders; while for the *FEELINGS* and the *ODISSEE++* systems, both with a 17×17 *DM*, $n_{\max} = 20$ is used.

Table 3.2 reports the *AO* budget for each system at different elevations; while Figure 3.11 plots the same information. The main interest for this thesis is to study the importance of temporal error within these budgets. Since predictive control reduces the temporal error, it will be more interesting cases where temporal error has a greater importance.

The two optical communication systems present a temporal error that is smaller than their fitting error. This is due to the fact that the profile considered has its turbulence concentrated at the ground layer, where the apparent wind speed is very low since the distance to the layer is low. Overall, the two systems show a very similar structure of their error budget. Nevertheless, the *FEELINGS* system has a lower total residual phase variance since, even if it has a larger telescope diameter, it has twice the number of *DM* sampling and a faster *AO* loop. As can be observed in the orange line plotting the total residual phase variance without temporal error, the gains by reducing temporal error are not very high, since fitting and aliasing dominate the error budget.

The satellite observation cases show a different scenario, where the temporal error is of greater importance in the *AO* budget. This is again due to the profile considered, since (in relative terms) most of the turbulence is located at the free

3. Adaptive Optics for LEO Satellite Tracking

3.4. Adaptive Optics Systems: Case Studies

atmosphere, where the apparent wind is higher in speed. This is especially true for the *ODISSEE++* system, since it has the same sampling frequency as *ODISSEE* but twice the actuator sampling. Considering more modes to be corrected implies that the temporal error will increase and the fitting error will decrease; therefore, this shifts in the *AO* budget. As a result, the performance gains for the satellite observation systems are higher. Assuming that it is possible to reduce the temporal error to a negligible quantity with respect to the other budget terms, the total residual phase variance can be reduced from $7.834 \cdot 10^{-1}$ to $9.830 \cdot 10^{-2}$ in the zenith case.

Remark

These results are more related to the structure of the C_n^2 profiles for both optical communications and satellite observation cases than to the application and its systems. The *AO* budget and the gains would be similar for optical communications if the same profile, meaning a night-time scenario, was considered.

* * *

Summary

This chapter introduced all the specific concepts of the applications considered in this thesis with respect to the use of adaptive optics. This thesis focuses on the improvement of adaptive optics for the specific case of *LEO* satellite applications, which differ in some points to the traditional problems of adaptive optics for astronomy.

In particular, adaptive optics for *LEO* applications faces a stronger layer (apparent) wind speed that results in a significantly greater temporal error. This fact will drive the interest of predictive controllers with respect to other applications. The presence of strong turbulence conditions leading to scintillation is also not common in astronomy applications, but it is key for adaptive optics if *LEO* optical links need to be extended below 20° elevations.

The chapter also provided an overview of the typical atmospheric conditions faced by adaptive optics in *LEO* satellite applications. The reference profiles for the case studies within this manuscript were defined.

Strehl ratio and fiber coupling efficiency were discussed as metrics for satellite imaging and optical communications, respectively, as well as the influence of atmospheric turbulence on them. Residual wavefront variance will be used to assess the performance of adaptive optics, while these metrics will describe the performance of the applications assisted by adaptive optics.

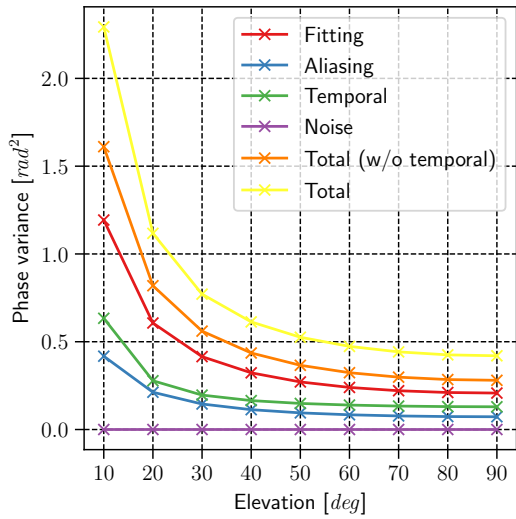
Finally, the four *AO* systems used as case studies within this manuscript were presented, including the error budgets for them. These budgets will be used in this thesis to assess the performance of adaptive optics correction.

3. Adaptive Optics for LEO Satellite Tracking
3.4. Adaptive Optics Systems: Case Studies

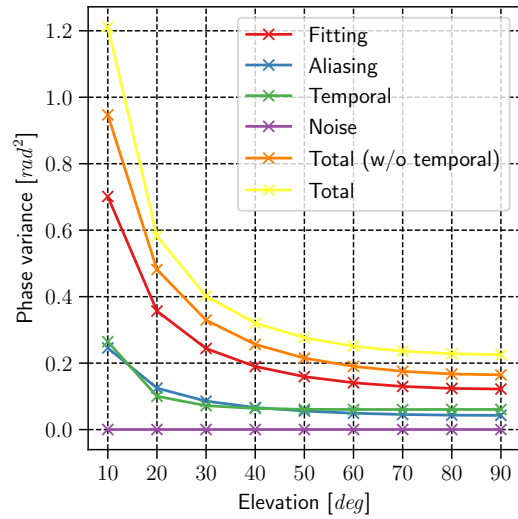
Table 3.2.: AO error budget for different elevations. Results are given in variance of the residual phase with units rad².

	Elevation	Fitting	Aliasing	Temporal	Total
<i>LISA</i>	10°	1.193	$4.177 \cdot 10^{-1}$	$6.336 \cdot 10^{-1}$	2.245
	20°	$6.067 \cdot 10^{-1}$	$2.123 \cdot 10^{-1}$	$2.778 \cdot 10^{-1}$	1.097
	30°	$4.151 \cdot 10^{-1}$	$1.453 \cdot 10^{-1}$	$1.961 \cdot 10^{-1}$	$7.566 \cdot 10^{-1}$
	40°	$3.229 \cdot 10^{-1}$	$1.130 \cdot 10^{-1}$	$1.648 \cdot 10^{-1}$	$6.008 \cdot 10^{-1}$
	50°	$2.710 \cdot 10^{-1}$	$9.485 \cdot 10^{-2}$	$1.486 \cdot 10^{-1}$	$5.145 \cdot 10^{-1}$
	60°	$2.397 \cdot 10^{-1}$	$8.390 \cdot 10^{-2}$	$1.393 \cdot 10^{-1}$	$4.630 \cdot 10^{-1}$
	70°	$2.209 \cdot 10^{-1}$	$7.732 \cdot 10^{-2}$	$1.336 \cdot 10^{-1}$	$4.319 \cdot 10^{-1}$
	80°	$2.108 \cdot 10^{-1}$	$7.378 \cdot 10^{-2}$	$1.305 \cdot 10^{-1}$	$4.151 \cdot 10^{-1}$
	90°	$2.076 \cdot 10^{-1}$	$7.266 \cdot 10^{-2}$	$1.295 \cdot 10^{-1}$	$4.098 \cdot 10^{-1}$
<i>FEELINGS</i>	10°	$7.014 \cdot 10^{-1}$	$2.455 \cdot 10^{-1}$	$2.644 \cdot 10^{-1}$	1.212
	20°	$3.566 \cdot 10^{-1}$	$1.248 \cdot 10^{-1}$	$1.003 \cdot 10^{-1}$	$5.820 \cdot 10^{-1}$
	30°	$2.440 \cdot 10^{-1}$	$8.540 \cdot 10^{-2}$	$7.193 \cdot 10^{-2}$	$4.016 \cdot 10^{-1}$
	40°	$1.898 \cdot 10^{-1}$	$6.644 \cdot 10^{-2}$	$6.369 \cdot 10^{-2}$	$3.202 \cdot 10^{-1}$
	50°	$1.593 \cdot 10^{-1}$	$5.575 \cdot 10^{-2}$	$6.100 \cdot 10^{-2}$	$2.763 \cdot 10^{-1}$
	60°	$1.409 \cdot 10^{-1}$	$4.931 \cdot 10^{-2}$	$6.039 \cdot 10^{-2}$	$2.508 \cdot 10^{-1}$
	70°	$1.299 \cdot 10^{-1}$	$4.545 \cdot 10^{-2}$	$6.039 \cdot 10^{-2}$	$2.359 \cdot 10^{-1}$
	80°	$1.239 \cdot 10^{-1}$	$4.337 \cdot 10^{-2}$	$6.052 \cdot 10^{-2}$	$2.280 \cdot 10^{-1}$
	90°	$1.220 \cdot 10^{-1}$	$4.271 \cdot 10^{-2}$	$6.058 \cdot 10^{-2}$	$2.255 \cdot 10^{-1}$
<i>ODISSEE</i>	10°	1.384	$4.843 \cdot 10^{-1}$	2.670	4.538
	20°	$7.084 \cdot 10^{-1}$	$2.479 \cdot 10^{-1}$	$9.567 \cdot 10^{-1}$	1.913
	30°	$4.854 \cdot 10^{-1}$	$1.699 \cdot 10^{-1}$	$6.889 \cdot 10^{-1}$	1.344
	40°	$3.778 \cdot 10^{-1}$	$1.322 \cdot 10^{-1}$	$6.246 \cdot 10^{-1}$	1.135
	50°	$3.171 \cdot 10^{-1}$	$1.110 \cdot 10^{-1}$	$6.118 \cdot 10^{-1}$	1.040
	60°	$2.805 \cdot 10^{-1}$	$9.818 \cdot 10^{-2}$	$6.139 \cdot 10^{-1}$	$9.928 \cdot 10^{-1}$
	70°	$2.586 \cdot 10^{-1}$	$9.049 \cdot 10^{-2}$	$6.193 \cdot 10^{-1}$	$9.686 \cdot 10^{-1}$
	80°	$2.467 \cdot 10^{-1}$	$8.635 \cdot 10^{-2}$	$6.235 \cdot 10^{-1}$	$9.568 \cdot 10^{-1}$
	90°	$2.430 \cdot 10^{-1}$	$8.504 \cdot 10^{-2}$	$6.244 \cdot 10^{-1}$	$9.526 \cdot 10^{-1}$
<i>ODISSEE++</i>	10°	$4.138 \cdot 10^{-1}$	$1.448 \cdot 10^{-1}$	3.017	3.575
	20°	$2.118 \cdot 10^{-1}$	$7.415 \cdot 10^{-2}$	1.144	1.430
	30°	$1.452 \cdot 10^{-1}$	$5.080 \cdot 10^{-2}$	$8.176 \cdot 10^{-1}$	1.014
	40°	$1.130 \cdot 10^{-1}$	$3.954 \cdot 10^{-2}$	$7.239 \cdot 10^{-1}$	$8.767 \cdot 10^{-1}$
	50°	$9.482 \cdot 10^{-2}$	$3.319 \cdot 10^{-2}$	$6.944 \cdot 10^{-1}$	$8.226 \cdot 10^{-1}$
	60°	$8.389 \cdot 10^{-2}$	$2.936 \cdot 10^{-2}$	$6.863 \cdot 10^{-1}$	$7.998 \cdot 10^{-1}$
	70°	$7.732 \cdot 10^{-2}$	$2.706 \cdot 10^{-2}$	$6.854 \cdot 10^{-1}$	$7.900 \cdot 10^{-1}$
	80°	$7.378 \cdot 10^{-2}$	$2.582 \cdot 10^{-2}$	$6.860 \cdot 10^{-1}$	$7.858 \cdot 10^{-1}$
	90°	$7.266 \cdot 10^{-2}$	$2.543 \cdot 10^{-2}$	$6.851 \cdot 10^{-1}$	$7.834 \cdot 10^{-1}$

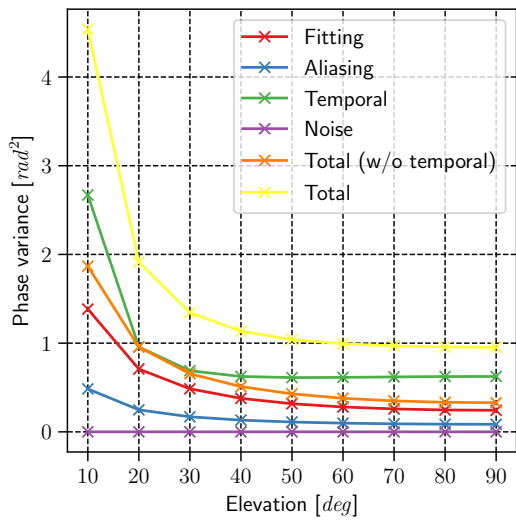
3. Adaptive Optics for LEO Satellite Tracking
 3.4. Adaptive Optics Systems: Case Studies



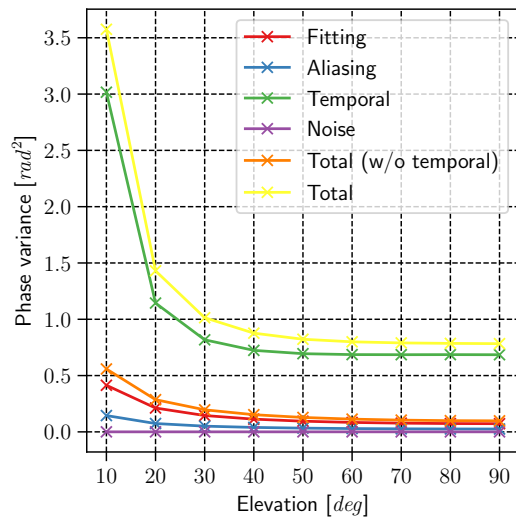
(a) *LISA*



(b) *FEELINGS*



(c) *ODISSEE*



(d) *ODISSEE++*

Figure 3.11.: AO budget for the four system configurations considered.

4. Atmospheric Turbulence Prediction

Contents

4.1. Temporal Prediction Problem	71
4.1.1. Mathematical Formulation	71
4.1.2. Predictive Control for Adaptive Optics	72
4.2. Autoregressive Predictive Models	74
4.2.1. VAR(p) Processes	74
4.2.2. Important Properties	75
4.2.3. Autoregressive Model Identification	78
4.2.4. Yule-Walker Estimator	79
4.2.4.1. Yule-Walker Equations	79
4.2.4.2. Process Noise Computation	81
4.2.5. Computation of Spatio-Temporal Covariance Matrices	82
4.2.5.1. Analytical Computation in Zonal Basis	83
4.2.5.2. Analytical Computation in Zernike Modal Basis	84
4.2.5.3. Data-Based Computation	85
4.3. Linear-Quadratic-Gaussian Controller as Predictive Controller	86
4.3.1. State-Space Representation for a Linear Stochastic System	87
4.3.2. Optimal Linear-Quadratic-Regulator (LQR)	88
4.3.2.1. General LQR Solution	88
4.3.2.2. LQR for Adaptive Optics	88
4.3.3. Kalman Filter	90
4.3.3.1. Update	91
4.3.3.2. Prediction	92
4.3.3.3. Kalman Gain Computation	92
4.3.3.4. State Reconstruction within the Kalman Filter	93
4.3.4. Synthesis of the LQG Controller	94
4.3.5. Use of the LQG in Adaptive Optics	94
4.3.6. Summary of the LQG Predictive Controller	95

Introduction

This chapter discusses the use of temporal prediction in adaptive optics controllers. A mathematical model of the temporal evolution of turbulence is used to predict its state two frames ahead of time, corresponding to the typical delay between adaptive optics correction and the last wavefront measurement. Using the predicted turbulence for correction instead of the outdated measured wavefront helps reduce temporal error in adaptive optics systems.

The temporal prediction problem for adaptive optics control is formulated. A review of the different predictive control strategies for adaptive optics is provided. The rest of the chapter introduces the two standard elements of predictive controllers for adaptive optics: (1) linear autoregressive processes as turbulence evolution models and (2) the use of the *linear-quadratic-Gaussian (LQG)* as predictive controller.

4.1. Temporal Prediction Problem

Adaptive optics loops present a delay between the wavefront measurement and its correction. This delay leads to the so-called temporal error, a residual phase aberration due to the difference between the measured phase and the phase at the time of correction. Predictive controllers reduce the temporal error by computing the adaptive optics correction from a prediction of the future phase rather than using the last available measurement. Temporal error, and therefore the interest in predictive controllers, becomes bigger in the case of fast turbulence evolution, such as in the presence of strong natural wind or the strong apparent wind in tracked-satellite applications.

The predictive models to be implemented within the adaptive optics loops need to be simple enough to run on a *RTC* at the *AO* loop frequency. The model also needs to be identified from available telemetry during the operation of the system.

4.1.1. Mathematical Formulation

The continuous-time turbulent phase is represented in discrete-time (Looze 2007, 2009; Kulcsár et al. 2006) form as:

$$\phi_k = \phi(t = t[k]) = \frac{1}{T} \int_{(k-1)T}^{kT} \phi(t) dt, \quad (4.1)$$

where t is the continuous time variable, discretized in temporal steps indexed by k with a period T corresponding to the integration time of a *WFS* frame.

The phase ϕ is expressed as a vector $\boldsymbol{\phi}$ of N components corresponding to one of the different spatial phase representations discussed in Section 1.3.

The goal is to estimate $\boldsymbol{\phi}_{k+s}$ assuming knowledge of a set of past phase vectors

$\{\phi_k, \phi_{k-1}, \phi_{k-2}, \dots\}$. A prediction horizon of integer time steps s is used, corresponding to the AO loop delay (typically 2 frame delay, i.e. $s = 2$). Extensions to fractional time steps are possible (Poyneer and Véran 2008; Raynaud et al. 2011) but are not considered in this work.

The discussion here is limited to a mono-layer of turbulence, be it one of the layers of a multi-layer turbulence profile or the resulting turbulent phase on the pupil plane of the telescope. The same methods can be extended to predict the evolution phase of several layers of turbulence.

The present discussion covers the prediction of the turbulent phase. Some methods for adaptive optics predictive control work in the slope space and therefore predict the slope evolution directly. Although this is not strictly equivalent from a physical point of view, the mathematical framework for the formulation of predictive controllers remains the same regardless of whether phase or slopes are considered.

4.1.2. Predictive Control for Adaptive Optics

The presence of temporal error due to insufficient wavefront sampling frequency and its impact on imaging systems has been acknowledged for a long time (Kane et al. 1991). The first mention, to the author's knowledge, of predictive control in adaptive optics as a solution to decrease temporal error can be traced back to Zuev and Lukin (1987), where a new class of adaptive optics systems is proposed: the "*predicting adaptive system*". This work was the first to suggest the use of turbulence statistics and the last measurements available to compute an estimation of the future phase in the presence of a control system delay.

Predictive controllers use a predictive model based on the spatio-temporal statistics of turbulence. Different works have suggested the use of different statistics, such as covariance matrices, correlation functions, or power spectral densities, all of them presenting different trade-offs such as availability of analytical expressions for their computation or ease to identify them from data.

Paschall and Anderson (1993) presented the development of the first use of the *linear-quadratic-Gaussian (LQG)* controller in AO, with predictive control as its main goal. Since then, this method has been one of the main predictive control methods in AO. The *LQG* provides the optimal control strategy for a linear system in the presence of uncertainties in the noise that drives the evolution of the controlled system in the measurements about the system. This is the case of adaptive optics, where the controlled system, i.e. the phase distortion due to turbulence, is stochastic in nature and the wavefront measurements are significantly noisy because of the limitations in flux available for wavefront sensing. To do so, the *LQG* uses a predictive model of the evolution of the turbulence. Many works have continued its development, mostly focusing on the search for a model that can provide good prediction performance, be computationally inexpensive and easily identifiable from available AO telemetry. *Autoregressive (AR)* models are one of the most common models assumed in adaptive optics; Section 4.2 introduces them.

4. Atmospheric Turbulence Prediction

4.1. Temporal Prediction Problem

The use of the LQG as a predictive controller is detailed in Section 4.3.

Dessenne et al. (1998, 1999) developed a predictive controller that models the AO loop in the frequency domain, including a linear predictive filter for the phase disturbance. The linear predictors are defined for each KL mode independently. Each predictor is optimized to decrease the residual wavefront error while accounting for measurement noise level, delay, and stability constraints in a similar fashion to the modal gain optimization method (Gendron and Lena 1994). The article proves that close-loop data can be used for model identification, which allows model identification during operation.

Other works have developed fully data-based methods (Hinnen et al. 2007; Beghi et al. 2007; Guyon and Males 2017; Sinquin et al. 2020). These methods assume a general structure of turbulence evolution and fit the data to it without considering any a priori information such as the spectrum of the turbulence or frozen flow. After pioneering work during the 1990s (Jorgenson and Aitken 1992; Lloyd-Hart and McGuire 1996), the last few years have seen the start of the development of machine learning techniques for adaptive optics, with a focus on predictive controllers Swanson et al. (2018); Liu et al. (2020); Landman et al. (2021); Pou et al. (2022); Nousiainen et al. (2022). This includes the first neural network predictive control with on-sky data Chen et al. (2021).

In astronomy predictive control has found different applications. Tomographic techniques often use the LQG framework for the implementation of phase reconstructors (Fusco et al. 2001; Lloyd-Hart et al. 2006) as part of a controller. In this case, even if temporal error reduction is not the main priority, the Kalman filter involved needs a temporal evolution model. As a result, many advances in the field of predictive control have come from tomography applications (Le Roux et al. 2003; Petit et al. 2009; Kulcsár et al. 2012; Correia et al. 2014; Cranney et al. 2020). Furthermore, accounting for the temporal signature of different layers in tomographic measurements can improve the performance of tomographic reconstructors, since it allows them to distinguish their contribution to the measured turbulence volume (Ammons et al. 2012).

Another application of predictive control for astronomy has been its use in high-contrast imaging systems for exoplanet detection using coronagraphs. In this case, high-performance adaptive optics systems are required to reduce the speckles in the coronagraphic imaging that can be confused with exoplanets (Macintosh 2001). In fact, the first operational predictive control systems for AO are found in the *Spectro-Polarimetric High-Contrast Exoplanet REsearch* (SPHERE) (Petit et al. 2014) and the *Gemini Planet Imager* (GPI) (Poyneer et al. 2016). Even after the success of the first high-performance AO systems (Keppler et al. 2018), Cantalloube et al. (2018) has observed how the temporal error causes the so-called wind-driven halo, which continues to contaminate the images of high-contrast instruments. This need to reduce temporal error has motivated a wave of new work on predictive control (Guyon and Males 2017; Landman et al. 2021; Haffert et al. 2021; Fowler et al. 2022; van Kooten et al. 2022).

Predictive control has also been used as a filter for the vibrations present in the *AO* optical path (Petit et al. 2008; Poyneer and Véran 2010; Guesalaga et al. 2012; Sivo et al. 2014).

Finally, tracked-satellite applications have also motivated the research of predictive controllers for adaptive optics Wild (1997) being among the first. Many of these works aim to include a priori information on wind speed and direction. This information may come from knowledge of the orbit in the case of or thanks to wind speed profiling techniques such as Guesalaga et al. (2014). A more thorough review of the different predictive control methods that account for wind priors is given in Section 6.2.

4.2. Autoregressive Predictive Models

Most works on temporal prediction of atmospheric turbulence assume that the temporal dynamics of turbulence can be captured by its temporal statistics, in particular its temporal covariances or an equivalent magnitude. *Autoregressive* (*AR*) processes are a useful mathematical tool in this context, since they are a way to model a temporal time series. *AR* models can be used both as a model for the evolution of a process that has certain temporal statistics (Assémat et al. 2006) or as a predictor of an underlying process.

AR models represent the evolution of a dynamic process in terms of linear combinations (i.e. regressions) of its previous states. In their vector form, *vector autoregressive* (*VAR*) models also capture the correlation between several time series; for example, between different models of the turbulent phase or different points within the pupil for a zonal phase description.

Autoregressive models are a common way to build linear models of dynamic processes that can be used for the analysis and prediction of atmospheric turbulence. The resulting models are also computationally inexpensive and suitable for their implementation within the adaptive optics system *RTC*.

The section is structured as follows. First, Section 4.2.1 introduces the definition of *VAR* processes, along with some relevant properties in Section 4.2.2. Next, a general discussion on the identification of *VAR* processes is given in Section 4.2.3. Section 4.2.4 deals with the Yule-Walker estimator for the identification of *VAR* processes from their autocovariance matrices. In this thesis, this estimator is used to compute *VAR* processes from the analytical expressions of their autocovariance matrices. Finally, Section 4.2.5 discusses the analytical computation of the required autocovariance matrices.

4.2.1. VAR(p) Processes

The turbulent phase in the telescope pupil plane is assumed to be represented by a weakly stationary discrete time series $\{\mathbf{x}_k\}_k$, where \mathbf{x}_k is a state vector representing

the turbulent phase at a given time step k , see Section 1.3 for possible vectorial phase representations.

A linear scalar autoregressive model of order p , denoted $AR(p)$, is defined as

$$x_{k+1} = \sum_{i=1}^p a_i x_{k-i+1} + v_k. \quad (4.2)$$

The future state of the process is the result of the linear combination of the previous p states using the coefficients a_i plus the innovation v_k . The innovations $\{v_k\}_k$ are zero mean white noise and statistically independent with respect to the turbulence states; they introduce a stochastic component in the evolution of the process.

This concept can be generalized to a set of time series as:

$$\mathbf{x}_{k+1} = \sum_{i=1}^p \mathbf{A}_i \mathbf{x}_{k-i+1} + \mathbf{v}_k, \quad (4.3)$$

where \mathbf{A}_i is a matrix of linear combination coefficients and \mathbf{v}_k is a vector of zero-mean white noise components that is also independent of all the previous process states such that:

$$\mathbb{E}\{\mathbf{v}_k\} = 0 \quad (4.4)$$

$$\mathbb{E}\{\mathbf{v}_k \mathbf{v}_k^\top\} = \boldsymbol{\Sigma}_v \quad (4.5)$$

$$\mathbb{E}\{\mathbf{v}_k \mathbf{x}_l^\top\} = 0, \text{ for } l \leq k. \quad (4.6)$$

The product $\mathbf{A}_i \mathbf{x}_{k-i-1}$ implies the linear combination of the different time series for time step k , while the summation is a further linear combination of the different time steps together. In this way, the model is able to account for the regression between different states and different time steps.

Remark

In the case of all matrices \mathbf{A}_i and matrix $\boldsymbol{\Sigma}_v$ being diagonal, a set of n independent autoregressive models, $AR(p)$ with no interaction between states is obtained. All mathematical developments for $VAR(p)$ also apply to $AR(p)$.

4.2.2. Important Properties

For a thorough discussion on VAR processes and their mathematical properties, the reader is invited to refer to the book Lütkepohl (2005). The main results from the VAR processes theory that are relevant to this work are listed below:

Property 4.1 *A VAR process is defined by its coefficient matrix \mathbf{A} and the covariance matrix of the process noise Σ_v .*

Property 4.2 (VAR(p) process as a VAR(1)) *Any VAR(p) process can be written in VAR(1) form.*

Starting from Equation 4.3 we stack all the past \mathbf{x} vectors as:

$$\mathbf{X}_k = [\mathbf{x}_k, \mathbf{x}_{k-1}, \dots, \mathbf{x}_{k-p+1}]^\top. \quad (4.7)$$

The time evolution of this vector is defined as:

$$\mathbf{X}_{k+1} = [\mathbf{x}_{k+1}, \mathbf{x}_k, \dots, \mathbf{x}_{k-p+2}]^\top. \quad (4.8)$$

The stacked process noise vector has only non-zero elements corresponding to \mathbf{x}_{k+1} :

$$\mathbf{V}_k = [\mathbf{v}_k, 0, \dots, 0]^\top. \quad (4.9)$$

Finally, we define:

$$\mathbf{A}_{\text{VAR}(1)}^{(p)} = \begin{bmatrix} \mathbf{A}_1 & \mathbf{A}_2 & \dots & \mathbf{A}_{p-1} & \mathbf{A}_p \\ \mathbb{I} & 0 & & 0 & 0 \\ 0 & \mathbb{I} & \dots & 0 & 0 \\ \vdots & & \ddots & \vdots & \vdots \\ 0 & 0 & \dots & \mathbb{I} & 0 \end{bmatrix}. \quad (4.10)$$

Using these elements, we define the equivalent VAR(1) process:

$$\boxed{\mathbf{X}_{k+1} = \mathbf{A}_{\text{VAR}(1)}^{(p)} \mathbf{X}_k + \mathbf{V}_k}. \quad (4.11)$$

Property 4.3 (Stability of a VAR(p) process) *A VAR(p) is stable if all eigenvalues of the matrix \mathbf{A} have modulus less than 1. See [Lütkepohl \(2005\)](#), page 15.*

Property 4.4 (VAR(p) autocovariance matrices) *A VAR(p) process is defined by its first $p+1$ autocovariance matrices ($\tau = 0, \dots, p$). The coefficient*

matrix \mathbf{A} and the covariance matrix of the process noise $\Sigma_{\mathbf{v}}$ can be computed from them, as well as the rest of its autocovariance matrices can be also computed. See [Lütkepohl \(2005\)](#), page 28. (See [Appendix A.2](#) for the definition of the autocovariance matrix).

As a result, a VAR model can be identified from an estimation of its autocovariance matrices, see [Section 4.2.4](#). In the same way, it is possible to compute the autocovariance matrices of a VAR(p) process.

Property 4.5 (VAR(p) optimal prediction) *If the underlying process for the generation of a time series is a VAR(p), the same VAR(p) (with the same order p) is the optimal linear predictor of the time series in the sense of prediction error MSE. See [Lütkepohl \(2005\)](#), page 36.*

For a process defined as in [Equation 4.11](#) the optimal estimate considering a s -step prediction horizon is:

$$\hat{\mathbf{X}}_{k+s} = \mathbf{A}\hat{\mathbf{X}}_{k+s-1} = \mathbf{A}^s \mathbf{X}_k, \quad (4.12)$$

where \mathbf{A}^s is the s power of the matrix \mathbf{A} . That means that the best one-step predictor is the \mathbf{A} matrix and the best s -step prediction is to apply the one-step predictor iteratively s times.

The prediction error covariance matrix is given by:

$$\Sigma_{\hat{\mathbf{X}}}(s) = \sum_{i=0}^{s-1} \mathbf{A}^i \Sigma_{\mathbf{V}} (\mathbf{A}^i)^{\top}. \quad (4.13)$$

Property 4.6 (VAR(p) prediction from estimated model) *If the underlying process for the generation of a time series is a VAR(p), an estimated model of the VAR(p) process (with the same order p) will produce an unbiased estimator. See [Lütkepohl \(2005\)](#), page 94.*

In this case, the coefficient matrix in [Equation 4.12](#) is substituted by its estimated version \mathbf{A}' the prediction error covariance matrix is given by:

$$\hat{\mathbf{X}}'_{k+s} = \mathbf{A}'\hat{\mathbf{X}}_{k+s-1} = (\mathbf{A}')^s \mathbf{X}_k. \quad (4.14)$$

The prediction error covariance matrix is given by:

$$\Sigma_{\hat{\mathbf{X}}'}(s) = \Sigma_{\hat{\mathbf{X}}} + \mathbb{E} \left\{ \left(\hat{\mathbf{X}}_{k+s} - \hat{\mathbf{X}}'_{k+s} \right) \left(\hat{\mathbf{X}}_{k+s} - \hat{\mathbf{X}}'_{k+s} \right)^{\top} \right\}. \quad (4.15)$$

That can be interpreted as the fact that the prediction error will be the prediction error with the true model plus a term that depends on the difference between the true model and its estimate.

Property 4.7 (VAR(p) modeling for unknown processes) *An unknown process can be approximated by a VAR(p). However, in this case, there is no optimality guaranteed and the order of the model is to be tested. See [Lütkepohl \(2005\)](#), Chapter 4.3.*

4.2.3. Autoregressive Model Identification

So far, the stochastic model structure of vector autoregressive processes has been discussed. The present section deals with the identification and computation of these models. All *VAR* models are defined by the following matrices: (1) the parameter matrix \mathbf{A} and (2) the process noise covariance matrix Σ_v . The task of model identification is to compute these two matrices from the available knowledge about the system to be modeled.

Different model identification methods are available. Data-based approaches make use of the available time series of the described process. The least squares estimator (see [Lütkepohl \(2005\)](#), page 69) computes the estimator that provides the lowest square error for a time series. Since *VAR* models can be written in a state space form, subspace identification methods can also be used, for example, [Doelman et al. \(2011\)](#) for the tip-tilt modes, [Tesch et al. \(2015\)](#) for low-order *KL* modes, and [Sinquin et al. \(2020\)](#) for low-order Zernike modes. Recursive estimation methods are very promising since they update the model while the turbulence changes (the case of *LEO* satellite tracking). [Monchen et al. \(2019\)](#) has proposed an iterative *VAR* process identification method based on the recursive least-squares method. Some works ([Meimon et al. 2010](#); [Yang et al. 2018](#)) use a combination of simple models derived from a priori physical knowledge and data-based identification. In these cases, the dynamics of the phase aberrations due to vibrations on the *AO* system are approximated by a mass-spring-damper model rewritten as a second-order autoregressive process.

This section does not aim to provide a complete review of *VAR* model identification methods. The reader can refer to [Juvenal et al. \(2015a\)](#) for a comparison of the performance of several *VAR* model identification methods in the context of adaptive optics.

This work uses the Yule-Walker estimator as the preferred method for the identification of processes; the method is introduced in the following section. The Yule-Walker estimator computes an autoregressive process from its autocovariance matrices. To do so, the estimator uses the Yule-Walker equations, which relate the parameter matrix of the *VAR* model to its autocovariance matrices. This method

is very flexible since different methods can be used to compute the autocovariance matrices. The autocovariance matrices can be estimated using data-based methods (Paschall and Anderson 1993) or from theoretical values when available (Assémat et al. 2006; Correia et al. 2014), as discussed in Section 4.2.5.

4.2.4. Yule-Walker Estimator

This section details the *VAR* process estimation method used in this thesis: the Yule-Walker estimator. The Yule-Walker estimator assumes that the autocorrelation matrices of the process are available and uses the Yule-Walker equations, the equations relating the *VAR* process auto-correlations to its model coefficients, to compute the process model.

Remark

The Yule-Walker estimator is a variant of the method of moments in statistics. The method of moments is an estimator of the parameters of a statistical distribution from its statistical moments. The method assumes that the statistical moments are known or can be computed with a sample estimator and expresses those moments as functions of the parameters to be estimated; the resulting equations are then solved for the parameters of interest.

In the following, the Yule-Walker equations are derived and used to compute the parameter matrix \mathbf{A} , followed by a method for the computation of the process noise covariance matrix Σ_v . The auto-correlations used in this section can be estimated from data or computed analytically when models are available. Section 4.2.5 will introduce the computation of analytical autocovariance for the case of phase aberrations due to frozen flow atmospheric turbulence.

Since *VAR* models are the best predictor for *VAR* processes (see Property 4.5) the Yule-Walker is a way of computing an optimal predictor for a *VAR* process from its autocovariance matrices.

An additional advantage of this method is that the Yule-Walker estimator always produces a process that is stable. However, the use of sample covariance matrices for the identification of the required autocovariances may lead to bias in the estimator. See Lütkepohl (2005), page 85.

4.2.4.1. Yule-Walker Equations

In order to derive the Yule-Walker equations, we right multiply Equation 4.11 by \mathbf{X}_k^\top and compute the expectation of the resulting expression:

$$\mathbb{E}\{\mathbf{X}_{k+1}\mathbf{X}_k^\top\} = \mathbb{E}\{\mathbf{A}\mathbf{X}_k\mathbf{X}_k^\top + \mathbf{V}_k\mathbf{X}_k^\top\}. \quad (4.16)$$

We use the linearity properties of the expected value operation:

$$\mathbb{E}\{\mathbf{X}_{k+1}\mathbf{X}_k^\top\} = \mathbf{A}\mathbb{E}\{\mathbf{X}_k\mathbf{X}_k^\top\} + \mathbb{E}\{\mathbf{V}_k\mathbf{X}_k^\top\}. \quad (4.17)$$

Finally, we remove the cross-terms between the state vector and the process noise, since they are statistically independent (see Equation 4.6):

$$\mathbb{E}\{\mathbf{X}_{k+1}\mathbf{X}_k^\top\} = \mathbf{A}\mathbb{E}\{\mathbf{X}_k\mathbf{X}_k^\top\}. \quad (4.18)$$

We can right-multiply by the inverse of $\mathbb{E}\{\mathbf{X}_k\mathbf{X}_k^\top\}$ to get a solution for \mathbf{A} :

$$\boxed{\mathbf{A} = \mathbb{E}\{\mathbf{X}_{k+1}\mathbf{X}_k^\top\}\mathbb{E}\{\mathbf{X}_k\mathbf{X}_k^\top\}^{-1}}. \quad (4.19)$$

All of the above covariance matrix expressions correspond to autocovariance matrices. We define the temporal autocovariance matrix of a zero-mean stochastic process \mathbf{X} as $\mathbf{\Gamma}_\mathbf{X}(\tau) = \mathbb{E}\{\mathbf{X}_{k+\tau}\mathbf{X}_k^\top\}$. For the covariance matrix expressions in Equation 4.19 this gives:

$$\begin{aligned} \mathbb{E}\{\mathbf{X}_k\mathbf{X}_k^\top\} &= \begin{bmatrix} \mathbb{E}\{\mathbf{x}_k\mathbf{x}_k^\top\} & \mathbb{E}\{\mathbf{x}_k\mathbf{x}_{k-1}^\top\} & \cdots & \mathbb{E}\{\mathbf{x}_k\mathbf{x}_{k-p+1}^\top\} \\ \mathbb{E}\{\mathbf{x}_{k-1}\mathbf{x}_k^\top\} & \mathbb{E}\{\mathbf{x}_{k-1}\mathbf{x}_{k-1}^\top\} & \cdots & \mathbb{E}\{\mathbf{x}_{k-1}\mathbf{x}_{k-p+1}^\top\} \\ \vdots & \vdots & \ddots & \vdots \\ \mathbb{E}\{\mathbf{x}_{k-p+1}\mathbf{x}_k^\top\} & \mathbb{E}\{\mathbf{x}_{k-p+1}\mathbf{x}_{k-1}^\top\} & \cdots & \mathbb{E}\{\mathbf{x}_{k-p+1}\mathbf{x}_{k-p+1}^\top\} \end{bmatrix} \\ &= \begin{bmatrix} \mathbf{\Gamma}_\mathbf{x}(0) & \mathbf{\Gamma}_\mathbf{x}(1) & \cdots & \mathbf{\Gamma}_\mathbf{x}(p-1) \\ \mathbf{\Gamma}_\mathbf{x}(-1) & \mathbf{\Gamma}_\mathbf{x}(0) & \cdots & \mathbf{\Gamma}_\mathbf{x}(p-2) \\ \vdots & \vdots & \ddots & \vdots \\ \mathbf{\Gamma}_\mathbf{x}(1-p) & \mathbf{\Gamma}_\mathbf{x}(2-p) & \cdots & \mathbf{\Gamma}_\mathbf{x}(0) \end{bmatrix}, \end{aligned} \quad (4.20)$$

and

$$\mathbb{E}\{\mathbf{X}_{k+1}\mathbf{X}_k^\top\} = \begin{bmatrix} \mathbf{\Gamma}_\mathbf{x}(1) & \mathbf{\Gamma}_\mathbf{x}(2) & \cdots & \mathbf{\Gamma}_\mathbf{x}(p) \\ \mathbf{\Gamma}_\mathbf{x}(0) & \mathbf{\Gamma}_\mathbf{x}(1) & \cdots & \mathbf{\Gamma}_\mathbf{x}(p-1) \\ \vdots & \vdots & \ddots & \vdots \\ \mathbf{\Gamma}_\mathbf{x}(-p) & \mathbf{\Gamma}_\mathbf{x}(1-p) & \cdots & \mathbf{\Gamma}_\mathbf{x}(0) \end{bmatrix}. \quad (4.21)$$

Remark

As stated in Property 4.4 coefficients of \mathbf{A} depend therefore on the temporal autocovariances of the vector \mathbf{x} from $\tau = 0$ to $\tau = p$. This requires the assumption that the modeled process is weak-sense stationary, which means that the mean and autocovariance of a process do not change in time and its second moment is finite at all times.

Remark

For the case of adaptive optics, the autocovariances defined in this section are equivalent to the spatio-temporal cross-covariance matrices of the turbulence. They are "temporal" since they are autocovariances, and "spatial" due to the cross-covariance between phase modes or pixels, which carry spatial information.

Remark

The computation above considers the \mathbf{A} matrix as defined in Equation 4.10. To save computational resources, the first row of this block matrix can be computed by considering $\mathbf{A} = \mathbb{E}\{\mathbf{x}_{k+1}\mathbf{X}_k^\top\}\mathbb{E}\{\mathbf{X}_k\mathbf{X}_k^\top\}^{-1}$, since the rest of the terms are known to be the identity matrix or zero.

4.2.4.2. Process Noise Computation

Once the coefficients of the *VAR* model are known. For example, computed using Equation 4.19. It is possible to compute the process noise covariance matrix Σ_v from Equation 4.2 by multiplying it by itself and taking the expectation so that:

$$\mathbb{E}\{\mathbf{X}_{k+1}\mathbf{X}_{k+1}^\top\} = \mathbb{E}\left\{(\mathbf{A}\mathbf{X}_k + \mathbf{V}_k)(\mathbf{A}\mathbf{X}_k + \mathbf{V}_k)^\top\right\}. \quad (4.22)$$

We develop the expression:

$$\mathbb{E}\{\mathbf{X}_{k+1}\mathbf{X}_{k+1}^\top\} = \mathbb{E}\{\mathbf{A}\mathbf{X}_k\mathbf{X}_k^\top\mathbf{A}^\top + \mathbf{A}\mathbf{X}_k\mathbf{V}_k^\top + \mathbf{V}_k\mathbf{X}_k^\top\mathbf{A}^\top + \mathbf{V}_k\mathbf{V}_k^\top\}. \quad (4.23)$$

We use the linearity properties of the expected value operator:

$$\begin{aligned} \mathbb{E}\{\mathbf{X}_{k+1}\mathbf{X}_{k+1}^\top\} &= \mathbf{A}\mathbb{E}\{\mathbf{X}_k\mathbf{X}_k^\top\}\mathbf{A}^\top + \mathbf{A}\mathbb{E}\{\mathbf{X}_k\mathbf{V}_k^\top\} \\ &\quad + \mathbb{E}\{\mathbf{V}_k\mathbf{X}_k^\top\}\mathbf{A}^\top + \mathbb{E}\{\mathbf{V}_k\mathbf{V}_k^\top\}. \end{aligned} \quad (4.24)$$

We remove the cross-terms between the state vector and the process noise since they are statistically independent, see Equation 4.6:

$$\mathbb{E}\{\mathbf{X}_{k+1}\mathbf{X}_{k+1}^\top\} = \mathbf{A}\mathbb{E}\{\mathbf{X}_k\mathbf{X}_k^\top\}\mathbf{A}^\top + \mathbb{E}\{\mathbf{V}_k\mathbf{V}_k^\top\}. \quad (4.25)$$

We replace by the cross-covariance matrices:

$$\Sigma_{\mathbf{X}} = \mathbf{A}\Sigma_{\mathbf{X}}\mathbf{A}^\top + \Sigma_{\mathbf{V}}. \quad (4.26)$$

Finally, we solve for $\Sigma_{\mathbf{V}}$ in the previous equation:

$$\boxed{\Sigma_{\mathbf{V}} = \mathbf{A}\Sigma_{\mathbf{X}}\mathbf{A}^\top - \Sigma_{\mathbf{X}}}. \quad (4.27)$$

Remark

Compared to other derivations of *AR* and *VAR* models found in the literature (Correia et al. 2015; Prengère et al. 2020), this method allows to compute the model for an arbitrary order.

Remark

The computation above considers the \mathbf{V} vector as defined in Equation 4.9. In order to save computational resources, the vector \mathbf{v} can be considered instead and compute its covariance matrix as $\Sigma_{\mathbf{v}} = \mathbf{A}\Sigma_{\mathbf{x}}\mathbf{A}^{\top} - \Sigma_{\mathbf{x}}$, where \mathbf{A} in this case is only the first row of the block matrix version in Equation 4.11. The rest of the elements of the vector \mathbf{V} are zero.

4.2.5. Computation of Spatio-Temporal Covariance Matrices

This section discusses the computation of the spatio-temporal covariance matrices necessary to compute a *VAR* model. As presented in Section 4.2.4 the Yule-Walker estimator computes a *VAR* model from known autocovariance matrices, which for the case of turbulence is equivalent to spatio-temporal covariance matrices.

There exist two options to obtain the turbulent phase spatio-temporal covariance matrices: (1) estimating them from data (Hinnen et al. 2008; Vidal et al. 2010; Piscaer et al. 2019; Sinquin et al. 2020) or (2) computing them using analytical expressions depending on known turbulence parameters.

In the same way that the computation of spatial statistics of turbulence is based on physical a priori knowledge (i.e. the concept of energy cascades leading to assumptions on the spatial energy spectrum such as the Kolmogorov or von Kármán spectra), the computation of temporal turbulence statistics requires certain assumptions about the turbulence evolution. The application of the frozen flow assumption (see Section 1.1.3) allows computing temporal statistics based solely on the spatial statistics, with the advantage that there exist analytical expressions for the latter. Sections 4.2.5.1 and 4.2.5.2 detail the application of the frozen flow assumption for the computation of the spatio-temporal covariance matrices for both zonal and Zernike modal basis respectively.

Finally, Section 4.2.5.3 discusses the identification of the spatio-temporal covariance matrices from data, which, in general, avoids relying on any frozen flow assumption.

Remark

The discussion here focuses on the computation of the spatio-temporal covariance matrices of phase for a given layer of turbulence. The corresponding matrices for the telescope pupil can be computed by summing the matrices of every layer.

4.2.5.1. Analytical Computation in Zonal Basis

In the case of a zonal representation (Assémat et al. 2006; Piatrou and Roggemann 2007; Correia et al. 2015; Jackson et al. 2015; Ono et al. 2018; Cranney et al. 2019; Prengère et al. 2020), the goal is to compute the following covariance:

$$\langle \phi(\mathbf{r}_1, t) \phi(\mathbf{r}_2, t + \tau) \rangle, \quad (4.28)$$

where \mathbf{r}_1 and \mathbf{r}_2 are the coordinates of two points in space, t is the temporal index, and τ temporal delay between the two frames considered.

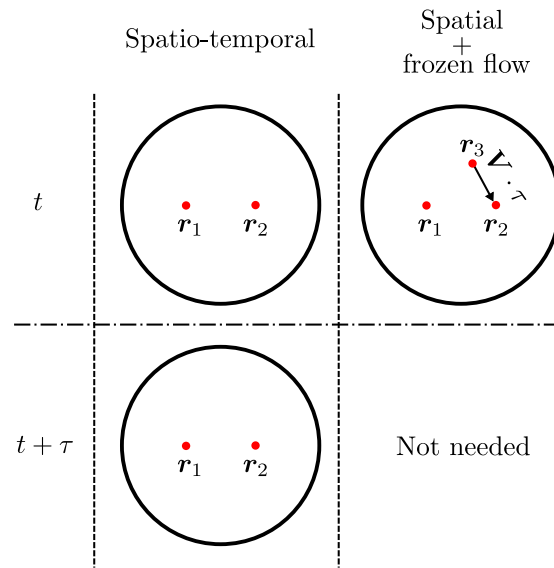


Figure 4.1.: Illustration of the use of frozen flow assumption to compute temporal phase covariances from spatial statistics.

Figure 4.1 depicts this arrangement. A black circle represents the aperture where the turbulent phase is defined, and the red points are the locations where the phase is considered. The first column in the figure, labeled "spatio-temporal" corresponds to Equation 4.28, which is the covariance between two different points at two different time steps. To compute this, it is necessary to have access to the spatio-temporal statistics of the phase field, which are not available analytically. For the turbulent phase, the spatial statistics are available using the Kolmogorov or von Kármán spectra (see Section 1.3.1.1). However, these statistics do not describe temporal evolution.

Introducing the frozen flow assumption allows for the analytical computation of the spatio-temporal covariances by using the available expressions for the spatial covariances. Under the frozen flow assumption, the phase $\phi(\mathbf{r}_2, t + \tau)$ is the phase of a third point at time t , $\phi(\mathbf{r}_3, t)$, where the location of the point \mathbf{r}_3 is given by the layer shift during the time interval τ :

$$\phi(\mathbf{r}_2, t + \tau) = \phi(\mathbf{r}_3 + \mathbf{V} \cdot \tau, t). \quad (4.29)$$

Figure 4.1 depicts this equivalence in its second column, labeled "spatial + frozen flow". As a result, it is obtained that:

$$\langle \phi(\mathbf{r}_1, t) \phi(\mathbf{r}_2, t + \tau) \rangle = \langle \phi(\mathbf{r}_1, t) \phi(\mathbf{r}_3 + \mathbf{V} \cdot \tau, t) \rangle. \quad (4.30)$$

The previous expression links the spatio-temporal covariances to purely spatial covariances thanks to the frozen flow assumption. The spatial phase covariances can be computed using Equation 1.38.

4.2.5.2. Analytical Computation in Zernike Modal Basis

Consider now the case of a Zernike modal basis (Whiteley et al. 1998a; Correia et al. 2014). A circular pupil centered at an angle α with respect to the line-of-sight and at time t is represented by the vector of Zernike coefficients $\phi(\alpha, t)$. In this case, and always under the assumption of Taylor frozen flow, it is possible to compute the temporal covariances between Zernike polynomials by using the analytical expressions for their angular covariances presented in Section 1.3.2.5.

The temporal covariances between Zernike coefficients are computed as:

$$\langle \phi_i(0, t) \phi_j(0, t + \tau) \rangle. \quad (4.31)$$

Under frozen flow assumption, the turbulence $\phi_j(0, t + \tau)$ is the same as the $\phi_t(\boldsymbol{\alpha}, t)$ where $\boldsymbol{\alpha} = (\alpha_x, \alpha_y)$ is the angle corresponding to a $\mathbf{d} = -\mathbf{V} \cdot \tau$ displacement, with $(\alpha_x, \alpha_y) = (-\mathbf{V} \cos \theta, -\mathbf{V} \sin \theta)$ for small angles, θ being the direction of the wind. As a result, the spatio-temporal covariance matrix can be computed as:

$$\langle \phi_i(0, t) \phi_j(0, t + \tau) \rangle = \langle \phi_i(0, t) \phi_j(\alpha, t) \rangle. \quad (4.32)$$

Remark

The angular cross-covariances between Zernike coefficients have been used here, note that the spatial cross-covariances could be used for the same purpose. In fact, the angular cross-covariances given in 1.3.2.5 are spatial cross-covariances where the (linear) spatial distance has been replaced by the angular distance.

In summary, these are the assumed inputs for the identification following the equations in Section 1.3.2.5:

- The layer speeds are known in magnitude and direction. This may include natural and apparent wind. Apparent wind can be computed from a known satellite trajectory, while natural wind needs to be measured by a meteorology instrument.

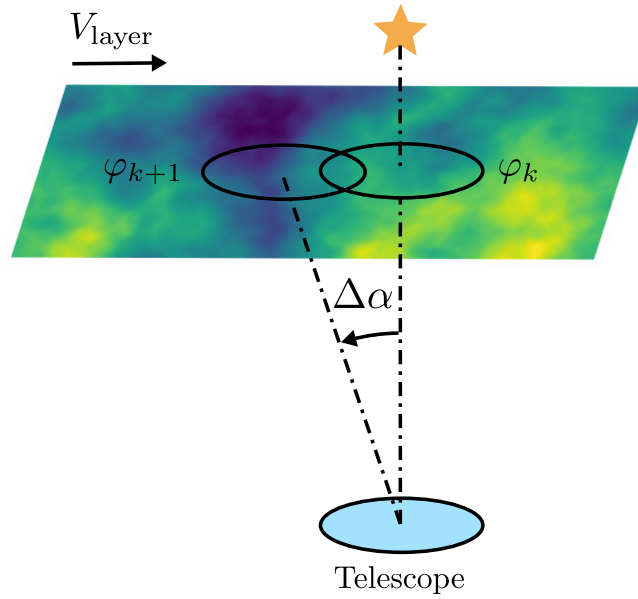


Figure 4.2.: Geometry for the computation of temporal cross-covariances of turbulence projected on Zernike polynomials using spatial statistics.

- The C_n^2 profile across the line of sight, including also the position of each layer.
- The outer scale of the turbulence, although its effect is not very important due to the expected outer scale sizes with respect to the telescope diameters considered for the application.

These assumptions are the same for the zonal computation.

4.2.5.3. Data-Based Computation

The identification of the spatio-temporal covariance matrices from data enables the use of data-driven *VAR* models. This kind of identification has as advantage that it does not require any knowledge of the turbulence $C_n^2(h)$ or wind profiles.

A simple method for the computation of the cross-covariance matrices from data is to use the sample covariance matrix [Vogel et al. \(2014\)](#):

$$\Sigma_{\mathbf{x}\mathbf{y}}^{\text{samp}} = \frac{1}{N-1} \sum_{k=1}^N (\mathbf{x}_k - \bar{\mathbf{x}}) (\mathbf{y}_k - \bar{\mathbf{y}})^\top, \quad (4.33)$$

where N is the total number of samples and $\bar{\mathbf{x}} = (1/N) \sum_{k=1}^N \mathbf{x}_k$ the sample mean. In the case of autocovariances, for a time series $\{\mathbf{x}_k\}$, this can be written as:

$$\Gamma_{\mathbf{x}}^{\text{samp}}(\tau) = \frac{1}{N-1} \sum_{k=1}^N (\mathbf{x}_k - \bar{\mathbf{x}}) (\mathbf{x}_{k+\tau} - \bar{\mathbf{x}})^\top. \quad (4.34)$$

The sample covariance matrix may not be a robust enough method. Better results in terms of convergence of the covariance matrix estimation and its robustness to measurement noise applying the methods are discussed in [Ivanov and Yakoub \(2023\)](#).

[Vidal et al. \(2010\)](#) proposed an identification for the slope-phase covariance matrices necessary to compute tomographic reconstructors. The method uses a parametric model of the slope-phase covariance matrices computed in the Fourier domain that can be fitted to the open-loop slope measurements. The convergence of this method was improved in [Martin et al. \(2012\)](#). [Cranney et al. \(2020\)](#) extended this method for the computation of temporal covariance matrices assuming frozen flow. Although this method is applicable in the slope space, an extension to Zernike polynomials or a zonal basis could be promising, as already pointed out by [Correia et al. \(2014\)](#).

4.3. Linear-Quadratic-Gaussian Controller as Predictive Controller

In this section, the *linear-quadratic-Gaussian (LQG)* controller is presented as a control strategy for the implementation of a predictive controller for an *AO* system. Other useful characteristics of the *LQG* in its application to adaptive optics are also highlighted.

The *LQG* controller is an optimal stochastic controller, which means that the controller can provide an optimal control policy that accounts for the presence of uncertainties in the states to be controlled and the measurements associated with them. Section 4.3.1 introduces the state-space representation of the stochastic system to be controlled. The principle of separation of estimation and control ([Åström 1970](#)) states that a controller for a stochastic system can be designed by considering separately an optimal state observer for the states to be controlled and an optimal controller for the equivalent deterministic system. This separation allows us to solve the estimation and optical control problems independently. As a result, the *LQG* is the combination of two control theory techniques: a multiple-input multiple-output optimal control strategy, the *linear-quadratic regulator (LQR)* controller (see Section 4.3.2); and an optimal estimator of the stochastic states to be controlled, the Kalman filter (see Section 4.3.3). The *LQR* provides the solution for the optimal gain to achieve optimal control in terms of a quadratic criterion. In the case of *AO* this criterion is the minimum variance of the residual phase. The *LQR* is a state feedback controller and therefore assumes that the states to be controlled are available. In the case of a stochastic system such as turbulence, the use of an observer like the Kalman filter allows to filter the measurements to produce estimates of the system states that are more accurate than the measurements themselves. Additionally, the Kalman filter includes a model of the temporal evolution of the system that is used to account for the

temporal correlation of the measurements to improve the accuracy of the filter estimates. This model can also be used as a predictive model for a predictive controller in the case of systems with delay.

4.3.1. State-Space Representation for a Linear Stochastic System

The state-space model of a dynamic system represents the temporal evolution of the system states as a function of the system inputs and outputs and some matrices that model the relationship between these variables. For a linear system and in the case of discrete-time, these relationships are written as:

$$\mathbf{x}_{k+1} = \mathbf{A}\mathbf{x}_k + \mathbf{B}\mathbf{u}_k + \mathbf{v}_k, \quad (4.35)$$

$$\mathbf{y}_k = \mathbf{C}\mathbf{x}_k + \mathbf{D}\mathbf{u}_k + \mathbf{w}_k. \quad (4.36)$$

The subindices correspond to the discrete-time step index for each variable. The first equation is the state evolution equation, it relates the evolution of the state vector \mathbf{x} from time step k to time step $k + 1$. The second equation is the measurement equation, it models the resulting measurement vector \mathbf{y} . The variables in the equations represent:

- $\mathbf{x} \in \mathbb{R}^{n_s}$, vector for the n_s state variables;
- $\mathbf{y} \in \mathbb{R}^{n_m}$, vector for the n_m measurement variables;
- $\mathbf{u} \in \mathbb{R}^{n_a}$, vector for the n_a control inputs;
- $\mathbf{v} \in \mathbb{R}^{n_s}$, vector for the process noise;
- $\mathbf{w} \in \mathbb{R}^{n_m}$, vector for the measurement noise;
- $\mathbf{A} \in \mathbb{R}^{n_s \times n_s}$, state transition matrix;
- $\mathbf{B} \in \mathbb{R}^{n_s \times n_a}$, control matrix;
- $\mathbf{C} \in \mathbb{R}^{n_m \times n_s}$, measurement matrix;
- $\mathbf{D} \in \mathbb{R}^{n_m \times n_a}$, feed-forward matrix.

Remark

The formulation above corresponds to a stochastic control problem. The states are not well known and need to be estimated. Two different stochastic components are present:

- The evolution of the system is not entirely deterministic, and thus the presence of process noise. This is the case for the phase of atmospheric turbulence.
- The state measurements contain noise. This is the case with wavefront sensors.

4.3.2. Optimal Linear-Quadratic-Regulator (LQR)

4.3.2.1. General LQR Solution

The infinite-horizon discrete-time *linear-quadratic regulator* (LQR) control problem searches to find the optimal control $\mathbf{u}_k \forall k \geq 0$ that minimizes the criterion:

$$J(\mathbf{u}) = \lim_{M \rightarrow \infty} \frac{1}{M} \sum_{k=0}^{M-1} (\mathbf{x}_k^\top \mathbf{Q} \mathbf{x}_k + \mathbf{u}_k^\top \mathbf{R} \mathbf{u}_k), \quad (4.37)$$

where \mathbf{Q} and \mathbf{R} are cost weight matrices such that $\mathbf{Q} = \mathbf{Q}^\top \geq \mathbf{0}$ and $\mathbf{R} = \mathbf{R}^\top > \mathbf{0}$. These matrices are design parameters that can be used to implement physical constraints such as saturation or penalties on the use of some inputs.

For the case in which the states of the system are known with no uncertainty (i.e. complete information), the solution to this minimization problem can be written as a state feedback law of the form:

$$\mathbf{u}_k = -\mathcal{K} \mathbf{x}_k, \quad (4.38)$$

where \mathcal{K} is a gain matrix. The gain matrix is computed to satisfy the optimality criterion as:

$$\mathcal{K} = \mathbf{R}^{-1} \mathbf{B}^\top \mathbf{P}_\infty, \quad (4.39)$$

where $\mathbf{P}_\infty = \mathbf{P}_\infty^\top \geq \mathbf{0}$ is the solution of the algebraic Riccati equation:

$$\mathbf{A}^\top \mathbf{P} + \mathbf{P} \mathbf{A} - \mathbf{P} \mathbf{B} \mathbf{R}^{-1} \mathbf{B}^\top \mathbf{P} + \mathbf{Q} = \mathbf{0}. \quad (4.40)$$

4.3.2.2. LQR for Adaptive Optics

In the case of adaptive optics (Kulcsár et al. 2006, 2012), the criterion in Equation 4.37 is generally considered to be the variance of the residual phase:

$$J(\mathbf{u}) = \lim_{M \rightarrow \infty} \frac{1}{M} \sum_{k=0}^{M-1} \|\phi_{k+1}^{\text{res}}\|^2. \quad (4.41)$$

The minimization of the residual phase can be related to the minimization of the Strehl ratio (Herrmann 1992), and therefore the improvement of image quality; as well as to the improvement in fiber coupling statistics (Canuet et al. 2018).

The AO corrected residual phase expression $\phi^{\text{res}} = \phi^{\text{tur}} + \phi^{\text{cor}}$ allows to write:

$$J(\mathbf{u}) = \lim_{M \rightarrow \infty} \frac{1}{M} \sum_{k=0}^{M-1} \|\phi_{k+1}^{\text{tur}} + \phi_{k+1}^{\text{cor}}\|^2, \quad (4.42)$$

where

4. Atmospheric Turbulence Prediction
4.3. Linear-Quadratic-Gaussian Controller as Predictive Controller

$$\phi_k^{\text{tur}} = \frac{1}{T} \int_{(k-1)T}^{kT} \phi^{\text{tur}}(t) dt \quad (4.43)$$

and

$$\phi_k^{\text{cor}} = \mathbf{N}\mathbf{u}_k. \quad (4.44)$$

This leads to the following criterion:

$$J(\mathbf{u}) = \lim_{M \rightarrow \infty} \frac{1}{M} \sum_{k=0}^{M-1} \|\phi_{k+1}^{\text{tur}} + \mathbf{N}\mathbf{u}_{k+1}\|^2. \quad (4.45)$$

The minimization of Equation 4.45 defines an *LQR*. The optimal solution to this problem is given by:

$$\mathbf{u}_{k+1} = \arg \min_u \|\phi_{k+1}^{\text{tur}} + \mathbf{N}\mathbf{u}\|^2. \quad (4.46)$$

The solution is obtained analytically by minimizing Equation 4.45 using a least-squares approach and it does not require the solution of the Riccati equation. The influence matrix of the *DM* needs to be full column rank, i.e. $\mathbf{N}^\top \mathbf{N}$ is invertible, so that:

$$\mathbf{u}_{k+1} = -(\mathbf{N}^\top \mathbf{N})^{-1} \mathbf{N}^\top \phi_{k+1}^{\text{tur}}. \quad (4.47)$$

Note that $\mathbf{u}_k = -\mathbf{K}\mathbf{x}_k$, with $\mathbf{K} = (\mathbf{N}^\top \mathbf{N})^{-1} \mathbf{N}^\top$, so it can be linked to the general *LQR* solution. In this case this is the least-square solution.

Remark

The computation of the feedback in Equation 4.47 requires a perfect measurement of ϕ_{k+1}^{tur} . This is typically not the case for three different reasons:

1. First, a measurement of the state may not be possible; in this case, the state needs to be reconstructed from other measurements. For example, if the states represent the turbulence wavefront, a measurement of phase is not possible. Instead, we may use the Shack-Hartmann slopes as measurements.
2. Second, the measurements (direct or not) of the states may be noisy.
3. Third, computing \mathbf{u} at time k requires knowledge of ϕ^{tur} at time k also. This is generally not possible, since there is a delay between the moment ϕ^{tur} is available and the moment \mathbf{u} is computed, i.e. loop delay.

Thanks to the separation principle, we can solve this problem by replacing ϕ_{k+1}^{tur}

with its estimate $\hat{\phi}_{k+1}^{\text{tur}}$. The *LQG* uses the Kalman filter as a state estimator for this purpose.

4.3.3. Kalman Filter

The *LQG* uses the Kalman filter as the optimal state estimator, so it can feed these estimates to the *LQG* optimal controller. This section discusses the Kalman filter and its application to the *LQG* for predictive control in adaptive optics. For a complete description of the Kalman filter, the reader is invited to consult [Simon \(2006\)](#).

For a stochastic linear dynamic system as described in Equations 4.35 and 4.36, the Kalman filter provides the optimal estimate $\hat{\mathbf{x}}$ of the system state \mathbf{x} . This estimate will be given by the conditional mean of the state:

$$\hat{\mathbf{x}}_{k|j} = \mathbb{E}\{\mathbf{x}_k | \mathcal{Y}_j\}, \quad (4.48)$$

where

$$\mathcal{Y}_j = \{\mathbf{y}_i, i \leq j\} \quad (4.49)$$

denotes all measurements available at time j . Depending on the value of k we have:

- The estimate of the state if $k = j$,
- the predicted value of the state if $k > j$, or
- the smoothed value of the state if $k < j$ (not discussed in this thesis).

The estimation error is defined as:

$$\tilde{\mathbf{x}}_{k|j} = \mathbf{x}_k - \hat{\mathbf{x}}_{k|j}. \quad (4.50)$$

While the covariance matrix of the estimation error is defined as:

$$\mathbf{P}_{k|j} = \mathbb{E}\left\{(\mathbf{x}_k - \hat{\mathbf{x}}_{k|j})(\mathbf{x}_k - \hat{\mathbf{x}}_{k|j})^\top\right\} \quad (4.51)$$

If $\{\mathbf{v}_k\}$ and $\{\mathbf{w}_k\}$ are Gaussian, zero-mean, uncorrelated, and white, then the Kalman filter provides the optimal solution to the minimization of the *MSE* of the estimation. Note, under these assumptions, it is also the minimum variance estimator.

The Kalman filter is made up of two steps: the update and the prediction. The Kalman filter starts with a guess of the conditional mean of the state and the covariance of the estimation error and propagates them across steps. The update step incorporates the information from a new measurement into the filter. The filter fuses this new information with its previous estimate by means of the Kalman

gain, a weighting matrix that is computed based on the uncertainties associated with the measurement and the predictive model. The prediction step advances the filter in time using a predictive model of the states. At any time step k , the filter provides both an estimate and a prediction based on the measurements available up to this moment.

4.3.3.1. Update

In the update step, the information from the new measurement and the previous prediction are combined together. The Kalman gain acts as a weighting of the importance of the innovation due to the measurement in this fusion:

$$\hat{\mathbf{x}}_{k|k} = \hat{\mathbf{x}}_{k|k-1} + \mathbf{H}_k(\mathbf{y}_k - \mathbf{C}\hat{\mathbf{x}}_{k|k-1}), \quad (4.52)$$

where $\mathbf{y}_k - \mathbf{C}\hat{\mathbf{x}}_{k|k-1}$ is called the filter innovations, i.e. the difference between the prediction of the state and the measurement associated with it, which can be seen as "the new information brought by the measurement"; and \mathbf{H}_k is the Kalman gain matrix, which is computed as:

$$\mathbf{H}_k = \mathbf{P}_{k|k-1}\mathbf{C}^\top (\mathbf{C}\mathbf{P}_{k|k-1}\mathbf{C}^\top + \boldsymbol{\Sigma}_w)^{-1}. \quad (4.53)$$

Although not shown here, the computation of \mathbf{H}_k in Equation 4.53 is the result of minimizing the estimation error. It computes the fusion of the prediction and the new measurement taking into account the process and measurement covariance matrices. In fact, the filter gain is "proportional" to the state process noise covariance, i.e. for high prediction uncertainty, the innovations are given a higher weight; and "inversely proportional" to the measurement noise variance, i.e. for high measurement uncertainty, the innovations are given a lower weight.

The information from the new measurement is also propagated to the covariance of the estimation error:

$$\mathbf{P}_{k|k} = (\mathbf{I} - \mathbf{H}_k\mathbf{C})\mathbf{P}_{k|k-1}. \quad (4.54)$$

Remark

The update step contains another feature that is especially relevant in the case of adaptive optics. The Kalman filter carries a regularized inversion of the measurement model that allows the reconstruction of the states from the measurements. See Section 4.3.3.4.

Remark

Some authors such as [Anderson \(1991\)](#) and [Petit et al. \(2006\)](#) have claimed that AR models can introduce the crosscorrelation between Zernike polynomials by including the non-diagonal spatial covariance matrix in the computation of the process noise.

In fact, doing this does not improve the prediction performance of the controller in the way that the use of VAR models does. However, it does help to improve the modal reconstruction within the Kalman filter, since it accounts for the spatial crosscovariances between modes. This is the reason for the better performance of these controllers compared to fully decoupled AR controllers.

4.3.3.2. Prediction

The prediction step advances one time-step the current estimate of the filter using the state transition matrix of the system:

$$\hat{\mathbf{x}}_{k+1|k} = \mathbf{A}\hat{\mathbf{x}}_{k|k} + \mathbf{B}\mathbf{u}_k. \quad (4.55)$$

The covariance of the estimation error is also propagated to the next time step:

$$\mathbf{P}_{k+1|k} = \mathbf{A}^\top \mathbf{P}_{k|k} \mathbf{A} + \Sigma_v. \quad (4.56)$$

Remark

The state matrix is a matrix that relates the future state and the present state in a linear Markovian fashion, i.e. the future state is a linear combination of the previous state, plus the process noise $\{\mathbf{v}_k\}$. In the case that the plant dynamics are unknown, or we desire to model them with a reduced model, it is possible to substitute \mathbf{A} by a similar linear predictive model of the state evolution. Finding this matrix and the covariance of the process noise is the object of the predictive modeling of this work and other works in the literature.

4.3.3.3. Kalman Gain Computation

The Kalman matrix, \mathcal{H}_k is computed for each time step from the propagation of the estimation error covariances. This does not depend on the particular states or measurements, so an asymptotic solution for the Kalman gain, \mathcal{H}_∞ can be computed before running the controller. By running Equations 4.53, 4.54, and 4.56 until convergence in the result.

4.3.3.4. State Reconstruction within the Kalman Filter

The Kalman filter includes a feature that is quite relevant for its use in adaptive optics. The measurement equation assumed in the state space model as presented in Equation 4.36 corresponds to the close-loop slopes case:

$$\mathbf{y}_k^{\text{CL}} = \mathbf{C}\mathbf{x}_k + \mathbf{D}\mathbf{u}_k + \mathbf{w}_k, \quad (4.57)$$

It is possible to write the pseudo-open loop slopes as:

$$\mathbf{y}_k^{\text{PSO}} = \mathbf{y}_k^{\text{CL}} - \mathbf{D}\mathbf{u}_k = \mathbf{C}\mathbf{x}_k + \mathbf{w}_k. \quad (4.58)$$

In order to compute an estimate of the state \mathbf{x}_k from the measurement $\mathbf{y}_k^{\text{PSO}}$, some sort of inversion of the measurement matrix \mathbf{C} is necessary. When the measurements are Shack-Hartmann slopes and the estimated states are the coefficients of open-loop turbulence projected on a polynomial basis (or a zonal representation of the phase), this can be seen as a modal (or zonal) reconstruction problem similar to the phase reconstruction problem discussed in Section 2.4.5.

Within the Kalman filter, the result of this reconstruction is $\hat{\phi}_{k|k}$, since it is the estimate of the phase from the measurements in the slope space. As a result, the Kalman filter provides a reconstruction of the phase that is regularized thanks to the turbulence statistics included in its model, in a similar way to the one provided by the *MAP* reconstructor. In fact, Correia (2010) showed that it is possible to derive a static optimal state reconstructor from the Kalman filter, which can be interpreted as the *MAP* phase reconstructor in the case of adaptive optics. First, it will be assumed that the phase is de-correlated in time, i.e. static assumption. This is equivalent to setting $\mathbf{A} = 0$ in Equation 4.35 to get the following state space equation:

$$\mathbf{x}_{k+1} = \phi_{k+1} = \mathbf{v}_k, \quad (4.59)$$

where \mathbf{v}_k is a Gaussian, zero-mean noise. The previous equation implies that $\Sigma_{\mathbf{v}} = \Sigma_{\phi}$.

The measurement equation is given by:

$$\mathbf{y}_k^{\text{PSO}} = \mathbf{C}\mathbf{x}_k + \mathbf{w}_k. \quad (4.60)$$

The update step in the Kalman filter can be written as:

$$\hat{\phi}_{k|k} = \hat{\phi}_{k|k-1} + \mathcal{H}_{\infty} \left(\mathbf{y}_k^{\text{PSO}} - \mathbf{C}\hat{\phi}_{k|k-1} \right), \quad (4.61)$$

where \mathcal{H}_{∞} is the Kalman gain for the static filter. $\hat{\phi}_{k|k-1}$ is the predicted phase, since the turbulence is supposed to be uncorrelated in time, the best prediction for it is its average, which is zero, thus:

$$\hat{\phi}_{k|k} = \mathcal{H}_{\infty} \mathbf{y}_k^{\text{PSO}}, \quad (4.62)$$

4. Atmospheric Turbulence Prediction

4.3. Linear-Quadratic-Gaussian Controller as Predictive Controller

$$\mathcal{H}_\infty = \Sigma_\phi \mathbf{C}^\top (\mathbf{C} \Sigma_\phi \mathbf{C}^\top + \Sigma_w)^{-1}. \quad (4.63)$$

Replacing the Kalman gain:

$$\hat{\phi}_{k|k} = \Sigma_\phi \mathbf{C}^\top (\mathbf{C} \Sigma_\phi \mathbf{C}^\top + \Sigma_w)^{-1} \mathbf{y}_k^{\text{PSO}}, \quad (4.64)$$

which is equivalent to the *MAP* phase reconstructor proposed by Wallner (1983). For the general case where the Kalman filter considers a temporal evolution model this reconstruction still takes place but it includes the temporal statistics of the phase and the iterative aspect, which helps increase its performance.

Remark

This analysis provides different insights. First, it shows that the Kalman filter works as a phase reconstructor. Second, it allows us to analyze the phase reconstructor within the Kalman filter separately using the *MAP* framework. Section 7.3.3 will discuss further the implications of this realization in the context of *LQG* applied to adaptive optics control.

4.3.4. Synthesis of the *LQG* Controller

The *LQG* controller runs a Kalman filter in parallel to the *LQR* controller, which allows to provide the estimate of the states and compute the control command using Equation 4.38 as:

$$\mathbf{u}_{k+1} = -\mathcal{K}_\infty \hat{\mathbf{x}}_{k+1|k}. \quad (4.65)$$

For the adaptive optics case, this has the form:

$$\mathbf{u}_{k+1} = -(\mathbf{N}^\top \mathbf{N})^{-1} \mathbf{N}^\top \hat{\phi}_{k+1|k}^{\text{tur}}. \quad (4.66)$$

Remark

Using the prediction of the phase $\hat{\phi}_{k+1|k}^{\text{tur}}$ allows to implement a predictive controller.

The *LQG* is optimal under the inherited assumptions from the *LQG* and the Kalman filter: the system state-space evolution and its measurements must be linear, the process and measurement noises need to be Gaussian, zero-mean, uncorrelated, and white.

4.3.5. Use of the *LQG* in Adaptive Optics

The first use of the *LQG* for adaptive optics was by Paschall and Anderson (1993). This work introduced the basic *LQG* structure, as presented above and a particular

way of identifying a turbulence evolution model. The two applications considered were predictive control and to account for the *DM* dynamics as later expanded by [Correia et al. \(2010\)](#).

The *LQG* has seen different applications in astronomy: as controller for the implementation of tomographic reconstructions, as vibration filter, and as predictive controller. [Kulcsár et al. \(2012\)](#) provides an overview of the use of the *LQG* in astronomy, while [Kulcsár et al. \(2017\)](#) contains a table with all the laboratory and on-sky demonstrations of *LQG* controllers in astronomical applications.

The will to increase the field of view in *AO* assisted astronomical observations, fostered research on phase reconstruction (modal or zonal) based on tomographic techniques. [Wallner \(1983\)](#) and [Fusco et al. \(2001\)](#) proposed static tomographic reconstructors that needed temporal filtering to achieve stable control loop. Until then, most *AO* control had been single-input single-output, either using a per actuator control or modal controllers (see Section 2.4.4). The tomographic reconstructors require multiple-input multiple-output control, so the use of the classical integral controllers was not possible. [Le Roux et al. \(2004\)](#) proposed the use of the *LQG* for the temporal filtering of tomographic reconstructors and [Petit et al. \(2009\)](#) developed it. [Costille et al. \(2010\)](#), [Parisot et al. \(2012\)](#), and [Sivo et al. \(2012\)](#) worked on the first laboratory demonstrations of tomographic methods using the *LQG* controller. No tomographic *LQG* has been demonstrated on-sky to this date.

[Petit et al. \(2006\)](#) suggested and demonstrated on-laboratory the use of vibration filtering using the *LQG*, followed by the on-sky demonstration of this method by [Sivo et al. \(2014\)](#). To this date, the only operational *LQG* are the vibration filtering controllers in the *SPHERE-SAXO* tip-tilt correction ([Petit et al. 2014](#)) and the *GPI* tip, tilt, and focus controller ([Poyneer et al. 2016](#)).

The work of [Massioni et al. \(2011\)](#) and [Gilles et al. \(2013\)](#) suggested schemes to take advantage of the sparse nature of the matrices involved in *LQG* controllers to optimize their computational needs so they can be used in bigger telescopes with thousands of states to be controlled.

4.3.6. Summary of the *LQG* Predictive Controller

In summary, the *LQG* predictive controller provides a minimum variance regulation of the controlled state for a stochastic linear system. It does so thanks to an optimal state feedback policy. Since the states of the system are only available via noisy measurements, it uses a Kalman filter to provide estimates of the states. The Kalman filter operates in two stages. In the first stage, once a measurement is available, it updates the state estimate with it, weighting it by the Kalman matrix gain. The second stage uses a predictive model to compute the optimal prediction of the future state based on all the measurements available until the present moment.

We have seen here that the *LQG* controller solves different problems related to the control of *AO* systems in the same algorithm:

1. It acts as a state (modal or zonal) reconstructor from slope measurements via a regularized inversion similar to the classical *MAP* reconstructor.
2. It acts as a predictive controller. It uses the previously reconstructed states to compute a prediction of turbulence at the time of applying the *deformable mirror (DM)* command.
3. It acts as an optimal gain strategy. The optimal gains for both the estimation and the control computation are optimally computed.

These are the same steps used in traditional *AO* control architectures but integrated with a unique (and optimal) algorithm.

* * *

Summary

This chapter has presented the problem of predictive control for adaptive optics. Every predictive controller requires the same main elements: (1) a predictive model and (2) a controller structure.

Linear predictive models are attractive because they offer a good trade-off between performance and ease of computation, identification, and analysis. Linear autoregressive models have been presented as the standard way of modeling and predicting linear processes. The use of vector autoregressive models allows accounting for the possible covariances between the different states and uses them to represent the turbulent wavefront. The Yule-Walker estimator was presented as a method to compute such a model from its spatio-temporal covariances. Finally, the assumption of frozen flow turbulence allows to compute these covariances from analytical formulas.

The *LQG* has been presented as the optimal controller for linear stochastic systems. The controller uses turbulence evolution models such as the autoregressive models discussed, or similar alternatives. The *LQG* does not only work as a predictive controller, it also solves other common *AO* problems such as optimizing the controller gain or the regularized reconstruction of phase from *WFS* measurements.

All of these elements will be used in the rest of this thesis. Chapter 5 will use the concepts of autoregressive processes as turbulence predictors and the computation of spatio-temporal covariance matrices to analyze the predictability of turbulence and the potential gains thanks to predictive controllers in the case of tracked satellite *AO* applications. One of these predictive models will then be used within a *LQG* controller as a predictive controller in Chapter 6.

Part II.

Predictive Controller

5. Assessment of Turbulence Predictability

Contents

5.1. <i>MMSE</i> Temporal Prediction	99
5.1.1. State of the Art	99
5.1.2. Linear <i>MMSE</i> Estimator	100
5.1.3. Temporal Prediction as a Linear Estimation Problem	101
5.1.4. Phase Representation	102
5.1.5. Prediction Error	102
5.1.6. No Prediction Error	104
5.1.7. Adaptive Optics Performance Assessment	104
5.1.8. <i>MMSE</i> vs. <i>VAR</i> Predictors	105
5.1.9. Data-based Version of the <i>MMSE</i> Predictor	106
5.2. Predictability of <i>LEO</i> Satellite <i>AO</i> Applications	106
5.2.1. Prediction Gain	107
5.2.2. Predictability	108
5.2.3. Effect of the Model Order	111
5.2.4. Results per Mode	113
5.2.5. Reduction of Loop Frequency	116
5.2.6. Performance on a Time Series	117
5.2.7. Effect of Unknown Natural Wind	119

Introduction

The framework introduced by Conan et al. (2023) for the computation of the performance boundaries of temporal predictive controllers is discussed. The spatio-temporal statistics of the optical turbulence are modeled in terms of the cross-covariance matrices of the Zernike polynomials. These spatio-temporal cross-covariances for the Zernike modes can be computed from analytical formulas for the case of frozen flow von Kármán turbulence by computing angular cross-covariances instead. The optimal linear estimator for the future state of turbulence, i.e. a predictor, is derived. The framework allows the pseudo-analytical evaluation of the performance of the optimal estimator and its comparison to other linear estimators.

5.1. MMSE Temporal Prediction

The adaptation of the *minimum mean square error* (*MMSE*) estimator for the case of temporal prediction suggested in Conan et al. (2023) is presented. The resulting estimator is the best possible linear predictor of the evolution of the turbulent phase. The optimality of the predictor allows the computation of upper performance boundaries for the turbulence prediction problem that can be extrapolated to *AO* system budgets and used to benchmark predictive control strategies.

The following section details the computation of a *minimum mean square error* (*MMSE*) estimator for temporal prediction. The classical *MMSE* estimator is first defined. In order to adapt the *MMSE* estimator to be a temporal predictor, the future phase is defined as the estimated parameter and a set of phase measurements are the observations used for the estimation.

5.1.1. State of the Art

There exist some previous attempts to assess the predictability of atmospheric turbulence and possible gains in *AO* performance thanks to predictive controllers. Aitken and McGaughey (1995) conducted a statistical analysis of Shack-Hartmann slopes to characterize the predictability of turbulence in an astronomical application and reported a "useful degree of predictability in the wavefront time series" that could be exploited to reduce the temporal bandwidth requirements of adaptive optics systems.

Doelman (2020) extended the classical frequency domain analysis of temporal error for integral action (Fried 1990; Harrington and Welsh 1994) but using an optimal prediction filter as the controller transfer function and provided prediction boundaries. Nevertheless, this analysis is conducted for a unique point in the pupil. This is equivalent to a diagonal *AR* (zonal) model for each point in an extended pupil. As has been shown in the literature before, for zonal predictive models, the

use of the correlation between several points, i.e. a *VAR* model brings additional advantages (Jackson et al. 2015).

Vogel et al. (2014) propose a method for spatio-temporal covariance based modeling and analysis of wavefront aberrations. They use a zonal basis for the representation of turbulence. The covariance matrices are computed from Shack-Hartman *WFS* measurements after reconstruction of the phase from the slope space. They use the covariance matrices to compute a first-order *VAR* model of the evolution of turbulence with an approach similar to the one described in Section 4.2.3. This method shares some similarities with the method proposed here, since it uses a spatio-temporal covariance matrix approach. However, the method is limited to a first-order *VAR* model; we prove here that the use of higher-order modes provides a significant improvement for the representation of turbulence evolution and its prediction.

Whiteley et al. (1998a) and Correia et al. (2014) already used the temporal properties of turbulence projected on Zernike polynomials. Nevertheless, the framework was limited to first-order models and was not applied for analysis of the predictability of turbulence, but for the development of predictive controllers.

5.1.2. Linear MMSE Estimator

First, consider the following measurement equation:

$$\mathbf{y} = \mathbf{D}\mathbf{x}, \quad (5.1)$$

where \mathbf{y} is a measurement vector, \mathbf{D} is a linear measurement model, and \mathbf{x} is a state vector of the measured system.

Remark

Since the aim is to provide upper boundaries in prediction performance the measurements are assumed to be noiseless. A similar estimator can be derived in the case of noisy measurements (see Appendix B.2). This extension allows both to account for the presence of measurement noise in the analysis and to compute an estimator that minimizes the noise propagation.

The goal is to find a linear estimator \mathbf{R} that produces an optimal estimate $\hat{\mathbf{x}}$ of \mathbf{x} given the measurement vector \mathbf{y} :

$$\hat{\mathbf{x}} = \mathbf{R}\mathbf{y}. \quad (5.2)$$

To define the optimality criterion, we define the estimation error, $\tilde{\mathbf{x}}$, given by:

$$\tilde{\mathbf{x}} = \mathbf{x} - \hat{\mathbf{x}}. \quad (5.3)$$

The *mean square error* (*MSE*) of the estimator can be written as:

$$\boxed{\text{MSE} = \text{Tr}(\mathbb{E}\{\tilde{\mathbf{x}}\tilde{\mathbf{x}}^\top\}) = \text{Tr}\left(\mathbb{E}\left\{(\mathbf{x} - \hat{\mathbf{x}})(\mathbf{x} - \hat{\mathbf{x}})^\top\right\}\right)}. \quad (5.4)$$

The *MMSE* is the optimal estimator in terms of *MSE* that solves the following estimation problem:

$$\min_{\hat{\mathbf{x}}} \text{MSE} \quad \text{s.t.} \quad \hat{\mathbf{x}}_{\text{MMSE}} = \mathbf{R}_{\text{MMSE}} \mathbf{y}. \quad (5.5)$$

Assuming that both \mathbf{x} and \mathbf{y} are zero mean random processes, the case for turbulent phase, the solution for this estimator (see Appendix B.1) is:

$$\boxed{\mathbf{R}_{\text{MMSE}} = \Sigma_{\mathbf{x}\mathbf{y}} \Sigma_{\mathbf{y}\mathbf{y}}^{-1}}, \quad (5.6)$$

where $\Sigma_{\mathbf{x}\mathbf{y}}$ and $\Sigma_{\mathbf{y}\mathbf{y}}$ are cross-covariance matrices as defined in Appendix A.1.

5.1.3. Temporal Prediction as a Linear Estimation Problem

Linear optimal estimators can be used for turbulence prediction under the assumption that the turbulence evolution is given by a linear model similar to a vector autoregressive process:

$$\phi_{k+1} = \mathbf{A}_1 \phi_k + \mathbf{A}_2 \phi_{k-1} + \dots + \mathbf{A}_n \phi_{k-p'-1} + \mathbf{v}_k, \quad (5.7)$$

where p' is unknown.

Remark

Regardless of whether the theory of autoregressive processes is used or not, all approaches considering prediction as a linear estimation problem assume this kind of underlying model.

The aim here is not to identify an autoregressive model but to compute an estimator that will estimate the ϕ_{k+s} value of the time series. The *MMSE* estimator can be used as an optimal temporal predictor by choosing the estimated vector to be the future state of turbulence:

$$\mathbf{x} = \begin{bmatrix} \phi_{k+s} \end{bmatrix} \quad (5.8)$$

and the measurement vector the concatenation of the last p phase measurements:

$$\mathbf{y} = \begin{bmatrix} \phi_k \\ \phi_{k-1} \\ \vdots \\ \phi_{k-p-1} \end{bmatrix}. \quad (5.9)$$

We introduce the notation $\mathbf{R}_{\text{MMSE}}^{(s,p)}$ for an estimator computed for s -step-ahead in time and p measurements using Equation 5.6 so that:

$$\mathbf{R}_{\text{MMSE}}^{(s,p)} = \mathbb{E} \left\{ \begin{bmatrix} \phi_{k+s} \\ \vdots \\ \phi_{k-p-1} \end{bmatrix} \begin{bmatrix} \phi_k \\ \phi_{k-1} \\ \vdots \\ \phi_{k-p-1} \end{bmatrix}^\top \right\} \mathbb{E} \left\{ \begin{bmatrix} \phi_k \\ \phi_{k-1} \\ \vdots \\ \phi_{k-p-1} \end{bmatrix} \begin{bmatrix} \phi_k \\ \phi_{k-1} \\ \vdots \\ \phi_{k-p-1} \end{bmatrix}^\top \right\}^{-1} \quad (5.10)$$

The resulting predictor is the optimal predictor for the turbulence states considered in the vector ϕ when using a given number of previous measurements p . The value of p for which prediction is enough will be the subject of study in the forthcoming sections.

5.1.4. Phase Representation

So far, the predictor has been derived in its more general form, without assuming any basis for the representation of the phase vectors within \mathbf{x} and \mathbf{y} . In principle, they can be defined on a zonal basis or on any modal basis as discussed in Section 1.3. The pros and cons of the different bases discussed for autoregressive models (see Section 4.2.5) also apply here. For the use of the *MMSE* predictor as an analytical tool for the upper prediction boundaries, it is assumed that both vectors are expressed in the Zernike polynomial basis to allow the analytical evaluation of the cross-covariance matrices. The computation of these matrices is detailed in Section 4.2.5.2. Other bases can be used if the spatio-temporal covariance matrices are available, either from analytical expressions or from data-based identification.

5.1.5. Prediction Error

The previous sections introduced the use of the *MMSE* estimator as an optimal predictor for the evolution of turbulence. This predictor depends on the spatio-temporal cross-covariance matrices between turbulence phases at different points in time. This section derives the matrix expression for the computation of the estimation error variance for a given linear estimator (*MMSE* or not) and the cross-covariance matrices of the estimated variables. In the case of prediction, this expression is equivalent to the prediction error variance and can be computed with the spatio-temporal cross-covariance matrices for the underlying process.

The estimation error is expressed by Equation 5.3. Inserting an arbitrary linear estimator $\hat{\mathbf{x}} = \mathbf{R}\mathbf{y}$ in Equation 5.3:

$$\tilde{\mathbf{x}} = \mathbf{x} - \mathbf{R}\mathbf{y}. \quad (5.11)$$

The variance of the prediction error is given by the trace of the covariance matrix of the prediction error. First, the covariance matrix is computed from Equation 5.11:

$$\Sigma_{\tilde{\mathbf{x}}\tilde{\mathbf{x}}} = \mathbb{E}\{\tilde{\mathbf{x}}\tilde{\mathbf{x}}^\top\} = \mathbb{E}\{(\mathbf{x} - \mathbf{R}\mathbf{y})(\mathbf{x} - \mathbf{R}\mathbf{y})^\top\}. \quad (5.12)$$

Developing the product:

$$\Sigma_{\tilde{\mathbf{x}}\tilde{\mathbf{x}}} = \mathbb{E}\{\mathbf{x}\mathbf{x}^\top - \mathbf{R}\mathbf{y}\mathbf{x}^\top - \mathbf{x}\mathbf{y}^\top\mathbf{R}^\top + \mathbf{R}\mathbf{y}\mathbf{y}^\top\mathbf{R}^\top\}. \quad (5.13)$$

Simplifying the expected value of the sum as the sum of the expected values:

$$\Sigma_{\tilde{\mathbf{x}}\tilde{\mathbf{x}}} = \mathbb{E}\{\mathbf{x}\mathbf{x}^\top\} - \mathbb{E}\{\mathbf{R}\mathbf{y}\mathbf{x}^\top\} - \mathbb{E}\{\mathbf{x}\mathbf{y}^\top\mathbf{R}^\top\} + \mathbb{E}\{\mathbf{R}\mathbf{y}\mathbf{y}^\top\mathbf{R}^\top\}. \quad (5.14)$$

Taking the linear estimator out of the expected value since it is constant:

$$\Sigma_{\tilde{\mathbf{x}}\tilde{\mathbf{x}}} = \mathbb{E}\{\mathbf{x}\mathbf{x}^\top\} - \mathbf{R}\mathbb{E}\{\mathbf{y}\mathbf{x}^\top\} + \mathbb{E}\{\mathbf{x}\mathbf{y}^\top\}\mathbf{R}^\top - \mathbf{R}\mathbb{E}\{\mathbf{y}\mathbf{y}^\top\}\mathbf{R}^\top. \quad (5.15)$$

Using the definition of the cross-covariance matrix:

$$\Sigma_{\tilde{\mathbf{x}}\tilde{\mathbf{x}}} = \Sigma_{\mathbf{x}\mathbf{x}} - \mathbf{R}\Sigma_{\mathbf{y}\mathbf{x}} - \Sigma_{\mathbf{x}\mathbf{y}}\mathbf{R}^\top + \mathbf{R}\Sigma_{\mathbf{y}\mathbf{y}}\mathbf{R}^\top. \quad (5.16)$$

Finally, using the identity $\Sigma_{\mathbf{y}\mathbf{x}} = \Sigma_{\mathbf{x}\mathbf{y}}^\top$:

$$\boxed{\Sigma_{\tilde{\mathbf{x}}\tilde{\mathbf{x}}} = \Sigma_{\mathbf{x}\mathbf{x}} - \mathbf{R}\Sigma_{\mathbf{x}\mathbf{y}}^\top - \Sigma_{\mathbf{x}\mathbf{y}}\mathbf{R}^\top + \mathbf{R}\Sigma_{\mathbf{y}\mathbf{y}}\mathbf{R}^\top}. \quad (5.17)$$

The estimation error variance, σ_{est}^2 , is thus:

$$\sigma_{\text{est}}^2 = \text{Tr}(\Sigma_{\tilde{\mathbf{x}}\tilde{\mathbf{x}}}). \quad (5.18)$$

The formula computes the estimation error variance of \mathbf{x} using any linear estimator \mathbf{R} and the measurements \mathbf{y} . For the phase temporal prediction setup presented in Section 5.1.3 we define $\mathbf{x} = \phi_{k+s}$, so that the estimation error is:

$$\tilde{\mathbf{x}} = \phi_{k+s} - \hat{\phi}_{k+s}. \quad (5.19)$$

Equation 5.17 can be used to compute the phase temporal prediction error covariance matrix of the wavefront at s steps ahead using the last p measurements of the wavefront.

Remark

The prediction error can be used to evaluate the linear prediction performance bound when using $\mathbf{R} = \mathbf{R}_{\text{MMSE}}$ or to compare the performance of the optimal predictor to other alternative predictors.

5.1.6. No Prediction Error

It is also possible to compare the *MMSE* predictor and other predictors to the case of *no prediction* (*NP*), which assumes that the turbulence did not evolve during the time elapsed between the last measurement available and the time to be predicted:

$$\hat{\phi}_{k+s}^{\text{NP}} = \phi_k. \quad (5.20)$$

This approach can be compared to a simplified control loop in the presence of delay, although in a true loop, the measurement will be filtered by the transfer function of the controller (Ferreira et al. 2018; Juvénal et al. 2018).

The prediction error of this predictor can be computed using Equation 5.17 with the covariance matrices computed for $\mathbf{x} = \phi_{k+s}$ and $\mathbf{y} = \phi_k$ and writing this predictor in matrix form as:

$$\boxed{\mathbf{R}_{\text{NP}} = \mathbb{I}}, \quad (5.21)$$

where \mathbb{I} is the identity matrix.

5.1.7. Adaptive Optics Performance Assessment

The framework developed above is used to assess the potential gain in adaptive optics performance thanks to the use of prediction. This assessment is done in terms of the predictability of the phase and is therefore equivalent to a simplified *AO* loop under the following assumptions:

1. The wavefront sensor can perfectly measure the basis selected for the phase representation and do it without noise
2. The deformable mirror can fit the same basis without any error
3. The control strategy is based on the application of the prediction without any temporal filtering by a control transfer function (in practice necessary due to the presence of noise and delay in the feedback loop). As a result of these simplifications, the performance results of this assessment are optimistic, but remain a good approximation.
4. The measurements of the system correspond to the open-loop (usually thanks to pseudo-open-loop) turbulent phase.

A two-frame delay loop is considered, therefore, a two-step ahead, $s = 2$, prediction is used. The baseline *AO* temporal error is computed using the no-prediction predictor. The residual temporal error after prediction is computed as the prediction error for the *MMSE* predictor. In both cases, the phase is predicted only for the radial orders which the analyzed system can correct with a *DM*. The higher orders are purely fitting error and are not part of the analysis.

5.1.8. MMSE vs. VAR Predictors

Two different predictors have been presented so far: the VAR(p) model and the MMSE estimator. Both methods assume an underlying autoregressive linear model as defined in Equation 5.7 and both are optimal regarding a MSE criterion. In the present section, a comparison of the two methods is provided.

The first observation is that for the case of $s = 1$ the MMSE estimator $\mathbf{R}_{\text{MMSE}}^{(1,p)}$ is equivalent to a VAR(p) model computed with Equation 4.19. This result was already presented in Property 4.5, which states that the optimal linear predictor for a VAR(p) process in terms of MSE is the process itself, while the process can be computed from its autocovariance matrices using the Yule-Walker estimator as in Equation 4.19.

In order to rewrite the MMSE predictor so that it can be iterated as the VAR predictor, we extend the vector \mathbf{x} firstly defined in Equation 5.8 as:

$$\mathbf{x} = \begin{bmatrix} \phi_{k+s} \\ \phi_{k+s-1} \\ \vdots \\ \phi_{k+s-p-1} \end{bmatrix}. \quad (5.22)$$

In this case, the resulting predictor $\mathbf{R}_{\text{MMSE}}^{(s,p)}$ is a square matrix that can be applied iteratively.

As a result, the MMSE predictor for $s = 1$ is equivalent to a VAR model of the same order p :

$$\mathbf{A}_{\text{VAR}(1)}^{(p)} = \mathbf{R}_{\text{MMSE}}^{(1,p)}. \quad (5.23)$$

The difference between the methods appears when a prediction horizon of $s > 1$ is considered. The VAR process prediction is a power of itself as introduced in Equation 4.12, something similar can be also achieved with the MMSE solution:

$$\left(\mathbf{A}_{\text{VAR}(1)}^{(p)}\right)^s = \left(\mathbf{R}_{\text{MMSE}}^{(1,p)}\right)^s = \mathbf{R}_{\text{MMSE}}^{(1,p,s)}, \quad (5.24)$$

where $\mathbf{R}_{\text{MMSE}}^{(1,p,l)} = \left(\mathbf{R}_{\text{MMSE}}^{(1,p)}\right)^l$, for any integer $l > 0$.

Remark

In general, $\mathbf{R}_{\text{MMSE}}^{(1,p,l=s)}$ is not equal to $\mathbf{R}_{\text{MMSE}}^{(s,p)}$. The former is the iterative application of the 1-step-ahead predictor; the latter is the optimal s -step-ahead predictor. They are only equal when the underlying process is a VAR(p) process and Property 4.5 is satisfied. Otherwise, the iterative application will be suboptimal and have lower performance.

When approximated by a linear autoregressive process, the real underlying

process to be predicted has an unknown order p' . For a given model order p , the resulting *VAR* predictor $\mathbf{R}_{\text{MMSE}}^{(1,p,s)}$ contains $p + 1$ autocovariance matrices, while the *MMSE* predictor $\mathbf{R}_{\text{MMSE}}^{(s,p)}$ contains $p + s$ autocovariance matrices. As a result, the latter contains more information and obtains better prediction performance. Only when the underlying process is a *VAR* process with $p' = p$ both predictors are equivalent since the autocovariances for $\tau > p + 1$ depend on the covariances for $\tau \leq p + 1$ and are therefore redundant (see Property 4.4).

In this work, $\mathbf{R}_{\text{MMSE}}^{(s,p)}$ predictors are used for the assessment of the maximum prediction possible with adaptive optics. Nevertheless, even if suboptimal, the *VAR* models equivalent to a $\mathbf{R}_{\text{MMSE}}^{(1,p,l=s)}$ predictor will be used for the implementation within *LQG* controllers as state space models since they are guaranteed to produce a stable process.

5.1.9. Data-based Version of the *MMSE* Predictor

A data-based version of the *MMSE* predictor can be obtained by estimating the covariance matrices required for its computation. For this, the simplest method is to use the sample covariance matrix as discussed in Equation 4.34. See also the discussion on the data-based identification of *VAR* models in Section 4.2.5.3 for further discussion on the identification of the cross-covariances.

5.2. Predictability of LEO Satellite AO Applications

The following section applies the predictability assessment method based on the *MMSE* estimator presented above to the case of *LEO* satellite *AO* applications. The aim of this analysis is to quantify the possible reduction of temporal error in these applications, thanks to the use of predictive controllers. The analysis presented also allows to observe and explain the different performance gains depending on the *AO* system parameters for each of the systems considered.

The four systems presented in Chapter 3 are used as a case study. The systems are modeled as perfect measurement and correction of the first n_{max} Zernike polynomial radial orders. For the *LISA* and *ODISSEE* systems, both with an 8×8 subapertures Shack-Hartmann wavefront sensor, a $n_{\text{max}} = 10$ is used, corresponding to the first 65 Zernike polynomials in Noll ordering after removing the piston mode. For the *FEELINGS* and *ODISSEE++* systems, both with an 16×16 subapertures Shack-Hartmann wavefront sensor a $n_{\text{max}} = 20$ is used, corresponding to 230 Zernike polynomials. The turbulence profiles are those assigned to each configuration in Section 3.2.1.

5.2.1. Prediction Gain

Table 5.1 reports the results of the use of the predictability assessment for the four systems considered across all elevation angles for the turbulence profile considered. The reported results are the sum of the prediction errors over all the Zernike modes considered. Those errors correspond to the residual phase variance of the wavefront for each of the corrected modes due to a two frame delay between measurement and correction. The present analysis does not include aliasing and measurement noise errors. The fitting error is also not considered here since only the corrected modes are analyzed.

Three predictors are considered: (1) $\mathbf{R}_{\text{MMSE}}^{(s=2,p=0)}$, the no-prediction case from Section 5.1.6; (2) $\mathbf{R}_{\text{MMSE}}^{(s=2,p=2)}$ the *MMSE* predictor using two measurements from the past, and (3) $\mathbf{R}_{\text{MMSE}}^{(s=2,p=8)}$ *MMSE* predictor using eight measurements from the past. The choice of $p = 2$ and $p = 8$ will be better understood after Section 5.2.3, so far they should be considered as "good enough" and "best performance" predictors, respectively.

The gain of both predictors with respect to the no-prediction case is reported in the same table as the percentage of prediction error variance with respect to the no-prediction variance:

$$\text{gain (\%)} = \frac{\text{residual phase variance for } \mathbf{R}_{\text{MMSE}}^{(s=2,p)}}{\text{residual phase variance for } \mathbf{R}_{\text{MMSE}}^{(s=2,p=0)}} \times 100. \quad (5.25)$$

Lower percentage means more reduction of residual variance and thus better prediction.

Several observations about the results are possible:

- The performance gains are considerable. In most of the cases, the phase variance is reduced by an order of magnitude.
- The performance gains seem to be consistent across the whole orbit in relative terms when expressed in variance.
- The *LISA* configuration presents less relative gain, around 25% of the no-prediction variance, than the other configurations, around 10%.

In general, prediction allows to reduce the temporal error significantly. However, the impact of this reduction on the final system performance will depend on the other elements of the *AO* budget. For example, the Strehl ratio (see Equation 3.6) is the negative exponential of the residual phase variance. The *ODISSEE* and the *ODISSEE++* have similar prediction errors, but since the former has a higher fitting, the later will end up having a better performance. The same happens at lower elevations, where the prediction error is higher. Even if there was no fitting error and the relative gains in phase variance are the same at all elevations, the final performance will be very different due to the non-linear relationship between Strehl

ratio and residual phase variance. For both the *LISA* and the *FEELINGS* cases, the chosen profile does not have a strong temporal error even with no-prediction, so the effect of prediction will be weaker when looking at final performance metrics such as Strehl ratio. The lower temporal error for the optical communication systems is due to the profile selected for this study, the day-time turbulence is concentrated at the ground, the apparent wind speed is slower at the lower layers, leading to less temporal error than for a profile with equivalent r_0 but with turbulence located at the higher layers. Additionally, the *FEELINGS* system has a loop sampling frequency of 4 kHz, therefore temporal error is already greatly reduced. As a result, the rest of the discussion on this study will be in terms of residual phase variance, see Chapter 7 for an analysis of the final system performance in terms of Strehl ratio or coupled flux thanks to the use of end-to-end adaptive optics simulations.

The smaller prediction gains for the *LISA* case are explained in Section 5.2.2, where the relationship between predictability and the temporal decorrelation of the predicted modes is illustrated.

5.2.2. Predictability

This section aims to discuss the predictability of different *AO* configurations. Predictability is measured by the percentage of prediction error variance with respect to the no-prediction variance; see Equation 5.25. Lower percentage means greater reduction of residual variance and, thus, better prediction.

Predictability is related to the temporal (de)-correlation between the future phase and the phase measurements used for prediction. As a result, several remarks are possible thanks to the *AO* systems parameters in the temporal correlation of the observed turbulence and the resulting predictability:

- Faster layers have lower predictability since the temporal decorrelation of phase is higher. However, their contribution to temporal error is greater, so even if a lower portion of the temporal error can be reduced by prediction, the absolute gains may be higher.
- Smaller telescope diameters lead to more temporal decorrelation and therefore less predictability too.
- The systems with faster sampling frequency are more predictable since this is equivalent to slower layer speed, so measurements are more correlated.
- The outer scale of the turbulence could also have an effect on the predictability of turbulence.

5. Assessment of Turbulence Predictability
5.2. Predictability of LEO Satellite AO Applications

Table 5.1.: Prediction gains for all AO configurations vs. elevation. Residual phase variance (in rad²) over the corrected modes.

	Elevation	$\mathbf{R}_{\text{MMSE}}^{(s=2,p=0)}$	$\mathbf{R}_{\text{MMSE}}^{(s=2,p=2)}$	Gain (%)	$\mathbf{R}_{\text{MMSE}}^{(s=2,p=8)}$	Gain (%)
<i>LISA</i>	10°	$5.326 \cdot 10^{-1}$	$1.568 \cdot 10^{-1}$	29.44	$1.428 \cdot 10^{-1}$	26.81
	20°	$2.214 \cdot 10^{-1}$	$5.367 \cdot 10^{-2}$	24.24	$4.857 \cdot 10^{-2}$	21.93
	30°	$1.571 \cdot 10^{-1}$	$3.866 \cdot 10^{-2}$	24.61	$3.502 \cdot 10^{-2}$	22.29
	40°	$1.344 \cdot 10^{-1}$	$3.565 \cdot 10^{-2}$	26.52	$3.221 \cdot 10^{-2}$	23.96
	50°	$1.240 \cdot 10^{-1}$	$3.556 \cdot 10^{-2}$	28.67	$3.205 \cdot 10^{-2}$	25.84
	60°	$1.189 \cdot 10^{-1}$	$3.644 \cdot 10^{-2}$	30.66	$3.296 \cdot 10^{-2}$	27.73
	70°	$1.160 \cdot 10^{-1}$	$3.744 \cdot 10^{-2}$	32.27	$3.387 \cdot 10^{-2}$	29.20
	80°	$1.145 \cdot 10^{-1}$	$3.815 \cdot 10^{-2}$	33.32	$3.450 \cdot 10^{-2}$	30.13
	90°	$1.140 \cdot 10^{-1}$	$3.840 \cdot 10^{-2}$	33.67	$3.472 \cdot 10^{-2}$	30.45
<i>FEELINGS</i>	10°	$2.204 \cdot 10^{-1}$	$2.736 \cdot 10^{-2}$	12.41	$2.193 \cdot 10^{-2}$	9.95
	20°	$8.436 \cdot 10^{-2}$	$9.942 \cdot 10^{-3}$	11.79	$7.749 \cdot 10^{-3}$	9.19
	30°	$6.043 \cdot 10^{-2}$	$7.151 \cdot 10^{-3}$	11.83	$5.560 \cdot 10^{-3}$	9.20
	40°	$5.334 \cdot 10^{-2}$	$6.342 \cdot 10^{-3}$	11.89	$4.982 \cdot 10^{-3}$	9.34
	50°	$5.084 \cdot 10^{-2}$	$6.226 \cdot 10^{-3}$	12.25	$4.872 \cdot 10^{-3}$	9.58
	60°	$5.011 \cdot 10^{-2}$	$6.229 \cdot 10^{-3}$	12.43	$4.922 \cdot 10^{-3}$	9.82
	70°	$4.991 \cdot 10^{-2}$	$6.242 \cdot 10^{-3}$	12.51	$4.968 \cdot 10^{-3}$	9.95
	80°	$4.989 \cdot 10^{-2}$	$6.319 \cdot 10^{-3}$	12.67	$5.043 \cdot 10^{-3}$	10.11
	90°	$4.990 \cdot 10^{-2}$	$6.352 \cdot 10^{-3}$	12.73	$5.071 \cdot 10^{-3}$	10.16
<i>ODISSEE</i>	10°	2.137	$2.173 \cdot 10^{-1}$	10.17	$1.513 \cdot 10^{-1}$	7.08
	20°	$7.859 \cdot 10^{-1}$	$6.916 \cdot 10^{-2}$	8.80	$4.812 \cdot 10^{-2}$	6.12
	30°	$5.638 \cdot 10^{-1}$	$5.088 \cdot 10^{-2}$	9.02	$3.516 \cdot 10^{-2}$	6.24
	40°	$5.053 \cdot 10^{-1}$	$4.743 \cdot 10^{-2}$	9.39	$3.310 \cdot 10^{-2}$	6.55
	50°	$4.904 \cdot 10^{-1}$	$4.902 \cdot 10^{-2}$	9.99	$3.406 \cdot 10^{-2}$	6.94
	60°	$4.893 \cdot 10^{-1}$	$5.139 \cdot 10^{-2}$	10.50	$3.583 \cdot 10^{-2}$	7.32
	70°	$4.918 \cdot 10^{-1}$	$5.416 \cdot 10^{-2}$	11.01	$3.779 \cdot 10^{-2}$	7.68
	80°	$4.941 \cdot 10^{-1}$	$5.602 \cdot 10^{-2}$	11.34	$3.901 \cdot 10^{-2}$	7.89
	90°	$4.943 \cdot 10^{-1}$	$5.654 \cdot 10^{-2}$	11.44	$3.938 \cdot 10^{-2}$	7.97
<i>ODISSEE++</i>	10°	2.486	$2.956 \cdot 10^{-1}$	11.89	$1.793 \cdot 10^{-1}$	7.21
	20°	$9.558 \cdot 10^{-1}$	$9.665 \cdot 10^{-2}$	10.11	$5.889 \cdot 10^{-2}$	6.16
	30°	$6.824 \cdot 10^{-1}$	$7.085 \cdot 10^{-2}$	10.38	$4.279 \cdot 10^{-2}$	6.27
	40°	$6.012 \cdot 10^{-1}$	$6.553 \cdot 10^{-2}$	10.90	$3.975 \cdot 10^{-2}$	6.61
	50°	$5.733 \cdot 10^{-1}$	$6.670 \cdot 10^{-2}$	11.63	$4.031 \cdot 10^{-2}$	7.03
	60°	$5.636 \cdot 10^{-1}$	$6.882 \cdot 10^{-2}$	12.21	$4.176 \cdot 10^{-2}$	7.41
	70°	$5.606 \cdot 10^{-1}$	$7.141 \cdot 10^{-2}$	12.74	$4.360 \cdot 10^{-2}$	7.78
	80°	$5.598 \cdot 10^{-1}$	$7.303 \cdot 10^{-2}$	13.05	$4.460 \cdot 10^{-2}$	7.97
	90°	$5.588 \cdot 10^{-1}$	$7.335 \cdot 10^{-2}$	13.13	$4.487 \cdot 10^{-2}$	8.03

Remark

The observations above correspond to one layer of turbulence. The contribution of each layer is weighted by its strength in terms of C_n^2 . For LEO satellite applications, the higher layers are faster due to the higher apparent wind; while their relative strength will depend on the time of the day, being higher during the night and lower during the day, when the ground layer is stronger.

Figure 5.1 confirms the previous remarks with one example. Figure 5.1a reports the predictability for $n_{\max} = 10$ Zernike radial orders, with $\lambda = 1.55 \mu\text{m}$, $L_0 = 10 \text{ m}$, and 30° elevation using different aperture diameters, two sampling frequencies, and two turbulence profiles. It can be observed how an increase of the aperture diameter leads to an improvement in the prediction of turbulence, the same happens with the sampling frequency. This explains why the LISA case shows a lower prediction gain than the order systems since its diameter is smaller. At the same time, smaller telescope diameters are of less interest for AO applications since the absolute effect of turbulence is smaller.

Figure 5.1b completes the study with the effect of changing the outer scale of turbulence. In this case, the outer scale does not show any effect on the predictability of turbulence.

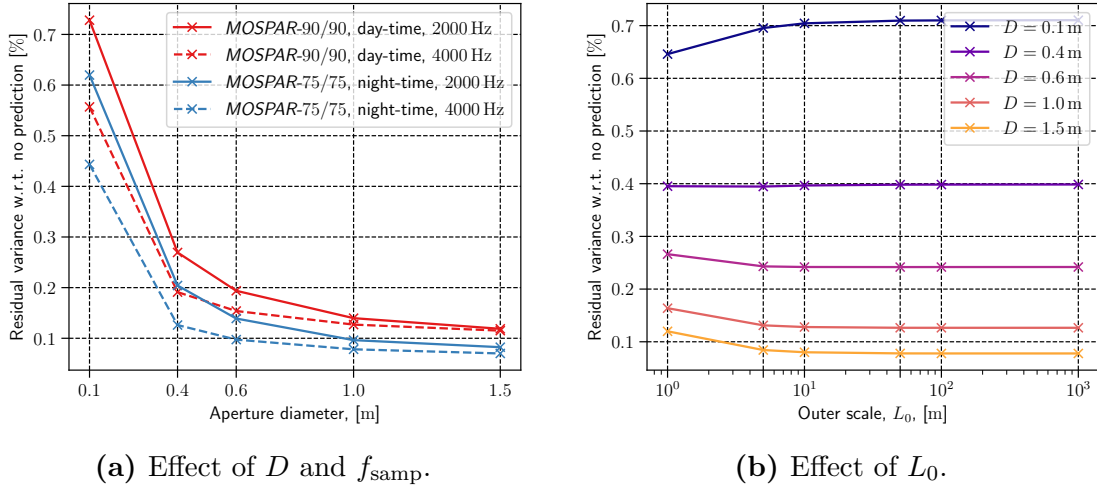


Figure 5.1.: Predictability for different AO system parameters that influence the temporal correlation of turbulence. Three parameters are considered: (a) the diameter of the telescope and the sampling frequency of the AO loop, and (b) the outer scale of the turbulence. The y-axis of the graphs is defined in Equation 5.25, but without multiplying by hundred.

5.2.3. Effect of the Model Order

Figure 5.2 plots the prediction error results vs. the model order considered for the four *AO* systems considered. Three different predictors are considered: the *MMSE* predictor $\mathbf{R}_{\text{MMSE}}^{(s=2,p)}$, the *VAR* predictor $\mathbf{R}_{\text{MMSE}}^{(s=1,p,l=2)}$, and the diagonal *AR* predictor $\mathbf{R}_{\text{MMSE}}^{(s=1,p,l=2)}$. The latter is computed as the *VAR* but with extra-diagonal terms in the autocovariance matrices set to zero. The comparison of the two first predictors allows to evaluate if their performance is similar; this is necessary since only the second (which is suboptimal) leads to a stable model that can be used within a predictive controller. The comparison between the *VAR* and the diagonal *AR* since many works in the literature have used diagonal models, which are computationally less expensive; this comparison allows to evaluate the performance loss when using diagonal models. Table 5.2 reports the results for the $\mathbf{R}_{\text{MMSE}}^{(s=2,p)}$ predictor.

Although the *MMSE* predictor has a better performance than the *VAR* predictor the difference is negligible. This result ensures that the use of a *VAR* predictive model within a predictive controller will provide near-optimal performance.

For all predictors, the performance improves when increasing the model order. This is thanks to the fact that increasing the model order will include more autocovariances of the process in the predictor. There is an important gain in performance when using $p = 2$ and the gains are less important after. This result shows that using at least a second-order model is necessary for predicting frozen flow. This contrasts with the typical Markovian (i.e. first order) assumption in astronomy cases (Gavel and Wiberg 2003; Correia et al. 2014). Other works, for example, Prengère et al. (2020) but using a zonal phase representation, have used second-order systems and observed better performance, but this kind of pseudo-analytical result is a demonstration of the need for at least second-order models for representing frozen flow turbulence. This finding may also be extrapolated to controllers working on zonal and slope spaces, although a theoretical framework for this space is not available at the moment.

Remark

The *MMSE* solutions are optimal for the data they are given. As explained in Section 5.1.8, the $\mathbf{R}_{\text{MMSE}}^{(s=2,p)}$ contains information on the temporal autocovariances from $\tau = 0$ to $\tau = p + 2$, since temporal information is considered for higher-orders those tend to have better predictive performance.

Due to the convergence in performance gains for a given model order p , the computational cost of the model can be reduced by limiting it to a second order without losing a lot of performance, at least in the case of frozen flow turbulence. This convergence is not always as strong, especially for the bigger systems (*FEELINGS* and *ODISSEE++*), where the performance continues to improve considerably for higher orders.

When the *AR* model is compared to the *VAR* it is clear that the performance

5. Assessment of Turbulence Predictability
 5.2. Predictability of LEO Satellite AO Applications

is degraded. This shows how accounting for the cross-covariance terms between modes brings a great gain in performance. Jackson et al. (2015) did an experiment for which zonal VAR(1) was compared with also zonal AR(1), AR(2), and AR(3). The experiment was conducted for astronomy cases where layer speeds are not as strong. They found that VAR(1) always provided better performance, but this is not the case for the configurations studied in this work. For the diagonal AR models the performance seems to converge for $p = 3$.

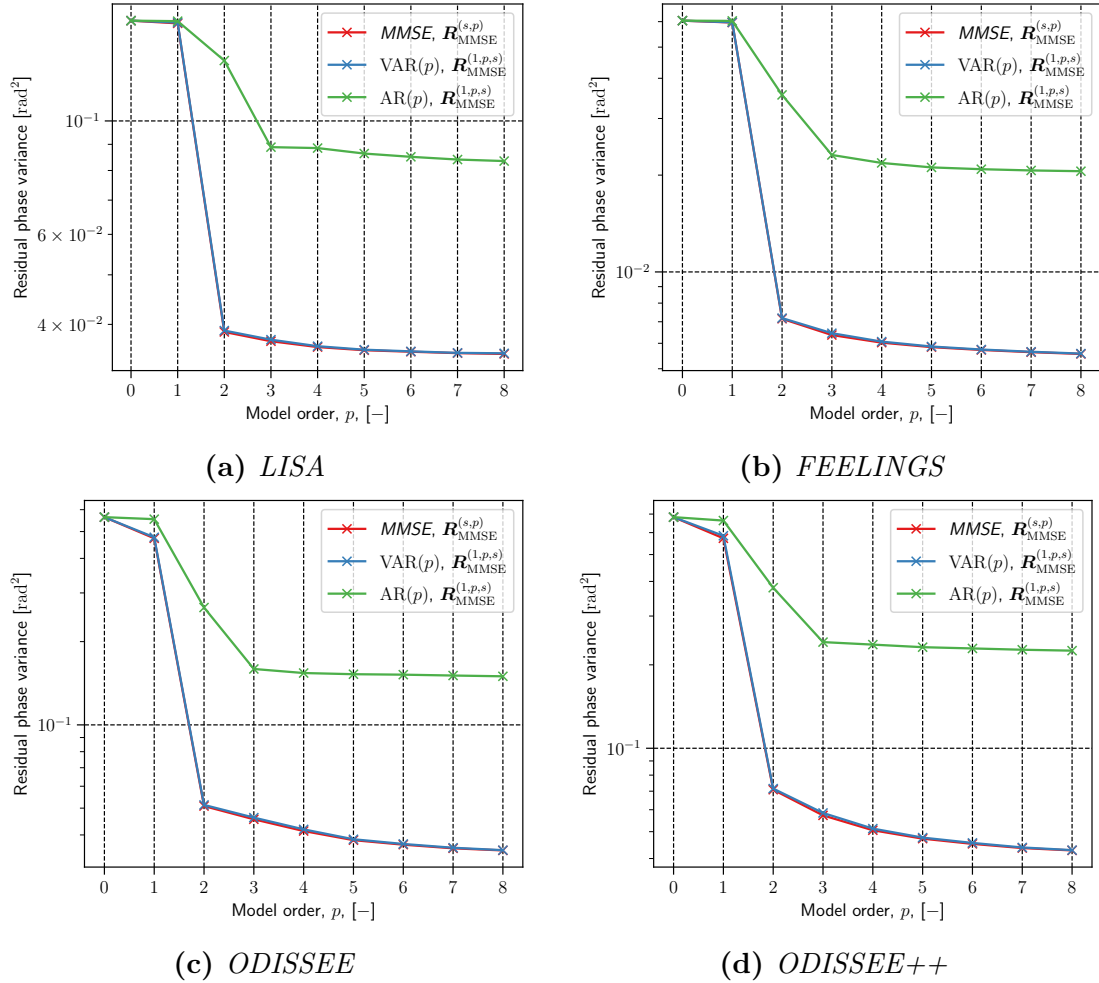


Figure 5.2.: Prediction performance vs. model order for different predictors. The performance of different predictors is compared for three models: (1) the *MMSE* predictor, (2) the *VAR* predictor, and (3) the diagonal *AR* predictor. The models are computed for different model orders, i.e. different number of previous measurements used to compute the prediction. The results are reported for the four *AO* systems considered.

Table 5.2.: Performance of the $\mathbf{R}_{\text{MMSE}}^{(s=2,p)}$ predictor for different model orders. Results are given in variance of the residual phase with units rad^2 .

		$p = 0$	$p = 1$	$p = 2$	$p = 8$
<i>LISA</i>	$\mathbf{R}_{\text{MMSE}}^{(s=2,p)}$	$1.571 \cdot 10^{-1}$	$1.552 \cdot 10^{-1}$	$3.866 \cdot 10^{-2}$	$3.502 \cdot 10^{-2}$
	Gain (%)	100.00	98.80	24.61	22.29
<i>FEELINGS</i>	$\mathbf{R}_{\text{MMSE}}^{(s=2,p)}$	$6.043 \cdot 10^{-2}$	$5.962 \cdot 10^{-2}$	$7.151 \cdot 10^{-3}$	$5.560 \cdot 10^{-3}$
	Gain (%)	100.00	98.67	11.83	9.20
<i>ODISSEE</i>	$\mathbf{R}_{\text{MMSE}}^{(s=2,p)}$	$5.638 \cdot 10^{-1}$	$4.728 \cdot 10^{-1}$	$5.088 \cdot 10^{-2}$	$3.516 \cdot 10^{-2}$
	Gain (%)	100.00	83.85	9.02	6.24
<i>ODISSEE++</i>	$\mathbf{R}_{\text{MMSE}}^{(s=2,p)}$	$6.824 \cdot 10^{-1}$	$5.725 \cdot 10^{-1}$	$7.085 \cdot 10^{-2}$	$4.279 \cdot 10^{-2}$
	Gain (%)	100.00	83.89	10.38	6.27

5.2.4. Results per Mode

This section analyzes the per mode performance of prediction using the *MMSE* predictor. The *MMSE* predictor with two steps into the future and two measurements, $\mathbf{R}_{\text{MMSE}}^{(s=2,p=2)}$, this predictor is used instead of the better performing $\mathbf{R}_{\text{MMSE}}^{(s=2,p=8)}$ since the performance differences are not too strong, while the computational cost is greatly reduced. Figure 5.3 provides the results for the *LISA* system and Figure 5.4 does it for the *ODISSEE*.

The performance results in this section are given in terms of residual phase variance after prediction, either per Zernike mode or Zernike radial order after averaging across all modes with the same radial order. In any case, when the sum of all contributions is given, it corresponds to the sum of the variance per Zernike mode.

Figure 5.5 plots the reduction in variance from the no prediction case to the $\mathbf{R}_{\text{MMSE}}^{(s=2,p=2)}$ case. It can be observed that the slowest changing modes have better prediction performance in terms of variance reduction. A possible explanation for this is that, due to the slower evolution, the decorrelation between the two measurements and the predicted state is lower, allowing for better predictability. One can also see that some modes are harder to predict with respect to their neighbors; the evolution of these modes is poorly related to the wind (frozen flow) since they are orthogonal to the direction of wind.

It can be observed how for the *ODISSEE* case the prediction performance decreases for the last radial orders considered. Figure 5.6 plots the same curve as in Figure 5.4b but for a different number of radial orders considered in the prediction, i.e. the baseline is the prediction of $n_{\text{max}} = 10$ radial orders measuring the same number of modes, in the figure a different number of radial orders is considered. The per mode performance of an AR(3) model is also plotted. The per mode performance of diagonal *AR* models does not change with the number of modes

5. Assessment of Turbulence Predictability

5.2. Predictability of LEO Satellite AO Applications

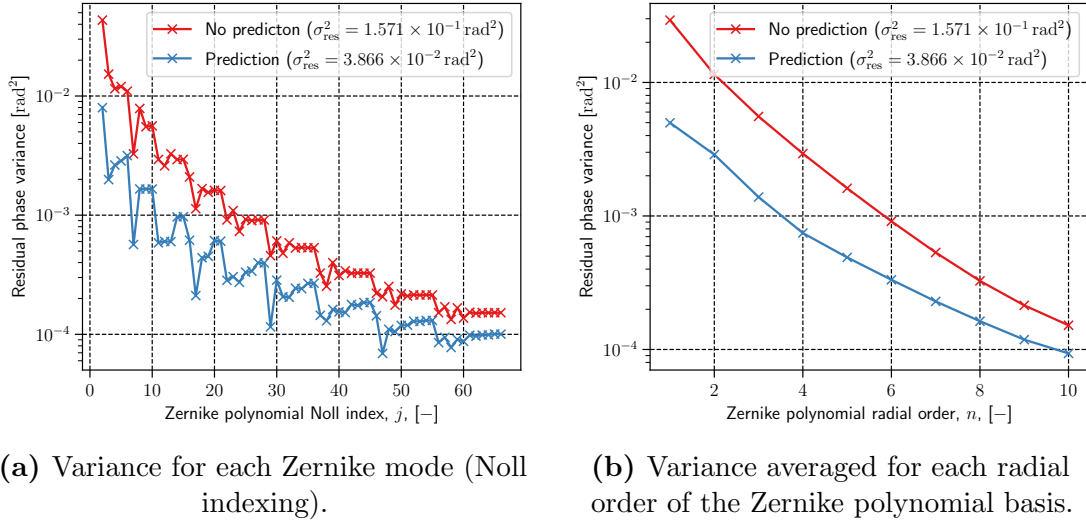


Figure 5.3.: Residual phase modal variance for the *LISA* case with and without *MMSE* temporal prediction.

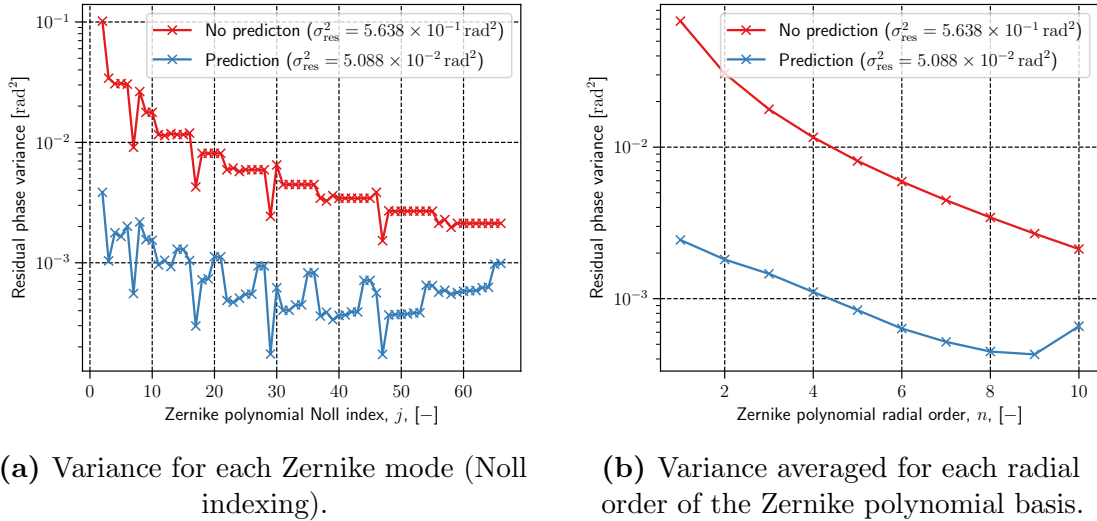


Figure 5.4.: Residual phase modal variance for the *ODISSEE* case with and without *MMSE* temporal prediction.

considered since they are considered to be decoupled. The following observations are possible:

- In general, for the *VAR* models, predicting a few more radial orders will increase the performance of the previous radial orders. For example, when $n_{\max} = 1$ (i.e. only tip-tilt) is considered, the prediction error variance for $n = 1$ is around $9 \cdot 10^{-3} \text{ rad}^2$. For $n_{\max} = 2$ the prediction error variance for the $n = 1$ modes goes down to $4 \cdot 10^{-3} \text{ rad}^2$.

5. Assessment of Turbulence Predictability

5.2. Predictability of LEO Satellite AO Applications

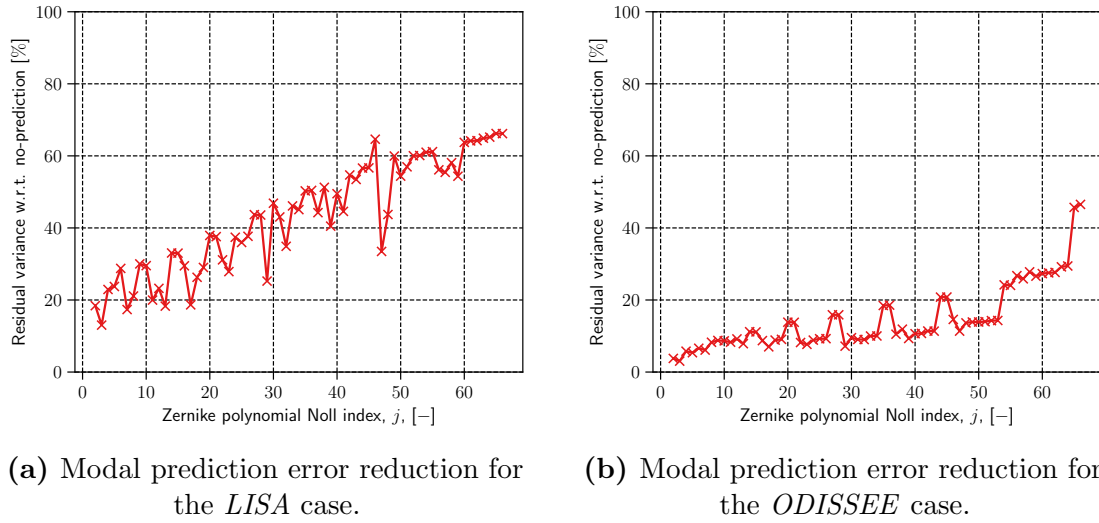


Figure 5.5.: Residual phase modal variance for the *ODISSEE* case with and without *MMSE* temporal prediction.

- Very higher-order modes do not contribute much to the prediction of lower-order modes. For example, adding modes beyond $n_{\max} = 6$ does not bring significant performance gains to the estimation of the $n = 1$ modes.
- The last radial orders predicted have a lower performance that is regained when considering more radial orders. For example, for $n_{\max} = 3$ the performance of the prediction for $n = 3$ is close to the AR(3) model. The prediction performance of these modes improves significantly after considering the $n_{\max} = 4$ modes.

It has been observed that neighboring radial orders provide the most information to the prediction of a given radial order. This can be explained from the fact that the autocovariance matrices present stronger correlations between neighboring modes. Figure 5.7 shows this behavior for the *LISA* case, it can be observed how the correlations decrease with their distance to the diagonal of each covariance matrix.

Since most of the error comes from the lower orders and they are fully predicted with a small number of radial orders, a smaller predictive controller that only includes the lower radial orders can be considered. Figure 5.8 illustrates this case. On the left subfigure, each curve corresponds to a given n_{\max} considered in the prediction. The modes until n_{\max} are predicted, while the modes until $n = 10$ are assigned the no-prediction error. The right subfigure plots the total residual phase variance for each curve in the left subfigure. It is observed that the total prediction error variance decreases to half with few predicted modes, i.e. $n_{\max} = 4$. This observation means that smaller predictive models, with fewer modes, can be enough to achieve a significant performance gain.

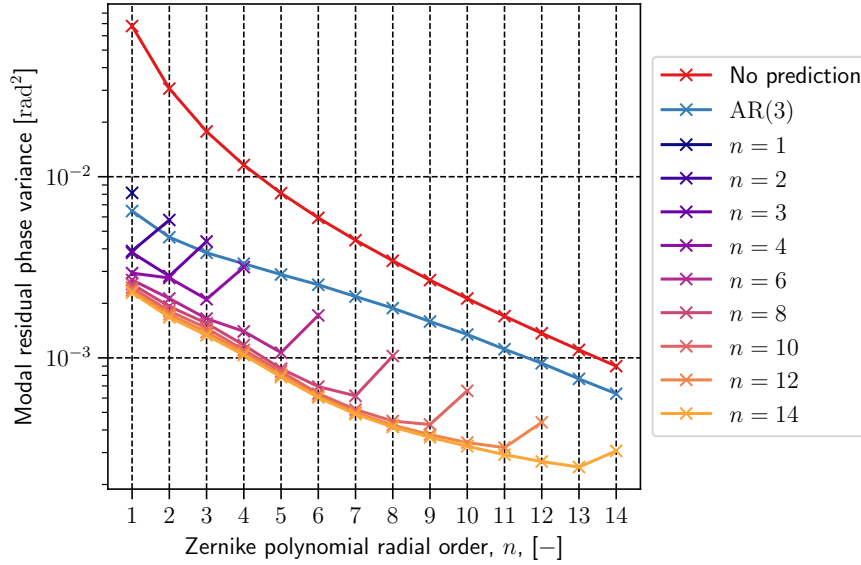


Figure 5.6.: Residual phase variance after prediction for a different number of predicted modes for the *ODISSEE* system.

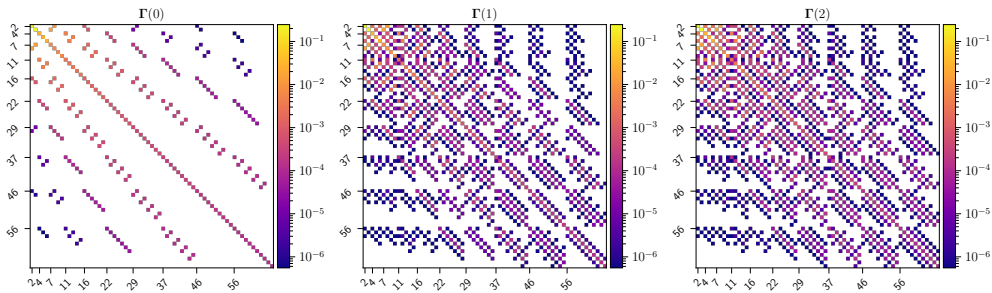


Figure 5.7.: Autocovariance matrices for the *LISA* case.

5.2.5. Reduction of Loop Frequency

The ability of predictive control to reduce temporal error can be used to run the *AO* system at a slower sampling frequency with equivalent performance, since the higher temporal error could be compensated for by the use of prediction. This approach would allow an increase in the integration time used for wavefront sensing and, therefore, benefit the applications that are limited in flux, such as the imaging of satellites from the ground. Reducing the loop sampling frequency while maintaining performance can also be useful when some of the components cannot operate at the required frequencies; for example, a *DM* that starts showing actuator dynamics or resonances in this regime.

Table 5.3 reports the prediction performance for the systems under study after halving and doubling their sampling frequencies. For example, the *ODISSEE* case could run at 750 Hz sampling frequency with a temporal error after prediction is

5. Assessment of Turbulence Predictability

5.2. Predictability of LEO Satellite AO Applications

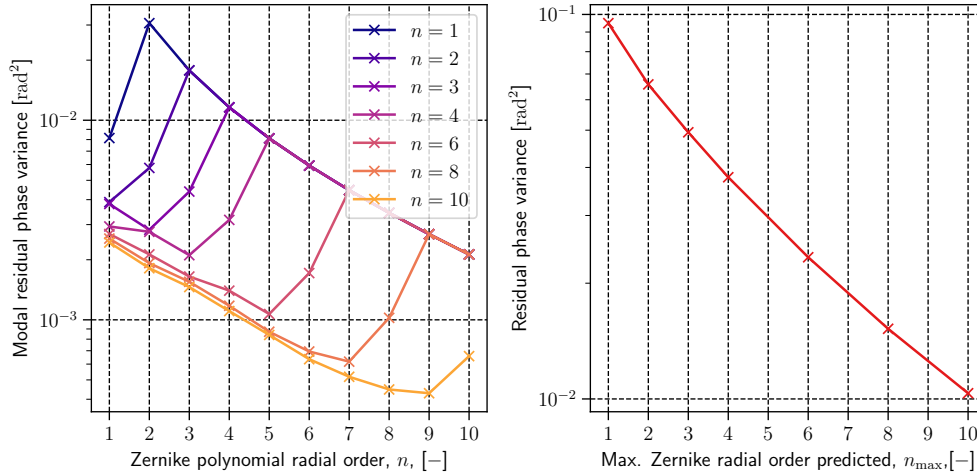


Figure 5.8.: Residual phase variance after prediction for a different number of predicted modes for the *ODISSEE* system. A total number of $n = 10$ radial orders is considered to be corrected; when prediction considers fewer radial orders, the no prediction error is used for the rest of radial orders. Left, residual phase variance averaged over radial order. Right, total residual phase variance.

equivalent to a system running twice or four times the speed without prediction.

Remark

The reduction of system frequency here considers that the delay is kept to two frames also with lower loop frequency. In reality, if a system is able to work at a given loop frequency f_{samp} with a 2 frame delay, when the frequency is reduced to $f_{\text{samp}}/2$, the system should be able to work at a 1.5 delay. This is so because the *WFS* detector read and control command computation take the same time as at higher frequency. Under these assumptions, the integrator results presented here are suboptimal, since a smaller delay is possible.

The approach in this section is representative when the implementation of the case where the higher loop frequency is not possible due to technological constraints like computational resources.

5.2.6. Performance on a Time Series

So far, the performance of the predictor has been evaluated using the analytical method described in Section 5.1.5 that computes the theoretical prediction error or a given linear predictor based on the covariances of the predicted process. The performance of the predictor is now evaluated against a time series of simulated turbulence. The time series corresponds to the multi-layer profile associated with each configuration. Each layer of the profile was shifted to simulate pure frozen flow. The phase is simulated as described in Section 7.1.2 and amounts to a total

5. Assessment of Turbulence Predictability
5.2. Predictability of LEO Satellite AO Applications

Table 5.3.: AO residual wavefront variance (in rad²) budget for *ODISSEE* configuration.

	f_{samp}	No-prediction	$\mathbf{R}_{\text{MMSE}}^{(s=2,p=2)}$	$\mathbf{R}_{\text{MMSE}}^{(s=2,p=5)}$
<i>ODISSEE</i>	3000 Hz	0.157	0.015	0.009
	1500 Hz	0.564	0.051	0.038
	750 Hz	1.701	0.274	0.196
<i>ODISSEE++</i>	3000 Hz	0.212	0.020	0.013
	1500 Hz	0.682	0.070	0.047
	750 Hz	1.828	0.314	0.211
<i>LISA</i>	4000 Hz	0.060	0.007	0.006
	2000 Hz	0.155	0.034	0.029
	1000 Hz	0.317	0.151	0.137
<i>FEELINGS</i>	9000 Hz	0.018	0.003	0.002
	4500 Hz	0.060	0.007	0.006
	2250 Hz	0.165	0.025	0.021

of 50 000 temporal samples. For each time step, the phase on the telescope pupil is projected onto the Zernike modes to obtain the time series of coefficients $\{\phi_k\}$. The previous phase vectors are used with the predictor to compute the two-step-ahead prediction:

$$\hat{\phi}_{k+2} = \mathbf{R}_{\text{MMSE}}^{(s=2,p)} \begin{bmatrix} \phi_k \\ \phi_{k-1} \end{bmatrix} \quad (5.26)$$

The prediction error is computed as $\tilde{\phi} = \phi_k - \hat{\phi}_k$ and its variance along the time series $\{\tilde{\phi}_k\}$ is reported as the predictor error variance. Two different predictors are compared, the *VAR*(2) and the *AR*(3). For each predictor, there are two versions, one computed from the theoretical covariance matrices and one using the data-based sample covariances computed from the same time series. The results are shown in Figure 5.9.

The data-based predictor delivers slightly better results since the covariance matrices are computed from the same time series. The theoretical predictor is expected to behave better on average and to converge to the optimal performance when the time series is infinite. The results for both predictors are close to the theoretical calculations reported in Figure 5.2. This confirms that the *MMSE* can work as a predictor and that the boundaries computed are respected. Additionally, the results confirm that temporal prediction using a Zernike polynomials representation can capture Taylor frozen flow turbulence evolution without the need for explicit shifting of the basis like the one proposed in Juvénal et al. (2016).

5. Assessment of Turbulence Predictability

5.2. Predictability of LEO Satellite AO Applications

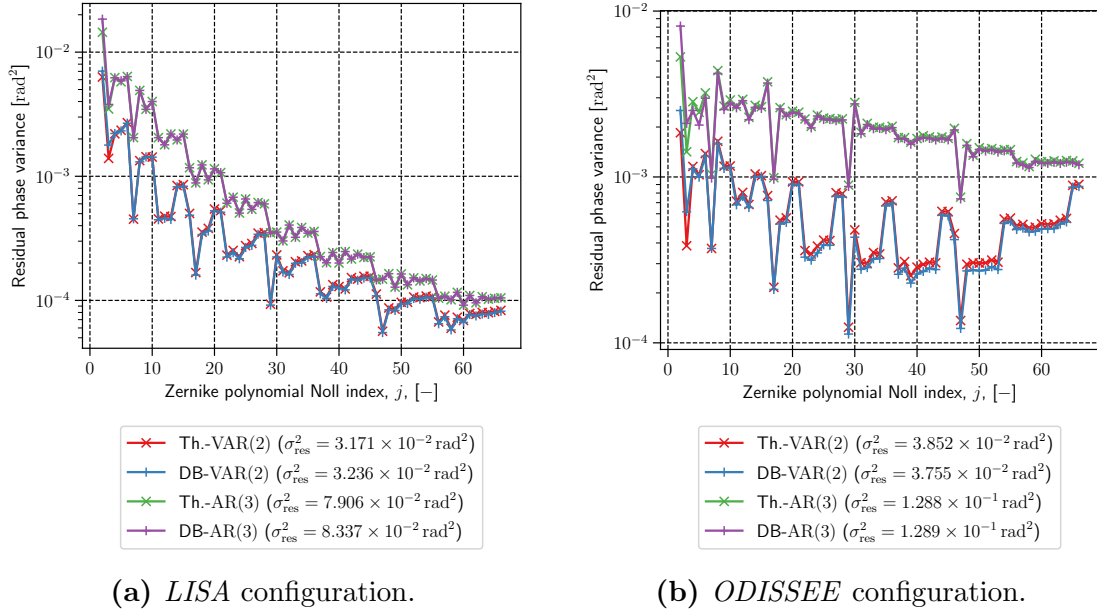


Figure 5.9.: Prediction of a time series using a predictor computed from theoretical covariance data and from the sample covariance data.

5.2.7. Effect of Unknown Natural Wind

This section studies the effect of an unknown natural wind component in the prediction of turbulence for *LEO* satellite tracking. So far, all computations have done the assumption that the shifting of each of the layers is driven only by the apparent wind due to the *LEO* satellite tracking, i.e. no natural wind was included, neither in the turbulence nor in the predictive model. This assumption is valid since the apparent wind speed and direction can be computed for each layer knowing the layer altitude and the satellite orbit. However, natural wind, although it could also be included in the model, is more difficult to obtain and may remain unmodeled.

The *MMSE* prediction assessment framework can include unmodeled phase dynamics by including them in the covariance matrices of the phase used for computing the prediction error of the predictor in Equation 5.17, while the predictor is computed using the covariance matrices that do not include the natural wind.

For the reported test, the natural wind profile used is a Bufton wind profile with a ground layer speed of 3 m/s and an upper layer speed of 20 m/s. The results of this analysis are presented in Figure 5.10.

The first observation is that the no-prediction temporal errors are higher than for the turbulence profiles without natural wind reported in Table 5.2. For the *LISA* case the no prediction error raises from $1.571 \cdot 10^{-1} \text{ rad}^2$ to $2.246 \cdot 10^{-1} \text{ rad}^2$, while for *ODISSEE* it does from $5.638 \cdot 10^{-1} \text{ rad}^2$ to $7.054 \cdot 10^{-1} \text{ rad}^2$. This is reasonable since the additional layer velocities bring additional temporal error. In the case of *LISA* the increase is more significant since most of the turbulence for

5. Assessment of Turbulence Predictability

5.2. Predictability of LEO Satellite AO Applications

its profile is concentrated at the lower layers; those layers had a very slow velocity before and now with the addition of natural wind start to contribute strongly.

Two prediction cases are reported, one in which the predictor was computed with knowledge of the natural wind (in blue in the figure) and one without knowledge of the natural wind (in green in the figure). When the natural wind is known and accounted for in the predictive model, prediction has the same relative performance gains as when only apparent wind was present. The absolute residual phase variance is higher, as the initial temporal error was greater. Therefore, the presence of natural wind, when included in the predictive model, does not change the performance of the prediction.

However, a lack of modeling of the natural wind will cause a loss in performance. The loss in performance for the *LISA* case is total, resulting in a performance close to the no-prediction case. This can be explained by the fact that this case considers a daytime turbulence profile, where the turbulence strength is concentrated in the layers close to the ground. For these layers, the apparent wind speed is not that high, and the turbulence evolution is driven by the natural wind speed; therefore, excluding this information from the predictive model leads to a very poor prediction. Since the *ODISSEE* case considers a night-time profile, the performance losses here are lower but still significant. Even in the least favorable case of *LISA* prediction still brings gains, those are related to the contribution of natural wind, which are still predicted; while the strong contribution of natural wind will not be predicted.

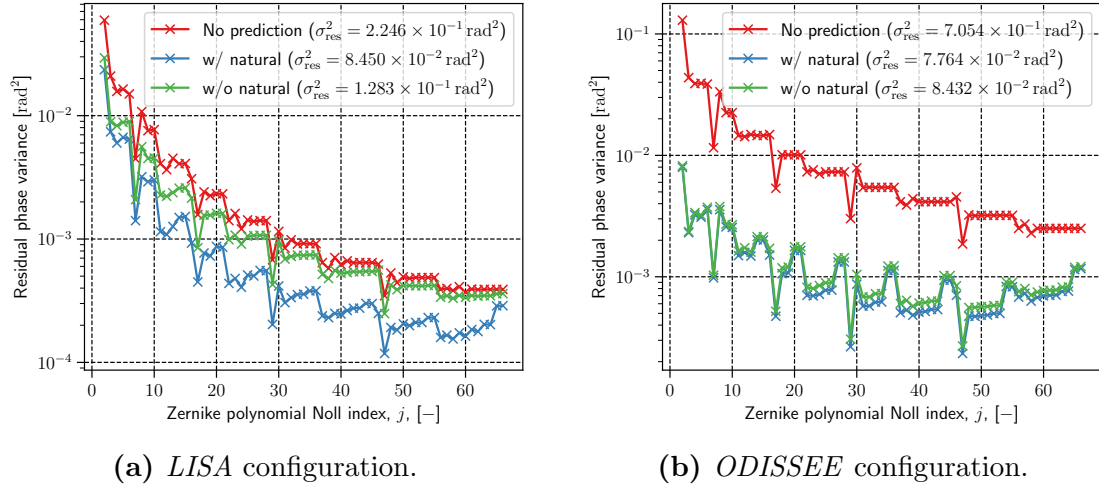


Figure 5.10.: Comparison of *MMSE* prediction performance in the case of known and unknown natural wind.

In conclusion, when the natural wind is included in the predictive model, it can be predicted in the same way as the apparent wind. The differences between both cases are related to their predictability and their absolute contribution to temporal error. The absolute contribution to the temporal error depends distribution of turbulence strength with respect to the wind profile: natural wind is slower but affects the

turbulence that has the most strength (i.e. ground turbulence, especially in day-time conditions), apparent wind is higher at high altitudes, where the turbulence is less strong. When the natural wind is not modeled, the loss of performance will depend on the relative contribution of the natural wind to the temporal error with respect to the apparent wind. For cases such as *ODISSEE*, where the turbulence strength is concentrated in the free atmosphere, the contribution of the apparent wind dominates, and excluding the natural wind from the prediction does not come with a strong penalty. For cases such as *LISA*, where the turbulence strength is concentrated in the ground layer, the contribution of the natural wind dominates, and excluding it from the prediction will result in significant performance losses. Even in this case, at least most of the apparent wind contribution appears to still be predicted, so the performance is still better with prediction. In the cases where it is necessary, the natural wind can be incorporated into the model and predicted using wind speed and direction information from metrology sources.

Remark

The (relative) robustness of the predictive models to the unmodeled wind shown in this section is only partial. The analysis presented here assumes that the measurements used for the prediction do not contain measurement noise. It still remains to see how the models behave when used in a control algorithm; several errors will propagate at the same time.

* * *

Summary

In this chapter, I presented a framework for analyzing the performance of linear predictors of atmospheric turbulence evolution for predictive control purposes. The framework uses the spatio-temporal covariances of the turbulence to compute the optimal predictor and to assess the prediction error associated to a simplified *AO* model, which allows us to evaluate the potential gains of predictive controllers. The method uses the Zernike polynomials as a modal basis for the turbulence description since they allow the analytical computation of the spatio-temporal covariance matrices for the case of frozen flow turbulence by using the expressions of angular covariance matrices between Zernike polynomials. The method can account for multi-layer turbulence, and the size of the derived predictor does not depend on the number of layers used since the turbulence is predicted at the telescope pupil from the sum of the covariance matrices of every layer.

I applied the predictability evaluation method to the case studies in this thesis and two applications were considered: satellite-to-ground optical com-

munications and ground-based satellite observation. The results show a significant reduction in temporal error due to prediction. The observed performance gains motivate the development of predictive adaptive optics controllers for *LEO* satellite applications. The results of this study left the following conclusions:

- The typical gain thanks to the use of prediction is a reduction of the residual phase variance due to temporal error to 10% of the original. However, the impact of this reduction on the performance metrics of the *AO* system such as Strehl ratio will depend on the overall *AO* error budget.
- Smaller telescope diameters lead to less predictability of the turbulence due to a higher temporal decorrelation of the turbulence integrated over the telescope pupil.
- The *MMSE* and the *VAR* predictors, although slightly different in theory (see 5.1.8) provide equivalent performance for the case of two-step-ahead prediction. This means that *VAR* model predictors can be used instead and provide the same performance, with the advantage that they are equivalent to a stable *VAR* process and therefore can be implemented as part of a predictive controller within a Kalman filter.
- The optimal prediction of turbulence requires at least a second-order model, while the gains for higher-order models are more modest. This result has been observed in *LEO* satellite applications and contradicts the literature on predictive control for astronomy.
- The prediction of the modes of a given Zernike radial order is associated with the use of their neighboring modes. For the tip-tilt prediction, little gains are observed after the first radial orders are taken into account in the prediction. This may lead to optimization of predictive controllers and their models, both in terms of performance and robustness.
- Prediction could allow the same performance in terms of temporal error to be obtained with a reduction in the *AO* loop sampling frequency by a factor of two or four.
- The pseudo-analytical framework based on covariance matrices was verified on a simulation of multi-layer turbulence. This successful verification confirms that the shifting of turbulence layers can be properly modeled in the Zernike polynomials space without the explicit shifting of the phase.

- This also means that the same model could be identified from data as in Section 5.2.6 and still represent the frozen flow turbulence without explicit modeling of layer shift.
- The presence of an unmodeled natural wind in the prediction causes a significant loss of performance in some cases, especially those with a strong ground layer, which is the case for daytime turbulence. This is due to the very strong contribution of (unpredicted) natural wind, while apparent wind is still predicted and some performance gains are still observed. In those cases, the speed and direction of the natural wind should also be taken into account for the computation of the predictor.

The analysis in this chapter has highlighted that the gains due to the use of prediction in the case of *LEO* satellite applications are very promising. At the same time, the covariance-based framework presented is also very promising for the development of a predictive controller. First, as already stated, the *VAR* models can be easily integrated into a *LQG* controller. At the same time, the controller can be identified from a priori knowledge of the wind speed and direction and $C_n^2(h)$ profile or from a data-based approach. Finally, the modal nature of the model brings the advantages of modal control presented in Section 2.4.4. The development of such a predictive controller is presented in Chapter 6.

6. Higher-Order VAR Zernike LQG

Contents

6.1. Controller Description	125
6.1.1. State-Space Representation	126
6.1.2. Stability	129
6.1.3. Predictive Model	130
6.2. Comparison to Other Methods	131
6.2.1. Covariance-Based Translation	132
6.2.2. Explicit Zonal Representation Translation	135
6.2.3. Explicit Fourier Domain Translation	136
6.3. Data-Based Identification	137
6.3.1. Identification of Spatio-Temporal Covariance Matrices	137
6.3.2. Learn & Apply Method	141
6.3.3. Other Identification Methods	144
6.4. Model Update and Adaptation	145
6.4.1. Analytical Model Update	145
6.4.2. Data-Based Recursive Model Update	145

Introduction

This chapter introduces the predictive controller that I developed during this thesis and discusses its potential extensions and limitations. Section 6.1 introduces the predictive controller and discusses its implementation. In Section 6.2 I compare the proposed predictive controller with similar controllers from the literature, to justify some of the choices and identify possible improvements. Section 6.3 I briefly discuss the requirements and possible techniques for a data-based identification of the controller, while Section 6.4 comments on possible adaptation strategies for the controller so that it can be adapted to changing turbulence conditions during the orbit of the tracked *LEO* satellite.

6.1. Controller Description

This chapter discusses the predictive controller developed during this thesis: the *higher-order vector autoregressive Zernike LQG*. The controller is based on an *LQG* predictive controller with a high-order *VAR* predictive model. The controlled states are the (pseudo-)open-loop turbulence at the telescope pupil projected on a Zernike polynomial basis. This controller is an extension of the controller presented in [Whiteley et al. \(1998a\)](#), [Correia et al. \(2014\)](#), and [Correia et al. \(2015\)](#), but with a high-order vector autoregressive model, while those original works used a first-order vector autoregressive model.

The predictive model in this controller is the same as in the predictability assessment in Chapter 5. The controller uses the *VAR* model discussed in Section 5.1.8, which has similar performances to the *MMSE* solution even if they are not equivalent; see the referred section for a more detailed discussion on the differences between the two models. For the implementation of the predictive controller, the *MMSE* predictor cannot be used, since it does not provide a stable process, a requirement for the stability of the *LQG* controller; instead the similar *VAR* model used.

The identification of the *VAR* model is very flexible and can be carried out using different strategies, as originally discussed in Section 4.2.3. In this work, the *VAR* model is computed from the spatio-temporal covariance matrices of the turbulence, those are computed analytically as explained in Section 4.2.5.2. Section 6.3 will discuss alternative strategies for the identification of the controller, but the development of those is beyond the scope of this thesis.

Such a predictive controller presents several advantages:

1. It uses the *LQG* framework, which is not only the optimal linear control policy, but also a well known control method in adaptive optics.
2. The turbulence is modeled only at the pupil, which allows reducing the computational load of the controller. This is possible because covariance modeling is able to capture frozen flow shifting of different layers at the pupil without explicit shifting of the layers.
3. The model can be identified in different ways. As a result, the controller will be extended in the future.
4. The model can be analytic. Analytical update may be beneficial since allows to compute the whole controller before the orbit. See Section 6.4. This includes wind information and is therefore especially interesting for its use in *LEO* satellite applications.

The rest of this section will introduce the structure of the controller and the details of its implementation.

6.1.1. State-Space Representation

This section details the state space representation of the predictive controller. The controller structure is based on the predictive *LQG* controller as presented in Section 4.3; the discussion in that section is extended here to incorporate details specific to the implementation of the proposed controller.

Remark

The state space representation introduced here is the same used by other predictive *LQG* controllers, where the state vector contains a vectorial representation of the turbulence (i.e. zonal basis, modal basis, *SH* slopes, etc.), different versions of this vector for different time steps, and (optionally but not in this case) several layers of turbulence.

Controller states: The state vector is split into two sub-vectors: (1) The open-loop turbulence states at different steps in time and (2) the past control commands.

The turbulence states vector represents the open-loop turbulent phase at the telescope pupil projected on a Zernike polynomial basis: ϕ^{tur} . The number of modes used by the controller is a design parameter that will be discussed later. The state vector needs to contain the different time steps of ϕ^{tur} , since the state-space model that will define the evolution of the system is an autoregressive process. Without loss of generality, the equations presented here consider two time steps saved, corresponding to a second-order autoregressive model; higher orders can be implemented by extending the vector. The vector is defined as:

$$\mathbf{x}_k^1 = \begin{bmatrix} \phi_k^{\text{tur}} \\ \phi_{k-1}^{\text{tur}} \end{bmatrix}. \quad (6.1)$$

The second state vector will act as a buffer keeping the last control commands as a vector \mathbf{u} . These commands are necessary to reconstruct the open-loop turbulence projection onto the Zernike polynomials from closed-loop measurements. Since a two-frame delay system is considered, the vector stores the last two commands sent to the *DM*:

$$\mathbf{x}_k^2 = \begin{bmatrix} \mathbf{u}_k \\ \mathbf{u}_{k-1} \end{bmatrix}. \quad (6.2)$$

The state model in Equations 4.35 and 4.36 can be rewritten as:

$$\mathbf{x}_{k+1}^1 = \mathbf{A}^1 \mathbf{x}_k^1 + \Gamma_v \mathbf{v}_k, \quad (6.3)$$

$$\mathbf{x}_{k+1}^2 = \mathbf{A}^2 \mathbf{x}_k^2 + \mathbf{B}^2 \mathbf{u}_k, \quad (6.4)$$

$$\mathbf{y}_k = \mathbf{C}^1 \mathbf{x}_k^1 + \mathbf{C}^2 \mathbf{x}_k^2 + \mathbf{w}_k. \quad (6.5)$$

The concrete definition of the matrices \mathbf{A}^1 , \mathbf{B}^1 , \mathbf{B}^2 , \mathbf{C}^1 , \mathbf{C}^2 , and $\mathbf{\Gamma}_v$ follows in the following paragraphs.

Within the Kalman filter there exist two estimates of the \mathbf{x}_k^1 vector, corresponding to the update and prediction phases; those are, respectively:

$$\hat{\mathbf{x}}_{k|k}^1 = \begin{bmatrix} \hat{\phi}_{k|k}^{\text{tur}} \\ \hat{\phi}_{k-1|k}^{\text{tur}} \end{bmatrix}, \quad (6.6)$$

and

$$\hat{\mathbf{x}}_{k+1|k}^1 = \begin{bmatrix} \hat{\phi}_{k+1|k}^{\text{tur}} \\ \hat{\phi}_{k|k}^{\text{tur}} \end{bmatrix}. \quad (6.7)$$

The vector \mathbf{x}_k^2 is not an estimate since the previous commands are known with absolute certainty.

Measurement model and correction step: The Kalman filter within the *LQG* needs a measurement model that connects the phase estimates from the vector $\hat{\mathbf{x}}_{k|k-1}$ to the measured slopes from vector \mathbf{y}_k . Additionally, it is necessary to account for the fact that the phase states and their estimates correspond to the open-loop phase, while the slope measurements correspond to the close-loop residual phase; Equation 6.5 combines in the computation of the closed-loop turbulence slope measurement the contribution of the open-loop turbulence, $\mathbf{C}^1 \mathbf{x}_k^1$, and the contribution of the *DM* figure, $\mathbf{C}^2 \mathbf{x}_k^2$.

In the same way, Equation 4.52 is modified to account for the pseudo-open-loop computation:

$$\hat{\mathbf{x}}_{k|k}^1 = \hat{\mathbf{x}}_{k|k-1}^1 + \mathcal{H}_k (\mathbf{y}_k - (\mathbf{C}^1 \hat{\mathbf{x}}_{k|k-1} + \mathbf{C}^2 \mathbf{x}_k^2)). \quad (6.8)$$

The matrix \mathbf{C}^1 corresponds to the phase $\hat{\phi}_{k-1|k-1}^{\text{tur}}$ as it would be seen by the *WFS*:

$$\mathbf{C}^1 = \begin{bmatrix} \mathbf{0} & \mathbf{M}_{\text{WFS}} \end{bmatrix}, \quad (6.9)$$

where the matrix \mathbf{M}_{WFS} captures the linear relationship between how each component (e.g. Zernike polynomial) of the open-loop phase vector is seen by the *WFS* in the slope space. Note the one-frame delay between the $\hat{\phi}_{k-1|k-1}^{\text{tur}}$ phase and its corresponding measurement \mathbf{y}_k .

The matrix \mathbf{C}^2 corresponds to the *DM* figure at the time where the measurement was performed as seen by the *WFS*:

$$\mathbf{C}^2 = \begin{bmatrix} \mathbf{0} & -\mathbf{M}_{\text{int}} \end{bmatrix}, \quad (6.10)$$

where the matrix \mathbf{M}_{int} is the interaction matrix that captures the linear response of the *WFS* to an actuator command. The minus sign corresponds to the subtraction of the corrected phase from the open-loop phase to obtain the residual one: $\phi^{\text{res}} = \phi^{\text{tur}} - \phi^{\text{cor}}$. Note how the command selected from \mathbf{x}_k^2 is \mathbf{u}_{k-1} , the command applied in the previous frame $k - 1$ to generate the measured phase, ϕ_{k-1}^{res} . This command was computed at frame $k - 2$ using measurement \mathbf{y}_{k-2} based on ϕ_{k-3}^{res} , corresponding to a two-frame delay between measurement and correction.

It remains the question of the computation of the matrices \mathbf{M}_{WFS} and \mathbf{M}_{int} . Both matrices can be computed from computational models of the *WFS* and *DM*, also known as synthetic matrices. This approach can be exact within computational simulations since the model used can be the same as the one used to simulate the system; however, it will lead to calibration errors when used in real systems since the models will never fully match reality. The interaction matrix, \mathbf{M}_{int} , can be computed synthetically, calibrated from the instrument, or obtained with a hybrid approach; the different methods offer different trade-offs (Oberti et al. 2006; Heritier et al. 2018). The matrix \mathbf{M}_{WFS} is a sort of interaction matrix between the Zernike polynomials and the wavefront sensor, so this matrix can only be computed synthetically, leading to potential calibration errors.

Prediction step: The prediction step of the Kalman filter can be rewritten from Equation 4.55 as:

$$\hat{\mathbf{x}}_{k+1|k}^1 = \mathbf{A}^1 \hat{\mathbf{x}}_{k|k}^1, \quad (6.11)$$

where

$$\mathbf{A}^1 = \begin{bmatrix} \mathbf{A}_1 & \mathbf{A}_2 \\ \mathbb{I} & \mathbf{0} \end{bmatrix}. \quad (6.12)$$

The matrices \mathbf{A}_1 and \mathbf{A}_2 are the block matrices of a predictive autoregressive model matrix as defined in Equation 4.3; further details of the model are given in Section 6.1.3. The identity matrix \mathbb{I} is used to shift the previous phase estimate within the estate vector. The matrix $\mathbf{\Gamma}_v$ relates the process noise only to the first element of \mathbf{x}_{k+1}^1 since it is the only one generated from the stochastic process:

$$\mathbf{\Gamma}_v = \begin{bmatrix} \mathbb{I}_{n_s} \\ \mathbf{0} \end{bmatrix}, \quad (6.13)$$

where \mathbb{I}_{n_s} is the identity matrix in $\mathbb{R}^{n_s \times n_s}$.

Kalman gain computation: The Kalman gain is computed with the asymptotic solution of the Riccati equation by propagating the estimation error covariance matrices (Equations 4.54 and 4.56) and the Kalman gain (Equation 4.53) until convergence is reached; see Section 4.3.3.3. This uses the covariance matrix of

the slopes measurement noise Σ_w and the process noise covariance matrix Σ_v computed as detailed in Section 4.2.4.2.

Remark

The use of the asymptotic Kalman gain is a common strategy in adaptive optics since it leads to computational savings. This strategy is near optimal since convergence is typically achieved after hundreds of iterations, corresponding to some milliseconds during which the controller does not perform optimally. This is usually not a problem, since turbulence is assumed to be stationary during a much longer period, during the time the controller does not need to be updated. In the case of *LEO* satellite tracking, the update of the predictive controller (see Section 6.4) will happen more often, the use of the non-stationary Kalman gain may be beneficial; especially in the case of optical communications, where no bump in performance during the link is desired.

DM command computation: The final *DM* command is computed as the projection of the predicted phase into the *DM*:

$$\mathbf{u}_{k+1} = \Gamma_{\text{proj}} \hat{\mathbf{x}}_{k+1|k}, \quad (6.14)$$

where the projection matrix, Γ_{proj} , selects the predicted phase for the next step and computes the *DM* command from it. The matrix is defined as:

$$\Gamma_{\text{proj}} = \begin{bmatrix} -\mathcal{K} \\ \mathbf{0} \end{bmatrix}, \quad (6.15)$$

where the minus sign corresponds to the negative feedback, i.e. the phase applied is the opposite to the one estimated, and $\mathcal{K} = (\mathbf{N}^\top \mathbf{N})^{-1} \mathbf{N}^\top$, with \mathbf{N} a matrix relating the voltage commands to their application their influence of the *DM* projected Zernike polynomials. This matrix can be obtained by a measurement (for example using a high-resolution phase metrology interferometer) of the *DM* influence functions on a zonal basis and then changing the basis to a Zernike polynomial basis defined on the same grid of points.

6.1.2. Stability

In order for the *LQG* controller to be stable, the following conditions need to be satisfied (Halevi 1994):

1. $\Sigma_v > 0$,
2. (\mathbf{A}, \mathbf{C}) is detectable,
3. $(\mathbf{A}, \Sigma_v^{1/2})$ is stabilizable, and

4. (\mathbf{A}, \mathbf{B}) is stabilizable.

These conditions imply the necessity of a stable predictive model \mathbf{A} , which implies: $|\text{eig}(\mathbf{A})| < 1$. Additionally, the computation of the $\Sigma_{\mathbf{v}}$ matrix needs also to ensure that it is positive-definite. In the case of VAR models, these two conditions can be checked for the identified model.

Remark

The stability conditions stated here assume that the models used in the LQG match with no deviation in the dynamics of the process being controlled, when this is not true, the stability of the controller is not guaranteed (Luo and Johnson 1993).

6.1.3. Predictive Model

The predictive model used in the controller is a second-order VAR model of the open-loop turbulence projected on the Zernike polynomials.

The stability constraints of the LQG controller require a stable stochastic process as a predictive model; this means that not any predictive model can be used, but only one leading to a stable stochastic process. This is the reason why autoregressive processes are a common choice in predictive controllers.

Remark

While the typical AO loop delay is of two frames, the VAR process prediction is one step ahead at a time; the prediction two-step-ahead prediction is achieved by the iteration of the predictive model (see Property 4.5).

The second order model chosen for the VAR is justified by the discussion in Section 5.2.3, since, for the case of LEO tracking, it brings significant gains with respect to first-order models; a higher order may lead to improved performance, but those gains are deemed low compared to the increase in computational load that increasing the state vector will entail.

The phase representation used for the controller is a Zernike modal basis, there are two main reasons for this: (1) The spatio-temporal covariance matrices necessary for the identification of the model can be computed analytically for this basis, and (2) this way the comparison to other analytical tools such as the predictability assessment method presented in Chapter 5 and other analytical tools are direct. The analytical computation of the model is of great advantage, since, using wind priors and a known turbulence profile, a predictive model can be computed for any point of the LEO satellite trajectory. Nevertheless, the results of this thesis are complementary to the controllers implemented in other bases; a comparison to the zonal basis is given in Section 6.2.1.

The baseline identification method for the controller is the one described in Section 4.2.5.2. However, other possible identification methods are discussed in Section 6.3.

Remark

Any other (stable) predictive model could be used. Possible variations of the predictive model are the use of a different basis, such as slopes space, zonal basis, or Fourier models; or a Zernike VAR model identified in a different manner (see Section 6.3).

The number of modes considered in the predictive model, which will therefore define the number of states used in the controller, is one of its main design parameters; it is driven especially by three factors:

1. The number of modes to be corrected. All the modes to be corrected need to be part of the Kalman filter; ultimately, the corrected phase space is the projection of the estimated modes onto the DM space.
2. The number of modes necessary for obtaining good prediction performance. As discussed in Section 5.2.4, to achieve near-optimal prediction performance on a set of modes, it is necessary to consider higher-order modes in the predictive model.
3. The number of modes needed to achieve a good phase reconstruction. The presence of aliasing in the Shack-Hartmann slopes requires the estimation of more modes to better reconstruct the lower order modes; with a sufficient number of estimated modes the regularized phase reconstruction within the Kalman filter (see Section 4.3.3.4) can reduce the effect of aliasing in the phase reconstruction.

Further discussion on the required number of modes for the controller is given in Section 7.3 based on the end-to-end simulation results for the controller.

6.2. Comparison to Other Methods

This section offers a review and comparison of predictive controllers that share similarities with the predictive controller presented in this chapter. The methods compared have in common that they all use the combination of LQG controller and autoregressive models (scalar or vectorial) as controller structure.

This review is organized in the different possibilities to model turbulence evolution as an autoregressive model. Most predictive models are based on the frozen flow assumption, so they try to model the translation of the phase of each layer due to the presence of frozen flow. This is achieved as a combination of a choice of modal

basis and a choice of autoregressive model structure. Three different methods are discussed here:

1. *Covariance-based translation*: The encoding of the translation in the spatio-temporal covariances that define the autoregressive model. This is the most flexible method, allowing the phase to be represented in a zonal basis, any modal basis, or even the Shack-Hartman *WFS* slopes space.
2. *Explicit zonal representation translation*: The phase is represented using a zonal representation, phase translation is conducted by interpolation of zonal values, and the autoregressive model is the matrix representation of such an interpolation.
3. *Explicit Fourier domain translation*: The phase is represented as Fourier modes, the phase translation is conducted in the Fourier domain, where it corresponds to a phase shift of the Fourier modes coefficients, and the autoregressive model is fitted from the dynamics associated to the temporal evolution of the coefficients due to such a phase shift.

Each of these methods presents its own advantages and disadvantages, which are briefly stated here from my point of view. While many criteria are possible to weight those, this thesis defines the identification of the predictive model as the main metric, both from analytical computations thanks to priors and from using a data-based identification. The purpose of this section is not to provide a discussion of the pros and cons of each method, but to establish links between the method presented in this thesis and other methods in the literature.

6.2.1. Covariance-Based Translation

Translation representation method: The principle of this method has been extensively discussed in Chapter 5. In brief, the method computes an autoregressive mode using the spatio-temporal covariance matrices of the underlying process. When the covariance matrices are computed analytically, the frozen flow assumption can be used to compute the temporal statistics from the spatial ones, resulting in implicit modeling of the frozen flow layer translation. When the covariances are identified from data this method can capture both the frozen flow as well as other kinds of temporal evolution such as mechanical vibrations and boiling turbulence.

Foundational work: Already the pioneering work of Anderson et al. ([Anderson 1991](#); [Paschall and Anderson 1993](#)) identified a diagonal autoregressive model using a Zernike modal basis and assuming frozen flow. They do not use autoregressive models explicitly; instead, they fit shaping filters to the autocorrelation functions between the modes, which are actually equivalent to a first-order autoregressive

(Markovian) process. The model used to compute the autocorrelation functions accounts for the wind speed and direction of each layer; however, the cross-correlations between modes are not modeled, and only diagonal autoregressive predictive models are used. They claim that cross-correlation is still introduced at the process covariance matrix, but this will only be used in the update step of the Kalman filter, but not for prediction, but as it is shown in Section 7.3 this does not benefit the prediction.

Equivalent methods: Several methods have used the identification of analytical covariances using a zonal representation or a Zernike modal basis as this work does.

Whiteley et al. (1998a) proposed a predictive model similar to the one used in this thesis, but for tip-tilt correction in the presence of moving targets. The model uses an *MMSE* estimator to compute a prediction of the tip and tilt modes based on the delayed measurement of these modes and higher-order Zernike polynomials; the phase is modeled only at the pupil of the telescope. The temporal covariances are computed in a fashion similar to the method described in Section 4.2.5.2, also based on the frozen flow assumption and a known wind thanks to the angular tracking speed and the distance to the target and also using only the phase at the pupil of the telescope. This work did not incorporate the predictive model in a controller, they only used the method to provide potential gains as in Chapter 5. Gavel and Wiberg (2003) developed a similar idea but using a zonal basis.

Correia et al. (2014) proposed this method again under the name of spatio-angular predictor and extended it to the prediction of the complete set of modes corrected by a tomographic system for astronomy for its use within a *LQG* controller. The method benefited of the analytical computation of the spatio-temporal covariances from priors to compute the covariances at the correction direction, where they cannot be directly measured. The two main differences with respect to this method are that (1) this thesis proposes to use higher order *VAR* models, since, at least for *LEO* satellite applications, this shows to provide a significant performance improvement and (2) the application of the method to single mode fiber coupling.

The same work was presented in Correia et al. (2015) and Jackson et al. (2015) using a zonal basis, equivalent to Gavel and Wiberg (2003); Prengère et al. (2020) extended this method to a *VAR(2)* model and showed performance gains with respect to the Markovian assumption originally proposed by Gavel and Wiberg (2003). Previously, Piatrou and Roggemann (2007) had implemented the zonal model of Gavel and Wiberg (2003) as an *LQG* in a similar manner as the method of Correia et al. (2015) and Prengère et al. (2020) but using the modeling phase of each layer separately. Historically, Correia et al. introduced the prediction only at the pupil, since this method in the context of *multi object adaptive optics (MOAO)* systems; while the previous works (Piatrou and Roggemann 2007) were applied to *multi conjugated adaptive optics (MCAO)*, where the estimation of each layer is necessary and not an inconvenient. Finally, the predictive version Cranney et al. (2020) of the *learn & apply (L&A)* by Vidal et al. (2010) is equivalent to pupil

plane covariance modeling but using slopes.

Data-based methods: All the previous methods used analytical computations; other works have implemented similar prediction algorithms based on the identification of *VAR* modes from data. These models have favored the use of slope space models, since this is the measurement space of the *WFS* and does not require less calibrations (Hinnen et al. 2007; Doelman et al. 2011); the work of Kelemu et al. (2022) is highlighted here since it is applied to *LEO* downlinks and it suggests the use of a VAR(2) model. Data-based methods using modal bases also exist in the literature: Siquin et al. (2020) uses a Zernike modal basis to allow prediction of low orders only and Guyon and Males (2017) uses data-based methods that generate an optimal modal basis for prediction with a VAR(1) model.

Boiling turbulence methods: Some models have used boiling models that only use the wind norm as AR(1) Le Roux et al. (2003) and AR(2) Petit et al. (2008), including laboratory Sivo et al. (2012) and on-sky Sivo et al. (2014).

Choice of phase representation: The bibliographical review in this section has shown that a similar method to that of this thesis has also been developed by Prengère et al. (2020) and Kelemu et al. (2022). A thorough comparison of those two methods with respect to the one presented in this thesis would be of great scientific interest, but it was not possible to conduct it during this thesis due to time constraints. Nevertheless, some remarks are possible:

- The predictive controller presented in this chapter uses a Zernike polynomial representation, an equivalent approach to this controller has been already presented in a zonal basis by Prengère et al. (2020). A possible question to be considered is whether one of both options is more convenient.
- In general and assuming a similar spatial frequency content, the Zernike and the zonal bases are equivalent; since none of them account for the temporal dynamics in their definition, they should not have better performance in terms of prediction, as it could be the case of *empirical orthogonal functions* (*EOF*) (Guyon and Males 2017).
- The zonal basis offers some advantages since it is not defined over a circular pupil, but only over the points of interest; this is not the case for the Zernike modal basis, since they are defined over a circle. Even if annular Zernike polynomials exist, they cannot benefit from the analytical computation of their spatio-temporal covariances. This may be a problem for the Zernike polynomials in the presence of telescope obscuration since it will need to estimate the phase at points where no direct measurements are available. On the other hand, the use of a modal basis is helpful if the predictive model is applied only to a subset of modes Siquin et al. (2020).

- As already mentioned, the use of the slope space is particularly interesting for data-based methods, since this is the native space of the *WFS* and requires fewer calibrations. Nevertheless, in the absence of phase reconstruction, such a method suffers from aliasing present in the slopes. It is still necessary to thoroughly study the behavior of aliasing in slope-based predictive controllers.
- Compared to zonal and modal bases with equivalent frequency content, the slopes space needs roughly twice the number of states.

6.2.2. Explicit Zonal Representation Translation

Using a zonal representation of the phase at one layer, it is possible to predict the evolution of the phase by shifting this layer in the direction of the layer velocity by an increment $(\Delta_x, \Delta_y) = (-V_x \Delta t, -V_y \Delta t)$. For a phase $\varphi_l(\mathbf{x}_i, \mathbf{y}_i, k)$, corresponding to the phase of layer l sampled at coordinates $(\mathbf{x}_i, \mathbf{y}_i)$ at time k , the future phase can be computed as:

$$\varphi_l(\mathbf{x}_i, \mathbf{y}_i, k + 1) = \varphi_l(\mathbf{x}_i + \Delta_x, \mathbf{y}_i + \Delta_y, k), \quad (6.16)$$

where the desired phase points are computed by bi-linear interpolation of the measured phase grid.

Since only the phase within the pupil is known, the points outside the pupil cannot be interpolated. This means that the new crescent of turbulence introduced in a circular pupil cannot be predicted in this manner. Different ways of dealing with these problems are possible, from assuming that the phase outside the pupil is zero or periodic, to trying to estimate the phase outside the pupil and then perform the shifting (Juvenal et al. 2015b; Cranney et al. 2018b; Prengère et al. 2020).

Bi-linear interpolation can be computed as a convolution operation, and convolution operations can be optimized using Fourier transforms. As a result, under the assumption of this kind of evolution, it is possible to use optimized by algorithms that use Fourier transforms for faster computations. Some works have used this structure to apply optimized versions of the *LQG* controller such as the *discrete Kalman filter (DKF)*, an optimization of the Kalman filter that takes advantage of the structure of the spatio-temporal evolution of turbulence to reduce the computational load to compute an approximation of the Kalman gain matrix based on Fourier transform computations. Note, Fourier transforms are used here for a more efficient computation of the controller, not to use a Fourier domain control. Even if the shifting operation is applied by layer, the resulting evolution model can be expressed for the phase on the pupil plane only. This method was first suggested by Massioni et al. (2011), initially for turbulence in the pupil plane and extended by Gilles et al. (2013) in a multilayer estimation approach for tomographic control applications.

Under the assumption of the shift-invariant transform, the spatio-temporal covariance matrices of the zonal representation of the phase also have a particular

structure, known as *block Toeplitz with Toeplitz block (BTTB)*. Cranney et al. (2017) suggested a method to identify the spatio-temporal covariance matrices required to compute a first-order VAR model with constraints on them so that the resulting model can be used within the DFK of Massioni et al. (2011). The method predicts the phase at the pupil and does not require knowledge of turbulence or wind profiles. The same structure of the spatio-temporal covariance matrices has been used to compute more efficient tomographic reconstructors (Ono et al. 2018). The method was extended in Cranney et al. (2018a) to constrain the identification to guarantee the stability of the identified model and in Cranney et al. (2018b) to deal with the crescent that cannot be modeled by shifting.

The motivation for this method has been to reduce the computational needs of 40 m class telescopes in tomographic settings. The complexity of the methods is not justified for the systems considered in the applications of this thesis.

A different approach by Juvénal et al. (2016) uses an explicit shift operation on a Zernike modal basis by zonal sampling of the basis. By doing this, the proposed method can use the traditional boiling turbulence methods on the Zernike basis plus the explicit effect of shifting due to frozen flow. The disadvantage of this method is the crescent problem and the need to model each layer independently, which increases the computational cost of the controller.

6.2.3. Explicit Fourier Domain Translation

Phase shifting can be modeled in the Fourier domain with two main advantages. Additionally, the Fourier domain offers a great advantage from a control system point of view, since the modes of the Fourier basis are spatially and temporally independent, allowing the design of a separate controller for each of the modes.

A Fourier modal basis for the representation of phase can be computed as the two-dimensional discrete Fourier transform of the phase sampled on a $(N \times N)$ points grid with sampling distance d corresponding to the DM sampling:

$$\Phi(u, v, k) = \mathcal{F}\{\varphi(x, y, k)\} = \sum_{u=0}^{N-1} \sum_{v=0}^{N-1} \varphi(x, y, k) e^{-2\pi i(xu+yv)/N}, \quad (6.17)$$

where $\Phi(u, v, k)$ is the coefficient associated with the mode with the pair of spatial frequencies (u, v) at a discrete time step k , and \mathcal{F} defines the two-dimensional discrete Fourier transform. The Fourier coefficients can be obtained from Shack-Hartmann slopes measurements thanks to a Fourier transform phase reconstructor Poyneer et al. (2002).

The translation of the mode is given by a phase shift in the Fourier domain for each of the Fourier coefficients:

$$\Phi(u, v, k + 1) = \Phi(k, l, k) e^{2\pi i(\frac{\Delta x}{d}l + \frac{\Delta y}{d}k)}. \quad (6.18)$$

The resulting phase can be obtained by computing the inverse Fourier transform:

$$\varphi(x, y, k) = \mathcal{F}^{-1}\{\Phi(u, v, k)\} = \frac{1}{N^2} \sum_{k=0}^{N-1} \sum_{l=0}^{N-1} \Phi(u, v, k) e^{2\pi i(xu+yv)/N}, \quad (6.19)$$

where \mathcal{F}^{-1} defines the two-dimensional discrete inverse Fourier transform.

The *predictive Fourier control (PFC)* method proposed by Poyneer et al. (2007) combines the use of shifting in the Fourier domain and an *LQG* controller to design a predictive controller for adaptive optics under frozen flow. When considering a unique layer of turbulence, the temporal *PSD* of the Fourier coefficient will have a unique peak at a spatial frequency:

$$\nu = -\frac{(uV_x + vV_y)}{Nd}. \quad (6.20)$$

An *AR(1)* model can be fit to the temporal *PSD* of the layer to identify a predictive model; this identification uses the peak of the *PSD* and its power level to identify the model without any other information than the close-loop measurements from a Fourier domain phase reconstructor. The details of the peak finding algorithm when turbulence is composed of several layers can be found in Poyneer et al. (2007); Poyneer et al. (2023) updated the algorithm to a new state space formulation and demonstrated this method in a laboratory emulation. Since the Fourier modes (and the layers) are decorrelated spatially and temporally, an *LQG* controller can be designed for each layer and each mode, reducing the computational cost of the controller.

The use of this method is more suitable for *AO* systems that already use Fourier methods for phase reconstruction, since it requires the computation of the Fourier transform of the data. Fowler et al. (2022) pointed problems with the identification of the method in the case of continuous wind profiles, but this can be circumvented if the wind data are known a priori. Additionally, it is not clear to the author how this method deals with the crescent problem in the shifting.

6.3. Data-Based Identification

This section provides suggestions on the data-based identification of the controller proposed in this chapter. Implementing a data-based identification for the controller is beyond the scope of this thesis; nevertheless, it is useful to relate the findings of this thesis to a potential data-based identification of the controller.

6.3.1. Identification of Spatio-Temporal Covariance Matrices

The main strategy suggested here is to rely on the closed-loop measurements of the Shack-Hartmann for the identification of the spatio-temporal covariance matrices

necessary to compute the predictive model while the *AO* is in operation. Such a method would benefit from all the developments presented in this thesis, since the structure of the controller would be the same; the only difference would be that the data-based computation of the spatio-temporal covariance matrices instead of their analytical computation.

In this thesis, the baseline identification method is the computation of those covariance matrices using analytical formulas; this assumes the prior knowledge of the atmospheric turbulence C_n^2 profile, the natural wind profile, and the apparent wind profile. Thus, this thesis assumes that those priors are known before computing the model and relies on external metrology sources for the identification of the C_n^2 profile and, optionally, the natural wind profile, although the latter can be neglected in some cases (see Section 5.2.7); whereas the apparent wind can be computed from a known satellite orbit.

Even if the model presented here can represent the wind explicitly, the same model can be identified from data without explicit modeling of the layer shifting, this was proved in Section Section 5.2.6, where the spatio-temporal covariance matrices necessary to compute the *VAR* model were computed using the sample cross-covariance.

Data-based Identification Advantages

The advantage of a data-based identification of the spatio-temporal covariances is that in this case the resulting model will capture not only the frozen flow behavior, but also other disturbances such as dome seeing, boiling turbulence, or mechanical vibrations. The use of the closed-loop *WFS* measurements as metrology source for the data-based identification also enables the update of the predictive model along the trajectory of the *LEO* satellite.

Measurement Concept

The identification method proposed for the predictive controller model developed in this thesis is the use of the spatio-temporal covariance matrices for the identification of a vector autoregressive process using the Yule-Walker equations; the method provides two advantages for the identification of the model: (1) Allows to compute the *VAR* model from its spatio-temporal covariance matrices, which can be computed analytically or measured from data; (2) the resulting model is guaranteed to be stable and does not require stability constraints as those searched in [Cranney et al. \(2018a\)](#).

Remark

This concept has already been tested by [Kelemu et al. \(2022\)](#) using a controller based on a VAR(2) model in the slopes space with very promising results for its application in predictive control. The concept is very interesting and should be emulated. However, the published results, although targeted for *LEO* downlinks use horizontal links simulations and their VAR(2) vs. VAR(1) tests do not allow to see the expected improvements in the case of *LEO* downlinks. They use an oversampled Shack-Hartmann to reduce the aliasing effect. Overall, this work is very interesting and should be merged with the findings of this thesis towards a future controller.

Requirements for the Data-Based Identification

The possible requirements for such an identification method are summarized below:

1. It shall use the Shack-Hartmann closed-loop measurements as primary data, with the satellite downlink as beacon.
2. It shall be robust to the measurement noise present in the Shack-Hartmann data.
3. It shall also provide a way to identify the statistics of the higher-order models necessary to reduce the effect of aliasing in the phase reconstruction within the associated controller.
4. It shall be recursive to enable the online update of the predictive model during the satellite trajectory.

The remainder of this section discusses how these requirements are satisfied.

Comparison to Tomographic Methods

As discussed in Chapter 5, the problems of temporal prediction and tomographic reconstruction are very similar in their nature and techniques. Most tomographic reconstructors are based on an *MMSE* ([Wallner 1983](#); [Whiteley et al. 1998b](#); [Fusco et al. 2001](#)) reconstructor that uses the covariances between the phases at the measurement directions and the correction direction; this is similar to the predictive modes such as the one discussed in this thesis, which is also based on such a *MMSE* solution but in this case applied to the covariances between the past phases and the future.

Nevertheless, there is an important difference between these two cases: For temporal prediction for the *LEO* satellite downlink, it is possible to measure both the past phases and the future phases (just with a delay) and compute the necessary covariance matrices; while tomographic reconstructors never measure the phase in

the correction direction. Instead, tomographic reconstructions need to identify the turbulence profile and compute the covariance matrices using analytical models. The identification of the profile can use an external metrology source or identify the profile from the measurements of the multiple *WFSs* available in the tomographic *AO* system.

Remark

The temporal covariance matrices can be measured in the case of the *LEO* downlink correction, since the corrected direction is the same as the measured direction; this is not the case in the tomographic cases [Correia et al. \(2014, 2015\)](#); [Cranney et al. \(2020\)](#), the temporal covariance matrices cannot be measured, as no measurement is available in the corrected direction.

Remark

The case of the *LEO* and *GEO* satellite uplinks are equivalent even closer to tomographic problems, since the measurement and correction directions are different. In this case, the covariance matrices can only be computed analytically and an identification method based on the downlink would be very beneficial.

This difference is noteworthy because the predictive controller can be identified directly from data by means of a sample covariance estimator.

Pitfalls of Naïve Covariance Matrix Estimation

The identification of the predictive model can be based on the computation of the necessary covariance matrices from data using the sample covariance estimator in Section 4.2.5.3; nevertheless, two possible problems may arise from such a naïve estimation:

1. The covariance estimator shall converge fast with respect to the change in turbulence conditions.
2. To reduce the effect of aliasing, the predictive controller needs the statistics of the modes of higher order than those that can be properly measured by the *WFS*; if this modes cannot be properly measured by the *WFS* it will be difficult to identify their statistics from these measurements.

Remark

The need for this convergence has not been identified yet; in the tests carried out during this thesis, the identification of the matrices was possible using between 5000 and 10000 time steps, corresponding to around 3 s and 6 s of data recording at $f_{\text{samp}} = 1500$ Hz, respectively. Nevertheless, within the simulation, the phase was projected onto a Zernike polynomial basis without any measurement noise; while in a instrumental implementation a Shack-Hartmann wavefront sensor and a phase reconstruction step are needed. As a result, new problems may arise during the estimation of covariance matrices that can be mitigated with the techniques discussed in this section.

6.3.2. Learn & Apply Method

The *learn & apply* ($L\mathcal{E}A$) method suggested by Vidal et al. (2010) is a very good source as a baseline of the identification strategy, since it deals with problems similar to those discussed above but for the case of tomographic reconstructors. The $L\mathcal{E}A$ is a method for identifying a tomographic reconstructor using data from several WFS s. This method is, in fact, very close to the predictive controller used in this thesis, since it only identifies the phase in the pupil plane; in fact, it can be seen as a specific implementation of the method of Correia et al. (2014) but, instead of using the covariances between phase vectors reconstructed on a Zernike polynomial basis, it uses the slopes measurements directly, avoiding additional calibration steps. In the following I present the method and the necessary extensions that it would require for its use for LEO satellite applications.

The method requires the covariances between the measurement and the correction direction, with the advantage that in this case it is only required at the pupil plane and not per layer as most tomographic reconstructions. As a result, at least part of these covariance matrices can be directly measured: the measurement-measurement covariances between different measurement directions can be estimated from the data; only the measurement-correction covariances cannot because the correction direction is not measured.

The main idea of the $L\mathcal{E}A$ method is to use a model of the covariance matrices that depends on different system parameters such as: the geometric configuration of the WFS s, possibly including the registration parameters between them; the altitude of each turbulence layer; the strength of each layer; etc. The measurement-measurement covariance matrices can be computed from data and the model can be fitted to them to obtain the parameters necessary for the rest of the covariances.

Remark

The Learn & Apply measurements are open-loop, while their application to the LEO tracking case would require pseudo-open-loop measurements.

The method is therefore divided into two steps:

1. *Learn*: Compute the covariance matrices from the data and fit a parametric model of the covariances to the measured covariance matrices.
2. *Apply*: Compute the covariance matrices from the fitted parameters, including the correction direction (not measured) thanks to the retrieved profile.

Thanks to these, four different problems are addressed:

1. The identification of the parameters that link the measurements between different wavefront sensors.
2. The acceleration of the convergence of the measurement.
3. The retrieval of the turbulence profile.
4. The computation of the covariances that cannot be measured directly thanks to the retrieved parameters (profile and *WFSs* registration parameters).

The first is not relevant for the case of *LEO* satellite downlink since it does not have several *WFSs*. The second will be discussed in Section 6.3.2. The third could be used in the case of the *LEO* satellite downlink to improve convergence or to compute higher order modes that cannot be estimated with the *WFS* measurements to reduce aliasing. Finally, the fourth is not necessary in the case of the *LEO* downlink, but it could be helpful for the *GEO* and *LEO* uplinks due to the presence of point ahead angle in the precompensation.

Remark

[Cranney et al. \(2020\)](#) has also extended the *LA* method to prediction. In this case, the article uses the fitted spatial model to compute the temporal model too, since in this case it cannot measure the temporal correlations at the direction of correction, as it was also the case for [Correia et al. \(2014, 2015\)](#). In the *LEO* satellite downlink case the temporal covariance matrices can be measured directly, so there is no need for a model; however, the model could be used to improve the convergence or to compute higher order modes for aliasing.

Improvement of Convergence

The acceleration of convergence is achieved thanks to the fitting of the model with an initial guess of the parameters, which helps by adding constraints based on physical priors to the covariance matrices and reduces the required number of samples for the estimation by imposing a structure on the model; the work of [Martin et al. \(2012\)](#) extended the study of the convergence of the covariance

matrix estimation and proposed an new model that allows faster fitting to improve convergence.

The need of this convergence for the case of temporal prediction needs to be studied; if necessary, it could be used, but to do this, it is necessary to make some modifications that will be discussed in Section 6.3.2.

Two other options are possible to improve the convergence of the of the covariance estimation without a model: (1) The use of a recursive covariance estimation, for example, using recursive least squares (van Kooten et al. 2019; Haffert et al. 2021; van Kooten et al. 2022), can also help to reduce this convergence issue without the need of fitting; (2) since the matrix structure in terms of non-zero entries and the order of magnitude of the entries are known, another option would be to use matrix tapering (Furrer et al. 2006; Ollila and Breloy 2021). These options are more interesting and should be investigated further since they would not require any optimization step and would allow the update of the model, see Section 6.4.

Profile Identification from *LEO* Downlink Beacon

The Learn & Apply method requires a modification to be used in with the measurement geometry of prediction in *LEO* satellite applications. The *LA* is able to retrieve the profile based on the measurement of the pupil plane covariances thanks to the fact that it uses several *WFS* measurements from different angles, which allows one to compute discriminate the layer heights by triangulation. Similar methods are also used for turbulence metrology, such as *slope detection and ranging* (*SLODAR*) (Wilson 2002; Butterley et al. 2006; Guesalaga et al. 2014); see Martin et al. (2016) for a comparison of the *LA* and those methods.

The work of Laidlaw et al. (Laidlaw et al. 2020, 2022) have worked on extending the models of *SLODAR* with the information of the wind layers. At the moment the method can still not discriminate layers in altitude, but only the strength and velocity of each layer, for the case of *LEO* tacking the altitude of the layers could be computed from assuming that only apparent wind is present, leading to complete retrieval of the profile using an *LA* like method.

Remark

Other single-source profile retrieval are possible (Habib et al. 2006; Védrenne et al. 2007; Tokovinin and Kornilov 2007); they use scintillation measurements and the associated correlations to discriminate the layer height. However, these methods require additional calibrations to measure scintillation, a significant increase of the number of variables in the estimation problem, and are limited to weak disturbances. However, these methodologies should still be taken into account, as they provide strong synergies with the work of Lognoné et al. (2022) for the estimation of the point-ahead angle anisoplanatism for *GEO* feeder links overcompensation by also using scintillation measurements in an *MMSE* method.

Identification of Higher Order Models

In order to reduce the effect of aliasing in the controller, the predictive controller requires an increase of the modes considered. This allows the phase reconstruction within the Kalman filter to better estimate the phase from aliased measurements. Section 7.3 will provide a detailed discussion on the effect of aliasing in the predictive controller and possible remedies.

When the predictive controller is identified from an analytical model, it is possible to compute as many modes as necessary. However, if the predictive controller is to be identified from *WFS* data, the identification of the higher order modes that are measurable but biased by aliasing will be challenging.

This is a challenge that still requires further optimizations; here, three solutions are envisioned, although not further investigated within this thesis:

1. Reconstruct more modes using an *MAP* phase reconstructor based on the theoretical spatial covariance matrix, which only requires r_0 but not the profile.
2. Use the fitted atmospheric profile from the *L&A* to compute the covariances analytically.
3. Use an over sampled Shack-Hartmann *WFS* to reduce aliasing. In this case there is no need to estimate more modes, only the modes to be corrected are estimated, but now they are not aliased. This could be done in optical communications case since there is more flux available; however, it comes with an additional computational cost, since it will increase the number of pixels in the *SH* detector, as well as the number of slopes to be processed.

6.3.3. Other Identification Methods

Another option for the data-based identification of the predictive model is to use general subspace identification methods (Chiuso et al. 2007) on modes (Sinquin et al. 2020), zonal basis, or slopes, that identify a state-space model from the closed-loop measurements.

The methods based on *principal component analysis* (*PCA*) can produce data-based identification of *VAR* models on an orthogonal modal basis that is optimized for the turbulence spatial statistics, in the case of *PCA* (Beghi et al. 2007), or in the spatio-temporal ones, in the case of *dynamic mode decomposition* (*DMD*) (Shaffer et al. 2021) and its related method the *empirical orthogonal functions* (*EOF*) (Guyon and Males 2017). It should be noted that if *DMD* methods are used, their higher order version (Le Clainche and Vega 2017) would lead to the same performance improvements observed with the *VAR* models. This method can lead to predictive models with an optimized number of modes, but since the modes depend on the turbulence statistics, they will need to be updated with the

adaptation of the controller, which adds additional complexity. Finally, the lack of physical constraints on the identification leads to slower convergence of the model identification.

6.4. Model Update and Adaptation

In *LEO* satellite applications, satellite tracking implies a fast change in the line of sight. Consequently, predictive models, which are specific to the turbulence conditions, must be frequently updated to maintain their performance. A comprehensive examination of predictive controller adaptation is beyond this thesis's scope, though some insights are provided below.

Two different model identification philosophies are possible:

1. Use the model identification based on analytical computations to precompute the controller model.
2. Identify the predictive model recursively from data.

In both cases, two different controller update strategies are suggested:

1. Update the model at every time step within the Kalman filter; this leads to a smooth trajectory since the variation of the model is not very big.
2. Update the model less frequently and use the method by [Raynaud et al. \(2016\)](#) to ensure a bumpless switching between controllers.

6.4.1. Analytical Model Update

The main advantage of the identification method proposed in this thesis is that the predictive model and the Kalman filter can be precomputed for the entire orbit before satellite tracking starts. Assuming that the turbulence profile (and possibly the natural wind profile) is available from another metrology source, the profile can be measured prior to the satellite tracking and extrapolated to all elevations from which the satellite will be observed by projecting it. The apparent wind component can be computed from the knowledge of the satellite.

6.4.2. Data-Based Recursive Model Update

As discussed in Section 6.3 the predictive method necessary for the controller can be computed from its covariance matrices. These matrices could be estimated recursively and used to compute a new predictive model at each time step after their update. This idea has been applied by [van Kooten et al. \(2019, 2020, 2022\)](#) to compute an *MMSE* predictor from covariance matrices computed with a recursive sample covariance estimator. The recursive update of the inverse of the

measurement-measurement covariance matrix provides computational savings. A forgetting factor is included to account for the change in turbulence conditions.

Alternatively, a recursive identification of the *VAR* model without the estimation of the spatio-temporal covariance matrices could be done. Haffert et al. (2021) suggested a data-based *VAR* identification method that uses recursive least squares instead of the Yule-Walker equations with estimated covariance matrices.

* * *

Summary

This chapter presented the predictive controller developed during this thesis, as well as possible improvements and extensions to it. The controller uses as a predictive model a Zernike polynomial phase representation and a *VAR* process identified from the analytical computation of the turbulence spatio-temporal covariance matrices. A second order *VAR* process is used, since it leads to an important increase with respect to the first order as seen in Section 5.2.3.

Compared to other methods, we find that the covariance matrices have several advantages. When identified from data, they can capture all types of turbulence, not only turbulence frozen flow. They can also benefit from the computation analytical formulas for their computation or, in the case of their data-based identification, from many robust covariance estimation methods from the literature, including all the methods in tomographic adaptive optics and adaptive optics turbulence profiling.

It has been highlighted that the analytical evaluation of those presents several advantages, but that their data-based identification should also be further investigated. It has also been seen how, in the case of *LEO* downlink, the spatio-temporal covariance matrices can be measured directly by the *WFS*. Finally, the spatio-temporal covariance matrices can be estimated recursively to allow the adaptation of the controller to adapt to the change in turbulence conditions during the orbit of the satellite.

The next chapter provides end-to-end simulations of the controller and studies the gains in performance associated with its use.

7. Predictive Controller Results

Contents

7.1. Simulation Methodology	148
7.1.1. Simulation Strategy	148
7.1.2. Simulations Implementation	149
7.2. Ideal Wavefront Sensor and Deformable Mirror	151
7.2.1. Comparison with the <i>MMSE</i> Predictability Assessment	152
7.2.2. Behavior in the Presence of Measurement Noise	154
7.2.3. Conclusions	154
7.3. Effect of Aliasing and Modal Reconstruction	156
7.3.1. Problem Statement	156
7.3.2. Aliasing in Predictive Controllers	156
7.3.3. Analytical Study of Modal Reconstruction with <i>MAP</i>	157
7.3.4. Methodology	157
7.3.5. Case 1: 8×8 <i>SH</i> and $n_{\text{cor}} = 10$ <i>DM</i>	161
7.3.6. Case 2: 16×16 <i>SH</i> and $n_{\text{cor}} = 20$ <i>DM</i>	164
7.3.7. Case 3: <i>LISA</i> and <i>FEELINGS</i>	165
7.3.8. Case 4: Oversampled 16×16 <i>SH</i> and $n_{\text{cor}} = 10$ <i>DM</i>	166
7.3.9. Case 5: Effect of Telescope Aperture Obscuration	167
7.3.10. Conclusions	167
7.4. End-to-End Simulations	170
7.5. Reduction of the Loop Sampling Frequency	172
7.6. Effect of Fadings	173
7.7. Strehl Ratio	175

Introduction

This chapter reports the end-to-end simulation results for the predictive controller proposed in this thesis. First, the performance of the controller is evaluated in terms of residual variance and compared to the *AO* error budget as a cross-validation of the simulation and the budgets; the results are also compared to the predictability assessment in Chapter 5 to evaluate if the expected gains due to prediction are achieved. Second, the performance is evaluated in terms of the metrics relevant for each application: fiber coupling for communications and the Strehl ratio for satellite observation. The end-to-end simulations also serve to study the impact of phase reconstruction and aliasing, which are not properly accounted for in the analytical modeling presented so far.

7.1. Simulation Methodology

End-to-end simulations are crucial in the development of controllers for adaptive optics systems. They provide a realistic model of various factors that could affect the controller during operation, including phenomena like aliasing in the wavefront sensor measurements. The simulations provide access to data that may be difficult to obtain in a lab environment, e.g. perfect measurement of phase, thereby making it easier to study the system's performance. The outcomes of these simulations serve as a performance model to validate the actual implementation of controllers in a real-world adaptive optics system.

The controller proposed in Chapter 6 is tested in the present chapter by means of end-to-end simulations. Section 7.1.1 provides an overview of the simulation strategy for the predictive controller evaluation. The details of the end-to-end simulation implementation are given in Section 7.1.2. The results for the simulations are reported and analyzed in the rest of this chapter.

7.1.1. Simulation Strategy

The first simulation of the controller employs a simplified *AO* system model, with results detailed in Section 7.2. This simulation is designed for better comparison with the *MMSE* predictability assessment. It uses an ideal wavefront sensor that directly measures Zernike polynomials, thereby eliminating issues related to modal reconstruction from Shack-Hartmann *WFS* slopes. The deformable mirror in the simulation is also ideal, perfectly fitting the Zernike polynomials without error.

In Section 7.3, the introduction of a realistic Shack-Hartmann wavefront sensor into the simulations shows that aliasing in slope measurements significantly degrades the controller performance. This section delves into the origins of this problem and proposes different solutions to address it.

After mitigating the effect of aliasing in the controller, the results of the end-to-end simulations for the controller applied to the different *AO* system configurations defined in Chapter 3 are analyzed in terms of residual phase variance. These results are compared with the theoretical expectations from the *AO* error budgets and the turbulence predictability assessment presented in Chapter 5. This analysis is complemented by Section 7.5, where the same simulations are carried out at a lower *AO* loop frequency to evaluate the feasibility of reducing system requirements using predictive control.

Finally, Section 7.6 and Section 7.7 report the analysis of the coupling performance and the Strehl ratio, respectively, for the end-to-end simulations carried out.

7.1.2. Simulations Implementation

The present section gives a brief description of the implementation of the end-to-end simulations reported in this chapter.

Operating point: In order to reduce the number of simulations conducted, all the simulations presented in this chapter correspond to an elevation of 30° , unless stated otherwise. A complete assessment of the controller performance across a *LEO* orbit would require simulations at all possible elevations. The aim of this thesis is not to provide a detailed analysis of the performance of any controller but to study the behavior of the controllers at the relevant regimes and compare those to the analytical performance assessments that allow the extrapolation of performances to other elevations.

An elevation of 30° is chosen since it is the case where the temporal error is the highest without facing too strong turbulence (see Figure 3.11), where the strong perturbation regime will pose additional challenges to the *AO* loop. Within this thesis, the performance of the predictive controller is only evaluated in the weak perturbation regime; an extension of the controller to the strong perturbation regime, especially the work under strong scintillation conditions, is a natural continuation of the work in this thesis.

Turbulence distorted electromagnetic field at the pupil: The atmosphere is simulated as a profile of phase screens (around 40 layers) that simulate the atmospheric layers. The phase screens are generated using the method of extrusion of phase screens by Assémat et al. (2006) and Fried and Clark (2008). A geometric propagation of the electric field from each of the layers to the pupil is used; no diffractive effects in phase or amplitude (i.e. scintillation) are part of the simulations. The use of geometric phase propagation reduced the computation time of the simulations and also enabled the analysis of residual phase without having to deal with phase unwrapping. This is also a common choice for the simulation of *AO* controllers (Correia et al. 2015; Prengère et al. 2020).

Wavefront sensor model: A geometric Shack-Hartmann *WFS* model is used. The model computes the slopes of the phase by computing the average phase difference between the edges of each subpupil; as a result, this model only accounts for the effect of phase in the Shack-Hartmann *WFS* and neglects scintillation. The simplified simulations presented in 7.2 use an ideal wavefront sensor that can directly measure Zernike modes; this is implemented as a direct projection of the turbulent phase at the telescope pupil onto the Zernike modes considered.

Measurement SNR levels: In order to test the controller at different measurement noise levels, the *SNR* is defined using Equation 3.17. For the geometric *SH* model, the measurement noise is computed in the slopes space, in units of pixels squared and added to the slopes measurements as a zero-mean Gaussian random variable with the variance computed using the formula provided. For the case of the ideal *WFS*, the noise per Zernike coefficient is computed using the noise propagation formulas from Rigaut and Gendron (1992).

pyGAOS simulation tool: All end-to-end adaptive optics simulations were performed using the *Python geometric adaptive optics simulator (pyGAOS)*; a tool I developed this tool as part of my thesis. Its core is a Python implementation of many different *IDL* codes by *ONERA* that have been reorganized and extended for the simulations of this thesis. All the functionalities are wrapped in an object-oriented architecture that allows the parametrization of simulations and the extension of the simulator, especially for the development of new control solutions. Despite its name, *pyGAOS* can also work with complex field inputs, for example, coming from the *TURANDOT* optical propagation tool.

Controllers: The *pyGAOS* simulator is able to run an arbitrary number of controllers for the same end-to-end simulation. All controllers see the same open-loop turbulence and have the same *DM* and *WFS* models. At every iteration of the simulation loop, the controller applies its corrected phase and measures the residual phase, then runs a routine to compute the next command based on the measurement and the data stored in the internal buffers of the controller. This common structure allows the implementation of new controllers and their comparison to others.

Integral action controller: The simulations presented in this chapter will use a scalar-optimized integrator as a comparison to the predictive controller. The scalar optimization is not the ultimate performance that could be achieved with an integral action controller, since it would be possible to use modal optimization, but it provides a sufficient benchmark. In any case, the integral action controller should have much lower performance than the predictive controller, so the comparison of the two is deemed enough to illustrate the two possible regimes in the system performance: with and without predictive control.

Residual phase variance: The results of the end-to-end simulations for the *AO* controllers are first reported in terms of their phase variance. This allows a better comparison of the results to the *AO* budgets and other theoretical predictions such as the predictability assessment from Chapter 5.

Additional performance metrics: Apart from the analysis of the residual phase variances, the analysis of the end-to-end simulations in this chapter will focus on two performance metrics, one per application considered: (1) The coupling into an optical fiber and the depth and frequency of fadings (see Section 3.3.2.1), for the case of optical communications; and (2) the Strehl ratio (see Section 3.3.1.2), for the satellite observation application.

7.2. Ideal Wavefront Sensor and Deformable Mirror

We first report and analyze the results of the simulations of the controller using simplified models for the wavefront sensor and deformable mirror, which can measure and correct, respectively, a given set of Zernike polynomials.

A Shack-Hartmann wavefront sensor measures local wavefront slopes, necessitating modal reconstruction to obtain wavefronts represented in a Zernike polynomial basis (see Section 2.4.5). Modal reconstruction introduces errors, including those stemming from poorly observed modes, numerical computations, measurement noise in the *WFS*, and aliasing. Similarly, deformable mirror influence functions cannot perfectly match the shape of Zernike polynomials. Initially, we avoid these errors to focus on the comparison of the performance of the predictive controller with respect to the predictability assessment in Chapter 5; since the predictive model used for both the controller and the predictability assessment is the same, the comparison is direct.

Remark

The results of similar simulations were presented at the *IEEE International Conference on Space Optical Systems and Applications (ICSOS) 2022* workshop as a talk without proceeding and at the *SPIE Astronomical Telescopes + Instrumentation 2022* conference as a talk with proceeding [Robles et al. \(2022\)](#).

Despite its inherent limitations, simulating an idealized system holds value in the development and validation of the predictive controller's performance for various purposes:

- To verify the implementation of the *LQG* controller.
- To compare the results of the simulations with the *AO* error budget.

- To compare the results of the simulations with the *MMSE* predictability assessment presented in Chapter 5.1.

7.2.1. Comparison with the *MMSE* Predictability Assessment

Table 7.1 reports the results of the simulations. Simulations were carried out for the two smaller systems: *LISA* and *ODISSEE*. Two controllers were simulated: a scalar optimized integral action controller and the predictive controller. Both systems were modeled with a *WFS* and *DM* that can measure and correct, respectively, a Zernike polynomial basis with maximum radial order $n_{\max} = 10$.

The average residual phase variance of the simulation is reported in three different terms:

- ϕ^{\parallel} , the phase projected onto the *DM*, which corresponds to the temporal error and the measurement noise error. There is no aliasing since an ideal *WFS* is used, for the case of the simulations with a realistic Shack-Hartmann *WFS* this will also include the errors due to phase reconstruction and aliasing.
- ϕ^{\perp} , the phase orthogonal to the *DM*, which corresponds to the fitting error. This term is the same for all controllers, as it depends only on the spatial frequencies of turbulence that can be corrected by the *DM*.
- ϕ^{res} , the sum of both terms.

The simulations use $\text{SNR} = 100$, so the measurement noise is negligible here. The simulations use a time series of 10000 steps per case. The table also gives the theoretical predictions using the *MMSE* predictability assessment, since the basis used is the same as the one used by the *WFS* and the *DM*, the comparison here is straightforward. The results are also compared with the *AO* error budgets from Table 3.2.

Remark

This thesis quantifies the gain from prediction as the percentage of temporal error remaining after prediction. Consequently, lower percentage values indicate superior prediction performance.

Firstly, the fitting error is consistent with the values of the error budget; the differences observed can be attributed to the lack of statistical convergence, since a unique simulation is used for each case, corresponding to a unique statistical realization of each phase screen.

In the same way, the integrator performance in terms of temporal error is in accordance with the error budgets for both cases. However, it is worse than the one given by the *MMSE* for the no prediction, $\mathbf{R}_{\text{MMSE}}^{(s=2,p=0)}$. This behavior is consistent with all simulations, which implies that the no-prediction *MMSE* may be

optimistic with respect to the integrator; if this was true, the gains due to predictive control with respect to the integrator could be even higher than expected from the *MMSE* predictability assessment. One possible explanation for the optimistic behavior of the *MMSE* assessment is that it is closer to the performance of a modal gain optimized integrator (under the assumption of no measurement noise); this hypothesis would require further investigation to be confirmed.

The performance of the predictive controller in terms of temporal error is consistent with the *MMSE* assessment for both cases. The observed gains are better than for the *MMSE* assessment due to the poorer performance of the integrator with respect to the case of no prediction. Once again, the observed discrepancies can be attributed to statistical convergence within the simulations; this assertion is supported by the fact that the simplified *LQG* implementation presented in this section is equivalent to the application of the predictive model to a time series as presented in Section 5.2.6, see the next remark box.

Table 7.1.: Results for the simplified *E2E* controller simulation and comparison with respect to the predictability assessment. Results are given in variance of the residual phase with units of rad^2 .

	<i>LISA</i>	<i>ODISSEE</i>
Integrator, ϕ^{\parallel}	$2.665 \cdot 10^{-1}$	$7.243 \cdot 10^{-1}$
Integrator, ϕ^{\perp}	$4.465 \cdot 10^{-1}$	$5.325 \cdot 10^{-1}$
Integrator, ϕ^{res}	$7.130 \cdot 10^{-1}$	1.257
<i>LQG</i> -VAR(2), ϕ^{\parallel}	$3.382 \cdot 10^{-2}$	$4.238 \cdot 10^{-2}$
<i>LQG</i> -VAR(2), ϕ^{\perp}	$4.465 \cdot 10^{-1}$	$5.325 \cdot 10^{-1}$
<i>LQG</i> -VAR(2), ϕ^{res}	$4.804 \cdot 10^{-1}$	$5.748 \cdot 10^{-1}$
Theo. $\mathbf{R}_{\text{MMSE}}^{(s=2,p=0)}$, ϕ^{\parallel}	$1.571 \cdot 10^{-1}$	$5.638 \cdot 10^{-1}$
Theo. $\mathbf{R}_{\text{MMSE}}^{(s=2,p=2)}$, ϕ^{\parallel}	$3.866 \cdot 10^{-2}$	$5.088 \cdot 10^{-2}$
Gain <i>LQG</i> -VAR(2) (%)	12.69	5.85
Gain Theo. <i>MMSE</i> (%)	24.61	9.02

Remark

In the context of the simplified simulation of the predictive controller in this section, the application of the LQG is analogous to the iterative implementation of the predictor, as discussed in Section 5.2.6.

Since no measurement noise, modal reconstruction errors, or DM mismatch are considered, the LQG merely executes the predictive model. Under these assumptions, the input data utilized by the predictive model for prediction computation lack uncertainty, resulting in prediction error as the only source of error.

7.2.2. Behavior in the Presence of Measurement Noise

In the absence of modeling errors in the turbulence evolution model (i.e. the predictive model) utilized by the Kalman filter, the LQG controller delivers optimal noise filtering. However, this optimality is not guaranteed when using an arbitrary predictive model, such as a vector autoregressive model in a Zernike modal basis, to approximate the real turbulence evolution caused by the combined effect of the shifting of each layer. Therefore, this test was conducted to determine that the LQG controller does not amplify noise due to modeling errors.

The controller was simulated at different SNR levels to test its behavior in the presence of noise; Table 7.2 presents the results of these simulations for the *ODISSEE* system.

For all noise levels, the predictive controller consistently outperforms the integrator. When measurement noise levels increase significantly, the performance of both controllers is driven by the propagation of measurement noise throughout the control system; here the importance of temporal error and the use of prediction decreases, but LQG still provides performance improvements thanks to its optimal filtering of measurement noise by the LQG controller. Notably, the predictive controller does not exhibit any unusual noise behavior that could be attributed to modeling errors in the predictive model.

7.2.3. Conclusions

The initial tests involving a simplified implementation of the predictive controller served the purpose of verifying the implementation of the LQG controller and its predictive model. The performance achieved aligns with the $MMSE$ predictability assessment, which promises significant performance gains if it can be maintained by a final controller implementation.

Furthermore, the simulations conducted with increasing noise levels demonstrated that the predictive controller does not amplify measurement noise due to modeling error and consistently outperforms the integral controller, even at high noise levels.

The next step in the testing of predictive controllers involves incorporating a realistic deformable mirror and, notably, a realistic wavefront sensor to investigate

7. Predictive Controller Results
7.2. Ideal Wavefront Sensor and Deformable Mirror

Table 7.2.: Performance of the controller as a function of *SNR*, *ODISSEE* case at 30° elevation. Results are given in variance of the residual phase with units of rad².

<i>SNR</i>	1	5	10	30
Integrator, ϕ^{\parallel}	1.660	$8.109 \cdot 10^{-1}$	$7.454 \cdot 10^{-1}$	$7.268 \cdot 10^{-1}$
Integrator, ϕ^{\perp}	$5.325 \cdot 10^{-1}$	$5.325 \cdot 10^{-1}$	$5.325 \cdot 10^{-1}$	$5.325 \cdot 10^{-1}$
Integrator, ϕ^{res}	2.199	1.343	1.278	1.259
<i>LQG</i> -VAR(2), ϕ^{\parallel}	$8.111 \cdot 10^{-1}$	$1.746 \cdot 10^{-1}$	$9.934 \cdot 10^{-2}$	$5.466 \cdot 10^{-2}$
<i>LQG</i> -VAR(2), ϕ^{\perp}	$5.325 \cdot 10^{-1}$	$5.325 \cdot 10^{-1}$	$5.325 \cdot 10^{-1}$	$5.325 \cdot 10^{-1}$
<i>LQG</i> -VAR(2), ϕ^{res}	1.344	$7.070 \cdot 10^{-1}$	$6.318 \cdot 10^{-1}$	$5.871 \cdot 10^{-1}$
Gain (%)	48.85	21.53	13.33	7.52
<i>SNR</i>	50	100	500	
Integrator, ϕ^{\parallel}	$7.251 \cdot 10^{-1}$	$7.243 \cdot 10^{-1}$	$7.241 \cdot 10^{-1}$	
Integrator, ϕ^{\perp}	$5.325 \cdot 10^{-1}$	$5.325 \cdot 10^{-1}$	$5.325 \cdot 10^{-1}$	
Integrator, ϕ^{res}	1.258	1.257	1.257	
<i>LQG</i> -VAR(2), ϕ^{\parallel}	$4.708 \cdot 10^{-2}$	$4.238 \cdot 10^{-2}$	$4.014 \cdot 10^{-2}$	
<i>LQG</i> -VAR(2), ϕ^{\perp}	$5.325 \cdot 10^{-1}$	$5.325 \cdot 10^{-1}$	$5.325 \cdot 10^{-1}$	
<i>LQG</i> -VAR(2), ϕ^{res}	$5.795 \cdot 10^{-1}$	$5.748 \cdot 10^{-1}$	$5.726 \cdot 10^{-1}$	
Gain (%)	6.49	5.85	5.54	

the controller's behavior when phase reconstruction becomes necessary and the presence of aliasing propagates across it.

7.3. Effect of Aliasing and Modal Reconstruction

7.3.1. Problem Statement

The introduction of a Shack-Hartmann wavefront sensor in the simulations brings two new problems:

1. The need for phase reconstruction from the *SH* slope space to the Zernike modal basis used by the controller.
2. The presence of aliasing in the *SH* measurements, which can be seen as an additional noise term that will propagate within the phase reconstruction.

This is also true for the integral controller, where the phase reconstruction is computed by the control matrix (see Section 2.4.2) from the slopes space to the *DM* actuator space, with the aliasing error in the slopes propagating to the residual phase variance as a given by Equation 2.5.2.2. This section presents a study of the effect of these problems on the predictive controller and possible solutions to them.

As stated in Section 4.3.3.4, the Kalman filter within the *LQG* includes the phase reconstruction of the measured wavefront from the slope measurements. This reconstruction is similar to a *MAP* reconstruction, but enhanced with the iterative estimation and temporal information that the Kalman filter adds with respect to static estimators.

Remark

Performing a phase reconstruction is not necessarily a disadvantage. As for traditional adaptive optics (see Section 2.4.5) modal reconstruction achieves better noise rejection by truncating modes with low *SNR* and both modal and zonal phase reconstruction provide (at least partially) dealiasing of the slope measurements.

7.3.2. Aliasing in Predictive Controllers

For *LQG* controllers, the aliasing error propagates in the controller and causes greater errors (Petit et al. 2009; Kulcsár et al. 2012; Juvénal et al. 2018). As a result, a solution to decrease aliasing needs to be considered in the design of this kind of controller.

Three main alternatives exist in order to reduce aliasing in a *LQG* controller:

1. Spatial filtering of the *PSF* before the wavefront sensor.
2. Conducting phase reconstruction on higher spatial frequencies, i.e. increasing the number of models considered in the controller.
3. Increasing the number of subpupils (i.e. oversampling) in the Shack-Hartmann.

Spatial filtering (Poyneer and Macintosh 2004; Fusco et al. 2005) allows filtering out all high-spatial frequencies that cannot be corrected by the *DM* but contribute to aliasing. This strategy is feasible for coronagraphic applications where it is possible to do spatial filtering on the close to diffraction-limited *PSF* delivered by an extreme *AO* system with very high performance.

Increasing the number of subapertures in the Shack-Hartmann wavefront sensor increases the maximum sampling frequency and reduces the amount of spectrum folding that affects the spatial frequencies that can be corrected by the *DM*. The drawback of this method is that it increases the size of the matrices involved in the controller computation, since the number of measurements increases and the photon flux needs to be split among more subapertures, reducing the *SNR* per subaperture.

Reconstructing higher frequencies with a phase reconstructor regularized with the phase statistics (such as the *MAP* reconstructor) decreases the aliasing error in the spatial frequencies of interest. In the case of modal controllers, this is equivalent to reconstructing more Zernike polynomial radial orders Petit et al. (2009); Juvénal et al. (2018), while in the case of zonal controllers, it is equivalent to oversampling the zonal reconstruction basis (Prengère et al. 2020). Prengère et al. (2020) establish the oversampling necessary to correct for aliasing by conducting end-to-end simulations with oversampling factors and choosing the one for which performance converges. The rest of this section is devoted to an analysis of the propagation of aliasing error in the case of the modal reconstruction into Zernike polynomials.

Additionally, a fourth method is presented by Poyneer and Véran (2010) to treat aliasing in the case of Fourier space predictive control (Poyneer et al. 2007); the method is able to identify the aliased components in the Fourier spectrum and filter them out.

7.3.3. Analytical Study of Modal Reconstruction with *MAP*

To gain deeper insight into the errors associated with the modal reconstruction within the *LQG* predictive controller, a study of the performance of the modal reconstruction using the *MAP* estimator was conducted. This analysis will help to understand the performance limitations observed in the end-to-end simulations of the predictive controller.

7.3.4. Methodology

As stated in Section 4.3.3.4, the *MAP* estimator is equivalent to a static Kalman filter. Since the *MAP* estimator performance is easier to analyze, it is used as a proxy to understand the behavior of the modal reconstruction within the Kalman filter. This analysis is similar to the one presented in Quirós-Pacheco et al. (2010) for the case of modal gain optimization for tomographic adaptive optics.

Juvé \acute{n} al et al. (2018) already provided an analysis of the aliasing error as a function of the number of modes considered in the LQG controller, this time using a transfer function model of the LQG . The advantage of their model is that it includes the propagation of the aliasing error in the closed-loop, whereas the analysis presented here only accounts for an approximation of the open-loop phase reconstruction. However, the results of the suggested approach have been proven to be consistent with the behavior of the LQG , and the analysis has the advantage that it is expressed in terms of covariance matrices as in the rest of the controller modeling.

Modeling of the problem using the Zernike polynomials: The Zernike polynomials are used to model the problem, and several bases are defined:

- The turbulent phase at the telescope pupil is projected onto a modal basis containing the first N_t Zernike polynomials, piston mode not included, or the equivalent n_{tur} radial order, resulting in the vector $\phi^{\text{tur}} \in \mathbb{R}^{N_t \times 1}$. Since this basis has a finite number of modes, the variance of the modes not considered by this truncation constitutes a modeling error, commonly known as superfitting.
- The number of modes considered in the estimation defines the vector $\phi^{\text{est}} \in \mathbb{R}^{N_e \times 1}$, where N_e is the number of estimated Zernike polynomials and n_{est} the equivalent radial order.
- The AO system DM corrects only a set of Zernike modes, $\phi^{\text{cor}} \in \mathbb{R}^{N_c \times 1}$, where N_c is the number of corrected Zernike polynomials and n_{cor} the equivalent radial order.
- The modes between N_c and N_t correspond to the fitting error, with $N_c \leq N_e$.

MAP reconstructor: Consider the resulting measurement vector of a Shack-Hartmann wavefront sensor represented by a linear model when facing turbulence projected on a Zernike modal basis:

$$\mathbf{y} = \mathbf{M}_{\text{WFS}}^{\text{est}} \phi^{\text{est}}, \quad (7.1)$$

where $\mathbf{M}_{\text{WFS}}^{\text{est}} \in \mathbb{R}^{N_s \times N_e}$ is the interaction matrix between the Zernike polynomial basis and the WFS , with N_s the number of slope measurements provided by the WFS , and $\mathbf{y} \in \mathbb{R}^{N_s \times 1}$ is the resulting slopes measurement vector.

We search to minimize the reconstruction error:

$$\phi^{\text{est}} - \mathbf{R}_{\text{MAP}} \mathbf{M}_{\text{WFS}}^{\text{est}} \phi^{\text{est}}, \quad (7.2)$$

where $\mathbf{R}_{\text{MAP}} \in \mathbb{R}^{N_e \times N_s}$ is the MAP reconstructor. The MAP reconstructor is computed as:

7. Predictive Controller Results
7.3. Effect of Aliasing and Modal Reconstruction

$$\mathbf{R}_{\text{MAP}} = \Sigma_{\phi^{\text{est}}} (\mathbf{M}_{\text{WFS}}^{\text{est}})^{\top} (\mathbf{M}_{\text{WFS}}^{\text{est}} \Sigma_{\phi^{\text{est}}} (\mathbf{M}_{\text{WFS}}^{\text{est}})^{\top} + \alpha \Sigma_{\mathbf{w}})^{-1}, \quad (7.3)$$

where $\Sigma_{\phi^{\text{est}}} \in \mathbb{R}^{N_e \times N_e}$ corresponds to the covariance matrix of the wavefront, $\Sigma_{\mathbf{w}} \in \mathbb{R}^{N_s \times N_s}$ is the covariance matrix of the measurement noise, and α is a fudge factor that can be tuned to act as regularization parameter to compensate for possible modeling errors.

Remark

While the theoretical formalism of the Kalman filter ensures that its estimates will be optimal, its practical implementation requires the use of fudge factors. Fudge factors are artificial adjustments made to the Kalman filter matrices to compensate for modeling inaccuracies in any of these matrices. These factors are usually applied to the measurement noise and process noise covariance matrices, and can also be seen as the empirical tuning of these matrices.

Traditionally, fudge factors in *AO* systems have been applied to the noise covariance matrix. Increasing the noise of the covariance matrix has two effects: (1) It helps the numerical stability of the phase reconstruction by providing a Tikhonov regularization, and (2) it introduces the uncertainty in the measurement model by increasing the noise associated with the measurements.

If the uncertainty is not in the measurement but in the predictive model, the fudge factor should be applied to the process noise covariance matrix instead. This is the case where temporal prediction is the main goal, such as in this thesis; so probably the system would benefit from both fudge factors, one for the prediction, and one for the phase reconstruction.

MAP reconstruction error: The total reconstruction error will be the sum of the reconstruction error and the propagation of noise in the reconstructor.

The reconstruction error is defined as:

$$\phi^{\text{est}} - \mathbf{R}_{\text{MAP}} \mathbf{M}_{\text{WFS}}^{\text{tur}} \phi^{\text{tur}}, \quad (7.4)$$

where $\mathbf{M}_{\text{WFS}}^{\text{tur}} \in \mathbb{R}^{N_s \times N_t}$ is the interaction matrix between the Zernike polynomial basis until N_s and the *WFS*, using $N_t > N_e$ allows to compute the reconstruction error accounting for the contribution of the turbulence that is not estimated, necessary to account for the effect of aliasing. The reconstruction error covariance matrix can be computed as:

$$\begin{aligned} \Sigma_e &= \Sigma_{\phi^{\text{est}}} - \mathbf{R}_{\text{MAP}} \mathbf{M}_{\text{WFS}}^{\text{tur}} \Sigma_{\phi^{\text{tur}}} \phi^{\text{est}} \\ &\quad - \Sigma_{\phi^{\text{est}}}^{\top} \phi^{\text{tur}} (\mathbf{M}_{\text{WFS}}^{\text{tur}})^{\top} \mathbf{R}_{\text{MAP}}^{\top} \\ &\quad + \mathbf{R}_{\text{MAP}} \mathbf{M}_{\text{WFS}}^{\text{tur}} \Sigma_{\phi^{\text{tur}}} (\mathbf{M}_{\text{WFS}}^{\text{tur}})^{\top} \mathbf{R}_{\text{MAP}}^{\top}, \end{aligned} \quad (7.5)$$

where $\Sigma_{\phi^{\text{tur}}\phi^{\text{est}}}$ in $\mathbb{R}^{N_t \times N_e}$ is the cross-covariance matrix between the vectors ϕ^{tur} and ϕ^{est} .

The reconstructor matrix, $\mathbf{R}_{\text{MAP}} \in \mathbb{R}^{N_e \times N_s}$, can be truncated to be an $(N_c \times N_s)$ matrix to consider only the reconstruction of the modes of interest, in this case the modes to be corrected.

The reconstruction error is computed as:

$$\sigma_{\phi}^2 = \text{Tr}(\mathbf{\Gamma}\Sigma_e\mathbf{\Gamma}^{\top}), \quad (7.6)$$

where $\mathbf{\Gamma}$ is a matrix that truncates the covariance matrix to account for only the modes that are corrected, i.e. up to N_c .

The propagation of the measurement noise across the reconstructor, assuming that measurement noise and the wavefront phase are statistically uncorrelated, is computed as:

$$\sigma_w^2 = \text{Tr}(\mathbf{\Gamma}\mathbf{R}_{\text{MAP}}\Sigma_w\mathbf{R}_{\text{MAP}}^{\top}\mathbf{\Gamma}^{\top}). \quad (7.7)$$

During this study, the systems under study will have a fixed n_{cor} depending on their DM while n_{est} will be varied to study the behavior of aliasing with respect to the number of corrected modes.

Remark

Using a higher number of modes for the computation of the *MAP* reconstructor will lead to better performance in the estimation. At the same time, the final size of \mathbf{R}_{MAP} after truncation is $(N_c \times N_s)$ and it does not depend on N_e , so the *MAP* reconstruction can be computed with as many modes as possible for better performance without increasing the size of the reconstructor once computed. This is not the case for phase reconstruction within the Kalman filter, where the number of states in the controller will be N_e , i.e. no truncation possible, so increasing it will lead to additional computational cost.

Cases considered: Two of the four *AO* systems are used here to illustrate the different system parameters and regimes:

- *Case 1:* The *ODISSEE* system, with an 8×8 subapertures Shack-Hartmann *WFS* and able to correct $n_{\text{cor}} = 10$ Zernike polynomial radial orders. This corresponds to the strategy of reconstructing more modes to de-alias the measurements.
- *Case 2:* The *ODISSEE++* system, with a 16×16 subapertures Shack-Hartmann *WFS* and able to correct $n_{\text{cor}} = 20$ Zernike polynomial radial orders. This corresponds to the strategy of reconstructing more modes to de-alias the measurements, but with a system that has higher spatial sampling of the phase, which should reduce aliasing too.

- *Case 3*: The *LISA* and the *FEELINGS* cases, whose *WFS* and *DM* correspond to the two previous cases, respectively.
- *Case 4*: The *ODISSEE* system, with a 16×16 subapertures Shack-Hartmann *WFS* and able to correct $n_{\text{cor}} = 10$ Zernike polynomial radial orders. This corresponds to the strategy of oversampling the *WFS* with respect to the *DM* actuator number to reduce aliasing.
- *Case 5*: The *ODISSEE* and *ODISSEE++* systems but with telescope aperture obscuration.

For the provided examples, the atmospheric turbulence profile corresponding to each *AO* system is used at 30° elevation.

7.3.5. Case 1: 8×8 SH and $n_{\text{cor}} = 10$ DM

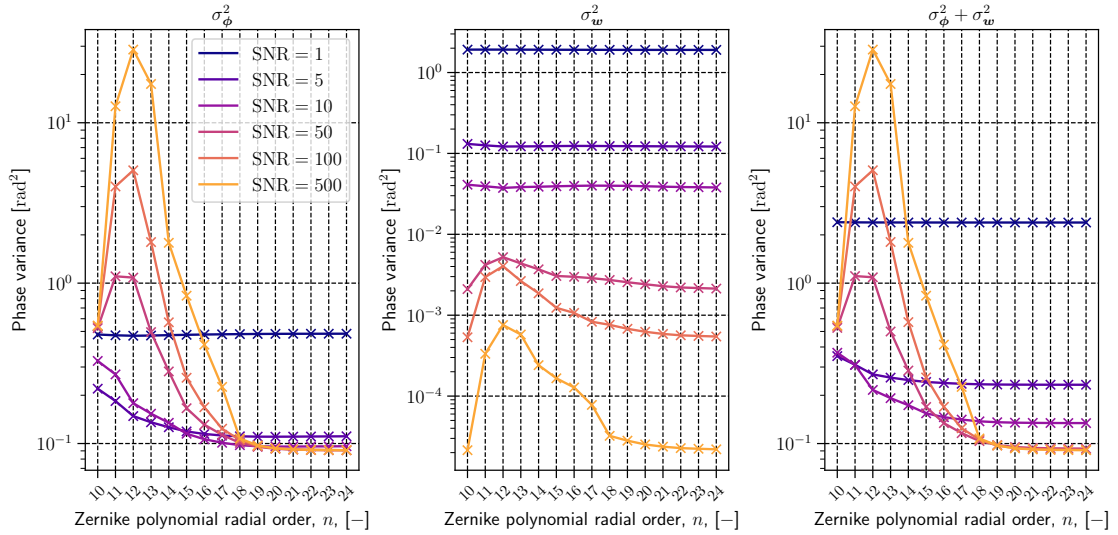


Figure 7.1.: Analytical *MAP* reconstruction performance, *ODISSEE*, 8×8 SH, $n_{\text{cor}} = 10$, several *SNRs*. From left to right, phase reconstruction, noise propagation variance, and total error variance; all according to the maximum radial order of estimated modes, n_{est} ; each curve has units of phase variance in rad^2 error for the corrected modes.

Figure 7.1 shows the results for this case. The different error terms are plotted for a range of *SNR* levels. A fudge factor of $\alpha = 1$ is used in Equation 7.3. The following observations are possible:

- Increasing the number of modes that are considered in the reconstruction reduces the reconstruction error.

- A good convergence in the reconstruction error is achieved for a reconstruction of two times the initial spatial sampling frequency; in this case, $n_{\text{est}} = 20$ for the initial $n = 10$ that the 8×8 *SH* samples properly.
- At high *SNR*, the reconstruction blows up and produces results that are significantly worse than the aliasing levels in traditional integrator controllers. These bad results are limited to an intermediate number of reconstructed modes; the reconstruction does not blow up if the number of modes is high enough. Reconstruction of more modes is necessary not only to improve reconstruction performance (as in the low *SNR* case) but also to avoid the reconstructor blowing up; this increases computational cost. The exact cause of this bump remains unclear, since the reconstructor assigns more variance to these modes than the total variance in the wavefront. The bump appears when the maximum number of modes estimated is equivalent to the maximum frequency measured by the Shack-Hartmann wavefront sensor; the modes with radial orders closed to the maximum frequency of the *WFS* are the ones that have the most aliasing error, so the reason for the presence of such a bump should be related to it.
- Even if a large number of modes is used, the reconstruction error remains significant within the error budget. In this case, it accounts for roughly $9 \cdot 10^{-2} \text{ rad}^2$, compared to $1.699 \cdot 10^{-1} \text{ rad}^2$ of the aliasing error in the *AO* budget (see Table 3.2), so *MAP* is able to reduce the aliasing, but the term is still present.
- At low *SNR*, the noise propagation also contributes to the total reconstruction error, which slightly reduces performance. At high *SNR*, the shape of noise propagation shows a large bump for a limited number of estimated modes, but the noise level is non-significant.

So far, it has been observed that at high *SNR* values the *MAP* reconstruction is not numerically stable and shows a bump in performance that leads to a total performance loss. We show here how the use of a fudge factor, α , can help reduce this effect, Figure 7.2 reports these results of the same experiment, this time with an *SNR* = 100 and different fudge factors. The following observations are possible:

- The right choice of fudge factor leads to a performance that is similar to the one observed with lower *SNR* values. The fudge factor can be understood as an artificial increase of the noise present in the measurements that makes that the estimator weights more the statistical priors in the reconstruction with respect to the measurement itself.
- To achieve the limit performance for the modal reconstruction, it is still necessary to increase the number of estimated modes.

7. Predictive Controller Results

7.3. Effect of Aliasing and Modal Reconstruction

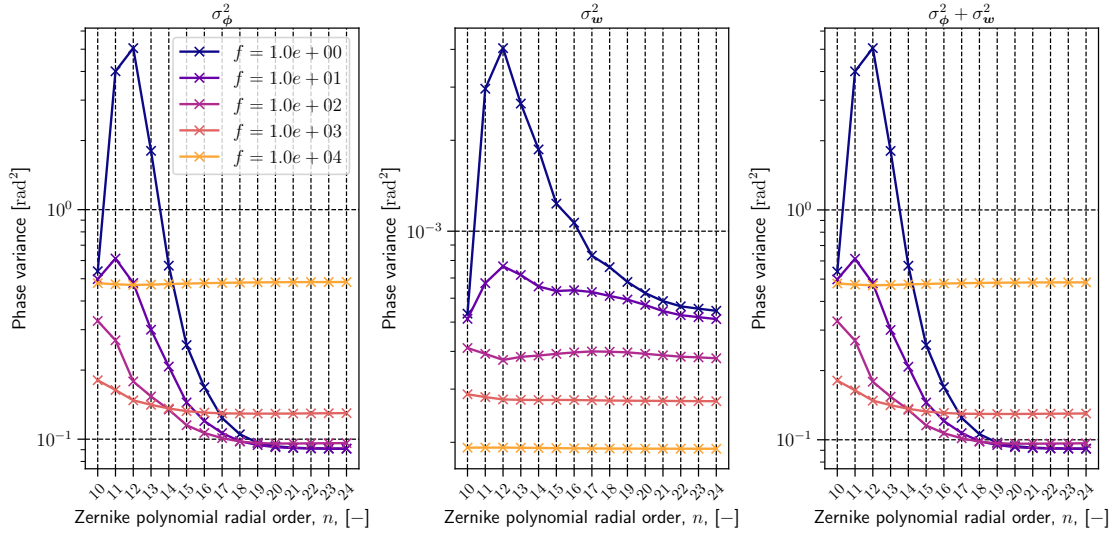


Figure 7.2.: Analytical *MAP* reconstruction performance, *ODISSEE*, 8×8 SH, $n_{\text{cor}} = 10$, $\text{SNR} = 100$, several fudge factors. From left to right, phase reconstruction, noise propagation variance, and total error variance; all according to the maximum radial order of estimated modes, n_{est} ; each curve has units of phase variance in rad^2 error for the corrected modes.

In conclusion, the interest of the fudge factor would be to use an intermediate performance level, in this case, the fudge factor avoids the bump due to numerical instability at high *SNR*. On the other hand, this requires tuning the fudge factor either by trial and error or by computing analytical curves as the ones presented in this analysis.

The results presented so far are based on analytical computations based on covariance matrices. These results are completed with the numerical simulation of the *MAP* controller performance computed analytically and the simulated performance using a time series of the phase screens simulation; the simulations are reported in Figure 7.3. All the numerical simulations use a grid of 256×256 pixels for the representation of the phase. The pupil turbulence time used for this experiment is the same as used for the simulation of the *ODISSEE* end-to-end controller simulations. Two different cases are shown: (a) without a fudge factor ($\alpha = 1$) and (b) with the best fudge factor according to Figure 7.2. It can be observed that in both cases the simulation results match the theoretical predictions relatively well, which allows us to verify the analysis presented here. Note that the deviation in case (b) appears to be larger due to the absence of an estimation error bump, causing a difference in scale between both plots.

7. Predictive Controller Results

7.3. Effect of Aliasing and Modal Reconstruction

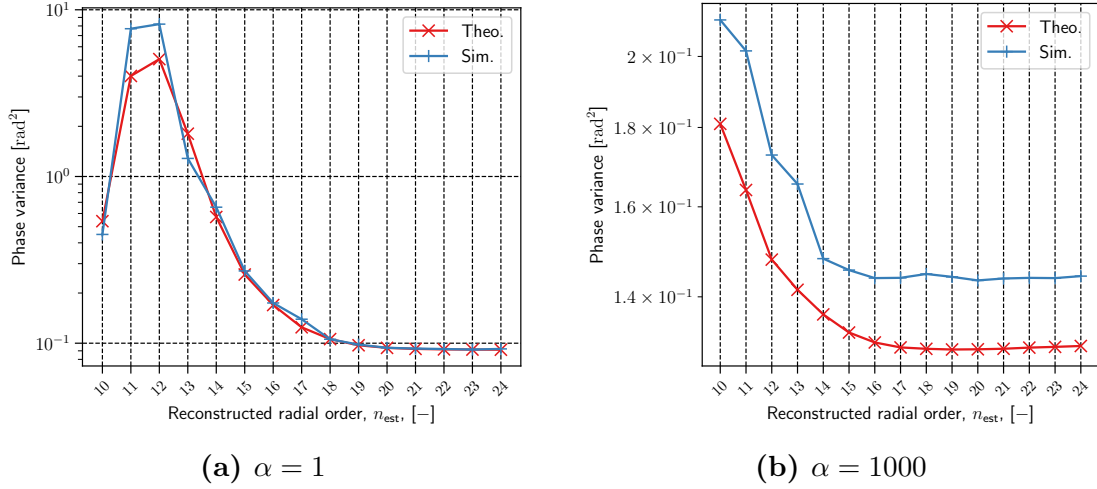


Figure 7.3.: Numerical verification of the *MAP* reconstruction performance for *ODISSEE*, 8×8 *SH*, $n_{\text{cor}} = 10$, $\text{SNR} = 100$. Total phase reconstruction error according to the maximum radial order of the estimated modes, n_{est} ; each curve has units of phase variance in rad^2 error for the corrected modes. Two different cases are shown: (a) without a fudge factor ($\alpha = 1$) and (b) with the best fudge factor according to Figure 7.2.

7.3.6. Case 2: 16×16 *SH* and $n_{\text{cor}} = 20$ *DM*

Figure 7.4 reports the result of the *MAP* analysis for the *ODISSEE++* case. The following observations are possible:

- The behavior is similar to the 8×8 *SH* since both the number of corrected modes and the sampling of the Shack-Hartmann are scaled by a factor two.
- From a performance point of view, with respect to the 8×8 *SH* there is less energy in the aliased modes since the sampling of the *SH* is now twice as high, i.e. less fitting error equals less aliasing error, which leads to an increase in the phase variance of the reconstructed error.
- The bump seems to appear only at the highest $\text{SNR} = 500$.
- The main difference is in the end-to-end simulation, reported in Figure 7.5, since in this case the simulation has significantly poorer performance than the analytical result. This difference has also been observed in the similar case of the *FEELINGS* system (Figure 7.6b) as well as in the controller simulations; no reason could be found for this error, which is not present in the smaller 8×8 system.

7. Predictive Controller Results

7.3. Effect of Aliasing and Modal Reconstruction

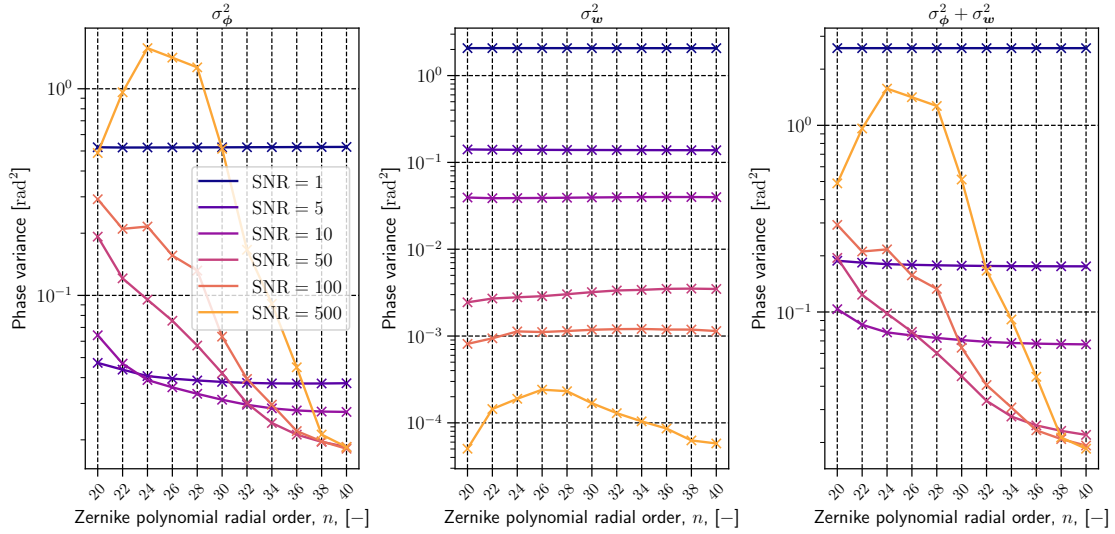


Figure 7.4.: Analytical *MAP* reconstruction performance, *ODISSEE++*, 16×16 SH, $n_{\text{cor}} = 20$, several *SNRs*. From left to right, phase reconstruction, noise propagation variance, and total error variance; all according to the maximum radial order of estimated modes, n_{est} ; each curve has units of phase variance in rad^2 error for the corrected modes.

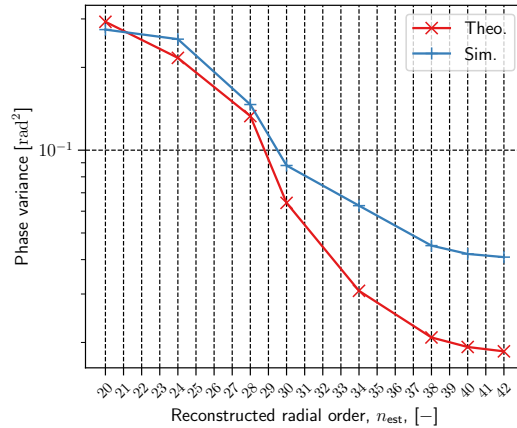


Figure 7.5.: Numerical verification of the *MAP* reconstruction performance for *ODISSEE++*, 16×16 SH, $n_{\text{cor}} = 20$, SNR = 100, no fudge factor. Total phase reconstruction error according to the maximum radial order of the estimated modes, n_{est} ; each curve has units of phase variance in rad^2 error for the corrected modes.

7.3.7. Case 3: *LISA* and *FEELINGS*

The same analysis conducted above for the *ODISSEE* and *ODISSEE++* systems is reported in Figure 7.6 for the *LISA* and *FEELINGS* systems. The absolute errors vary slightly due to the use of a different profile and telescope diameter size, but the trends are similar to the results found for the other two systems.

7. Predictive Controller Results
7.3. Effect of Aliasing and Modal Reconstruction

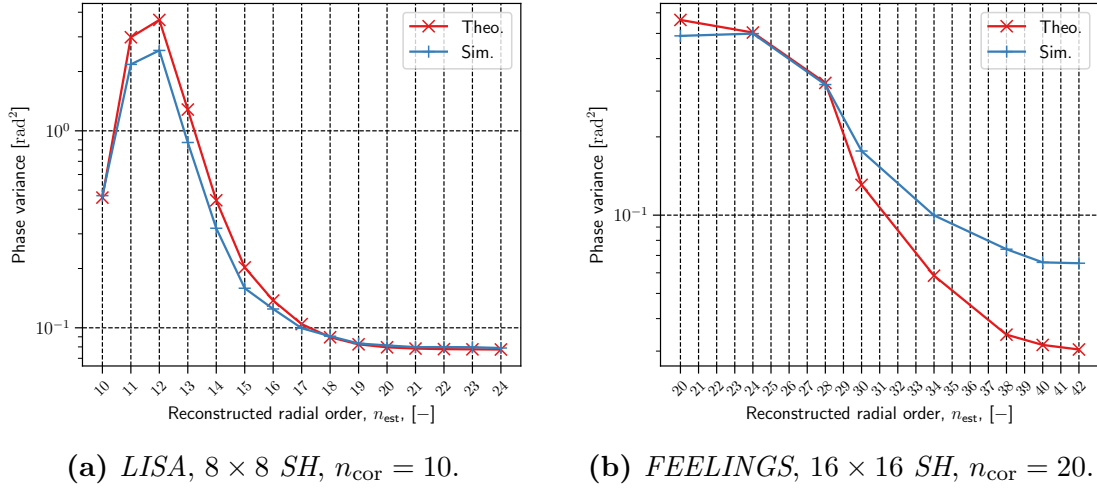


Figure 7.6.: Numerical verification of the *MAP* reconstruction performance for the communication systems. Total phase reconstruction error according to the maximum radial order of the estimated modes, n_{est} ; each curve has units of phase variance in rad^2 error for the corrected modes.

7.3.8. Case 4: Oversampled 16×16 *SH* and $n_{\text{cor}} = 10$ *DM*

The use of an oversampled Shack-Hartmann *WFS* is included in this study, although it will not be further investigated as part of this thesis. The results of the analytical *MAP* study for the *ODISSEE* system with an oversampling of the *SH* from 8×8 to 16×16 subpupils are reported in Figure 7.7 and Figure 7.8 for all *SNR* values and for $\text{SNR} = 100$ with different values of the fudge factor, respectively. The following observations are possible:

- Oversampling obtains better performance than when using the 8×8 case, even when using a lower number of reconstructed modes. Thus, oversampling proves to be a good solution to avoid increasing the computational load and the need of tuning, even if increasing the number of slopes used also has an impact on the computational cost of the Kalman filter.
- For high *SNR* values oversampling provides flat (better said oscillating) performance as a function of the number of reconstructed modes.
- The use of a fudge factor corrects this and reach an improvement of one order of magnitude with respect to the 8×8 case.
- At low *SNRs* the performance is better that at higher *SNRs*, but this is not true anymore when the noise propagation across the reconstructor is also accounted for.

In fact, the oversampling of the Shack-Hartmann extends the maximum spatial frequency that can be measured, and therefore the radial order for which aliasing

occurs. As a result, the results for the 8×8 sensor are shifted, including the bump; thus, if fudge factor is not used at high SNR the estimation error when estimating radial orders between 20 and 24 will explode.

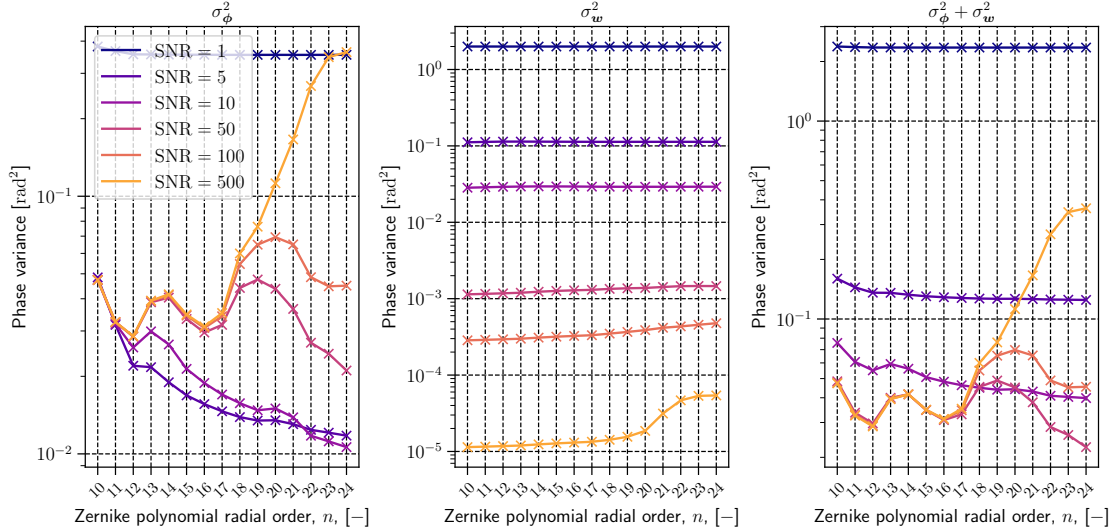


Figure 7.7.: Analytical MAP reconstruction performance, *ODISSEE*, 16×16 SH, $n_{\text{cor}} = 10$, several $SNRs$. From left to right, phase reconstruction, noise propagation variance, and total error variance; all according to the maximum radial order of estimated modes, n_{est} ; each curve has units of phase variance in rad^2 error for the corrected modes.

7.3.9. Case 5: Effect of Telescope Aperture Obscuration

So far in these tests, no telescope aperture obscuration has been considered. Figure 7.9 reports the end-to-end results of the MAP reconstructor in this case. The same modes (full-aperture Zernike modes) are used as modal basis. In both cases, the MAP is able to reconstruct the modal basis, but with a loss in the reconstruction performance compared to the results without obscuration given in Figure 7.3 and Figure 7.3.

7.3.10. Conclusions

Summary of the findings: A summary of the conclusions of the MAP study and a extrapolation to the LQG controller performance is presented below:

- In the case of the LQG controller, if aliasing is not properly handled, for example using a fudge factor or estimating more modes than the corrected modes, its effect will be greater than for integral controllers and will result in a total loss of performance.

7. Predictive Controller Results
 7.3. Effect of Aliasing and Modal Reconstruction

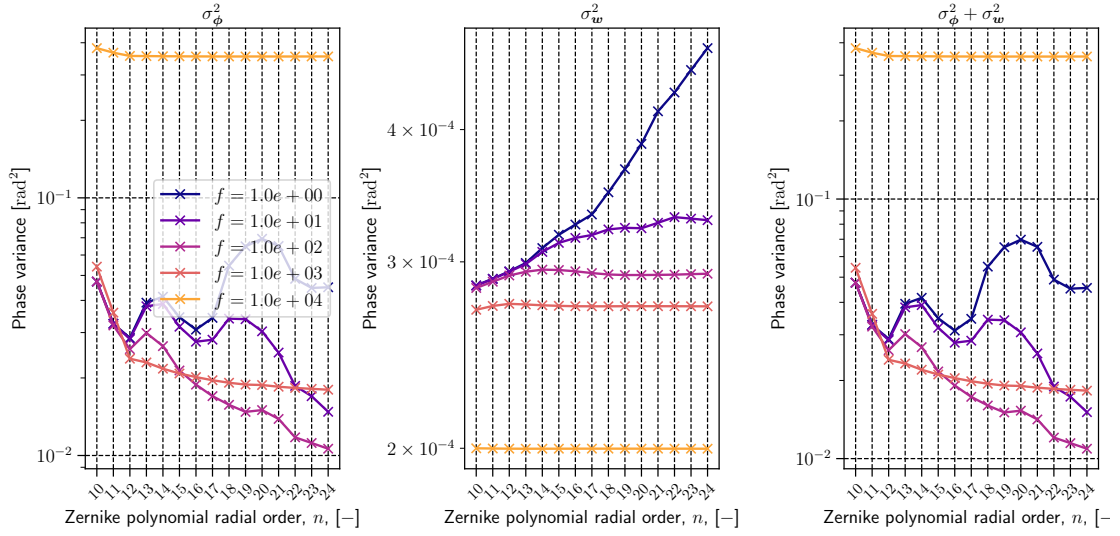
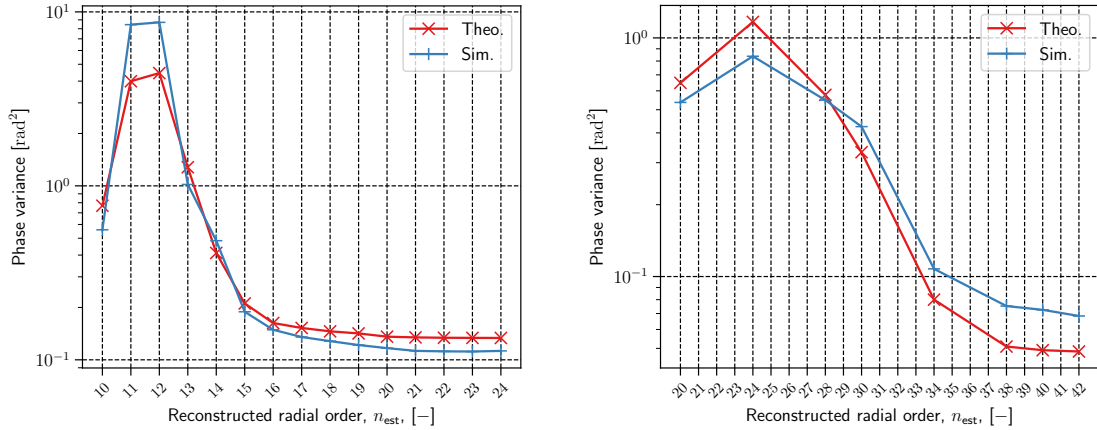


Figure 7.8.: Analytical *MAP* reconstruction performance, *ODISSEE*, 16×16 SH, $n_{\text{cor}} = 10$, $\text{SNR} = 100$, several fudge factors. From left to right, phase reconstruction, noise propagation variance, and total error variance; all according to the maximum radial order of estimated modes, n_{est} ; each curve has units of phase variance in rad^2 error for the corrected modes.



(a) *ODISSEE*, 8×8 SH, $n_{\text{cor}} = 10$ (b) *ODISSEE++*, 16×16 SH, $n_{\text{cor}} = 20$.

Figure 7.9.: Numerical verification of the *MAP* reconstruction performance in the presence of a 25% obscuration, $\text{SNR} = 100$, no fudge factor. Total phase reconstruction error according to the maximum radial order of the estimated modes, n_{est} ; each curve has units of phase variance in rad^2 error for the corrected modes.

- Even with proper aliasing handling, it is not possible to reconstruct Zernike polynomials from slope measurements with arbitrary accuracy. A modal reconstruction error will always be present and, in most cases, it will be higher or similar to the prediction error. This reconstruction error is a mix of aliasing

and the mismatch between the slope space and the reconstruction basis.

- The use of modal reconstruction with statistical priors reduces the reconstruction error, i.e. the aliasing, at the cost of increased computational cost.
- When using an oversampled SH , special attention needs to be taken to the behavior at high SNR since the results show that to reach the best performance it is necessary to use a fudge factor, regardless of the number of modes reconstructed.
- The reconstruction performance converges when the number of estimated modes corresponds to roughly twice the spatial frequency of the SH .
- Introducing a fudge factor allows us to achieve the same behavior as with a lower SNR , i.e. no blow-up. As a result, using a fudge factor it is possible to avoid the blow-up without increasing the number of modes. However, it requires tuning of the fudge factor.
- Reconstructing more modes is more costly from a computational point of view but it does not require any tuning, only the availability of the statistics for the reconstructed modes.
- There exists a trade-off between fudge factor, number of modes, and final performance that can be optimized to keep a good performance while containing the computational complexity.

Repercussion in laboratory testing: The fact that phase estimation is more robust at low $SNRs$ is especially relevant for laboratory testing; first tests may be done at high SNR thinking that it will provide better conditions when it will actually lead to more challenging conditions.

Extrapolation to zonal reconstruction: A similar analysis should be conducted for the case of the zonal reconstructor as in [Pren g re et al. \(2020\)](#). The use of a zonal reconstructor may have the advantage of having better performance in the presence of a telescope obscuration, since the base is only defined within the valid pupil. Although this thesis will not compare the analysis presented with a zonal basis reconstruction like the one conducted by [Pren g re et al. \(2020\)](#), the number of resulting states reconstructed should be roughly the same since both methods need more or less the same number of states to represent a given frequency coverage. [Annex C](#) contains an analysis of the equivalence between the frequency coverage of the Zernike polynomial basis and the zonal basis.

Comparison to similar results: The results here are consistent with the examples used in the literature, for example, [Sinquin et al. \(2020\)](#) reconstructs 495 modes for a 14×14 Shack-Hartmann, i.e. 30 radial orders, corresponding to roughly twice the spatial frequency of the Shack-Hartmann sampling, the same result obtained by [Juvénal et al. \(2018\)](#) and in this thesis. In the zonal space, [Prengère et al. \(2020\)](#) goes even further using a factor of three with respect to the sampling of the *SH*, this time using a zonal basis.

Impact on the predictive model identification: The preferred solution for reducing the impact of aliasing is to increase the number of modes required. This means that the statistics of the turbulence projected onto the modal basis need to be available up to the modes used. Given that the Shack-Hartmann wavefront sensor cannot properly measure the modes that are beyond its spatial sampling frequency, a data-based identification will not be able to identify those modes; as a result, the analytical computation of the model may be necessary. The priors necessary for this computation, mainly the turbulence profile, could come from an external metrology source or use a similar approach to the learn and apply method; see Section 6.3.2.

Note that in the case of the *MAP* only the spatial covariance matrix of the turbulence is necessary, while in the case of the Kalman filter, also the spatio-temporal covariance matrices need to be identified, since the predictive model must also increase the number of modes used.

Extension of the analysis: This section discussed an analytical study of the *MAP* reconstructor as a modal reconstructor from the Shack-Hartmann slopes to the Zernike polynomials. This analysis could be extended to include also temporal prediction as in Chapter 5 to combine the limitations of temporal prediction using slope measurements instead of the Zernike polynomial coefficients, an assumption made in the predictability assessment that cannot be used in real systems, since no wavefront sensor can measure those directly.

7.4. End-to-End Simulations

Table 7.3 shows the results for the end-to-end simulations of the four adaptive optics systems considered in this thesis using a number of modes high enough to achieve the best possible reduction of aliasing. For the *LISA* and *ODISSEE* cases this is equivalent to $n_{\text{est}} = 20$ for $n_{\text{cor}} = 10$, i.e. $N_e = 230$; while for *FEELINGS* and *ODISSEE++* it is $n_{\text{est}} = 40$ for $n_{\text{cor}} = 20$, i.e. $N_e = 860$. The number of states for the *LQG* controller is twice N_e , since a second-order vector autoregressive model is used.

The theoretical *MMSE* assessment of the residual phase variance for ϕ^{\parallel} does not contain aliasing, neither for the integrator nor for the *LQG*. The simulations

Table 7.3.: Results for the controller simulations using an increased number of modes. Results are given in variance of the residual phase with units of rad^2 .

	<i>LISA</i>	<i>FEELINGS</i>	<i>ODISSEE</i>	<i>ODISSEE++</i>
Integrator, ϕ^{\parallel}	$3.154 \cdot 10^{-1}$	$1.721 \cdot 10^{-1}$	$8.996 \cdot 10^{-1}$	$9.242 \cdot 10^{-1}$
Integrator, ϕ^{\perp}	$3.574 \cdot 10^{-1}$	$2.589 \cdot 10^{-1}$	$4.947 \cdot 10^{-1}$	$1.552 \cdot 10^{-1}$
Integrator, ϕ^{res}	$6.727 \cdot 10^{-1}$	$4.311 \cdot 10^{-1}$	1.394	1.079
<i>LQG</i> -VAR(2), ϕ^{\parallel}	$1.154 \cdot 10^{-1}$	$9.424 \cdot 10^{-2}$	$1.549 \cdot 10^{-1}$	$1.177 \cdot 10^{-1}$
<i>LQG</i> -VAR(2), ϕ^{\perp}	$3.575 \cdot 10^{-1}$	$2.590 \cdot 10^{-1}$	$4.948 \cdot 10^{-1}$	$1.552 \cdot 10^{-1}$
<i>LQG</i> -VAR(2), ϕ^{res}	$4.729 \cdot 10^{-1}$	$3.532 \cdot 10^{-1}$	$6.497 \cdot 10^{-1}$	$2.729 \cdot 10^{-1}$
Theo. $\mathbf{R}_{\text{MMSE}}^{(s=2,p=0)}$, ϕ^{\parallel}	$1.571 \cdot 10^{-1}$	$6.043 \cdot 10^{-2}$	$5.638 \cdot 10^{-1}$	$6.824 \cdot 10^{-1}$
Theo. $\mathbf{R}_{\text{MMSE}}^{(s=2,p=2)}$, ϕ^{\parallel}	$3.866 \cdot 10^{-2}$	$7.151 \cdot 10^{-3}$	$5.088 \cdot 10^{-2}$	$7.085 \cdot 10^{-2}$
<i>AO</i> error budget, ϕ^{\parallel}	$3.414 \cdot 10^{-1}$	$1.573 \cdot 10^{-1}$	$8.588 \cdot 10^{-1}$	$8.684 \cdot 10^{-1}$
Gain <i>LQG</i> -VAR(2) (%)	36.60	54.75	17.22	14.72
Gain Theo. <i>MMSE</i> (%)	24.61	11.83	9.02	10.38

contain aliasing for both, so the comparison is fair, but in this case, ϕ^{\parallel} contains both the prediction error and the propagation of phase reconstruction error, which is affected by aliasing. For the case of the integral controller, ϕ^{\parallel} can be compared to the sum of the temporal error and aliasing error terms in the *AO* error budgets reported in Table 3.2; this values are reported in the Table 7.3 as well.

In comparison of the integrator performance to the *AO* error budget, both the ϕ^{\parallel} corresponding to the temporal and aliasing error terms in the budget, as well as ϕ^{\perp} corresponding to the fitting error, are within less than a 10%, with these differences mainly attributed to the statistical convergence of the simulation due to the finite number of simulation time steps and the unique statistical realization per phase screen.

Compared to the integrator, the *LQG* for the *LISA* system has reduced the residual phase variance in the *DM* space to 36.60% of the same value for the integrator. However, the result is far from the theoretical prediction: $1.154 \cdot 10^{-1} \text{ rad}^2$ vs. $3.866 \cdot 10^{-2} \text{ rad}^2$. This loss in performance is due to the effect of phase reconstruction, which according to Figure 7.6a is of around $8 \cdot 10^{-2} \text{ rad}^2$. This error propagates across the predictive model, leading to the reported performance. As a result, it is the phase reconstruction error that limits the *LQG* performance and not the prediction. However, since the integrator also suffers from aliasing, the relative performance gains are still similar to those in the case without aliasing. The same behavior is found for the *ODISSEE* and *ODISSEE++* systems.

For the *FEELINGS* system, the relative gain with respect to the integrator is

less, since it only reduces the residual variance in the DM space to 54.75%. The performance of the LQG can still be explained by the limits of modal reconstruction, since according to Figure 7.6b it will be limited to around $7 \cdot 10^{-2} \text{ rad}^2$, and after propagation across the predictive model, will amount to $9.424 \cdot 10^{-2} \text{ rad}^2$. The only difference here is that the temporal error for this system is so little that the residual phase on the DM space is mainly driven by the reconstruction error, so the gains with respect to the integral controller come only from the improvement of the reconstruction, but not from a reduction of temporal error.

In conclusion, the predictive controller can still provide gains, but those are reduced with respect to the $MMSE$ predictability assessment since the presence of modal reconstruction error and its propagation across the predictive controller increases the residual phase variance. Nevertheless, the relative gains with respect to the integral controller are very promising; the effect of these gains will be evaluated in the next sections with respect to the Strehl ratio and the coupling gains.

7.5. Reduction of the Loop Sampling Frequency

Previous results in this chapter have shown how the use of temporal prediction reduces the temporal error in adaptive optics. Temporal error is the driver of the loop frequency in an adaptive optics system; usually, the loop frequency is increased to reduce the impact of temporal error. The increase of the loop frequency impacts the system design and imposes different technological challenges: (1) it requires that components such as the DM and the WFS detector work at the required frequency; (2) it limits the time available for the computations necessary to compute the next command; and (3) it limits the integration time available for wavefront sensing. If predictive control can be used as an alternative to increasing the loop frequency, all these constraints can be relaxed. This was already shown using the $MMSE$ predictability assessment method in Section 5.2.5; these results are now verified with end-to-end simulations.

Table 7.4 shows the results of simulations similar to the previous section but for the case of a reduction of the AO loop frequency by a factor of two. The *FEELINGS* system achieves roughly the same performance for the predictive controller at 2250 Hz than the integrator at 4500 Hz. For the *ODISSEE++* system, the performance of the predictive controller is even better than the performance of the integrator at twice the sampling speed, so it is possible to achieve a gain performance and at the same time reduce the sampling frequency of the loop. This is probably a very optimistic case, but it shows a promising gain for this application.

For communication applications, where the flux available for wavefront sensing is relatively high, a reduction in the loop sampling frequency can be used to reduce the cost and complexity of the AO system. For satellite observation applications,

Table 7.4.: Results for the controller simulations reducing the *AO* loop frequency by a factor of two. Results are given in variance of the residual phase with units of rad^2 .

f_{samp}	<i>ODISSEE++</i>		<i>FEELINGS</i>	
	750 Hz	1500 Hz	2250 Hz	4500 Hz
Integrator, ϕ^{\parallel}	2.660	$9.242 \cdot 10^{-1}$	$3.192 \cdot 10^{-1}$	$1.721 \cdot 10^{-1}$
Integrator, ϕ^{\perp}	$1.549 \cdot 10^{-1}$	$1.552 \cdot 10^{-1}$	$2.574 \cdot 10^{-1}$	$2.589 \cdot 10^{-1}$
Integrator, ϕ^{res}	2.814	1.079	$5.766 \cdot 10^{-1}$	$4.311 \cdot 10^{-1}$
<i>LQG</i> -VAR(2), ϕ^{\parallel}	$3.679 \cdot 10^{-1}$	$1.177 \cdot 10^{-1}$	$1.917 \cdot 10^{-1}$	$9.424 \cdot 10^{-2}$
<i>LQG</i> -VAR(2), ϕ^{\perp}	$1.549 \cdot 10^{-1}$	$1.552 \cdot 10^{-1}$	$2.575 \cdot 10^{-1}$	$2.590 \cdot 10^{-1}$
<i>LQG</i> -VAR(2), ϕ^{res}	$5.228 \cdot 10^{-1}$	$2.729 \cdot 10^{-1}$	$4.492 \cdot 10^{-1}$	$3.532 \cdot 10^{-1}$
Gain <i>LQG</i> -VAR(2) (%)	13.83	12.74	60.06	54.75

where wavefront sensing operates at low *SNR* values, reducing the loop frequency leads to an increase of the time available for wavefront sensing, improving the system performance, and especially enabling the imaging of fainter targets.

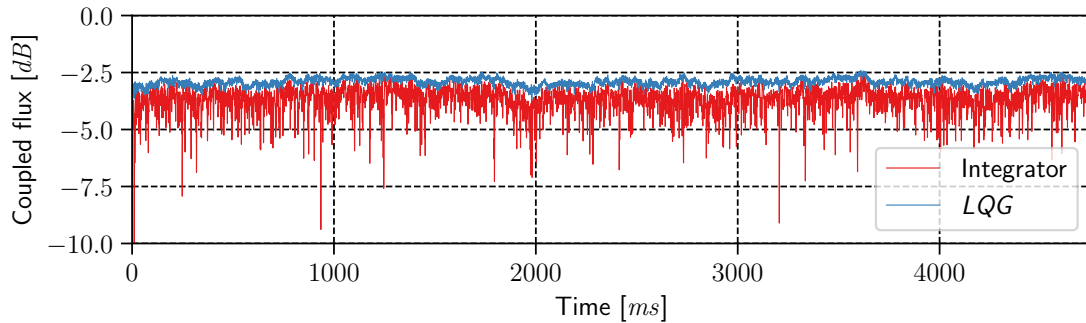
7.6. Effect of Fadings

The previous sections showed the gains in adaptive optics performance thanks to the reduction of temporal error by the use of a predictive controller; this discussion was in terms of residual phase variance, a metric that is the closest to the adaptive optics correction of phase distortions and that allows comparison to analytical performance expectations. This section will study the impact of these gains in terms of a metric that is more relevant for the laser communication application: the effect of phase correction in single-mode fiber coupling and the reduction of fadings in this coupling.

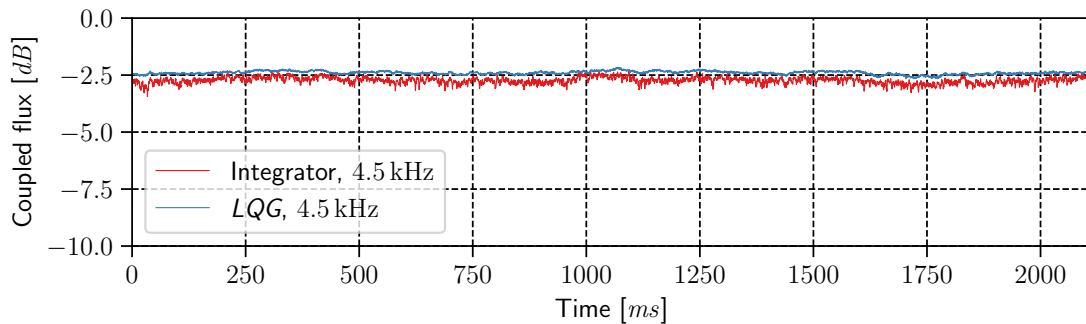
Figure 7.10 shows the coupling time series for the three simulated cases (*LISA* system and *FEELINGS* at two loop frequencies), while Figure 7.11 reports the *CDF* of each of the coupling time series.

For the *LISA* system it can be observed how the use of the integrator provides a clear fading reduction from around 7 dB to around 3.5 dB at a probability of $P = 1 \cdot 10^{-3}$. For the *FEELINGS* case the gains are not very big, barely 1 dB, but the integrator in this case does not have any fading to be avoided, so its performance is already very good. When analyzing the coupling of the slower *FEELINGS* system, running at 2.25 kHz, the integrator shows some fadings, going up to around 6 dB at a probability of $P = 1 \cdot 10^{-3}$. The *LQG* has the ability to decrease fading effects; in fact, it achieves a performance similar to that of the

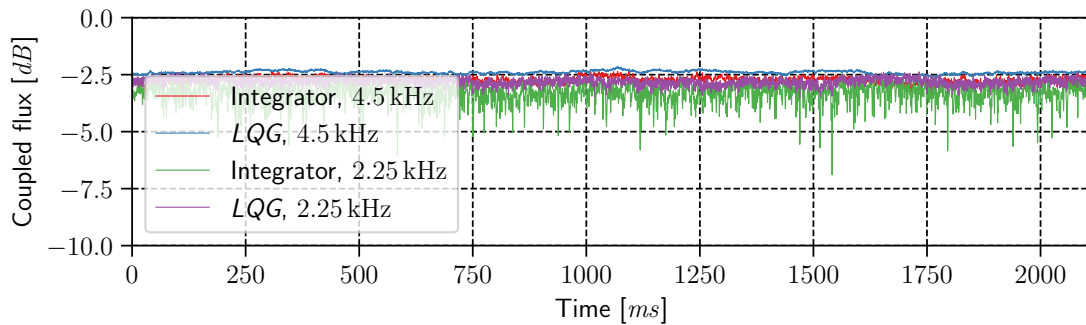
integrator at half the sampling frequency. These results demonstrate how the predictive controller can reduce fadings.



(a) *LISA*



(b) *FEELINGS*, $f_{\text{samp}} = 4.5 \text{ kHz}$



(c) *FEELINGS*, $f_{\text{samp}} = 2.25 \text{ kHz}$

Figure 7.10.: Coupled flux time series for different controller simulations.

Influence of tip and tilt modes: One may wonder why the fadings are reduced by the predictive controller even if there is still a big remaining fitting error and even aliasing. A possible hypothesis is that, at this regime of correction, the fadings are mainly caused by tip and tilt aberrations. To test this hypothesis, the same simulations were modified to provide a synthetic perfect tip and tilt

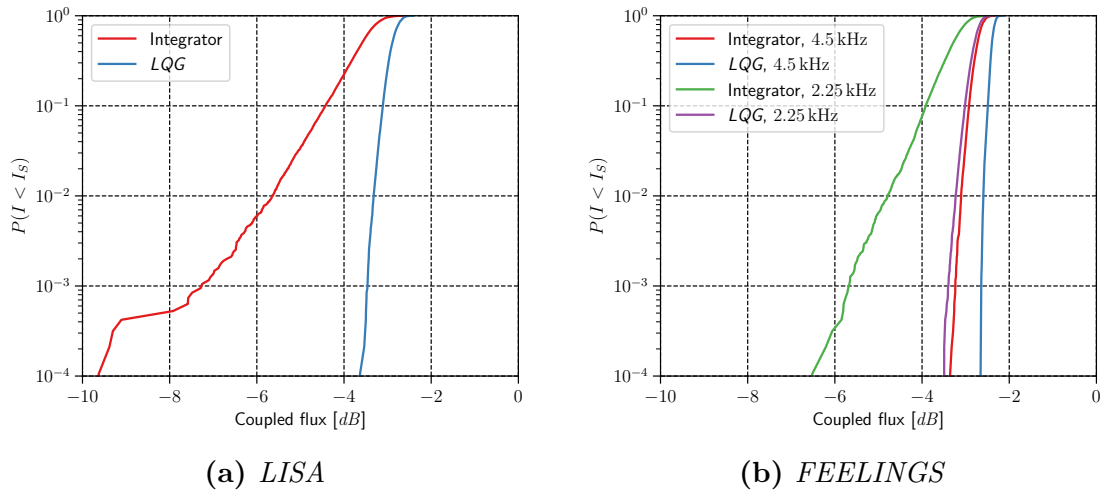


Figure 7.11.: Coupled flux CDF for different controller simulations.

correction, the coupling results for this case are reported in Figure 7.12. It can be observed how the performance with a perfect tip-tilt correction provides around half the improvement in the reduction of the fading fluctuations, while for the LQG controller, the difference is very low since the error in tip and tilt is already low.

These results suggest that a tip-tilt-only predictive controller may reduce at least part of the fadings and simplify the controller. Another option that has not been investigated is the effect of aliasing in coupling. Since coupling is mainly influenced by tip, tilt, and other lower-order modes and aliasing only affects higher-order modes, the controller only needs to provide the prediction and high-performance correction of those modes. The controller can be simplified by reducing the number of estimated modes, and only needs to avoid performance blow-up due to the aliasing propagation.

7.7. Strehl Ratio

In the same way that coupling efficiency was used to evaluate the performance of post-adaptive optics performance in laser communication systems, Strehl ratio is used here as a performance metric for the satellite observation systems, i.e. $ODISSEE$ and $ODISSEE++$.

Here the Strehl ratio is calculated as the ratio between the average of the absolute value of the aberrated OTF and the same value for the diffraction-limited OTF .

Figure 7.13 and Figure 7.14 show the time series of the Strehl ratio for both $ODISSEE$ and $ODISSEE++$, respectively. These results are summarized in Table 7.5. The results are very promising, in all cases the predictive controller provides a significant gain in Strehl. The most interesting result is again the fact that the predictive controller delivers a performance similar or better than the integrator, even the $ODISSEE$ system with an LQG is able to deliver a better performance

7. Predictive Controller Results
7.7. Strehl Ratio

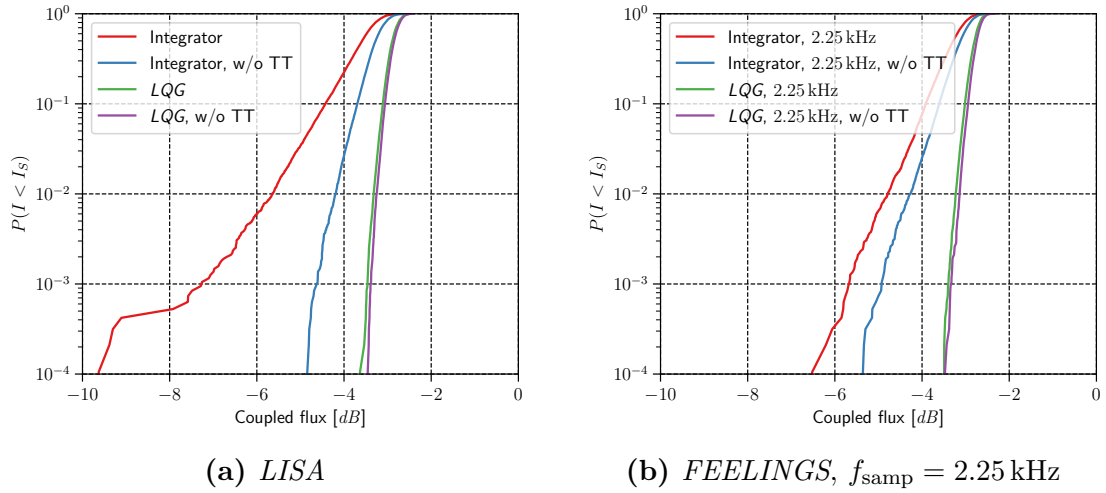


Figure 7.12.: Coupled flux *CDF* for different controller simulations with perfect tip-tilt correction.

than *ODISSEE++* with an integrator. If this kind of performance can be obtained on sky, it would suppose a great increase of performance or conversely a significant increase in the objects that can be observed, since the flux available for wavefront sensing could be duplicated by decreasing the loop frequency by a factor of two.

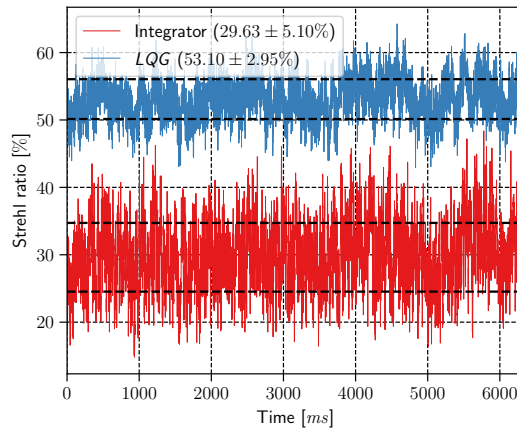


Figure 7.13.: End-to-end simulation Strehl ratio time series for the *ODISSEE* system.

* * *

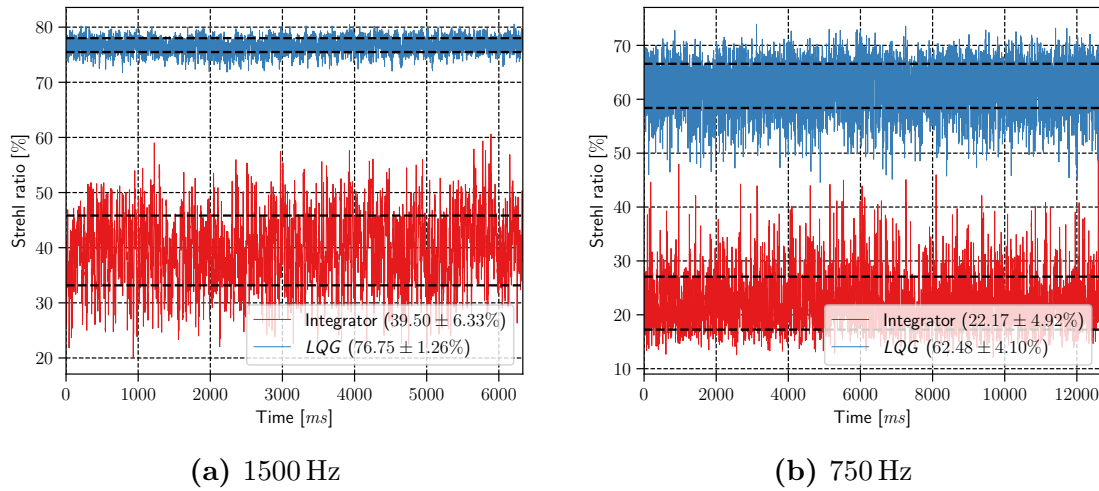


Figure 7.14.: End-to-end simulation Strehl ratio time series for the *ODISSEE++* system.

Table 7.5.: End-to-end simulation Strehl ratio results, units of %.

	Integrator	<i>LQG</i>
<i>ODISSEE</i>	29.63 ± 5.10	53.10 ± 2.95
<i>ODISSEE++</i>	39.50 ± 6.33	76.75 ± 1.26
<i>ODISSEE++</i> (750 Hz)	22.17 ± 4.92	62.48 ± 4.10

Summary

This chapter provided end-to-end simulations of the predictive controller developed during this thesis. The end-to-end simulations serve as a proof of concept for the predictive controller and establish a performance benchmark for the laboratory verification of the controller. Additionally, they also serve as a digital twin, facilitating the testing of the controller in an actual adaptive optics system.

The performance of the predictive controller was compared, in terms of residual phase variance, with an integral controller that employs an optimized scalar gain. The controller performance was also compared with the predictability assessment presented in Chapter 5, which shows good agreement.

This chapter also presented a detailed analysis of the effect of modal reconstruction errors and aliasing in the controller; this analysis used the *MAP* reconstructor as a proxy for the Kalman filter modal reconstruction. The analysis identified that the propagation of aliasing within the Kalman filter at high *SNR* values is higher and leads to a total loss of performance; this effect can be compensated for by estimating more modes or using a fudge factor. At least at high *SNR* values, the effect of phase reconstruction and

aliasing needs to be mitigated with those solutions; otherwise, the performance loss is total. The analysis defined the need to use more modes in the *LQG* controller than the modes that are corrected, with the number of modes necessary roughly equivalent to a spatial frequency twice as high as the wavefront sensor sampling. The analysis also showed the influence of the fudge factor on improving the modal reconstruction within the *MAP* and the Kalman filter.

After the study of the effect of aliasing on the controller, the rest of the chapter focused on the evaluation of the performance of the controller in the different applications considered. Predictive control has been observed to help reduce the *AO* loop frequency by a factor of two while maintaining a performance similar to that of the integral action controller. For fiber coupling, predictive control proved effective in reducing fadings. However, a system study would be necessary to quantify the exact gains for a communication system by comparing the fading statistics to its link budget.

In summary, the predictive controller developed in this thesis and predictive control in general are identified as a promising solution for the improvement of the performance of adaptive optics systems in the applications considered. Several recommendations for the further development of this solution are derived from the results presented in this chapter:

- The controller could be optimized to reduce the number of modes that are used and to reduce its computational cost. This can be done by reducing the modes that are predicted to only tip and tilt, or a larger set of low-order modes.
- For communications systems and fiber coupling, the possibility of using fewer modes and working with an acceptable aliasing error should be studied; this error is concentrated in the higher corrected orders, while the coupling depends mostly on the low order ones.
- For satellite observation, the priority would be the reduction of sampling frequency, since this will increase the flux available for wavefront sensing and, therefore, the objects that can be imaged. An optimization of the number of modes estimated for the aliasing error mitigation should be studied; depending on the required performance, it may be interesting to avoid the blow-up of the reconstruction performance without searching for the maximum reconstruction performance to keep the number of estimated modes reasonable.

Moreover, the controller presented here should be further compared to the slopes and zonal based controllers. This comparison should take into account the aliasing and noise propagation of each controller, its identification

and calibration, and other facts such as performance in the case of pupil obscuration.

The robustness of the controller with respect to modeling errors derived from the difference between the identified model and the real turbulence evolution should also be studied further; this error may come from the limitation of the identification or from the change in turbulence conditions with elevation if the controller is not updated with enough frequency.

Part III.

Experimental Validation

8. *PICOLA* Turbulence Emulator

Contents

8.1. Context	184
8.2. Optical Turbulence Emulation	185
8.3. Bench Definition	188
8.3.1. Turbulence Profile Compression	188
8.3.2. Propagation Path Geometrical Scaling	190
8.3.3. Phase Screen Specification	192
8.3.4. Opto-mechanical Design	193
8.4. Characterization	195
8.4.1. Phase Characterization	195
8.4.1.1. Measurement Setup	196
8.4.1.2. Results	197
8.4.2. Scintillation Characterization	198
8.4.2.1. Measurement Setup	199
8.4.2.2. Numerical Simulations	199
8.4.2.3. Characterization Metrics	200
8.4.2.4. Spatial Scintillation Results	201
8.4.2.5. Temporal Scintillation Results	204
8.5. Operating Conditions	206
8.6. Conclusion	206

Introduction

The purpose of my thesis is to contribute to the improvement of adaptive optics assisted *LEO*-to-ground optical links. At low elevations, the length of the line of sight increases, and so does the volume of turbulence traversed and the resulting turbulence strength. Stronger turbulence and longer propagation lengths lead to more important amplitude distortions on the wavefront. These amplitude distortions manifest themselves as irradiance spatial fluctuations at the pupil plane of the telescope, also known as scintillation. The fluctuations that are close to the size of the telescope contribute to the fluctuation of the collected power by the pupil, while the fluctuations smaller than the pupil will have the same effect but at the Shack-Hartmann subpupil level, causing extinctions of some of the subpupil due to the lack of flux on them among other effects. The temporal variation of scintillation is given by the displacement of the layers under the frozen flow assumption, and for *LEO* satellites it will be particularly fast due to the presence of apparent wind. The operation of adaptive optics under scintillation conditions is very challenging and is not yet well studied, as other applications such as astronomy do not need to operate at low elevations. A laboratory emulator for these conditions will allow testing and developing adaptive optics systems, components, and algorithms in a controlled but realistic environment. The close match of the numerical simulations of the bench to its behavior will allow the comparison and understanding of the effects of scintillation on adaptive optics systems, still not fully understood and yet to be mitigated in the path to enable the operation of adaptive optics assisted optical links at low elevations.

When I started my PhD I inherited the *PICOLO* bench that had been designed, procured, and aligned by my team. Before the bench was aligned, Louis Le Leuch conducted a first phase characterization of the phase screens using a Shack-Hartmann wavefront sensor for the acceptance of the screens. After the integration and alignment of the bench, I took it over and prepared all the calibrations necessary for the characterization of the bench and the routines for the post-processing of the data; I also adapted and conducted the *TURANDOT* numerical simulations of the bench. The bench was first presented before the start of my PhD by Marie-Thérèse Velluet as a talk in the *SPIE Remote Sensing 2020* conference (Velluet et al. 2020) and summarizes the previous work on the bench before my arrival.

The present chapter reproduces verbatim the article I wrote on the development and characterization of the bench, published as Robles et al. (2023). The article describes the methodology for the design of the bench, including a discussion on the characteristics of turbulence that are of importance for the application considered and what is the best method to produce it, as well as the main phases of the bench definition, in particular the different steps followed to optimize and validate the sampling of the turbulence vol-

ume by only three layers and the down-scaling of the experimental setup to be representative of phase and scintillation effects. The second part of the article is devoted to the characterization of the phase and scintillation of the turbulence produced by the bench and a comparison to numerical simulations, the main contribution of this thesis to the article. Finally, we discuss the perspective of upgrading the bench to meet future needs.

The emulator will serve as a testing platform for adaptive optics systems and other free-space optical communication components under strong turbulence conditions, especially for *LEO* satellite downlinks. Some of preliminary tests conducted during this thesis are presented in the Chapter 9.

*Emulating and characterizing strong turbulence
conditions for space-to-ground optical links:
The PICOLO bench*

P. Robles, C. Petit, M.-T. Velluet, L. Le Leuch, A. Montmerle-Bonnefois, L. Paillier, J.-M. Conan, F. Cassaing, J. Montri, B. Neichel, N. Védrenne

Published in
the Journal of Astronomical Telescopes, Instruments, and Systems (2023)

Abstract: We present a method to develop a turbulence emulation bench for low-Earth-orbit satellite-to-ground optical communication links under strong turbulence. We provide guidelines to characterize the spatio-temporal dynamics of phase disturbances and scintillation produced by the emulator on a laser beam. We implemented such an emulator for a link at 10° elevation and discuss here its design method and characterization. The characterization results are compared to numerical simulations; this characterization results in the validation of a digital twin of the emulator. The emulator will serve as a testing platform for adaptive optics systems and other free-space optical communication components under strong turbulence conditions.

8.1. Context

Optical communication between satellites and optical ground stations will deliver high speed data transfer between space and Earth (Volland et al. 2019; Hauschildt et al. 2019). In the case of *low Earth orbit (LEO)* satellites, higher throughput would enable *direct-to-Earth (DTE)* links, which download high resolution sensor data directly from the satellite hosting the payload to the ground. *DTE* links serve as an alternative to geostationary satellite relay architectures, which may not be available for small constellations.

High data-rate optical communications rely on single-mode fiber coupling for different techniques such as optical amplification and coherent detection. Unfortunately, the atmospheric turbulence present in the few tens of kilometers close to the ground impacts the quality of the optical beam and hinders fiber coupling (Shaklan and Roddier 1988), leading to a reduction of the possible data rate due to signal fading (Giggenbach 2008). Atmospheric turbulence causes phase distortions on the wavefront of the transmitted laser beam. The use of *adaptive optics (AO)* provides phase correction of the wavefront and thus improves coupling. However, unlike in traditional astronomical applications, *LEO-to-ground* links may face strong turbulence conditions that lead to amplitude distortions. The amplitude distortions result in spatio-temporal variations in optical intensity known as scintillation (Fante 1975). Scintillation causes variations in the intensity of the received optical

signal (Yura and McKinley 1983) and impairments in the wavefront measurements (Barchers et al. 2002). Two factors lead to this strong turbulence regime. First, *LEO* links need to work at low elevation angles (desirably down to 10°) in order to extend the link duration. At these angles, the propagation distance in the atmosphere is very long (> 50 km), leading to a longer propagation path and a larger volume of turbulence crossed, increasing the total turbulence distortion strength. Second, day-time operation faces stronger turbulence due to temperature gradients caused by solar radiation.

In order to test *AO* systems and optical communication components under strong turbulence, *ONERA* has developed the *PICOLO* bench (Velluet et al. 2020): a turbulence emulation for a *LEO*-to-ground optical link. This laboratory emulator will complement the current efforts in numerical simulations (Vedrenne et al. 2012) and experimental tests (Petit et al. 2022). The development of satellite-to-ground links requires extensive testing of the different subsystems. Testing with satellites (Boroson and Robinson 2014; Fischer et al. 2015; Petit et al. 2016) is limited by link duration and the lack of *LEO* satellites equipped with onboard optical terminals. Different ground-to-ground experiments (Brady et al. 2017; Bitachon et al. 2022; Bonnefois et al. 2022) have been designed to replicate the conditions of those links, but it is difficult to achieve realistic and reproducible turbulence conditions. Turbulence emulators (Qu and Djordjevic 2016; Brady et al. 2019; Kudielka et al. 2019) provide well-known, reproducible, and available optical turbulence conditions that enable the testing of *AO* systems and other optical communication components.

The originality of this work is three-fold: first, this emulator is one of the few systems representative of low elevation *LEO*-to-ground links including phase but also scintillation effects emulation; second, we provide a thorough laboratory characterization of these effects and compare them to numerical simulations; and third, we have produced a digital twin of the laboratory emulator. The digital twin complements the experimental validation of new instrumental concepts in a two-stage process: first, it is used to assess the expected performances and, later, to interpret the experimental results.

8.2. Optical Turbulence Emulation

Most approaches and experiments for turbulence emulation have been developed for either astronomical cases (i.e. weak turbulence) or horizontal links (DiComo et al. 2016) (i.e. constant turbulence profile), but those do not cover the specific needs of the propagation channel of a *LEO*-to-ground link at low elevation: multi-layer profile, strong turbulence, and high layer translation speeds. Having multiple layers of turbulence is necessary since satellite-to-ground links are slanted links that go across different atmospheric altitudes. The strong turbulence is a result either of day-light conditions, where turbulence is stronger due to solar radiation, or of low elevations, where the path across the turbulence is longer and therefore

turbulence is stronger. Per-layer translation speeds are higher for *LEO* links since there are two different components: Natural wind and apparent wind. Natural wind corresponds to the atmospheric local wind that causes a shifting of the different turbulence layers; its vertical profile depends on the dynamics of the atmosphere. Apparent wind corresponds to the apparent translation of the different turbulence layers due to the relative movement of the line-of-sight with respect to the layers during satellite tracking. The apparent wind speed depends on the angular tracking velocity of the telescope and the distance to a given layer. These speeds are typically an order of magnitude higher at the upper atmospheric layers than the typical wind speeds in astronomical applications and therefore, they represent an additional emulation challenge.

Different methods are available for generating laser beam distortions similar to the ones caused by atmospheric turbulence in a laboratory setup. We discuss briefly the methods available (see (Jolissaint 2006) for a more detailed overview) and motivate our choice for the emulator design. We distinguish three methods for turbulence production: passive screens, active screens, and turbulence chambers.

Passive phase screens (Butler et al. 2003; Mantravadi et al. 2004) use an optical surface with a fixed phase mask structure providing the *optical path difference* (*OPD*) corresponding to atmospheric turbulence distortions. This mask can be in transmission or reflection. The *OPD* is generated by controlling the thickness of the surface in a homogeneous optical index medium, or by using a controlled inhomogeneous optical index. The phase screens are often mounted on a rotating stage, which produces a shift that approximates the linear displacement of atmospheric turbulence layers due to wind. Since the phase mask pattern used is specified by the user, the phase screens produce deterministic turbulence and can implement profiles by employing one layer per screen. This is a method that has been preferred by several astronomical projects (Thomas 2004; Hippler et al. 2006a; Roberts et al. 2018; Mieda et al. 2018). The *OPD* is engraved on the optical surface by different methods such as index matching by Lexitek (Mantravadi et al. 2004; Zhou et al. 2017), acrylic paint spraying (Thomas 2004; Rampy et al. 2010) or the cumulative etching by *OPD* Technologies (Hippler et al. 2006b) used by several *AO* systems coordinated by the *European Southern Observatory* (*ESO*). This approach ensures an accurate control of the phase distortion but loses versatility, as the distortions are not reconfigurable except by changing the phase screens.

Active phase screens use optical devices such as *spatial light modulator* (*SLM*) (Rickenstorff et al. 2016) and *liquid crystal* (*LC*) (Giles et al. 2000; Corley et al. 2010) devices as phase modulators that act as reconfigurable phase screens. Those are able to produce a linear phase displacement (unlike the rotating static phase screens, which only approximate it) and can also combine it with boiling turbulence, as their phase mask is fully programmable. Likewise passive phase screens, active phase screens also create deterministic turbulence and can represent multi-layer profiles. Unfortunately, these solutions pose problems of polarization conservation, chromatism and, more importantly, are limited in reconfiguration rate. Deformable

mirrors (Tyson and Frazier 2001) can provide a higher reconfiguration rate and achromaticity, but present problems related to cost, spatial frequencies, and opto-mechanical design for multi-layer arrangements.

Turbulent fluid chambers create turbulence by mixing two fluids at different temperatures. For example, hot air turbulence chambers (Keskin et al. 2006) use two streams of hot and cold air. The turbulence strength can be modified by changing the temperature difference between the two streams, while the wind speed can be regulated by the speed of the fans that inject them into the chamber. Nevertheless, this method is not able to produce the turbulence strength profile characteristic of slanted links, neither is able to produce the wind speed profile derived from satellite tracking apparent wind. Additionally, the turbulence produced cannot be reproduced in a deterministic manner.

A completely different alternative (Geisler et al. 2019) to turbulence emulation uses a variable optical attenuator to create fade profiles in an optical fiber signal derived from numerical simulations (incorporating both turbulence disturbances and the *AO* system). This is a cost-effective solution to emulate a communication channel under the effect of turbulence, with *AO* correction or not. However, this method requires knowledge of the fiber coupling statistics with *AO* correction (Canuet et al. 2018), which are not available for complex *AO* operating conditions such as strong turbulence or feeder links precompensation (Lognoné et al. 2022).

Although most turbulence emulators described in the literature target astronomical applications, some were developed for optical communication. For instance, the bench in (Brady et al. 2019) is dedicated to the validation of an *AO* for ground-to-satellite uplink pre-compensation. It is composed of a single phase screen and presents an underestimated beam wandering due to a scaling problem. The emulator in (Kudielka et al. 2019) is representative of an uplink at 30° elevation, so it does not focus on a strong turbulence case and the effect of scintillation. Finally, the work in (Qu and Djordjevic 2016) uses two *SLMs* with an intermediate reflection to produce a second footprint on each *SLM*, obtaining four different phase screens. The emulated link corresponds to strong atmospheric turbulence, but the link is horizontal and there is no detailed characterization of the scintillation produced on the beam. In summary, the existing emulators target different cases, and therefore answer trade-offs different from ours, while, at the same time, a detailed methodology for the characterization of phase and amplitude fluctuations is usually lacking.

For our emulator, we decided to use passive phase screens mounted on rotation stages, with the possibility of using an *SLM* to introduce additional boiling turbulence or bursts of turbulence. Several criteria were considered in this decision: (1) to specify a precise turbulence strength with the correct statistics, (2) to reproduce the delivered turbulence conditions, (3) to produce strong enough turbulence (high phase modulation dynamic), and (4) to be able to adjust the speed of every layer to the strong apparent displacements due to satellite tracking.

8.3. Bench Definition

The definition of the bench started with the selection of a reference turbulence profile. We compressed the profile to a three-layer profile that could be implemented on the bench as phase screens (see Section 8.3.1). The profile was then geometrically scaled to reduce its size so it could fit on an optical table (see Section 8.3.2). We specified and procured the manufacturing of the three phase screens according to the selected three-layer profile (see Section 8.3.3). Finally, we designed the opto-mechanics that allow propagating a laser beam through the turbulence emulator and providing the generated turbulence to a client system and an analysis camera (see Section 8.3.4).

8.3.1. Turbulence Profile Compression

We used as a reference profile a modified Hufnagel-Valley 5/7 model (Valley 1980) (following the *ITU-R P.1621-2* recommendation) with a turbulence strength at the ground surface level of $C_n^2 = 1 \cdot 10^{-13} \text{ m}^{-2/3}$ and an upper-level wind speed of $V_{rms} = 21 \text{ m/s}$ that influences the turbulence strength of the upper layers of the atmosphere. Another possibility for the profile selection is to use a database of in situ C_n^2 profile measurements to define typical or worst-case profiles (Farley et al. 2019; Chabé et al. 2020). Note, that our overall emulator design methodology does not depend on the selection of the reference profile.

The reference profile was first compressed to a 50-layer profile to allow Monte-Carlo numerical simulations. The compression to 50 layers is carried by optimization of layer height and strength under the condition of keeping constant the following turbulence integrated parameters: r_0 as a quantification of the phase distortion strength, θ_0 for the anisoplanatism, and σ_χ^2 for the scintillation strength. The method is similar to the methods presented in Saxenhuber et al. (2017) but includes the scintillation effects too.

A second profile compression was necessary to reduce the number of phase screens required for the implementation of the emulator. The number of layers, and therefore phase screens, on the emulator, should be limited in order to reduce the system's complexity and cost. At the same time, a multi-layer profile is also needed to generate a representative turbulence profile: with the proper representation of phase and scintillation effects and the corresponding temporal dynamics derived from the natural and apparent wind profiles. Additionally, the use of several screens limits the periodicity in the generated turbulence (see Section 8.4.2.5 for a discussion on the periodicity).

We decided to use three layers since we consider that three layers allow representing qualitatively the scintillation characteristics of the link. In fact, the scintillation irradiation pattern depends on both turbulence strength and propagation distance, therefore we can design each of the three layers to represent one of the possible combinations and its resulting scintillation. The first layer is

located at the telescope pupil and emulates the atmospheric ground layer: very strong in turbulence but with short propagation distance, so negligible scintillation contribution. The time evolution of this layer is mainly driven by natural wind, i.e. slow layer speed (typical order of magnitude 10 m/s). The second layer is located at a more significant propagation distance. This will produce a typical size of the irradiation pattern smaller than the size of the telescope pupil. When using a Shack-Hartmann wavefront sensor, the typical size of the irradiation pattern is similar to the size of one of the subpupils, so scintillation contributes to the flux variation at the subpupil level, impairing wavefront sensing. The third layer will be located far away and will represent the free atmosphere: weaker turbulence but with a long propagation path. The resulting typical size of the irradiation pattern will have a size close to the telescope pupil, which contributes to the variation of available flux with time, and therefore the stability of the signal regardless of the *AO* performance. The temporal evolution of the second and third layers is mostly driven by the apparent wind component due to *LEO* satellite tracking, i.e. very fast layer speed (typical order of magnitude 150 m/s).

While 50 layers are enough to properly represent the original turbulence profile, the restriction to three layers poses a greater challenge. The first layer was fixed to be at the telescope pupil. The positions and strengths of the second and third layers were found using the same optimization based on integrated parameters as for the 50-layer profile. The natural wind velocity profile was chosen as 10, 15, and 30 m/s respectively, while the apparent wind is computed from the satellite tracking slew rate and the distance to the corresponding layer. We consider a 10° elevation and an orbit altitude of 500 km that result in a slew rate of $3.834 \text{ mrad} \cdot \text{s}^{-1}$.

Table 8.1 reports the integrated parameters of the 50-layer and the three-layer profiles. It can be observed that the compression of the profile managed to keep the targeted integrated parameters very close. A more detailed comparison of the 50-layer and the three-layer profiles is available in [Velluet et al. \(2020\)](#).

Table 8.1.: Integrated turbulence parameters for the 50-layer profile and the compressed three-layer profile.

Parameter	50-layer	Three-layer
r_0 (cm)	2.56	2.56
θ_0 (μrad)	1.75	1.68
τ_0 (μs)	338	315
σ_χ^2	0.58	0.58

8.3.2. Propagation Path Geometrical Scaling

We performed a down-scaling of the link geometry in order to fit it within a laboratory optical table. The complete process is a trade-off between available technologies for phase screen manufacturing (including resolution and stroke), opto-mechanical design, and required space (as we wish to keep the system compact). We provide a simplified discussion of this trade-off.

To achieve a physically equivalent system in terms of turbulence and diffractive effects, the down-scaling must preserve the following dimensionless groups constant: $D/\sqrt{\lambda L}$ for layer at distance L and a telescope of diameter D to be representative of scintillation effects on the pupil due to each layer; D/r_0 and the contribution to it of each layer through the $C_n^2 \cdot dz$ profile; and finally $V/(D \cdot f_{\text{samp}})$, which relates the layer displacement in a sampling interval to the size of the pupil. In the following, for each parameter X we use the notation X_{sky} for its value on sky and X_{bench} for its effective value on the bench and express the relationships between them.

Conservation of scintillation effects leads to:

$$D_{\text{bench}} = \sqrt{\frac{L_{\text{sky}}}{L_{\text{bench}}}} \cdot D_{\text{sky}}, \quad (8.1)$$

$D_{\text{bench}}/D_{\text{sky}} = \sqrt{L_{\text{sky}}/L_{\text{bench}}}$ is a geometric compression factor defined by the ratio between the initial and final propagation lengths. The maximum propagation distance available from the top layer to the telescope will therefore drive the scaling of the telescope diameter. At the same time, reducing the total propagation distance requires reducing the telescope diameter too. The telescope diameter in the bench defines the beam footprint on the phase screens, therefore it cannot be reduced too much, otherwise, the resolution of the manufacturing of the screens limits the turbulence that can be achieved.

Considering conservation of D/r_0 , the turbulence strength is down-scaled as:

$$r_{0,\text{bench}} = \frac{D_{\text{bench}}}{D_{\text{sky}}} \cdot r_{0,\text{sky}}. \quad (8.2)$$

To obtain the downscaling of the $C_n^2 \cdot dz$ of every layer, we use $r_{0,\text{bench}}$. Since the relative $C_n^2 \cdot dz$ profile is conserved, the absolute values of $C_n^2 \cdot dz$ can be scaled to achieve $r_{0,\text{bench}}$.

Finally, each layer's velocity depends on two factors: the relationship between diameters and a temporal scaling factor. For a given layer the velocity is down-scaled as:

$$V_{\text{bench}} = \frac{D_{\text{bench}}}{D_{\text{sky}}} \cdot \frac{f_{\text{samp,bench}}}{f_{\text{samp,sky}}} \cdot V_{\text{sky}} = \frac{D_{\text{bench}}}{D_{\text{sky}}} \cdot \frac{1}{\tau} \cdot V_{\text{sky}}. \quad (8.3)$$

The first factor of the last right hand term is related to the previously defined geometric compression factor. The second factor, $\tau = f_{\text{samp,sky}}/f_{\text{samp,bench}}$, is a

time scaling factor and it allows a temporal down-scaling of the layer speeds, by operating the bench at lower sampling frequency. As a result, any time interval Δt_{sky} on the original system is equivalent to $\Delta t_{\text{bench}} = \tau \cdot \Delta t_{\text{sky}}$ on the down-scaled system.

For example, for an *AO* system working at a 5 kHz sampling frequency on-sky and 50 Hz on the bench, the equivalent time scaling factor is $\tau = 5000/50 = 100$, this means that everything on the emulator runs 100 times slower than on-sky. For the same reason, to acquire a time series of $\Delta t_{\text{sky}} = 60$ s of duration, it would be necessary to record during $\Delta t_{\text{bench}} = \tau \cdot \Delta t_{\text{sky}} = 100 \cdot 60 \text{ s} = 100 \text{ min}$ on the bench.

Ideally, one would test a system with $\tau = 1$, so the system operates at its nominal frequency. Two different factors make temporal scaling convenient: first, reducing the rotational speed of the phase screens, and second, allowing the use of slower components in the emulator or client system. Indeed, due to the apparent wind speed of the *LEO* satellite, the upper layer speed is quite high; so high that the rotational speed of the phase screen to achieve such a layer velocity would push the limits of the rotation stage and produce possible vibrations and safety issues in case of component malfunction. In addition, the *PICOLO* bench is dedicated to the development and testing of new concepts and systems, cases in which it may not be possible to run certain components as fast as in operational conditions on sky. Temporal scaling is then a useful option. As an example, operating at a slower time scale also allows the use of an *SLM*, located in the pupil, whose operation is usually limited at 50 Hz, to add user-defined non-stationary turbulence, bursts, or specific perturbations. Finally, during the characterization of the bench, the infrared camera used is limited to an acquisition frequency of 100 Hz, so the scaling was also necessary during the characterization to obtain an equivalent sampling frequency of 10 kHz.

Note that the geometrical scaling of the emulator is independent of the diameter chosen for the telescope since the relationships are all in terms of the ratio $D_{\text{bench}}/D_{\text{sky}} = \sqrt{L_{\text{sky}}/L_{\text{bench}}}$. If one would like to change the telescope diameter, one could compute D_{bench} using Equation 8.1 and the optical propagation characteristics in the emulator would not change.

In the following, we provide the scaling for our implementation of the emulator. We wish to have a telescope diameter in the bench equivalent to $D_{\text{sky}} = 40$ cm diameter telescope on-sky. The results of the scaling exercise are summarized in Table 8.2. From the top layer, the propagation distance towards the telescope is $L_{\text{sky}} = 57$ km on sky, and we want to limit the maximum propagation distance on the bench to 1.4 m. Equation 8.1 leads to a telescope pupil of $D_{\text{bench}} = 2$ mm. The wavelength is the same on the bench: $\lambda_{\text{sky}} = \lambda_{\text{bench}} = 1.55 \mu\text{m}$. For the temporal down-scaling, we consider two scenarios: one where a $f_{\text{samp,sky}} = 5$ kHz is equivalent to $f_{\text{samp,bench}} = 2$ kHz, close to the current *AO* systems, and one where $f_{\text{samp,sky}} = 5$ kHz is equivalent to $f_{\text{samp,bench}} = 50$ Hz for testing new components that cannot work at higher rates at the moment. The layer velocities in the table are reported for the later case, $f_{\text{samp,bench}} = 50$ Hz, they must be multiplied by 40

for an *AO* loop running at $f_{\text{samp,bench}} = 2$ kHz. These values lead to acceptable specifications for the procurement of the phase screens and their rotating stages while achieving a compact bench design.

Table 8.2.: Resulting geometric down-scaling for the different phase screens.

Parameter	On-sky	Bench
Propagation distance	57 km	1.4 m
Pupil diameter	0.4 m	2 mm
Wavelength, λ , (μm)	1.55	1.55
Layer 1		
Position, z	0 m (pupil)	0 m (pupil)
Wind speed, V , (m/s)	10.00	$5 \cdot 10^{-4}$
Layer 2		
Position, z	2.88 km	0.072 m
Wind speed, V , (m/s)	26.04	$1.3 \cdot 10^{-3}$
Layer 3		
Position, z	57.8 km	1.4 m
Wind speed, V , (m/s)	250.84	$1.2 \cdot 10^{-2}$

8.3.3. Phase Screen Specification

The phase screens have been manufactured by the company *SILIOS* Technologies. We have provided the phase screen specification as a 2D phase map of the desired phase. The maps were generated from the specified r_0 and L_0 for each layer and with a von Kármán spectrum. The maps were scaled to keep the same relationship with respect to the telescope diameter after the down-scaling of the bench. The phase screens are manufactured with a $40 \mu\text{m}$ resolution, that for a $D_{\text{bench}} = 2$ mm and $D_{\text{sky}} = 0.4$ m is equivalent to a maximum spatial frequency representation of $62.5 \text{ cycle} \cdot \text{m}^{-1}$ on-sky.

The technical constraints in the manufacturing process led to reducing the turbulence strength in *PS1*, the strongest layer, since the resulting peak-to-valley distance in the screen was not attainable. This resulted in a change of the specification of $C_n^2 \cdot dz$ from $4.615 \cdot 10^{-11} \text{ m}^{\frac{1}{3}}$ to $2.545 \cdot 10^{-11} \text{ m}^{\frac{1}{3}}$. The change in the turbulence strength of *PS1* results in a change of the global r_0 from 2.6 cm to 3.3 cm, while the scintillation characteristics remain the same, since *PS1* is located at the pupil of the telescope. This loss of turbulence strength was considered acceptable since it does not affect the scintillation characteristics.

Table 8.3 summarizes the different profiles used in this work. All $C_n^2 \cdot dz$ values provided correspond to the on-sky values, i.e. before down-scaling. All

Table 8.3.: Summary of the different three-layer profiles considered in this work.

Layer	z	$C_n^2 \cdot dz \text{ (m}^{\frac{1}{3}}\text{)}$		
		Compressed	Specified	Measured
Layer 1	0 m (pupil)	$4.615 \cdot 10^{-11}$	$2.545 \cdot 10^{-11}$	$2.563 \cdot 10^{-11}$
Layer 2	2.88 km	$1.605 \cdot 10^{-11}$	$1.616 \cdot 10^{-11}$	$1.396 \cdot 10^{-11}$
Layer 3	57.8 km	$8.492 \cdot 10^{-13}$	$8.553 \cdot 10^{-13}$	$1.015 \cdot 10^{-12}$

the numerical simulations conducted in this work simulate the equivalent on-sky system and therefore use these values. The "compressed" profile corresponds to the compression from the original 50-layer profile to a three-layer profile (see Section 8.3.1). The "specified" profile corresponds to the profile specified to the phase screen manufacturer, where the strength of layer 1 had to be reduced due to manufacturing constraints (see Section 8.3.3). Finally, the "measured" profile corresponds to the profile measured during the phase characterization of the screens (see Section 8.4.1). This is the profile used in Section 8.4.2 for the numerical simulations that are compared to the characterization measurements, it is therefore considered as the most representative with respect to the experimental setup.

8.3.4. Opto-mechanical Design

Figure 8.1 depicts the opto-mechanical layout of the bench, while Figure 8.2 provides an image of the bench implementation. The main optical path is marked with a red line. A laser source is injected in the bench using a fibre collimator. A first phase screen (PS3) is positioned close to the source at the highest altitude, while *PS2* is close to the ground and *PS1* is located as close as possible to the entrance pupil of the telescope. The screens are placed on rotation stages. Two mirrors mounted on tip-tilt stages allow proper alignment of the input beam. A filter wheel equipped with neutral density filters allows different power attenuation levels on the laser input.

The telescope is emulated by a combination of lenses. The entrance pupil of the telescope is located at a mechanical stop in front of the first lens of the telescope. We use afocal lens systems to re-image the pupil plane and re-scale it. The output beam of the telescope is finally collimated. A periscope is placed at the output of this main path to ease coupling with a client system. The second path (in blue) is dedicated to the analysis of the perturbed beam. A beamsplitter picks a fraction of the flux and sends it to a near-infrared camera. A flip lens allows to switch between focal plane and pupil plane imaging on the camera. Three planes are conjugated to the entrance pupil (marked with a purple arrow): the first may accept a SLM, though it is a plane mirror for the moment; the second to the first mirror of the output periscope; and the third to the infrared camera (if in pupil

8. *PICOLO* Turbulence Emulator
8.3. Bench Definition

imaging configuration). The emulator is integrated on a 600 mm × 900 mm optical breadboard.

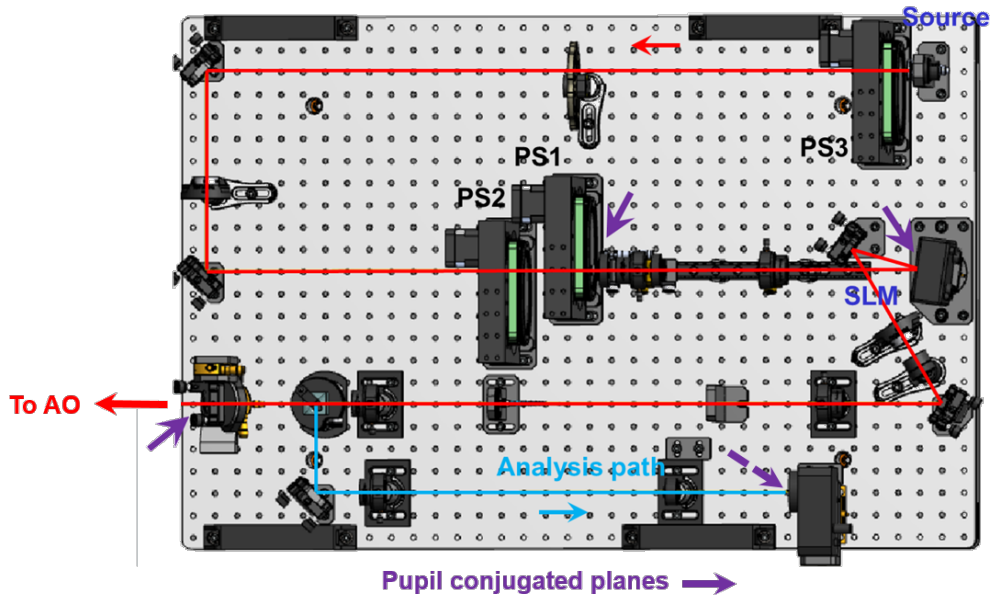


Figure 8.1.: Opto-mechanical design of the *PICOLO* turbulence emulator.

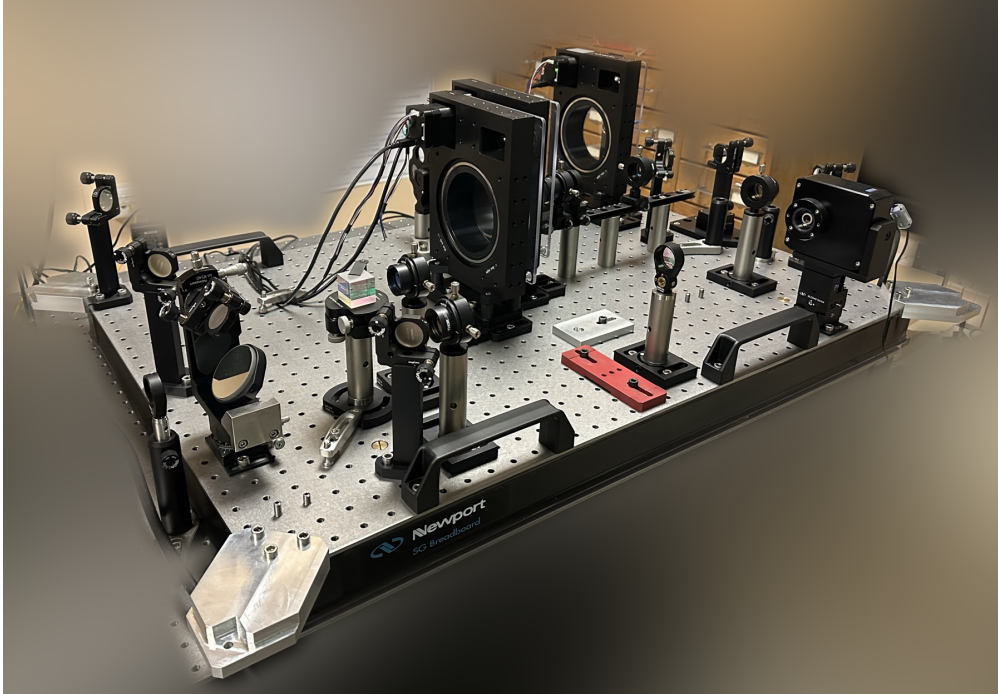


Figure 8.2.: Image of the implementation of the *PICOLO* bench.

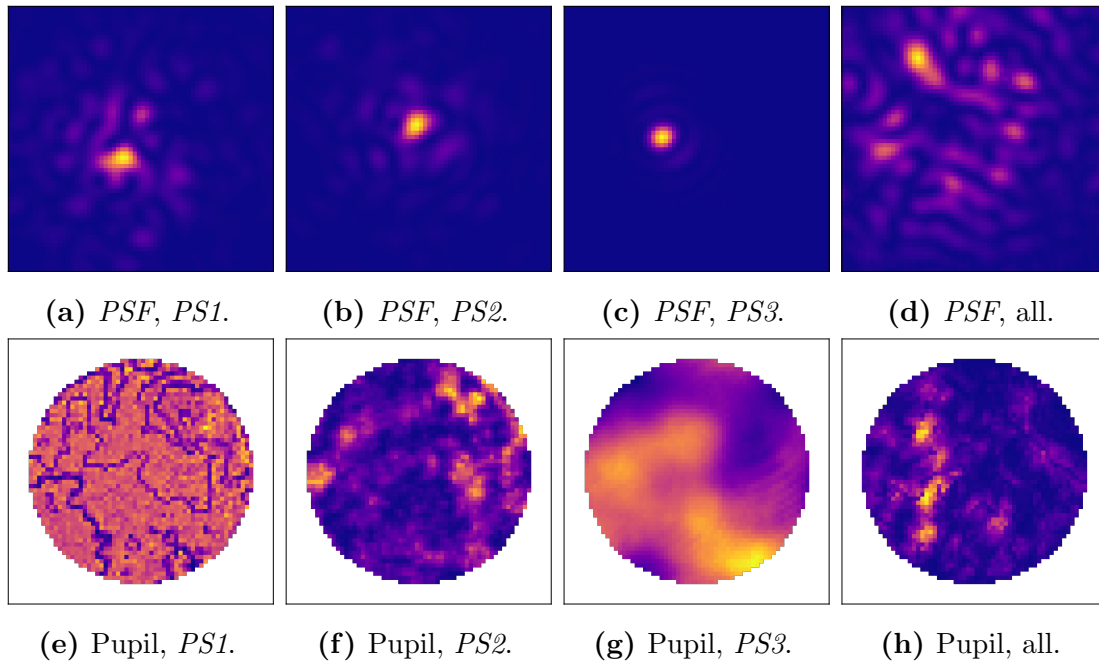


Figure 8.3.: Exemplary experimental acquisitions of short-exposure *PSF* and pupil images for the different phase screen configurations.

8.4. Characterization

We present here our methodology for the characterization of the turbulent link channel emulator. The goal of this characterization is to ensure that the phase screens have been properly manufactured, that the emulator produces the correct turbulence conditions, and that those are understood.

We provide measurements of both phase and scintillation on both a per-screen basis and for the three-screen configuration. The study of scintillation covers both its spatial and temporal behavior. We also compare the results to a numerical simulation of the emulator using *TURANDOT* (Vedrenne et al. 2012), an optical physics propagation tool developed by *ONERA* for *CNES* (the French Space Agency). The result of this comparison is a digital twin of the *PICOLO* bench to support cross-validation between experiments and simulations during future developments.

8.4.1. Phase Characterization

Different methods are possible to characterize the phase introduced by the phase screens and verify that they provide the desired phase distortions in terms of phase variance and spectrum. A first method (Tokovinin 2002) uses the measurement of the full-width-half-maximum of the long-exposure seeing-limited *point spread function* (*PSF*) and compares it to the theoretical expectation from the prescribed

phase. This method is not applicable on the bench in our case due to both the strong beam wander (resulting in *PSF* cropping) and speckles in the *PSF* derived from the strong turbulence conditions (see Figure 8.3). Alternatively, we chose to use a dedicated set-up to measure wavefront slopes with a Shack-Hartmann wavefront sensor, reconstruct the phase associated with these measurements, and compare the reconstructed phase statistics to the statistics of the prescribed phase screens. The phase reconstruction is conducted using a Zernike polynomials basis, obtaining modal variances for each mode. To compare the estimated modal phase variances to the screen prescription, a theoretical model of these variances assuming a von Kármán spectrum is fitted using the two model parameters: the Fried number (r_0) and outer scale (L_0). The fitting provides an estimation of these two parameters, which can be compared to corresponding values for each of the prescribed phase screens. The details of this method and the required setup are discussed in the next section.

The phase characterization presented here was the method used to accept the phase screens from the manufacturer, while further characterization was conducted after acceptance. The characterization of the scintillation power spectral densities in Section 8.4.2 provides supplementary phase verification, since the scintillation characteristics depend on the phase.

8.4.1.1. Measurement Setup

We first obtained Shack-Hartmann measurements of the phase screens, to achieve that we illuminated a circular section of the phase screen with a collimated laser source at a wavelength $\lambda = 1.55 \mu\text{m}$. A 4f imaging relay was used to conjugate the footprint of the collimated beam on the phase screen to the pupil of the Shack-Hartmann wavefront sensor. Conjugation of the planes avoids further propagation of the wave between the phase screen and the wavefront sensor, which would produce scintillation and therefore bias the wavefront measurement. The Shack-Hartmann wavefront sensor used is an *Imagine Optic HASO4 SWIR 1550*, which is capable of providing absolute slope measurements thanks to the calibration provided by its manufacturer.

The collimator beam footprint was placed at the same distance from the center of rotation of the phase screen as used in the bench. Different samples of the screen were taken by rotating the screen. We decided to measure only the disk that will be illuminated during the rotation of the phase screens since the distance between the rotation center and the beam footprint is constant. This strategy ignores the rest of the screen and provides a limited number of measurements, however, it corresponds to a characterization of the only area of the phase screen that is used. The total number of statistically independent measurements available is around 50 per phase screen; although overlapping measurements were used to average measurement noise even if they do not bring statistical convergence. The same discussion applies to the scintillation characterization.

The acquired slope measurements were used to reconstruct the Zernike coefficients (using the least-squares method (Cubalchini 1979)) for each spatial sample; the variance of each coefficient across all samples provides an estimation of the variance for the corresponding Zernike mode. We chose to reconstruct up to the 10th Zernike polynomials radial order, considering the number of available Shack-Hartmann subpupils. The resulting Zernike modes variances were averaged by radial order and fitted to their theoretical values assuming a von Kármán spectrum Andrews and Phillips (2005) using as fitting parameters the Fried number (r_0) and outer scale (L_0). The fitting was computed by solving a non-linear least squares problem using a Levenberg-Marquardt optimization routine. Special attention needs to be paid to the fitting: The modal variance of the atmospheric turbulence follows a power law with very different orders of magnitudes between radial orders (see Figure 8.4); if the least squares cost function is computed using all modal variances, the low order modes, which have bigger variances, will dominate the fitting and bias the estimation. In the von Kármán spectrum, the low radial order modes are influenced by both the outer scale and the Fried parameter, while the high radial order modes are only influenced by r_0 . As a result, r_0 can be estimated by first fitting the high radial orders to a von Kármán spectrum with a fixed outer scale; we use the Kolmogorov spectrum which is equivalent to an infinite outer scale. A second fitting of all modal variances is used to estimate L_0 , this time assuming a von Kármán spectrum with the previously estimated r_0 as a fixed parameter.

8.4.1.2. Results

Figure 8.4 illustrates, for the case of *PS2*, the measured Zernike coefficient variances averaged per radial order and a comparison to the best fit to a von Kármán spectrum. The close fitting of the measurements to the theoretical spectrum shape confirms that the measured phase follows the power law of the von Kármán spectrum. The deviations at higher radial orders (i.e. high spatial frequencies) are related to noise propagation and the reconstruction of higher Zernike orders (aliasing effect). The results of the Zernike mode variance fitting for the three screens are summarized in Table 8.4 by means of the resulting r_0 and L_0 estimates. In terms of relative error between the expected and the measured quantities, r_0 error is 10% in the worst case, while for L_0 it can be as high as 65%. The bigger mismatch in L_0 can be explained by the difficulty of estimating the variance at low spatial frequencies with a limited number of measurements; since low frequencies have fewer periods over one measurement, it is necessary to use more measurements to estimate low spatial frequencies than to estimate high frequencies. This lack of accuracy could be improved in the future by increasing the number of available phase measurements by measuring all the phase screen area and not only the annular section that is illuminated during the operation of the bench.

In conclusion, these results provide an estimation of the r_0 and L_0 of the screens and confirm that they follow the desired von Kármán spectrum in their spatial

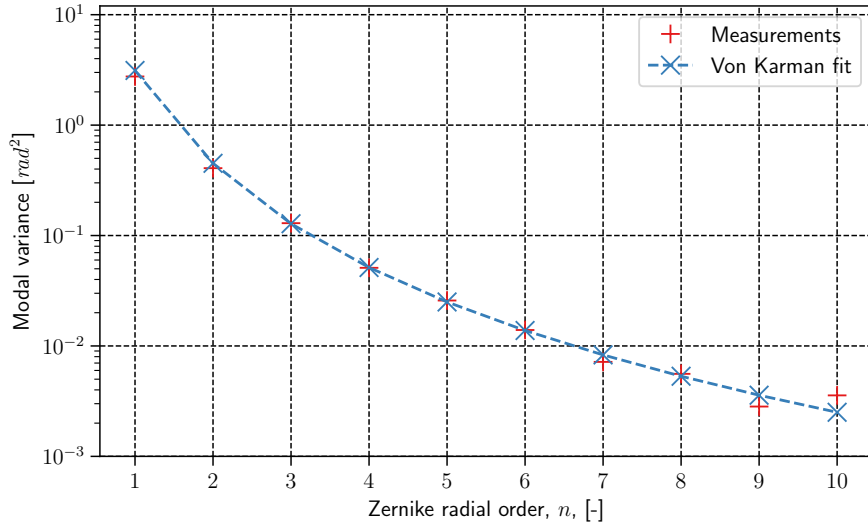


Figure 8.4.: Reconstructed Zernike mode variances vs. their fit to a von Kármán spectrum for PS2.

Table 8.4.: Reconstructed Zernike mode variances fitting results to von Kármán spectrum.

Screen	D/r_0 theo.	D/r_0 meas.	L_0/D theo.	L_0/D meas.
PS1	8.889	8.964	3.000	3.945
PS2	6.780	6.227	3.000	8.585
PS3	1.159	1.292	10.000	16.592

statistics. This first characterization allowed us to test the quality of the phase screens and accept them. The later characterization of the scintillation presented in the next section served as a supplementary characterization of the phase produced by the screens. We also used the measured per-screen r_0 to derive the equivalent $C_n^2 \cdot dz$ for each screen, reported in Table 8.3 as "measured" profile. These values were used for the numerical simulations of the wave propagation in the bench.

8.4.2. Scintillation Characterization

Optical wave scintillation, unlike phase, can be directly measured as intensity on the pupil plane. We characterized the scintillation on the emulator by analyzing images of irradiance patterns on the pupil using a matrix detector. The scintillation characterization was conducted in both spatial and temporal domains. We compared the measured results to a numerical simulation of the same propagation case. This results in a cross-validation of the specification of the phase screens and the resulting spatial and temporal signatures for scintillation.

8.4.2.1. Measurement Setup

As pointed out in Section 8.3.4, the bench allows pupil imaging by an afocal telescope that relays the pupil plane from the telescope entrance aperture to an imaging matrix detector. This allows recording the irradiance distribution (i.e. sampled value proportional to the irradiance on each pixel in $\text{W} \cdot \text{m}^{-2}$) over the pupil of the system, which is used to characterize the scintillation.

The acquisitions are taken in two different ways for spatial and temporal characterization. For spatial characterization, the phase screens are rotated so that for every acquisition the beam footprints on the screen do not overlap. In this way, we reduce the spatial correlation between measurements. For temporal characterization, the phase screens are rotated to a speed that produces the equivalent layer velocity for the given layer, achieving the desired temporal correlation.

For the spatial characterization, the integration time and the screen rotational speed were adjusted to reduce the displacement during exposure to less than a tenth of the pixel size, therefore negligible. In the case of the temporal characterization, the $50 \mu\text{s}$ exposure time used is equivalent to a 500 ns exposure time on-sky (see the temporal compression discussed in Section 8.3.2) and as a result negligible too.

The bottom row of Figure 8.3 presents a typical image of the experimental acquisitions of pupil irradiance patterns used for scintillation characterization.

We carried all characterizations first on a per-screen basis and later with the three screens together. The individual screen characterization provides the verification of every screen, while the three-screen setup characterizes the operating conditions of the bench.

The fiber collimator used as source (i.e. emitter) beam has a 7 mm beam waist diameter at the pupil of the telescope, while the pupil is 2 mm . This results in a truncated Gaussian illumination pattern on the pupil. The effect of the Gaussian shape and its wandering was confirmed to be negligible via numerical simulations. As a result, the rest of the numerical simulations conducted do not model this effect and consider a homogeneous illumination pattern.

8.4.2.2. Numerical Simulations

We compared the experimental results to numerical simulations using the optical propagation code *TURANDOT*. The numerical simulation does not use the phase maps specified to the manufacturer. Instead, it generates phase screens with von Kármán statistics and a $C_n^2 \cdot dz$ reported as "measured" profile in Table 8.3, which was derived from the fitting of r_0 summarized in Table 8.4. As a consequence, the results of the numerical simulations are expected to be statistically equivalent to the perturbations generated by the emulator, but not strictly the same. For spatial characterization statistics, each realization uses news statistically independent draws of the phase screens from the prescribed $C_n^2 \cdot dz$. For the temporal characteristics, a time series is generated from a unique realization of the phase screens, for each time step the layers are shifted according to their wind speed achieving the time

series. After propagation, the irradiance over the pupil is computed, obtaining the equivalent of the experimental measurements. Once the equivalent data to the experiment is produced, experiment and simulation data are post-processed in the same fashion.

The numerical simulations do not contain any measurement noise in the resulting irradiance. This is not the case for the experimental measurements, where read-out noise and shot noise are not negligible. The laser power was adjusted to be as high as possible during the characterization. This is limited by the saturation of the matrix detector pixels due to the finite dynamic range, while the dynamic range (i.e. variance) of the scintillation speckles increases with the turbulence strength.

8.4.2.3. Characterization Metrics

We characterize scintillation by two main metrics: the power spectral density of the normalized irradiance distribution over the pupil and the scintillation index.

First, we define a normalization of $\mathcal{I}(x, y, k)$, the irradiance distribution across the spatial coordinates x and y , with k being either a temporal or an ensemble index:

$$\bar{\mathcal{I}}(x, y, k) = \frac{\mathcal{I}(x, y, k) - \langle \mathcal{I} \rangle_k(x, y)}{\langle \mathcal{I} \rangle_k(x, y)}. \quad (8.4)$$

The bracket operation corresponds to the sample average of the magnitude, defined in general as:

$$\langle \mathcal{I}(x, y, k) \rangle_{x,y,k} = \sum_{i_x=1}^{N_x} \sum_{i_y=1}^{N_y} \sum_{i_k=1}^{N_k} X(x_{i_x}, y_{i_y}, k_{i_k}) / (N_x \cdot N_y \cdot N_k), \quad (8.5)$$

while in this case it is $\langle \mathcal{I}(x, y, k) \rangle_k = \sum_{i_k=1}^{N_k} X(x, y, k_{i_k}) / N_k$. Note that the normalization is different for each pixel over the pupil of the telescope, therefore it allows the comparison of the scintillation regardless of the average irradiance impinging on the pupil, i.e. it removes any fixed irradiance pattern.

The scintillation index is defined as the variance of the normalized irradiance distribution:

$$\sigma_{\bar{\mathcal{I}}}^2 = \text{Var}(\bar{\mathcal{I}}) = \langle (\bar{\mathcal{I}} - \langle \bar{\mathcal{I}} \rangle)^2 \rangle = \frac{\langle \bar{\mathcal{I}}^2 \rangle}{\langle \bar{\mathcal{I}} \rangle^2} - 1 \quad (8.6)$$

The variance of the normalized irradiance field can be computed either as a sample variance of the normalized pixel values or from the integral of their power spectral density. For the spatial scintillation index, the sample variance is computed for all pixels in the pupil for each acquisition and then the resulting variances are averaged for all realizations:

$$\sigma_{\bar{\mathcal{I}}}^2 = \langle \text{Var}_{x,y}(\bar{\mathcal{I}}(x, y, k)) \rangle_k = \langle \langle (\bar{\mathcal{I}} - \langle \bar{\mathcal{I}} \rangle_{x,y})^2 \rangle_{x,y} \rangle_k. \quad (8.7)$$

The temporal computation is the same but computed per pixel using all the samples in the time series of every pixel and then averaged across all pixels:

$$\sigma_{\bar{\mathcal{I}}}^2 = \langle \text{Var}_k (\bar{\mathcal{I}}(x, y, k)) \rangle_{x,y} = \langle \langle (\bar{\mathcal{I}} - \langle \bar{\mathcal{I}} \rangle_k)^2 \rangle_k \rangle_{x,y}. \quad (8.8)$$

We also compute the spatial and temporal *PSD* of the scintillation patterns. For the spatial characterization, we compute a 2D *PSD* (using a 2D fast Fourier transform) for every acquisition and then we compute the average of the 2D *PSDs* of all acquisitions. After computation of the azimuthal average, the spatial *PSD* is reported as a 1D *PSD*. For the temporal *PSD* computation, we compute the 1D *PSD* (using the Welch method) of the per-pixel irradiance time series and then take an average of all *PSDs* for all pixels.

For the temporal characterization, we also provide the pupil-averaged flux. To compute this we do a spatial average of the normalized irradiance across all pixels for every acquisition, obtaining a unique time series that is analyzed as the per-pixel time series. This is a proxy measurement of the effect of scintillation on the flux measurement of a mono-detector on the focal image plane but computed on the pupil plane from the measurement of the matrix detector. This measurement may be of interest to assess the performance of mono-detectors in these conditions. Nevertheless, this approximation neglects the variation of the angle of arrival, which may lead to a loss of flux if the mono-detector is not large enough.

8.4.2.4. Spatial Scintillation Results

The left column of Figure 8.5 presents the spatial 1D *PSD* for *PS2*, *PS3*, and the three-screen profile respectively. The solid line labeled *PICOLO*, corresponds to the experimental measurements, while the dashed line, labeled *TURANDOT*, depicts the numerical simulation result. In all cases, both lines overlap for the most for the most part. At least three different factors can explain these deviations: (1) The manufacturing defects and limitations of the phase screens, (2) the presence of noise in the irradiance measurements, and (3) the presence of aliasing due to the finite sampling of the irradiance. In any case, those deviations do not result in strong deviations of the total variance; Figure 8.6 illustrates this by reporting the cumulative integral for each of the *PSD*. Note also that the low and high frequencies have low power and their contribution to the variance is small, so it is the contribution of any small difference between the spectra.

With respect to the manufacturing process effects, the highest spatial frequency present in the phase screens is about 60 cycles/m, corresponding to a 40 μm pixel size in the phase screens with a 2 mm beam diameter and an equivalent 0.4 m telescope diameter on sky. Any frequency beyond that one is not supposed to be correctly represented by the phase screen; in addition, the phase screens were subject to a subpixel smoothing process by the manufacturer to remove high-frequency defects, this process could also affect the spatial frequencies close to the.

Regarding measurement noise, we can distinguish two different contributions: detector read-out noise and photon noise. Detector read-out noise can be estimated by taking dark frames with the characterization camera and its *PSD* subtracted from the irradiance one. The presented data was corrected from the data, although its effect is negligible in the variance and in the power spectral densities. The contribution of photon noise cannot be easily estimated, since by definition the irradiance measurements under strong scintillation have a high dynamic range, it is therefore not possible to measure the spectrum of this contribution, and the measurements reported contain this signature.

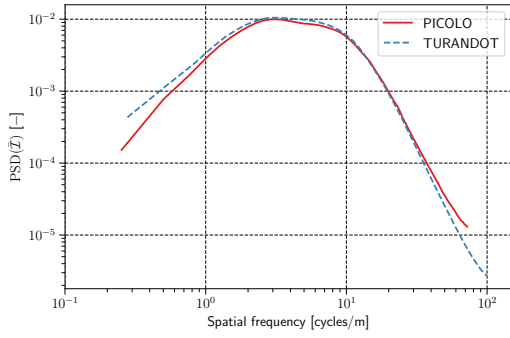
The presence of aliasing has not been quantified either. In conclusion, although it is not possible to allocate the deviations measured to one of the possible causes stated, those are small and have a negligible contribution to the scintillation index. Instead, we highlight the good fitting of all the cut-off frequencies that define the main spectrum features. Since *PS2* is stronger in turbulence, it is closer to scintillation saturation and, therefore, the *PSD* of the spatial scintillation presents two regimes with cut-offs (Andrews et al. 1999; Sechaud et al. 1999) at a spatial frequency proportional to $r_0/\lambda z$ and $1/r_0$, while the weaker *PS3* has its only cut-off at a spatial frequency proportional to $1/\sqrt{\lambda z}$, where z is the propagation distance from the layer to the telescope pupil plane.

Table 8.5.: Spatial scintillation index comparison between numerical simulation and experiment.

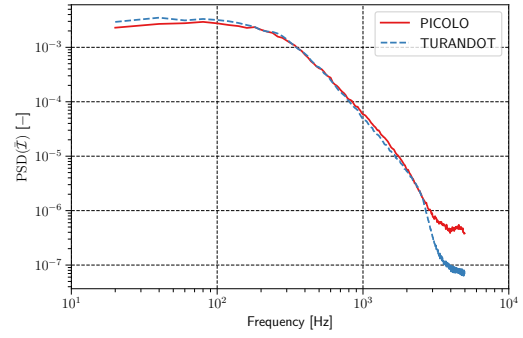
	<i>PS1</i>	<i>PS2</i>	<i>PS3</i>	All
TURANDOT	0.000 ± 0.000	0.985 ± 0.006	0.767 ± 0.018	2.050 ± 0.020
PICOLO	0.102	0.972	0.770	2.090

Table 8.5 provides a comparison of the spatial scintillation indices for both numerical simulation and experiment. The scintillation index is computed as the sample variance of the normalized irradiance measurements (see Section 8.4.2.3). For *PS1*, the expected scintillation index is zero since the screen is located at the pupil of the telescope and there is no propagation distance. This is the case in the numerical simulation, while in the experimental setup, we measure some scintillation. The reason for this is two-fold. First, it is not physically possible to place the screen exactly at the pupil, so there is some propagation. For example, the same screen placed at a distance of 1 mm from the telescope pupil results in an equivalent distance of 40 m on sky and would lead to a scintillation index of 0.064. Second, some diffractive effects are observed (see filament-like structures in the pupil *PS1* image in Figure 8.3) that also contribute to the inhomogeneity of the pupil illumination. Nevertheless, as can be observed in the three-screen configuration, the scintillation from phase screen 1 does not result in a significant contribution.

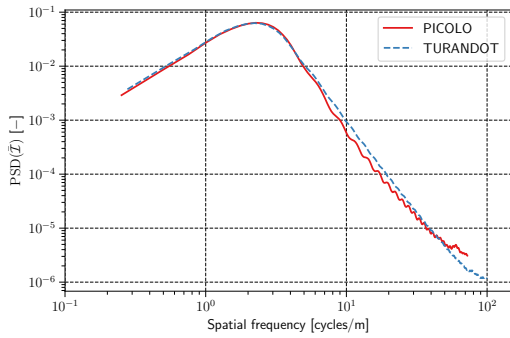
8. PICOLO Turbulence Emulator
8.4. Characterization



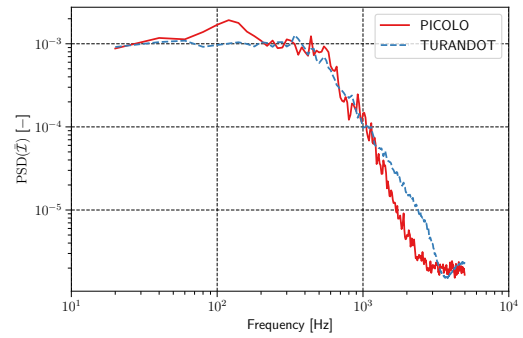
(a) Spatial, $PS2$ at $P2$.



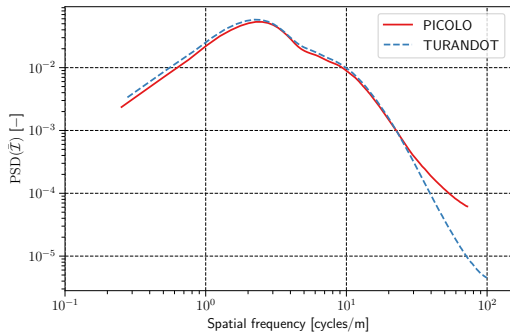
(b) Temporal, $PS2$ at $P2$.



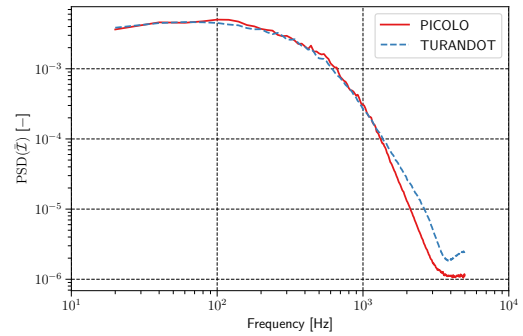
(c) Spatial, $PS3$ at $P3$.



(d) Temporal, $PS3$ at $P3$.



(e) Spatial, three screens.



(f) Temporal, three screens.

Figure 8.5.: Spatial and temporal one-dimensional power spectral densities of the normalized irradiance distributions produced by the phase screens.

Regarding the uncertainty quantification of the results, we provide the error bars for the numerical simulation. The uncertainty of the numerical simulation is due to the statistical convergence of the results. For the computation of the error bars, we used a bootstrapping method, where we divided the available number of samples in groups and computed the average scintillation index from it, where the error bars correspond to the standard deviation among all results.

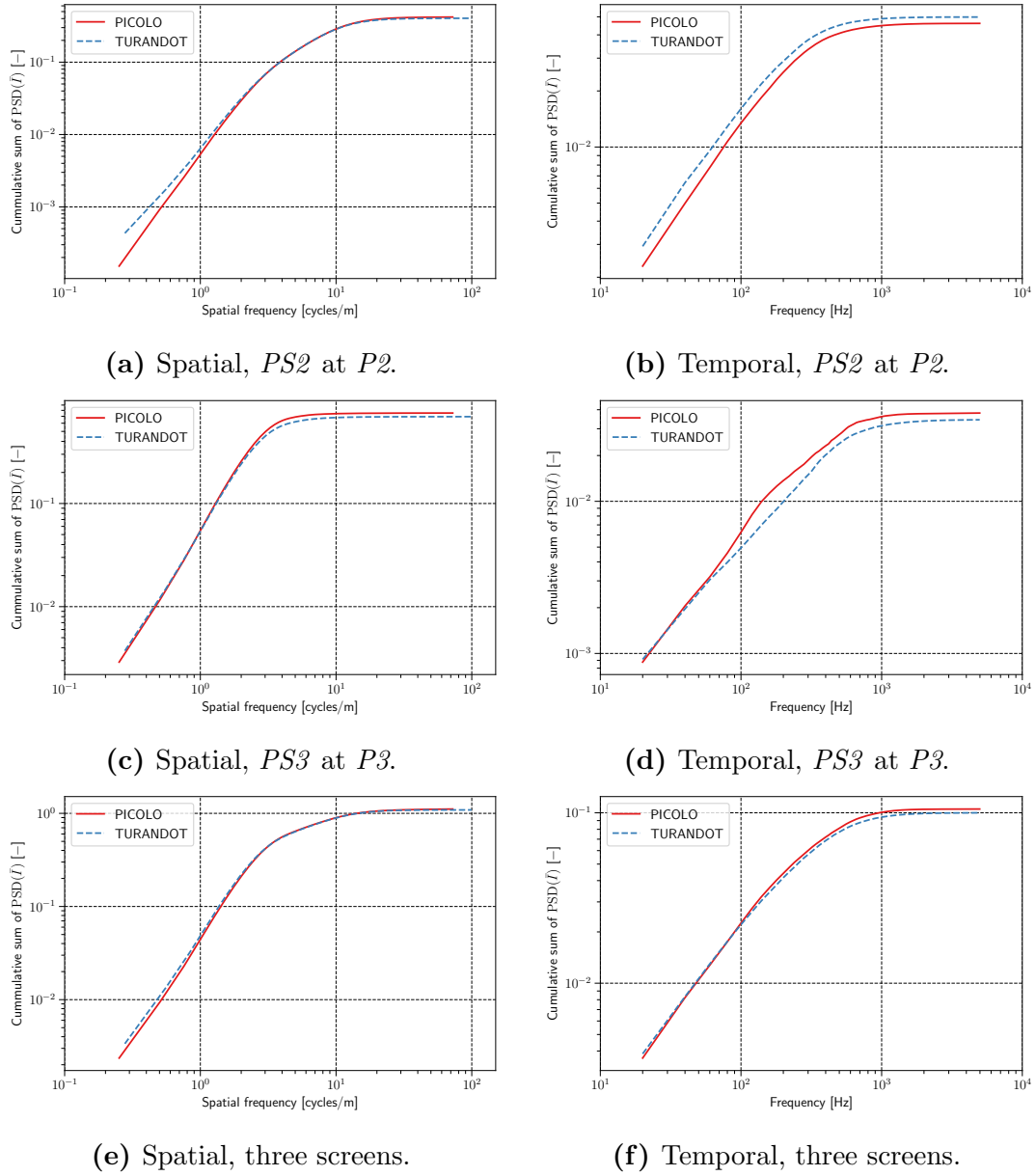


Figure 8.6.: Cumulative sum of spatial and temporal one-dimensional power spectral densities of the normalized irradiance distributions produced by the phase screens.

8.4.2.5. Temporal Scintillation Results

The right column of Figure 8.5 presents the temporal 1D *PSD* for *PS2*, *PS3*, and the three-screen profile respectively. The solid line labeled *PICOLO*, corresponds to the experimental measurement, while the dashed line, labeled *TURANDOT*, depicts the numerical simulation result. In all cases, the cut-off frequency [Andrews and Phillips \(2005\)](#) is proportional to $V/\sqrt{z/k}$, with V the transversal velocity of

the layer, and $k = 2\pi/\lambda$ the angular wavenumber. The experimental curves show in this case a noise floor at high frequencies, especially for *PS2*, where the curve has a different floor to the noise floor from the simulation. The causes for these noise floors are the same as for the spatial spectra, since the temporal spectra are given by filtering of the spatial spectra due to the shifting of the layers. Both *PS3* and the three-layer case show in the *TURANDOT* case a bump on the high frequencies due to a simulation artifact currently being analyzed. Apart from this, the fit of the curves and their cut-offs shows a satisfactory agreement between the simulation and experiment.

Table 8.6 provides a comparison of the temporal scintillation indices for both numerical simulation and experiment. The scintillation index is computed as the sample variance of the normalized irradiance measurements (see Section 8.4.2.3). Note that, following the ergodicity hypothesis, the scintillation indices in this table should be the same as the spatial scintillation indices reported in Table 8.5, which proves to be consistent with our results. We provide the error bars for the temporal simulation with all phase screens computed as the standard deviation of the scintillation indices computed for five simulations of the same case with different random seeds for the phase screen generation.

Table 8.6.: Temporal scintillation index comparison between numerical simulation and experiment.

	<i>PS1</i>	<i>PS2</i>	<i>PS3</i>	All
TURANDOT	0.000	1.056	0.692	2.055 ± 0.052
PICOLO	0.101	0.968	0.765	2.138

Finally, we study the variation of the integrated flux after *PICOLO*. This computation is based on the time series resulting from the averaging of the intensity measurements for every pupil pixel at every frame. Note, this is not an equivalent of the coupled flux, since it does not take into account the phase and amplitude effects in the coupling into a single mode fiber. Even with perfect *AO* (i.e. phase) correction, the mismatch between the wavefront amplitude and the Gaussian mode of the fiber will cause further losses that are not accounted for in this measurement. This measurement is closer to the flux measured by a mono-detector big enough that the variation of the angle of arrival due to turbulence and the *PSF* size does not cause a loss of flux during the measurement of the time series, i.e. the power in the bucket at the telescope aperture level.

Figure 8.7 shows a part of the time series obtained, both for the experiment, labeled *PICOLO*, and the numerical simulation, labeled *TURANDOT*. The time series is further analyzed by computing its *PSD*, shown in Figure 8.8, while a histogram of the time series is provided in Figure 8.9. The comparison of the *PSD* shows how the time series have the same time characteristics, including the

two regimes with cut-offs around 500 Hz and 1000 Hz. At high frequencies, the experimental results show a similar noise floor to the one observed in the temporal spectra. The same high-frequency noise presence can be observed in the time series plot. The shape of the histograms is similar too and the variance of the power (reported in the same figure), equivalent to the scintillation index of the irradiation pattern filtered by the pupil, is also close.

We take this opportunity to discuss the periodicity of the turbulence generated. Note that the emulator only uses a small area of the phase screen, which is the ring resulting from the illumination of the circular beam footprint when the screen rotates. The screens rotate to generate the displacement equivalent to the one produced by the wind for each layer. After a given period of time, the screen completes a turn and the beam starts sampling the same phase distortion as previously, generating a periodic behavior. This effect is diminished by the fact that there are three phase screens rotating at different speeds, so the combination of the three reduces the periodicity of the overall turbulence. The previous statement is true for the phase disturbance since the three screens participate in it. We computed the period for this case, and it corresponds to hours, longer than the typical minute scale time series expected from the emulator. Still, for the scintillation, this period is reduced, since only *PS2* and *PS3* are involved. Note that both phase and scintillation contribute to fiber coupling, so the periodicity of the coupled flux will be impacted. Finally, the case of the pupil averaged flux presented above is the one most affected by periodicity. Since the speckles produced by *PS2* are much smaller than the pupil size, their effect is averaged out in this metric, and only the *PS3* speckles (similar in size to the pupil) contribute to it. As a result, the pupil-averaged flux shows a periodicity corresponding to the time that it takes *PS3* to complete a rotation. For the time series presented above, over a total duration of 1 s we detected a total of 7 periods by computing its autocorrelation, corresponding to the 7 rotations of the screen during that amount of time. All these periodical effects are limitations of the emulator that once understood are considered of minor importance since they result from the limitation in the number of phase screens that are used, which answers a trade-off between physical fidelity and setup complexity and cost.

8.5. Operating Conditions

Table 8.7 summarizes the effective parameters of the bench after the characterization reported in this work.

8.6. Conclusion

We have presented the methodology for the design and characterization of a turbulence emulator representative of a downlink between a *LEO* satellite and a

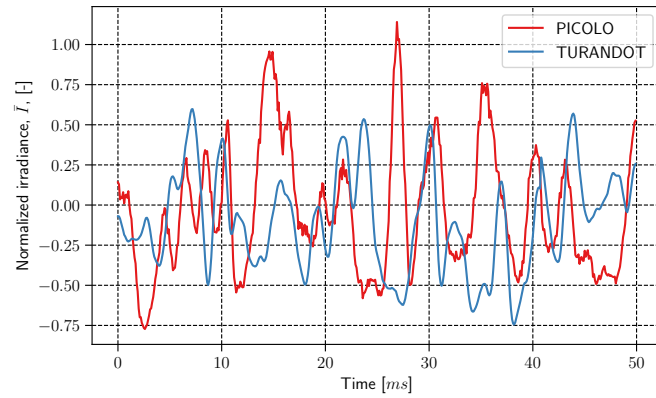


Figure 8.7.: Zoom in on the time series of the pupil averaged flux.

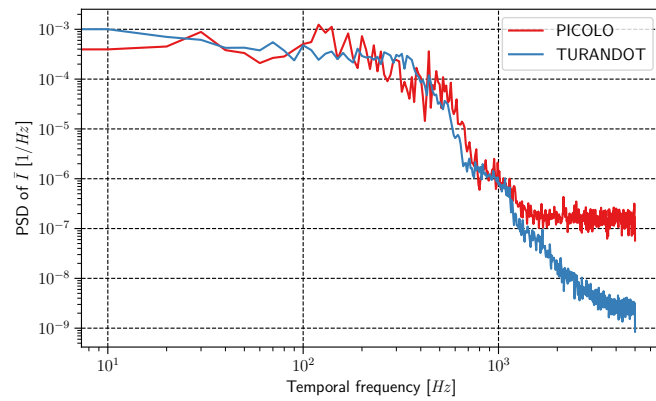


Figure 8.8.: Power spectral density of the time series of the pupil averaged flux.

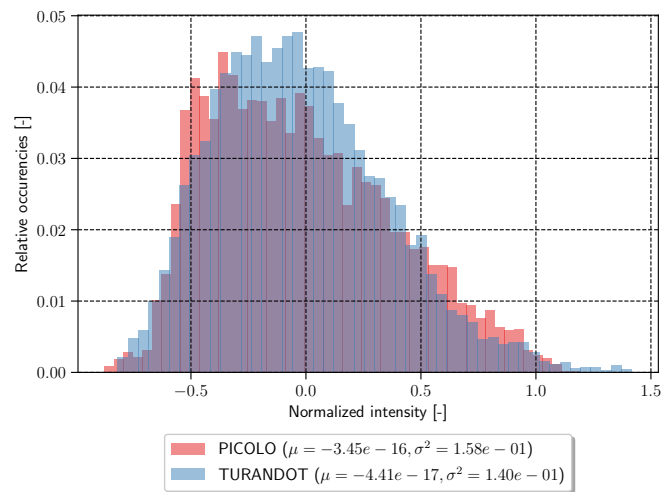


Figure 8.9.: Histogram of the time series of the pupil averaged flux.

Table 8.7.: Operating conditions of the turbulence delivered by the emulator.

Name	Value	Comment
Pupil diameter	40 cm	Equivalent telescope size.
Wavelength	1.55 μm	
Exit pupil diameter	3.3 mm	Telescope pupil conjugated to periscope mirror. Interface to client systems.
Orbit height	500 km	
Culmination point	90°	
Distance to satellite	1965 km	
Satellite trackign speed	2 mrad \cdot s ⁻¹	
Line-of-sight elevation	10°	
r_0	3.39 cm	Sum from the per-layer results in Table 8.4.
D/r_0	11.8	From the r_0 reported above.
θ_0	1.603 μrad	Computed from formula for the "measured" profile in Table 8.3.
τ_0	3.125 μs	Computed from formula for the "measured" profile in Table 8.3.
σ_I^2	2.138	Temporal scintillation index, as measured in the characterization (see Table 8.6).

ground station at 10° elevation. The bench is able to simulate both the strong turbulence conditions at low elevation, as well as the dynamics due to the fast apparent wind caused by the satellite motion. The emulator is able to host different instruments by coupling them to its exit pupil. Therefore, the emulator is able to provide a long time series of the disturbed field at the pupil of a telescope under realistic turbulence conditions.

The characterization presented proves that the bench delivers the turbulence conditions expected. This includes a detailed characterization of the scintillation conditions, which is necessary for future investigations regarding the performance of *AO* systems under scintillation. The agreement found with respect to the numerical simulation motivates the use of the numerical simulation as a digital twin of the bench for performance estimations before testing components on the bench.

As a result, *ONERA* has a testing platform for future *AO* systems (wavefront measurement and control laws) under strong turbulence perturbations (scintillation and unsteady turbulence). *ONERA* uses this platform for its own research and also offers access to it to the community (Billaud et al. 2022). The system will be used to test new *AO* and free-space optical communication concepts and integrate and validate them before on-sky campaigns. For example, the integration and

testing of the *AO* system for *ONERA*'s *FEELINGS* ground station (Petit et al. 2022), study Shack-Hartmann wavefront sensors under scintillation conditions and how to improve their performance, test new *AO* control algorithms (such as predictive control (Robles et al. 2022)), test new turbulence correction concepts such as *photonic integrated circuit* (*PIC*) (Billaud et al. 2022) and test new telecommunication components or digital signal processing architectures. An upgrade of the bench to add the effect of anisoplanatism in the feeder links (Vedrenne et al. 2017) cases is currently under study.

9. Experimental Validation

Contents

9.1. Towards a Predictive Controller Demonstration	211
9.2. <i>LISA</i> Adaptive Optics System	212
9.3. Coupling to the <i>PICOLO</i> Turbulence Emulator	214
9.4. Coupling Optimization	216
9.5. Coupling Measurements	217
9.6. Integrator Validation	218
9.6.1. <i>RTC</i> Implementation	219
9.6.2. Temporal Characterization	219
9.6.3. Results	221

Introduction

This chapter presents my work towards the experimental demonstration of the implementation of the predictive controller developed in this thesis, using the *LISA* adaptive optics bench and the *PICOLO* turbulence emulator.

The chapter provides an overview of the strategy followed for this demonstration and reports the steps accomplished during my thesis. These steps include the coupling between the adaptive optics system and the turbulence emulator, the optimization and calibration of the fiber coupling, and the validation of an integral control law.

The aim of this laboratory experiment is to replicate the results of end-to-end adaptive optics simulations to cross-validate the simulation and experiment and to investigate the practical implementation of this kind of control law. During this thesis these goals were achieved for an integral controller, the tests with the predictive controller will be the subject of future research.

Future work on this setup will enable studying the behavior of the controller under scintillation and testing different model identification strategies for the predictive model. Other adaptive optics control and wavefront sensing techniques will be tested on the same setup. All these developments will lead to the final implementation of a predictive controller in FEELINGS ([Petit et al. 2022](#)), ONERA's optical ground station for *GEO*-feeder links research.

9.1. Towards a Predictive Controller Demonstration

Figure 9.1 represents the different steps of the plan for the preparation of the demonstration of the predictive controller using the *LISA* adaptive optics system and the *PICOLO* bench emulator:

1. *Characterization of PICOLO + development of a digital twin:* To facilitate the performance assessment and comparison of experimental results to numerical simulations using the turbulence-distorted beam provided by the *PICOLO* emulator, an initial characterization of the emulator's distortions is requisite. During this thesis, such a characterization was conducted and is reported in Chapter 8. This characterization includes the development of numerical simulations for optical propagation across the emulator and their subsequent comparison to laboratory measurements. These simulations result in digital twin of the emulator than can be used for end-to-end adaptive optics simulations.
2. *Optimization and calibration of the coupling:* The main metric used to evaluate the performance of the *AO* correction will be the single-mode fiber coupling. Conducting fiber coupling experiments requires proper alignment and optimization of the setup in order to maximize the coupling in diffraction-limited conditions before introducing turbulence distortions. These optimizations include the coupling between the adaptive optics system and the exit pupil of the telescope, the optimization of the coupling using the precision alignment stage included in the fiber injection module, and the optimization of the adaptive optics reference state (i.e. reference slopes).
3. *Characterization of temporal behavior:* The implementation of the adaptive optics loop in a *RTC* requires the verification of the temporal behavior of the loop, especially the characterization of the loop delay. Without this characterization, the adaptive optics temporal error assessment would be biased.
4. *Implementation of the LQG on the RTC:* In order to implement the predictive controller on the *RTC*, the *LQG* control structure needs to be implemented. The basic *LQG* structure is a general observer-based control that can be used to implement many different control algorithms. Once this structure is available, implementing the *LQG* requires the computation of the different matrices involved. Some of these matrices need to be calibrated; the calibration needs of the predictive controller will be an output of such a demonstration.
5. *Comparison to simulations:* The final stage of the demonstration implies the comparison of the laboratory performance to the expected performance using all the tools developed during this thesis: adaptive optics error budgets, end-to-end simulations, and emulator digital twin.

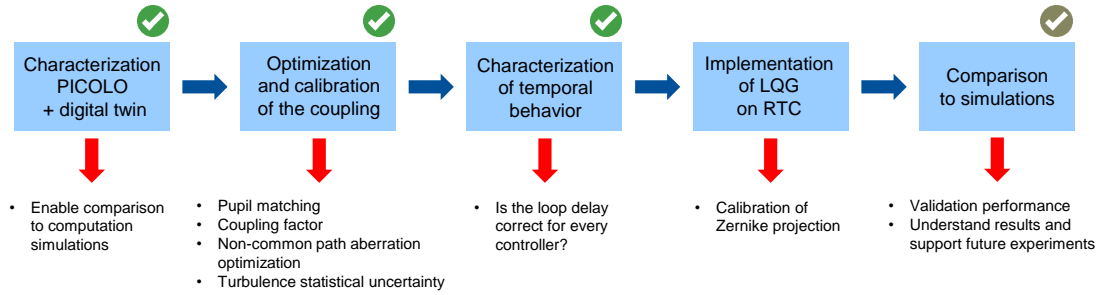


Figure 9.1.: Strategy for the demonstration of the predictive controller using the *PICOLO* bench. Green and gray ticks represent the tasks accomplished and partially accomplished during this thesis, respectively.

Remark

The plans and preliminary results for the validation of the adaptive optics predictive controller were presented in a talk titled “*Laboratory validation of an adaptive optics predictive controller for LEO satellite tracking applications*” at the *COAT 2023* conference in Durham (United Kingdom).

The remainder of this chapter reports the contribution of this thesis to the demonstration and outlines the open points and future work necessary to conclude it.

9.2. LISA Adaptive Optics System

The *LIght and Small Adaptive optics (LISA)* adaptive optics system is a compact adaptive optics bench designed by *ONERA*. The bench has been used for conducting *AO*-assisted *LEO*-to-ground links at the *Observatoire de la Côte d’Azur (OCA)* using the *Metrology and Optics (MEO)* telescope (Lim et al. 2018; Phung et al. 2021). Details on the telescope and the tracking implementation can be found in Phung et al. (2021).

LISA uses a Shack-Hartmann wavefront sensor with 8×8 square subpupils, where the field of each subpupil spans 10×10 pixels on the detector at Shannon sampling. The *WFS* camera is a *RAPTOR Owl* camera based on *InGaAs PIN* photodiodes with 320×256 pixels and a 80% quantum efficiency at $1.55 \mu\text{m}$. The slope computation algorithm is a thresholded center of gravity. The threshold value is adjusted to limit the detector read-out noise background effect on the slopes computation. The phase correction is performed by an ALPAO magnetic DM with 97 actuators, used in a 9×9 configuration; each actuator can provide a maximum $\pm 5 \mu\text{m}$ stroke. The *AO* loop runs on an *RTC* implemented in a Linux personal computer; the *RTC* implements a set of features for wavefront sensing and control.

Figure 9.2 shows the *LISA* adaptive optics system; an overview of its optical path is provided below:

1. The input beam is injected on the system using its entrance pupil. The stop of the system is defined by stop aperture located at the *DM*; the entrance pupil of the system is located upstream of the *DM* and corresponds to the image of the stop by an afocal system.
2. In the image, a reference point source is used, located at the bottom-right corner of the image. The beam moves leftward from the source along the green path, toward the *DM*. The source is composed of an optical fiber and a collimating lens focused on the fiber end to provide a collimated beam. These two elements (fiber and collimating lens) are not part of the setup once *LISA* coupled to *PICOLO*; see Section 9.3 for a description of this coupling.
3. The other two lenses between the source and the *DM* correspond to the afocal system that relays the stop so that the entrance pupil of the system is more accessible.
4. The beam follows the green path toward the *DM* and arrives at a first beamsplitter (*BS1*). The transmission path of the beamsplitter goes to the *WFS*; the reflection path continues along the pink path, the fiber injection path.
5. The pink path arrives at the second beamsplitter (*BS2*). The transmission path of the beamsplitter goes to the *fiber injection module (FIM)*; the reflection path continues toward the green path. The *FIM* is composed of an *SMF* attached to a fiber collimator. The fiber collimator is mounted on a 5-axis motorized stage for precision alignment. The the end of the *SMF* is coupled to the injection photodiode (*PDI*).
6. The blue path corresponds to a focal plane of the beam on the reference photodiode (*PDR*) used for the computation of the coupling efficiency. Both photodiodes are *Femto ST* photodiode detectors.
7. Finally, the orange path can be used by inserting a flip mirror into the blue path to focus the beam on an *InGaAs* camera (*IMG*) to obtain post-*AO PSF* images of the system.

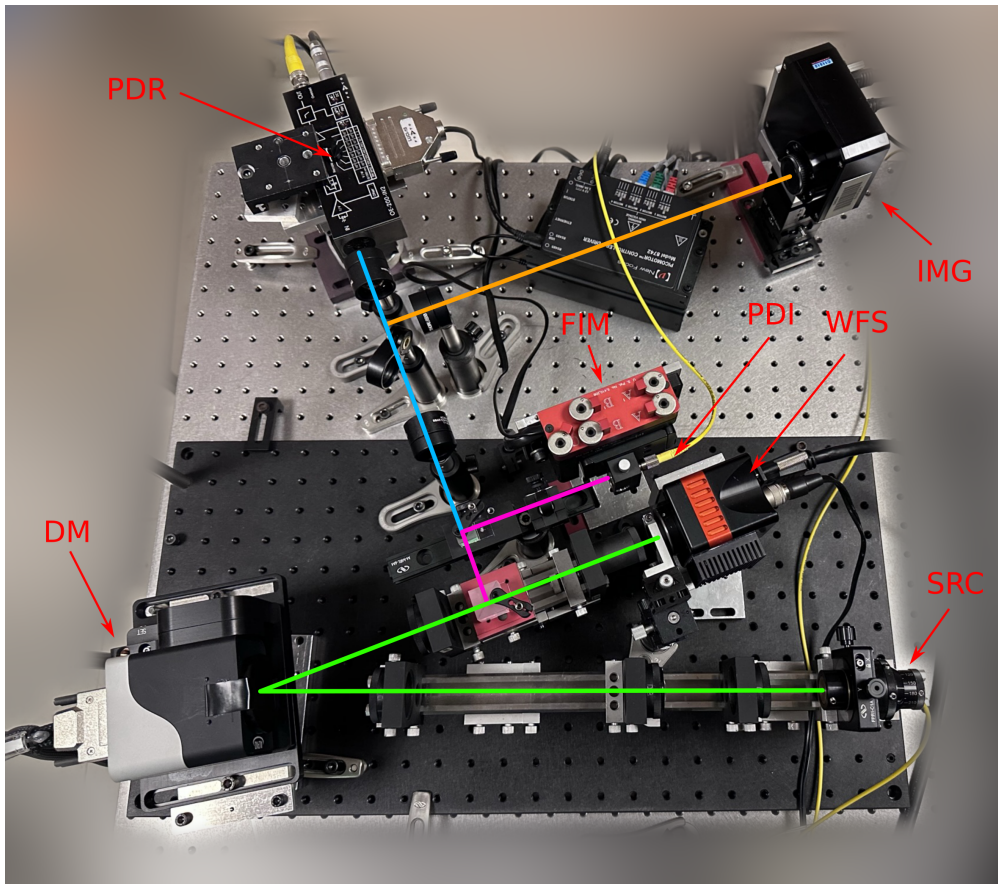


Figure 9.2.: *LISA* adaptive optics system. The input beam is injected on the system using its entrance pupil, located in front of the *DM*; in this case a focal plane point source (*SRC*) is used. Different colors are used to indicate the beam path until the different points in the bench.

9.3. Coupling to the *PICOLO* Turbulence Emulator

The coupling between the *PICOLO* turbulence emulator and the *LISA* adaptive optics bench requires matching the exit pupil of the former (located after the periscope) and the entrance pupil of the latter (located upstream of the *DM*). An afocal telescope allows the demagnification of the beam to match the two pupil sizes, as well as the folding of the beam to accommodate the two systems on an optical table. Figure 9.4 illustrates this setup:

1. The *PICOLO* bench is on the right side of the picture, with the *LISA* bench on the left side.
2. A (distorted) beam is delivered by *PICOLO* at its exit pupil, located after its periscope (*PM1* and *PM2* mirrors in the image).

9. Experimental Validation
9.3. Coupling to the *PICOLO* Turbulence Emulator

3. The afocal system consists of two lenses ($L1$ and $L2$ in the image) and a folding mirror ($FM1$) between them.
4. A second folding mirror ($FM2$) is located on the first rail of *LISA*. Both folding mirrors allow for tip-tilt adjustments to co-align the two pupils both in line of sight (two angles) as in decenters (two shifts), thus the need of four degrees of freedom.

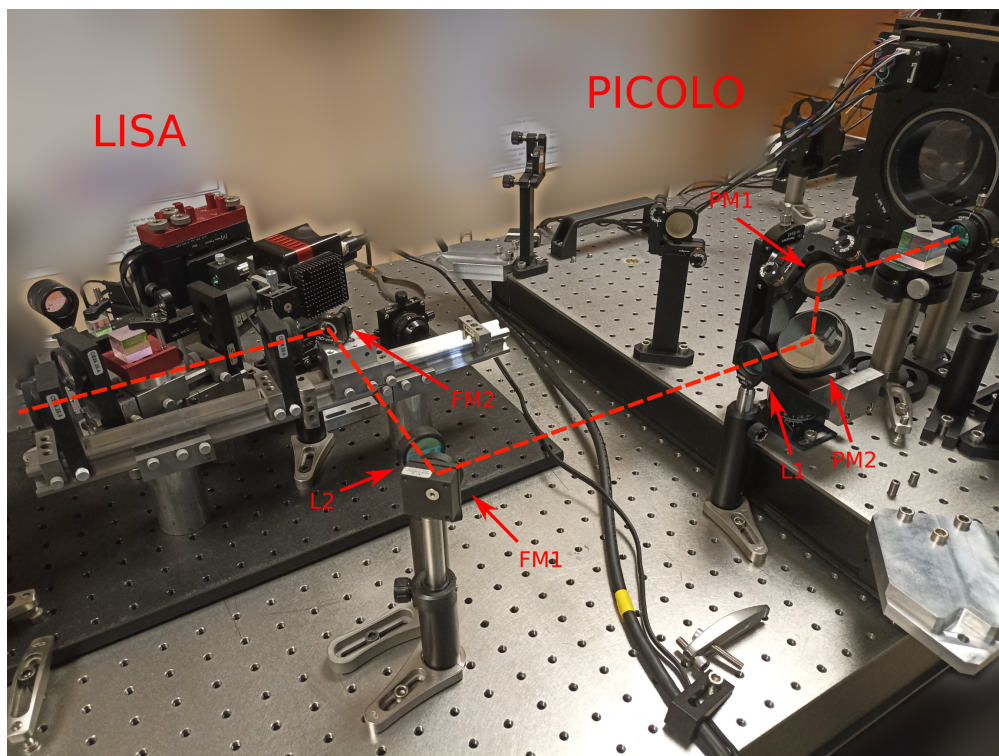


Figure 9.3.: Coupling between the *PICOLO* turbulence emulator and the *LISA* adaptive optics bench.

Before coupling, both benches were aligned separately. Since the *LISA* bench does not have an internal source for alignment, an external source was used; see Figure 9.2. The coupling between the two benches followed three steps:

1. First, the distance between different mechanical references (i.e., the periscope and the two folding mirrors) was measured to accommodate the two benches on the optical table.
2. A microscope was utilized to aid in alignment by measuring the conjugation of various planes, including the stop at the *DM*, the exit pupils of *LISA* and *PICOLO*, as well as the telescope stop and its exit pupil before the periscope.

3. The fine alignment between the two pupils used the tip-tilt degrees of freedom of the two folding mirrors. The pupil match was measured using the measurement of the *PICOLO* beam on the Shack-Hartman detector by generating an image of 8×8 pixels where each pixel was computed as the sum of all pixels within one subpupil, i.e. a map of the flux for each subpupil. All phase screens on the *PICOLO* bench were removed during this process to have a flat reference beam.

9.4. Coupling Optimization

The coupling *SMF* has a mode that has a Gaussian intensity profile and a flat wavefront, while in the absence of scintillation, a perfectly corrected field will have a uniform amplitude and a flat phase, which limits the theoretical maximum value for coupling to 82% (Shaklan and Roddier 1988). This maximum coupling can only be obtained in ideal conditions where the alignment of the bench is perfect and the optics in the system present no aberrations. These conditions are not met under experimental conditions, where the maximum coupling performance will be lower; however, to reach the best coupling possible, an optimization of the coupling under diffraction-limited conditions is conducted during the calibration of the bench.

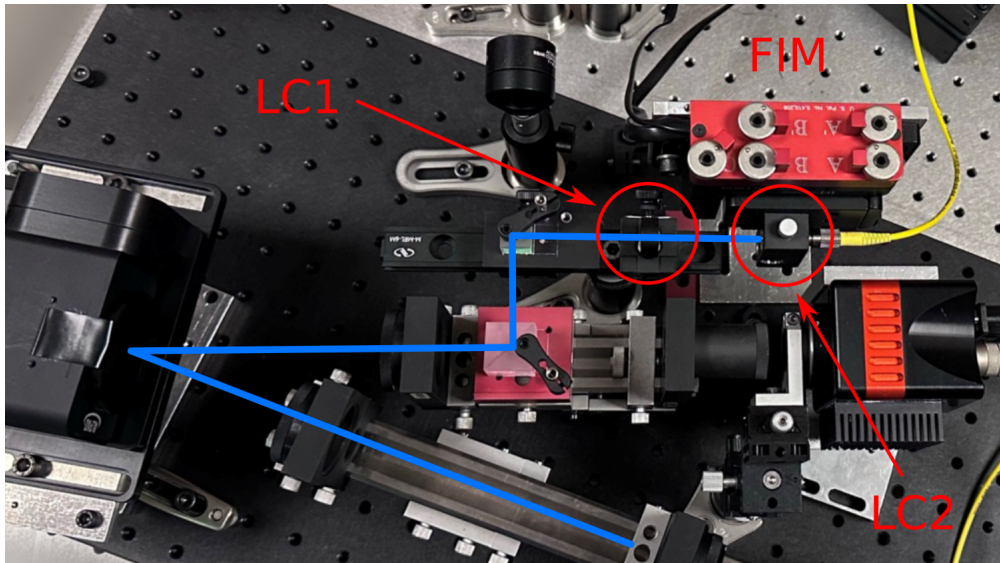


Figure 9.4.: Zoom in the coupling path of the *LISA* system. The blue line marks the optical path across the system toward the *SMF*. The beam is focused onto the *SMF* using two lenses: *LC1* and *LC2* (a fiber collimator). The alignment between the two lenses is crucial for coupling, so a picomotor alignment stage is used for fine tuning.

The corrected beam is focused and injected into the *SMF* using two lenses *LC1* and *LC2*. The latter is a fiber collimator and therefore provides high-precision

alignment with respect to the fiber. As a result, the alignment between the optical collimator and the fiber is crucial to achieve maximum coupling; a study of the sensitivity of this alignment is given in [Lim et al. \(2018\)](#). A 5-axis picomotor alignment stage is used to perform this alignment, which implements three translation directions and two rotations (the two rotation axes orthogonal to the propagation direction), with < 30 nm and 1 μ rad resolution.

The alignment provided by the precision alignment stage is not enough to achieve maximum coupling, since it cannot correct for the defocus between the lenses or other aberrations, such as astigmatism or coma, produced by the misalignment of the bench. Nevertheless, these aberrations can be corrected by *AO* by providing a set of reference slopes that account for them.

Optimization of the non-common path aberration is performed by adjustment of the reference slopes, i.e. the set point of the *AO* loop. The reference slopes are obtained by generation of reference slopes using a geometrical model of the Shack-Hartmann to convert Zernike modes to slopes offsets. A sequential manual optimization is performed to find the best combination of aberrations that give the best coupling. Alternatively, this procedure could be automated using a stochastic gradient method to optimize the coupling ([Saab 2017](#)).

9.5. Coupling Measurements

The *LISA* system has two *InGaAs PIN* monodetectors with 300 μ m diameter that are used to compute the coupling efficiency into the single-mode fiber after *AO* correction.

Notation: For each photodetector, three possible power measurements are considered: P^{FS} , P^{SMF} , P^{MMF} , corresponding to the power measured by free-space focusing of the beam on the monodetector, focusing the beam on a *SMF* and focusing it on a *multi-mode fiber (MMF)*, respectively.

Theoretically, the coupling efficiency is given by the overlap integral between the fiber mode and the complex amplitude of the beam after *AO* correction, as discussed in Section 3.3.2.1. Experimentally, coupling efficiency can be measured as the ratio between the power coupled in the fiber, P_I^{SMF} and the power before the fiber P_I^{FS} :

$$\rho = \frac{P_I^{\text{SMF}}}{P_I^{\text{FS}}}. \quad (9.1)$$

P_I^{SMF} is the quantity measured during the experiments using an *SMF* coupled to the photodiode *PDI*. P_I^{FS} cannot be measured directly, neither during operation nor during calibration, since it is not physically accessible due to optomechanical constraints. Instead, a part of the flux is split to a different optical path to be measured by a second photodiode, the reference photodiode (*PDR*), to measure P_R^{FS} . Unfortunately, P_R^{FS} and P_I^{FS} are not equivalent, since the transmission losses

on the optical paths are different. This difference needs therefore to be calibrated by measuring this ratio on the bench. Since the optomechanics of the system make it impossible to measure the power in front of the fiber, a multi-mode fiber is used as an approximation under the assumption that it is able to couple the flux even in the presence of residual aberrations, i.e. $P_I^{\text{FS}} \approx P_I^{\text{MMF}}$. Putting this together:

$$\rho = \frac{P_I^{\text{SMF}}}{P_R^{\text{FS}}} \frac{P_R^{\text{SF}}}{P_I^{\text{MMF}}} \frac{P_I^{\text{MMF}}}{P_I^{\text{FS}}}. \quad (9.2)$$

In summary:

- $P_I^{\text{SMF}}/P_R^{\text{FS}}$ is measured during the *AO* operation by the reference and injection photodiodes.
- $P_R^{\text{SF}}/P_I^{\text{MMF}}$ is a calibration constant that can be measured before using the bench by placing a multi-mode fiber in the fiber injection mode.
- $P_I^{\text{MMF}}/P_I^{\text{FS}}$ accounts for the difference coupling losses of the multi-mode fiber, since the assumption is that the modal coupling is perfect $P_I^{\text{FS}} \approx P_I^{\text{MMF}}$, this factor is assumed to be 1.

Table 9.1 gives the results of these measurements for the calibrations conducted during the experiment on 13/03/2023.

Table 9.1.: Coupling calibrations for the 13/03/2023 experiment. (*) assumed quantity, (†) computed quantity.

$P_I^{\text{SMF}}/P_R^{\text{FS}}$	$P_R^{\text{SF}}/P_I^{\text{MMF}}$	$P_I^{\text{MMF}}/P_I^{\text{FS}}$	ρ
0.686	0.711	1*	0.488†

The value obtained for the maximum coupling after injection optimization, $\rho = 0.488$, is in line with the value of $\rho = 0.47$ reported in [Lim et al. \(2018\)](#); see this publication for a budget of the *SMF* coupling that accounts for all the tolerances in the alignment that justify this value in coupling.

The calibration explained above allows to measure the coupling efficiency during *AO* operation by measuring the power coupled into the *SMF* and the power measured at the reference photodetector. The maximum coupling value, ρ can also be used to normalize the experimental measurements so they can be compared with numerical simulations that are free of alignment errors.

9.6. Integrator Validation

Before the implementation of the *LQG* controller can be conducted, it is necessary to study and understand the *AO* system performances for a simpler controller

such as the integral action controller. This section discusses the experimental implementation of such a controller in the *LISA* adaptive optics bench and its validation and comparison against numerical simulations.

9.6.1. RTC Implementation

The integral control implemented on the *RTC* using the same structure that is needed for the *LQG*. This allowed not only to validate the performance of the integral controller, but to verify the implementation of the control structure that is common to the *LQG*.

All control laws implemented on the *LISA RTC* use the following observer structure:

$$\mathbf{x}_{k+1} = \mathbf{M}_1 \mathbf{x}_k + \mathbf{M}_2 (\mathbf{y}_k + \mathbf{M}_3 \mathbf{u}_{k-1}) , \quad (9.3)$$

$$\mathbf{u}_{k+1} = \mathbf{M}_4 \mathbf{x}_{k+1} , \quad (9.4)$$

where \mathbf{M}_1 , \mathbf{M}_2 , \mathbf{M}_3 , and \mathbf{M}_4 are used to define the specific control law. The implementation of the integrator using this structure defines:

$$\mathbf{x}_k = \mathbf{u}_k . \quad (9.5)$$

The rest of the matrices are $\mathbf{M}_1 = \mathbf{I}$, $\mathbf{M}_3 = \mathbf{0}$, $\mathbf{M}_4 = \mathbf{I}$, and:

$$\mathbf{M}_2 = -g \mathbf{M}_{\text{ctrl}} , \quad (9.6)$$

where g is the integrator gain and \mathbf{M}_{ctrl} is the control matrix of the system computed as discussed in Section 2.4.2.

The same structure can be used to implement the *LQG* controller. The matrices involved here are not the control matrix, but the matrices discussed in Section 6.1.1. As stated in Section 6.1.1, the matrices needed for the implementation of the predictive controller must be obtained from calibration, in addition to the predictive model matrices that are obtained using the identification method described in this thesis.

9.6.2. Temporal Characterization

A characterization of the rejection transfer function of the integral controller was conducted. This characterization allows to compare and fit the measurement of the rejection transfer function to its theoretical model to characterize the delay present in the *AO* loop.

The rejection transfer function is estimated from experimental measurements of open and closed-loop slopes for an *AO* loop frequency of 2 kHz. The slope measurements are transformed to the *DM* command space (space used by the

integrator) using the control matrix. The power spectral density of each of the time series is computed using the Welch method and the ratio of the closed-loop over the open-loop *PSDs* is the rejection transfer function, more precisely, the gain of the complex transfer function, since the phase is not characterized. This method is based on the transfer model presented in [Dessenne et al. \(1999\)](#) and assumes the absence of measurement noise and aliasing in the slope measurements; the theoretical model for the rejection transfer function can be found in the same reference.

Figure 9.5 plots the rejection transfer function measured in the *LISA* adaptive optics system. The turbulence used for the measurement only included the first phase screen of the *PICOLLO* bench, located at the pupil, to avoid any scintillation. The best fit of the theoretical rejection transfer function is colored red for comparison. The *RTF* has two parameters, the gain of the integrator and the delay of the loop; only the latter was used as fitting parameter, since the former is known to certainty. The best fit of the *RTF* was for a delay of $\tau = 2$ frames.

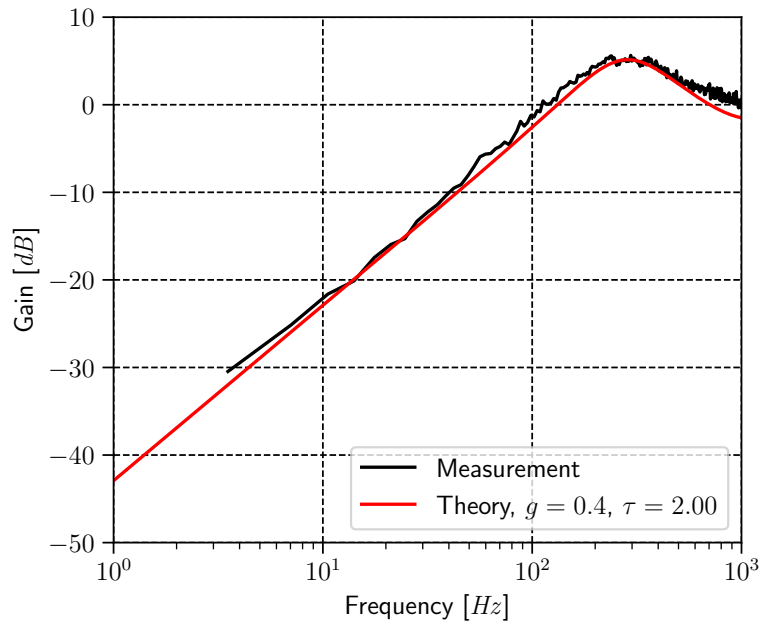


Figure 9.5.: Comparison of the integrator rejection transfer function measured on the laboratory vs. its theoretical model.

The temporal characterization presented in this section demonstrated that the integrator provides the expected disturbance rejection and measured the delay in the *AO* loop. The next section presents the results of the integrator in terms of coupling and compares it to computational end-to-end simulations.

9.6.3. Results

The experiment was conducted for an *AO* loop frequency of 2 kHz, only the first phase screen of the *PICOLO* bench was used, with a layer speed of $10 \text{ m} \cdot \text{s}^{-1}$ on sky. The integrator was set to a gain of $g = 0.4$. The same integrator was simulated using end-to-end simulations similar to the ones presented in Chapter 7. The predictive controller developed in this thesis was also simulated, with a total number of modes corresponding to the first $n = 24$ radial orders of the Zernike polynomials, i.e. 324 modes.

Figure 9.6 plots the comparison of the results of the experiment and the numerical simulations. The experimental coupling measurements were calibrated using the procedure described on the same scale as the numerical simulations, i.e. the coupling results were divided by the maximum coupling under diffraction-limited conditions, reported in Table 9.1. The comparison of the experimental results of the integrator and its simulation give similar results in *CDF* and average coupling. Only a difference of less than 2 dB is observed at $P = 1 \cdot 10^{-3}$, the origin of this difference needs to be investigated further. The results of the predictive controller simulation serve as a demonstration of the potential gains in coupling thanks to predictive control; a significant gain of more than 2 dB at $P = 1 \cdot 10^{-3}$ could be expected, according to the simulation results.

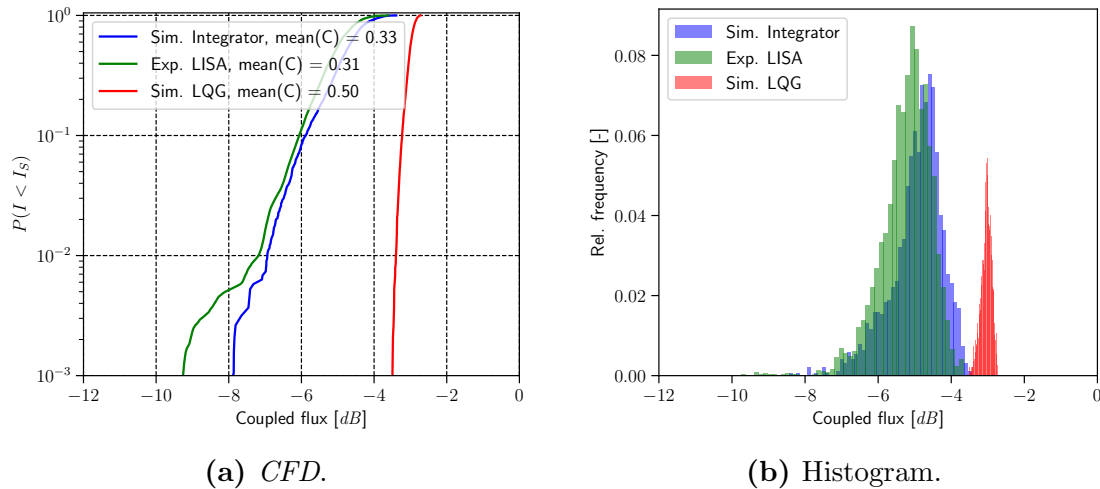


Figure 9.6.: Coupling efficiency results, comparison between the experiment (integral action controller) and the numerical simulations (integral action controller and predictive controller).

Thanks to the characterization of the *PICOLO* bench, its coupling to the *LISA AO* bench, and characterization of the coupling, the next step, i.e. *LQG* implementation, now only relies on the computation of the required matrices based on *PICOLO* turbulence profile.

* * *

Summary

This chapter discussed the strategy for the experimental validation of the predictive controller developed during this thesis using the *LISA* adaptive optics system and the *PICOLO* turbulence emulator.

This thesis advanced towards this demonstration with the characterization of the *PICOLO* bench (reported in Chapter 8) and with the first preliminary tests of the *LISA* adaptive optics system and *PICOLO*. Unfortunately, completing the demonstration of the predictive controller was not possible during this thesis due to time constraints.

The chapter presented the *LISA* adaptive optics bench and the procedure for coupling optimization and characterization that will allow the study of coupled flux efficiency with adaptive optics correction.

The chapter also showed some preliminary results with the coupling statistics with an integral controller. These results showed good agreement with the numerical end-to-end simulations of the *PICOLO* turbulence emulator and *LISA AO* system developed during this thesis. The simulations were completed by a simulation of the predictive controller in this scenario, which showed the promising performance improvements that predictive control may bring. The output of this work is a digital twin of the *PICOLO* and *LISA* benches that will serve to investigate performance and robustness of different control laws in the setup.

Further work beyond this thesis is planned at *ONERA* to finish this demonstration. The setup developed during this thesis will contribute to the first demonstration of the predictive controller, which in the future will also include the study of different predictive model identification strategies, the robustness of the control law with respect to scintillation, and potential improvements of the control law to improve its performance under strong scintillation conditions.

Conclusion

Summary and Conclusions

The work presented in this manuscript focused on improving the atmospheric turbulence correction of adaptive optics in the case of *LEO*-to-ground optical downlinks and imaging of satellites from ground-based telescopes.

In Chapter 1 I introduced the origin of optical turbulence and its effects on a beam propagating across it. I showed how the phase aberrations introduced by atmospheric turbulence will also become amplitude distortions through propagation, especially in strong turbulence cases, leading to irradiance fluctuations across the pupil of the telescope, known as scintillation. I also introduced the statistical description of turbulence and its representation as a projection on a Zernike polynomial basis, which is the core of the identification of the predictive models introduced later in this manuscript.

In Chapter 2 I presented the principle of adaptive optics and its components. The chapter also gave an introduction to adaptive optics control and the importance of delay, a concept crucial to this thesis as it is the origin of the need for predictive control. Finally, I introduced the concept of adaptive optics budget, the main tool for the design and performance assessment of adaptive optics systems.

Chapter 3 described the effect of atmospheric turbulence on the imaging quality of telescopes and on fiber coupling and communication systems. I also introduced the different systems considered in the case studies of this manuscript. Four different systems were introduced, two for optical communications and two for satellite observation, covering two system specifications, one more performing and complex and one simpler and with lower cost.

In Chapter 4 I discussed the two main elements of the predictive controller of this thesis and most controllers in the literature: autoregressive models and the *LQG* controller as a predictive controller. I highlighted how the *LQG* controller incorporates three necessary tasks that many adaptive optics systems implement separately: (1) phase reconstruction from the wavefront sensor slope space to the desired phase space (zonal, modal or *DM* space), (2) controller gain optimization and (3) estimation of the future phase to reduce the effect of time delay between measurement and correction, i.e. predictive control.

In Chapter 5 I presented the turbulence predictability method originally introduced in Conan et al. (2023) and applied it to the systems under study. I analyzed both the predictability of the systems, as well as the possibility to reduce the *AO* loop frequency. The method showed very promising gains for most of the systems.

Only the *FEELINGS* systems seemed to already have a very good performance in terms of temporal error. Other findings include the need need of higher order *VAR* models to achieve greater prediction performance in the case of *LEO* satellite applications for adaptive optics.

Chapter 6 presented the predictive controller developed in this thesis: the *high-order VAR Zernike LQG*. I discussed how the model is identified and its similarities to the predictor used in Chapter 5. I also provided an analysis of possible data-identification schemes that could lead to an online identification of the controller and its adaptation along the *LEO* trajectory.

Chapter 7 provided the end-to-end simulations for the controller in different scenarios. A first simulation used a simplified wavefront sensor and deformable mirror to verify the performance of the predictive model within the *LQG* and to compare it with the predictability assessment; the comparison proved that under the simplified conditions the controller can achieve the performance expected by the assessment. This simulation was also used to show the robustness of the controller with respect to measurement noise. The introduction of a Shack-Hartmann wavefront sensor in the simulations requires that the controller also performs a modal reconstruction from slope measurements to the Zernike polynomials used by the predictive model. This and the presence of aliasing cause an additional error in the controller that if it is not managed properly results in an error that is much bigger than the aliasing error present in the classical integral action controller. I proposed an analysis of this reconstruction using the *MAP* reconstructor as a proxy for the reconstruction within the Kalman filter. The *MAP* reconstructor was used to study the optimal number of modes necessary to decrease the reconstruction error, the influence of the fudge factor, and measurement noise in this reconstruction. While a fudge factor can be used to improve the reconstruction performance without increasing the number of reconstructed modes, the recommendation of this thesis is to reconstruct more modes (roughly the equivalent modes to twice the sampling frequency of the Shack-Hartmann). The end-to-end simulations of the controller showed how predictive controllers significantly reduce temporal error in adaptive optics systems. The impact of this reduction in the specific performance metrics of the system depends on the rest of the *AO* budget and the nature of the metric. For single mode fiber coupling, predictive control is able to reduce fadings; for satellite observation, the reduction of the residual variance leads to strong improvements in Strehl ratio. In all cases, predictive controllers can be used to relax the adaptive optics loop frequency to half of the nominal one while maintaining the performance of an integral controller. For satellite observation, this means imaging of fainter targets.

Chapter 8 reported the work of my work on the scintillation characterization of the *PICOLO* turbulence emulator for *LEO*-to-ground links under strong turbulence conditions. I conducted the experimental measurements of scintillation on the bench, first per screen and later for the complete turbulence profile, and compared it to numerical simulations using the *TURANDOT* simulation code. The

characterization showed that the bench delivers the scintillation features expected and the resulting digital twin can now be used to compare the performance of the experiments in the bench to computational simulations. This characterization is critical to prepare further experimental validation of innovative concepts in wavefront sensing and control to allow adaptive optics to cope with scintillation at low elevation. To prepare for this future work I also performed the first experiments with the emulator using the *LISA* adaptive optics system as I reported in Chapter 9.

Limitations and Recommendations

This section presents my recommendations based on the results of this thesis and their limitations. My particular suggestions are outlined below:

1. This thesis defined a set of four adaptive optics systems and their associated turbulence profiles trying to cover the most common operating points and situations. Although the methodology proposed can be applied to any system and the trends observed should be consistent for other operating points, only a case study for each system in consideration could give definitive results.
2. The identification method in this thesis, based on analytical expressions of the angular covariances between the coefficients of turbulent phase projected onto a Zernike polynomial basis, has great value not only for theoretical evaluations, but also for an on sky implementation and adaptation of the controller thanks to priors. Still, a method based on the identification of the spatio-temporal covariance matrices from data, following the discussion in Section 6.3 should be investigated, especially one based on the recursive identification to allow the adaptation of the predictive model across the *LEO* satellite trajectory.
3. It has been shown how the computational cost of the predictive controller needs to increase to reduce the propagation of aliasing across the controller's modal reconstruction and predictive model. For the case of fiber coupling, the higher-order models have less effect on fadings; the proposed controller could be simplified by reducing the number of modes that are predicted.
4. Slope space controllers should be further investigated due to their ease of identification and fewer needs of calibrations, especially in the cases where aliasing in higher-order modes may not be tolerated.
5. This thesis limited the testing of the controller to phase-only wavefront distortions and a geometric propagation of the turbulent phase. The performance of the predictive controller should be tested at strong turbulence conditions. Two points will be crucial: (1) The analytical formulas for the computation of

- phase statistics may not work under strong turbulence conditions and highly diffracted phase; here the use of a data-based identification may be required to obtain those statistics. (2) The robustness of the controller to scintillation effects on wavefront sensing should be studied too.
6. The predictive controller presented in this thesis could be extended to be combined with the approach proposed by [Lognoné et al. \(2022\)](#), which proposes an estimator of the point-ahead angle of optical uplinks using phase and scintillation statistics.
 7. The predictive controller could also be extended to other applications such as high-performance adaptive optics for high-contrast imaging coronagraphs or laser directed energy systems.
 8. The use of predictive control may be used as a mitigation technique for the effects of scintillation on the Shack-Hartmann wavefront sensor. The presence of scintillation will cause subpupil extinctions due to low flux over the subpupil; the lacking measurements can be replaced with predictions of the phase, i.e. no update step if there is no measurement, instead of using a poor measurement. Two additional techniques can be used to make the controller more robust to scintillation:
 - a) The use of a sequential Kalman filter that updates slope measurements independently (assuming no correlation between measurement noise in the slope measurements, an assumption already in use) and skip the update step when the slope measurement is annotated as not valid due to the effects of scintillation; in this case only the prediction step will be used.
 - b) The use of a zonal basis to maximize the decoupling between points in the telescope's pupil. The presence of scintillation will mean that some areas of the pupil will have no flux; reconstructing the phase over the pupil may impose strong constraints and worsen the reconstruction of points that do not have scintillation problems. The use of a zonal basis for control may help to deal with wavefront where there are no measurements available for several points in the pupil.
 9. The next step in the development of the predictive controller should its laboratory demonstration using the *PICOLO* turbulence emulator before its on-sky validation. This thesis started this work but could not finish it. A first demonstration should use only one phase screen at the pupil of the telescope to avoid any scintillation effect. Later, the bench can also be used to test the controller under strong turbulence conditions and scintillation. Different identification methods can also be tested on the bench.

Bibliography

- V. M. Acosta, D. Dequal, M. Schiavon, A. Montmerle-Bonnefois, C. B. Lim, J.-M. Conan, and E. Diamanti. Improvement of satellite-to-ground QKD secret key rate with adaptive optics. In *2023 Optical Fiber Communications Conference and Exhibition (OFC)*, pages 1–3, Mar. 2023. doi:[10.1364/OFC.2023.M2I.5](https://doi.org/10.1364/OFC.2023.M2I.5). (Cited on page: [47](#))
- G. Agapito, E. Pinna, A. Puglisi, and F. Rossi. Elephants, goldfishes and SOUL: A dissertation on forgetfulness and control systems, Nov. 2019. (Cited on page: [36](#))
- G. Agapito, F. Rossi, C. Plantet, A. Puglisi, and E. Pinna. Advances in control of a pyramid single conjugate adaptive optics system. *Monthly Notices of the Royal Astronomical Society*, 508(2):1745–1755, Oct. 2021. ISSN 0035-8711, 1365-2966. doi:[10.1093/mnras/stab2665](https://doi.org/10.1093/mnras/stab2665). (Cited on page: [36](#))
- G. J. M. Aitken and D. McGaughey. Predictability of Atmospherically-distorted Stellar Wavefronts. In *Adaptive Optics (1995), Paper TuA5*, page TuA5. Optica Publishing Group, Oct. 1995. doi:[10.1364/ADOP.1995.TuA5](https://doi.org/10.1364/ADOP.1995.TuA5). (Cited on page: [99](#))
- S. M. Ammons, L. Poyneer, D. T. Gavel, R. Kupke, C. E. Max, and L. Johnson. Evidence that wind prediction with multiple guide stars reduces tomographic errors and expands MOAO field of regard. In *Adaptive Optics Systems III*, volume 8447, page 84471U. International Society for Optics and Photonics, Sept. 2012. doi:[10.1117/12.927283](https://doi.org/10.1117/12.927283). (Cited on page: [73](#))
- D. J. Anderson. *LQG Control of a Deformable Mirror Adaptive Optics System with Time-Delayed Measurements*. PhD thesis, 1991. (Cited on pages: [92](#), [132](#))
- L. C. Andrews and R. L. Phillips. *Laser Beam Propagation through Random Media*. SPIE Press, Bellingham, Wash, 2nd ed edition, 2005. ISBN 978-0-8194-5948-0. (Cited on pages: [197](#), [204](#))
- L. C. Andrews, R. L. Phillips, C. Y. Hopen, and M. A. Al-Habash. Theory of optical scintillation. *Journal of the Optical Society of America A*, 16(6):1417, June 1999. ISSN 1084-7529, 1520-8532. doi:[10.1364/JOSAA.16.001417](https://doi.org/10.1364/JOSAA.16.001417). (Cited on pages: [19](#), [202](#))
- T. Anfray, S. Mariojouis, A. Laurent, H. Porte, J. Hulin, W. Atitallah, J. Hauden, T. Schmitt, P. Berceau, A. Mottet, J.-J. Bonnefois, and R. Cousty. Assessment of the Performance of DPSK and OOK Modulations at 25 Gb/s for

- Satellite-Based Optical Communications. In *2019 IEEE International Conference on Space Optical Systems and Applications (ICSOS)*, pages 1–6, Oct. 2019. doi:[10.1109/ICSOS45490.2019.8978982](https://doi.org/10.1109/ICSOS45490.2019.8978982). (Cited on page: [62](#))
- F. Assémat, R. Wilson, and E. Gendron. Method for simulating infinitely long and non stationary phase screens with optimized memory storage. *Optics Express*, 14(3):988, 2006. ISSN 1094-4087. doi:[10.1364/OE.14.000988](https://doi.org/10.1364/OE.14.000988). (Cited on pages: [21](#), [74](#), [79](#), [83](#) et [149](#))
- K. J. Åström. *Introduction to Stochastic Control Theory*. Academic Press, New York, 1970. ISBN 978-0-08-095579-7. (Cited on page: [86](#))
- M. T. Banet and M. F. Spencer. Compensated-beacon adaptive optics using least-squares phase reconstruction. *Optics Express*, 28(24):36902–36914, Nov. 2020. ISSN 1094-4087. doi:[10.1364/OE.409134](https://doi.org/10.1364/OE.409134). (Cited on page: [36](#))
- J. D. Barchers, D. L. Fried, and D. J. Link. Evaluation of the performance of Hartmann sensors in strong scintillation. *Applied Optics*, 41(6):1012, Feb. 2002. ISSN 0003-6935, 1539-4522. doi:[10.1364/AO.41.001012](https://doi.org/10.1364/AO.41.001012). (Cited on page: [185](#))
- A. Beghi, A. Cenedese, and A. Masiero. Atmospheric turbulence prediction: A PCA approach. In *2007 46th IEEE Conference on Decision and Control*, pages 566–571, Dec. 2007. doi:[10.1109/CDC.2007.4434459](https://doi.org/10.1109/CDC.2007.4434459). (Cited on pages: [73](#), [144](#))
- A. Billaud, A. Reeves, A. Orioux, H. Friew, F. Gomez, S. Bernard, T. Michel, D. Allieux, J. Poliak, R. M. Calvo, and O. Pinel. Turbulence Mitigation via Multi-Plane Light Conversion and Coherent Optical Combination on a 200 m and a 10 km Link. In *2022 IEEE International Conference on Space Optical Systems and Applications (ICSOS)*, pages 85–92, Kyoto City, Japan, Mar. 2022. IEEE. ISBN 978-1-66543-439-3. doi:[10.1109/ICSOS53063.2022.9749710](https://doi.org/10.1109/ICSOS53063.2022.9749710). (Cited on pages: [208](#), [209](#))
- B. I. Bitachon, Y. Horst, L. Kulmer, T. Blatter, K. Keller, A. M. Bonnefois, J.-M. Conan, C. Lim, J. Montri, P. Perrault, C. Petit, B. Sorrente, N. Védrenne, D. Matter, L. Pommarel, H. Lindberg, L. Francou, A. L. Kernec, A. Maho, S. Lévêque, M. Sotom, B. Baeuerle, and J. Leuthold. Tbit/s Single Channel 53 km Free-Space Optical Transmission - Assessing the Feasibility of Optical GEO-Satellite Feeder Links. In *European Conference on Optical Communication (ECOC) 2022 (2022), Paper Th3A.6*, page Th3A.6. Optica Publishing Group, Sept. 2022. (Cited on page: [185](#))
- A. M. Bonnefois, M.-T. Velluet, M. Cissé, C. B. Lim, J.-M. Conan, C. Petit, J.-F. Sauvage, S. Meimon, P. Perrault, J. Montri, and N. Védrenne. Feasibility demonstration of AO pre-compensation for GEO feeder links in a relevant environment. *Optics Express*, 30(26):47179–47198, Dec. 2022. ISSN 1094-4087. doi:[10.1364/OE.470705](https://doi.org/10.1364/OE.470705). (Cited on pages: [51](#), [52](#), [66](#) et [185](#))

- H. Bonnet, F. Biancat-Marchet, M. Dimmler, M. Esselborn, N. Kornweibel, M. L. Louarn, P.-Y. Madec, E. Marchetti, M. Müller, S. Oberti, J. Paufigue, L. Pettazzi, B. Sedghi, J. Spyromilio, S. Stroebele, C. Vérinaud, and E. Vernet. Adaptive optics at the ESO ELT. In *Adaptive Optics Systems VI*, volume 10703, pages 327–335. SPIE, July 2018. doi:[10.1117/12.2312407](https://doi.org/10.1117/12.2312407). (Cited on page: 28)
- D. M. Boroson and B. S. Robinson. The Lunar Laser Communication Demonstration: NASA’s First Step Toward Very High Data Rate Support of Science and Exploration Missions. *Space Science Reviews*, 185(1):115–128, Dec. 2014. ISSN 1572-9672. doi:[10.1007/s11214-014-0122-y](https://doi.org/10.1007/s11214-014-0122-y). (Cited on page: 185)
- A. Brady, R. Berlich, N. Leonhard, T. Kopf, P. Böttner, R. Eberhardt, and C. Reinlein. Experimental validation of phase-only pre-compensation over 494 m free-space propagation. *Optics Letters*, 42(14):2679, July 2017. ISSN 0146-9592, 1539-4794. doi:[10.1364/OL.42.002679](https://doi.org/10.1364/OL.42.002679). (Cited on page: 185)
- A. Brady, R. Eberhardt, A. Tünnermann, and C. Reinlein. Demonstration of Adaptive Optical Pre-Compensation in Horizontal Tests. In *2019 IEEE International Conference on Space Optical Systems and Applications (ICSOS)*, pages 1–5, Oct. 2019. doi:[10.1109/ICSOS45490.2019.8978973](https://doi.org/10.1109/ICSOS45490.2019.8978973). (Cited on pages: 185, 187)
- D. J. Butler, E. Marchetti, J. Bahr, W. Xu, S. Hippler, M. E. Kasper, and R. Conan. Phase screens for astronomical multiconjugate adaptive optics: Application to MAPS. In P. L. Wizinowich and D. Bonaccini, editors, *Astronomical Telescopes and Instrumentation*, page 623, Waikoloa, Hawai’i, United States, Feb. 2003. doi:[10.1117/12.458862](https://doi.org/10.1117/12.458862). (Cited on page: 186)
- T. Butterley, R. W. Wilson, and M. Sarazin. Determination of the profile of atmospheric optical turbulence strength from SLODAR data. *Monthly Notices of the Royal Astronomical Society*, 369(2):835–845, June 2006. ISSN 0035-8711. doi:[10.1111/j.1365-2966.2006.10337.x](https://doi.org/10.1111/j.1365-2966.2006.10337.x). (Cited on page: 143)
- F. Cantalloube, E. H. Por, K. Dohlen, J.-F. Sauvage, A. Vigan, M. Kasper, N. Bharmal, T. Henning, W. Brandner, J. Milli, C. Correia, and T. Fusco. Origin of the asymmetry of the wind driven halo observed in high-contrast images. *Astronomy & Astrophysics*, 620:L10, Dec. 2018. ISSN 0004-6361, 1432-0746. doi:[10.1051/0004-6361/201834311](https://doi.org/10.1051/0004-6361/201834311). (Cited on page: 73)
- L. Canuet. *Fiabilisation Des Transmissions Optiques Satellite-Sol*. These de doctorat, Toulouse, ISAE, Apr. 2018. (Cited on page: 62)
- L. Canuet, N. Védrenne, J.-M. Conan, C. Petit, G. Artaud, A. Rissons, and J. Lacan. Statistical properties of single-mode fiber coupling of satellite-to-ground laser links partially corrected by adaptive optics. *Journal of the Optical Society of America A*, 35(1):148, Jan. 2018. ISSN 1084-7529, 1520-8532. doi:[10.1364/JOSAA.35.000148](https://doi.org/10.1364/JOSAA.35.000148). (Cited on pages: 88, 187)

- J. Chabé, E. Aristidi, A. Ziad, H. Lantéri, Y. Fanteï-Caujolle, C. Giordano, J. Borgnino, M. Marjani, and C. Renaud. PML: A generalized monitor of atmospheric turbulence profile with high vertical resolution. *Applied Optics*, 59(25):7574–7584, Sept. 2020. ISSN 2155-3165. doi:[10.1364/AO.384504](https://doi.org/10.1364/AO.384504). (Cited on page: [188](#))
- F. Chassat. *Propagation Optique a Travers La Turbulence Atmospherique : Etude Modale de l'anisoplanetisme et Application a l'optique Adaptative*. These de doctorat, Paris 11, Jan. 1992. (Cited on page: [25](#))
- F. Chassat, G. Rousset, and J. Primot. Theoretical And Experimental Evaluation Of Isoplanatic Patch Size For Adaptive Optics. In *Active Telescope Systems*, volume 1114, pages 14–22. SPIE, Sept. 1989. doi:[10.1117/12.960805](https://doi.org/10.1117/12.960805). (Cited on page: [24](#))
- J. G. Chen, V. Shah, and L. Liu. Performance of a U-Net-based neural network for predictive adaptive optics. *Optics Letters*, 46(10):2513–2516, May 2021. ISSN 1539-4794. doi:[10.1364/OL.422656](https://doi.org/10.1364/OL.422656). (Cited on page: [73](#))
- A. Chiuso, R. Muradore, and E. Fedrigo. Adaptive Optics Systems: A Challenge for Closed Loop Subspace Identification. In *2007 American Control Conference*, pages 2949–2954, July 2007. doi:[10.1109/ACC.2007.4282939](https://doi.org/10.1109/ACC.2007.4282939). (Cited on page: [144](#))
- J.-M. Conan, G. Rousset, and P.-Y. Madec. Wave-front temporal spectra in high-resolution imaging through turbulence. *JOSA A*, 12(7):1559–1570, July 1995. ISSN 1520-8532. doi:[10.1364/JOSAA.12.001559](https://doi.org/10.1364/JOSAA.12.001559). (Cited on pages: [23](#), [36](#) et [66](#))
- J.-M. Conan, C. Petit, P. Robles, and P. Lognoné. Turbulence temporal prediction performance assessment for adaptive optics: Application to observation of, and space-ground optical links with, LEO satellites. *in preparation*, 2023. (Cited on pages: [x](#), [xi](#), [3](#), [4](#), [99](#) et [223](#))
- C. M. S. Corley, M. Nagashima, and B. N. Agrawal. Beam control and a new laboratory testbed for adaptive optics in a maritime environment. In *2010 IEEE Aerospace Conference*, pages 1–13, Mar. 2010. doi:[10.1109/AERO.2010.5446710](https://doi.org/10.1109/AERO.2010.5446710). (Cited on page: [186](#))
- C. Correia. *Conception de Lois de Commande à Hautes Performances Pour l'optique Adaptative Des Grands / Très Grands Télescopes*. These de doctorat, Paris 13, Jan. 2010. (Cited on page: [93](#))
- C. Correia, H.-F. Raynaud, C. Kulcsár, and J.-M. Conan. On the optimal reconstruction and control of adaptive optical systems with mirror dynamics. *JOSA A*, 27(2):333–349, Feb. 2010. ISSN 1520-8532. doi:[10.1364/JOSAA.27.000333](https://doi.org/10.1364/JOSAA.27.000333). (Cited on page: [95](#))

- C. Correia, K. Jackson, J.-P. Véran, D. Andersen, O. Lardière, and C. Bradley. Static and predictive tomographic reconstruction for wide-field multi-object adaptive optics systems. *Journal of the Optical Society of America A*, 31(1):101, Jan. 2014. ISSN 1084-7529, 1520-8532. doi:[10.1364/JOSAA.31.000101](https://doi.org/10.1364/JOSAA.31.000101). (Cited on pages: [73](#), [79](#), [84](#), [86](#), [100](#), [111](#), [125](#), [133](#), [140](#), [141](#) et [142](#))
- C. M. Correia, K. Jackson, J.-P. Véran, D. Andersen, O. Lardière, and C. Bradley. Spatio-angular minimum-variance tomographic controller for multi-object adaptive-optics systems. *Applied Optics*, 54(17):5281, June 2015. ISSN 0003-6935, 1539-4522. doi:[10.1364/AO.54.005281](https://doi.org/10.1364/AO.54.005281). (Cited on pages: [82](#), [83](#), [125](#), [133](#), [140](#), [142](#) et [149](#))
- A. Costille, C. Petit, J.-M. Conan, C. Kulcsár, H.-F. Raynaud, and T. Fusco. Wide field adaptive optics laboratory demonstration with closed-loop tomographic control. *JOSA A*, 27(3):469–483, Mar. 2010. ISSN 1520-8532. doi:[10.1364/JOSAA.27.000469](https://doi.org/10.1364/JOSAA.27.000469). (Cited on page: [95](#))
- J. Cranney, J. D. Dona, P. Piatrou, F. Rigaut, and V. Korhikoski. Modeling and identification of adaptive optics systems to satisfy distributed Kalman filter model structural constraints. In *2017 Australian and New Zealand Control Conference (ANZCC)*, pages 17–22, Dec. 2017. doi:[10.1109/ANZCC.2017.8298437](https://doi.org/10.1109/ANZCC.2017.8298437). (Cited on page: [136](#))
- J. Cranney, J. De Dona, V. Korhikoski, and F. Rigaut. Identification Scheme with Stability Constraints for High Velocity Turbulence in Adaptive Optics. In *2018 Australian & New Zealand Control Conference (ANZCC)*, pages 358–361. IEEE, 2018a. (Cited on pages: [136](#), [138](#))
- J. Cranney, J. D. Dona, V. Korhikoski, and F. Rigaut. An integrated identification and predictive control strategy for high wind velocity adaptive optics applications. In *Adaptive Optics Systems VI*, volume 10703, page 107034U. International Society for Optics and Photonics, July 2018b. doi:[10.1117/12.2313090](https://doi.org/10.1117/12.2313090). (Cited on pages: [135](#), [136](#))
- J. Cranney, J. D. Doná, F. Rigaut, and V. Korhikoski. Evaluation of a Multi-rate Predictive Control Strategy for Adaptive Optics Systems. In *2019 Australian New Zealand Control Conference (ANZCC)*, pages 128–132, Nov. 2019. doi:[10.1109/ANZCC47194.2019.8945637](https://doi.org/10.1109/ANZCC47194.2019.8945637). (Cited on page: [83](#))
- J. Cranney, H. Zhang, N. Doucet, F. Rigaut, D. Gratadour, V. Korhikoski, J. D. Doná, Y. Hong, H. Ltaief, and D. Keyes. Predictive learn and apply: MAVIS application - apply. In *Adaptive Optics Systems VII*, volume 11448, pages 552–559. SPIE, Dec. 2020. doi:[10.1117/12.2561914](https://doi.org/10.1117/12.2561914). (Cited on pages: [73](#), [86](#), [133](#), [140](#) et [142](#))

- R. Cubalchini. Modal wave-front estimation from phase derivative measurements. *Journal of the Optical Society of America*, 69(7):972, July 1979. ISSN 0030-3941. doi:[10.1364/JOSA.69.000972](https://doi.org/10.1364/JOSA.69.000972). (Cited on pages: [36](#), [197](#))
- G.-m. Dai. Modal compensation of atmospheric turbulence with the use of Zernike polynomials and Karhunen–Loève functions. *JOSA A*, 12(10):2182–2193, Oct. 1995. ISSN 1520-8532. doi:[10.1364/JOSAA.12.002182](https://doi.org/10.1364/JOSAA.12.002182). (Cited on page: [37](#))
- C. Dessenne, P.-Y. Madec, and G. Rousset. Optimization of a predictive controller for closed-loop adaptive optics. *Applied Optics*, 37(21):4623–4633, July 1998. ISSN 2155-3165. doi:[10.1364/AO.37.004623](https://doi.org/10.1364/AO.37.004623). (Cited on pages: [36](#), [73](#))
- C. Dessenne, P.-Y. Madec, and G. Rousset. Sky implementation of modal predictive control in adaptive optics. *Optics Letters*, 24(5):339–341, Mar. 1999. ISSN 1539-4794. doi:[10.1364/OL.24.000339](https://doi.org/10.1364/OL.24.000339). (Cited on pages: [73](#), [220](#))
- G. DiComo, M. Helle, J. Peñano, A. Ting, A. Schmitt-Sody, and J. Elle. Implementation of a long range, distributed-volume, continuously variable turbulence generator. *Applied Optics*, 55(19):5192–5197, July 2016. ISSN 2155-3165. doi:[10.1364/AO.55.005192](https://doi.org/10.1364/AO.55.005192). (Cited on page: [185](#))
- N. Doelman. The minimum of the time-delay wavefront error in adaptive optics. *Monthly Notices of the Royal Astronomical Society*, 491(4):4719–4723, Feb. 2020. ISSN 0035-8711. doi:[10.1093/mnras/stz3237](https://doi.org/10.1093/mnras/stz3237). (Cited on page: [99](#))
- N. J. Doelman, P. R. Fraanje, and R. den Breeje. Optimal control of tip-tilt modes on-sky adaptive optics demonstration. *2nd International Conference on Adaptive Optics for Extremely Large Telescopes, AO for ELT 2011, 25-30 September 2011, Victoria, BC, Canada*, 2011. (Cited on pages: [78](#), [134](#))
- B. L. Ellerbroek. Efficient computation of minimum-variance wave-front reconstructors with sparse matrix techniques. *JOSA A*, 19(9):1803–1816, Sept. 2002. ISSN 1520-8532. doi:[10.1364/JOSAA.19.001803](https://doi.org/10.1364/JOSAA.19.001803). (Cited on page: [37](#))
- R. Fante. Electromagnetic beam propagation in turbulent media. *Proceedings of the IEEE*, 63(12):1669–1692, 1975. ISSN 0018-9219. doi:[10.1109/PROC.1975.10035](https://doi.org/10.1109/PROC.1975.10035). (Cited on pages: [15](#), [19](#) et [184](#))
- O. J. D. Farley, J. Osborn, T. Morris, M. Sarazin, T. Butterley, M. J. Townson, P. Jia, and R. W. Wilson. Representative optical turbulence profiles for ESO Paranal by hierarchical clustering. *Monthly Notices of the Royal Astronomical Society*, 481(3):4030–4037, Dec. 2018. ISSN 0035-8711. doi:[10.1093/mnras/sty2536](https://doi.org/10.1093/mnras/sty2536). (Cited on page: [51](#))
- O. J. D. Farley, J. Osborn, T. Morris, T. Fusco, B. Neichel, C. Correia, and R. W. Wilson. Identifying optical turbulence profiles for realistic tomographic error

- in adaptive optics. *Monthly Notices of the Royal Astronomical Society*, 488(1): 213–221, Sept. 2019. ISSN 0035-8711. doi:[10.1093/mnras/stz1669](https://doi.org/10.1093/mnras/stz1669). (Cited on page: [188](#))
- E. Fedrigo, R. Donaldson, C. Soenke, R. Myers, S. Goodsell, D. Geng, C. Saunter, and N. Dipper. SPARTA: The ESO standard platform for adaptive optics real time applications. In *Advances in Adaptive Optics II*, volume 6272, pages 322–331. SPIE, June 2006. doi:[10.1117/12.671919](https://doi.org/10.1117/12.671919). (Cited on page: [43](#))
- F. Ferreira, E. Gendron, G. Rousset, and D. Gratadour. Numerical estimation of wavefront error breakdown in adaptive optics. *Astronomy & Astrophysics*, 616: A102, Aug. 2018. ISSN 0004-6361, 1432-0746. doi:[10.1051/0004-6361/201832579](https://doi.org/10.1051/0004-6361/201832579). (Cited on page: [104](#))
- E. Fischer, T. Berkefeld, V. Kaltenbach, D. Soltau, R. Czichy, J. Kunde, S. GmbH, K. Saucke, F. Heine, M. Gregory, H. Kämpfner, T.-S. GmbH, and C. Kg. Development, integration and test of a transportable adaptive optical ground station. page 6, 2015. (Cited on page: [185](#))
- R. Flicker, F. J. Rigaut, and B. L. Ellerbroek. Comparison of multiconjugate adaptive optics configurations and control algorithms for the Gemini South 8-m telescope. In *Adaptive Optical Systems Technology*, volume 4007, pages 1032–1043. SPIE, July 2000. doi:[10.1117/12.390347](https://doi.org/10.1117/12.390347). (Cited on page: [37](#))
- M. Foster. An Application of the Wiener-Kolmogorov Smoothing Theory to Matrix Inversion. *Journal of the Society for Industrial and Applied Mathematics*, 9(3): 387–392, Sept. 1961. ISSN 0368-4245. doi:[10.1137/0109031](https://doi.org/10.1137/0109031). (Cited on page: [38](#))
- J. Fowler, M. A. M. V. Kooten, and R. Jensen-Clem. Battle of the predictive wavefront controls: Comparing data and model-driven predictive control for high contrast imaging. In *Adaptive Optics Systems VIII*, volume 12185, pages 2527–2541. SPIE, Aug. 2022. doi:[10.1117/12.2629521](https://doi.org/10.1117/12.2629521). (Cited on pages: [73](#), [137](#))
- D. L. Fried. Least-square fitting a wave-front distortion estimate to an array of phase-difference measurements. *JOSA*, 67(3):370–375, Mar. 1977. doi:[10.1364/JOSA.67.000370](https://doi.org/10.1364/JOSA.67.000370). (Cited on page: [36](#))
- D. L. Fried. Probability of getting a lucky short-exposure image through turbulence*. *JOSA*, 68(12):1651–1658, Dec. 1978. doi:[10.1364/JOSA.68.001651](https://doi.org/10.1364/JOSA.68.001651). (Cited on pages: [36](#), [37](#))
- D. L. Fried. Anisoplanatism in adaptive optics. *Journal of the Optical Society of America*, 72(1):52, Jan. 1982. ISSN 0030-3941. doi:[10.1364/JOSA.72.000052](https://doi.org/10.1364/JOSA.72.000052). (Cited on pages: [17](#), [18](#) et [40](#))

- D. L. Fried. Time-delay-induced mean-square error in adaptive optics. *JOSA A*, 7 (7):1224–1225, July 1990. ISSN 1520-8532. doi:[10.1364/JOSAA.7.001224](https://doi.org/10.1364/JOSAA.7.001224). (Cited on pages: [18](#), [99](#))
- D. L. Fried and T. Clark. Extruding Kolmogorov-type phase screen ribbons. *JOSA A*, 25(2):463–468, Feb. 2008. ISSN 1520-8532. doi:[10.1364/JOSAA.25.000463](https://doi.org/10.1364/JOSAA.25.000463). (Cited on page: [149](#))
- R. Q. Fugate, B. L. Ellerbroek, C. H. Higgins, M. P. Jelonek, W. J. Lange, A. C. Slavin, W. J. Wild, D. M. Winker, J. M. Wynia, J. M. Spinhirne, B. R. Boeke, R. E. Ruane, J. F. Moroney, M. D. Oliner, D. W. Swindle, and R. A. Cleis. Two generations of laser-guide-star adaptive-optics experiments at the Starfire Optical Range. *JOSA A*, 11(1):310–324, Jan. 1994. ISSN 1520-8532. doi:[10.1364/JOSAA.11.000310](https://doi.org/10.1364/JOSAA.11.000310). (Cited on page: [41](#))
- R. Furrer, M. G. Genton, and D. Nychka. Covariance Tapering for Interpolation of Large Spatial Datasets. *Journal of Computational and Graphical Statistics*, 15 (3):502–523, 2006. ISSN 1061-8600. (Cited on page: [143](#))
- T. Fusco, J.-M. Conan, G. Rousset, L. M. Mugnier, and V. Michau. Optimal wave-front reconstruction strategies for multiconjugate adaptive optics. *Journal of the Optical Society of America A*, 18(10):2527, Oct. 2001. ISSN 1084-7529, 1520-8532. doi:[10.1364/JOSAA.18.002527](https://doi.org/10.1364/JOSAA.18.002527). (Cited on pages: [38](#), [73](#), [95](#) et [139](#))
- T. Fusco, C. Petit, G. Rousset, J.-M. Conan, and J.-L. Beuzit. Closed-loop experimental validation of the spatially filtered Shack–Hartmann concept. *Optics Letters*, 30(11):1255–1257, June 2005. ISSN 1539-4794. doi:[10.1364/OL.30.001255](https://doi.org/10.1364/OL.30.001255). (Cited on pages: [42](#), [157](#))
- T. Fusco, C. Petit, G. Rousset, J.-F. Sauvage, K. Dohlen, D. Mouillet, J. Charton, P. Baudoz, M. Kasper, E. Fedrigo, P. Rabou, P. Feautrier, M. Downing, P. Gigan, J.-M. Conan, J.-L. Beuzit, N. Hubin, F. Wildi, and P. Puget. Design of the extreme AO system for SPHERE, the planet finder instrument of the VLT. In *Advances in Adaptive Optics II*, volume 6272, page 62720K. International Society for Optics and Photonics, June 2006. doi:[10.1117/12.670794](https://doi.org/10.1117/12.670794). (Cited on page: [42](#))
- D. T. Gavel and D. Wiberg. Toward Strehl-optimizing adaptive optics controllers. In *Adaptive Optical System Technologies II*, volume 4839, pages 890–901. International Society for Optics and Photonics, Feb. 2003. doi:[10.1117/12.459684](https://doi.org/10.1117/12.459684). (Cited on pages: [111](#), [133](#))
- D. J. Geisler, K. S. Y. Wong, R. T. Schulein, J. P. Wang, P. S. Bedrosian, F. Q. Hakimi, C. M. Schieler, N. W. Spellmeyer, D. O. Caplan, B. S. Robinson, and S. A. Hamilton. Atmospheric Emulation and Testing Methodology for Laboratory Verification of FSO Communications Transceivers. In *2019 IEEE International*

- Conference on Space Optical Systems and Applications (ICSOS)*, pages 1–5, Oct. 2019. doi:[10.1109/ICSOS45490.2019.8978991](https://doi.org/10.1109/ICSOS45490.2019.8978991). (Cited on page: [187](#))
- E. Gendron and P. Lena. Astronomical adaptive optics. 1: Modal control optimization. *Astronomy and Astrophysics*, 291:337–347, Nov. 1994. ISSN 0004-6361. (Cited on pages: [36](#), [73](#))
- D. Giggenbach. Fading-loss assessment in atmospheric free-space optical communication links with on-off keying. *Optical Engineering*, 47(4):046001, Apr. 2008. ISSN 0091-3286. doi:[10.1117/1.2903095](https://doi.org/10.1117/1.2903095). (Cited on page: [184](#))
- M. K. Giles, A. J. Seward, M. A. Vorontsov, J. Rha, and R. Jimenez. Setting up a liquid crystal phase screen to simulate atmospheric turbulence. In *High-Resolution Wavefront Control: Methods, Devices, and Applications II*, volume 4124, pages 89–97. SPIE, Nov. 2000. doi:[10.1117/12.407491](https://doi.org/10.1117/12.407491). (Cited on page: [186](#))
- L. Gilles, P. Massioni, C. Kulcsár, H.-F. Raynaud, and B. Ellerbroek. Distributed Kalman filtering compared to Fourier domain preconditioned conjugate gradient for laser guide star tomography on extremely large telescopes. *Journal of the Optical Society of America A*, 30(5):898, May 2013. ISSN 1084-7529, 1520-8532. doi:[10.1364/JOSAA.30.000898](https://doi.org/10.1364/JOSAA.30.000898). (Cited on pages: [95](#), [135](#))
- C. Giordano, A. Ziad, E. Aristidi, J. Chabé, Y. Fantéi-Caujolle, C. Renaud, and A. Rafalimanana. CATS: Continuous turbulence characterization station for both optical link and astronomical support. In Z. Sodnik, B. Cugny, and N. Karafolas, editors, *International Conference on Space Optics — ICSO 2020*, page 83, Online Only, France, June 2021. SPIE. ISBN 978-1-5106-4548-6 978-1-5106-4549-3. doi:[10.1117/12.2599373](https://doi.org/10.1117/12.2599373). (Cited on page: [51](#))
- C. Giordano, A. Ziad, E. Aristidi, J. Chabé, Y. Fantéi-Caujolle, C. Bailet, T. Charbonnel, A. Gillioën, E. Jacqmart, and A. Rafalimanana. The upgraded Calern Atmospheric Turbulence Station. In *Adaptive Optics Systems VIII*, volume 12185, pages 1868–1876. SPIE, Aug. 2022. doi:[10.1117/12.2629818](https://doi.org/10.1117/12.2629818). (Cited on page: [51](#))
- J. W. Goodman. *Introduction to Fourier Optics*. W.H. Freeman, Macmillan Learning, New York, fourth edition edition, 2017. ISBN 978-1-319-11916-4. (Cited on page: [12](#))
- M. E. Gracheva and A. S. Gurvich. Strong fluctuations in the intensity of light propagated through the atmosphere close to the earth. *Soviet Radiophysics*, 8(4):511–515, July 1965. ISSN 1573-9120. doi:[10.1007/BF01038327](https://doi.org/10.1007/BF01038327). (Cited on page: [18](#))
- D. Gratadour, L. M. Mugnier, and D. Rouan. Sub-pixel image registration with a maximum likelihood estimator - Application to the first adaptive optics observations of Arp 220 in the L' band. *Astronomy & Astrophysics*, 443(1):357–365,

- Nov. 2005. ISSN 0004-6361, 1432-0746. doi:[10.1051/0004-6361:20042188](https://doi.org/10.1051/0004-6361:20042188). (Cited on page: [31](#))
- A. Guesalaga, B. Neichel, F. Rigaut, J. Osborn, and D. Guzman. Comparison of vibration mitigation controllers for adaptive optics systems. *Applied Optics*, 51(19):4520–4535, July 2012. ISSN 2155-3165. doi:[10.1364/AO.51.004520](https://doi.org/10.1364/AO.51.004520). (Cited on pages: [44](#), [74](#))
- A. Guesalaga, B. Neichel, A. Cortés, C. Béchet, and D. Guzmán. Using the $\{C_{-n}\}^2$ and wind profiler method with wide-field laser-guide-stars adaptive optics to quantify the frozen-flow decay. *Monthly Notices of the Royal Astronomical Society*, 440(3):1925–1933, May 2014. ISSN 0035-8711. doi:[10.1093/mnras/stu366](https://doi.org/10.1093/mnras/stu366). (Cited on pages: [10](#), [74](#) et [143](#))
- O. Guyon and J. Males. Adaptive Optics Predictive Control with Empirical Orthogonal Functions (EOFs), July 2017. (Cited on pages: [73](#), [134](#) et [144](#))
- A. Habib, J. Vernin, Z. Benkhaldoun, and H. Lanteri. Single star scidar: Atmospheric parameters profiling using the simulated annealing algorithm. *Monthly Notices of the Royal Astronomical Society*, 368(3):1456–1462, Apr. 2006. ISSN 0035-8711. doi:[10.1111/j.1365-2966.2006.10235.x](https://doi.org/10.1111/j.1365-2966.2006.10235.x). (Cited on page: [143](#))
- S. Y. Haffert, J. R. Males, L. M. Close, K. V. Gorkom, J. D. Long, A. D. Hedglen, O. Guyon, L. Schatz, M. Y. Kautz, J. Lumbres, A. T. Rodack, J. M. Knight, H. Sun, and K. Fogarty. Data-driven subspace predictive control of adaptive optics for high-contrast imaging. *Journal of Astronomical Telescopes, Instruments, and Systems*, 7(2):029001, Apr. 2021. ISSN 2329-4124, 2329-4221. doi:[10.1117/1.JATIS.7.2.029001](https://doi.org/10.1117/1.JATIS.7.2.029001). (Cited on pages: [73](#), [143](#) et [146](#))
- P. Haguenaer, A. Guesalaga, and T. Butterley. Comparison of atmosphere profilers at Paranal and atmosphere parameters statistics: AOF-profiler, STEREO-SCIDAR, MASS-DIMM, LGS-WFS. In *Adaptive Optics Systems VII*, volume 11448, pages 345–359. SPIE, Dec. 2020. doi:[10.1117/12.2562267](https://doi.org/10.1117/12.2562267). (Cited on page: [51](#))
- Y. Halevi. Stable LQG controllers. *IEEE Transactions on Automatic Control*, 39(10):2104–2106, 1994. ISSN 00189286. doi:[10.1109/9.328801](https://doi.org/10.1109/9.328801). (Cited on page: [129](#))
- P. M. Harrington and B. M. Welsh. Frequency-domain analysis of an adaptive optical system’s temporal response. *Optical Engineering*, 33(7):2336–2342, July 1994. ISSN 0091-3286, 1560-2303. doi:[10.1117/12.172895](https://doi.org/10.1117/12.172895). (Cited on page: [99](#))
- H. Hauschildt, C. Elia, L. Moeller, and J. M. Perdigués Armengol. HyDRON: High throughput optical network. In H. Hemmati and D. M. Boroson, editors, *Free-Space Laser Communications XXXI*, page 18, San Francisco, United States, Mar. 2019. SPIE. ISBN 978-1-5106-2462-7 978-1-5106-2463-4. doi:[10.1117/12.2511391](https://doi.org/10.1117/12.2511391). (Cited on page: [184](#))

- C. T. Heritier, S. Esposito, T. Fusco, B. Neichel, S. Oberti, R. Briguglio, G. Agapito, A. Puglisi, E. Pinna, and P. Y. Madec. A new calibration strategy for adaptive telescopes with pyramid WFS. *Monthly Notices of the Royal Astronomical Society*, Sept. 2018. ISSN 0035-8711, 1365-2966. doi:[10.1093/mnras/sty2485](https://doi.org/10.1093/mnras/sty2485). (Cited on page: [128](#))
- J. Herrmann. Least-squares wave front errors of minimum norm. *JOSA*, 70(1): 28–35, Jan. 1980. doi:[10.1364/JOSA.70.000028](https://doi.org/10.1364/JOSA.70.000028). (Cited on page: [36](#))
- J. Herrmann. Phase variance and Strehl ratio in adaptive optics. *JOSA A*, 9(12): 2257–2258, Dec. 1992. ISSN 1520-8532. doi:[10.1364/JOSAA.9.002257](https://doi.org/10.1364/JOSAA.9.002257). (Cited on page: [88](#))
- K. Hinnen, M. Verhaegen, and N. Doelman. Exploiting the spatiotemporal correlation in adaptive optics using data-driven H_2 -optimal control. *JOSA A*, 24(6): 1714–1725, June 2007. ISSN 1520-8532. doi:[10.1364/JOSAA.24.001714](https://doi.org/10.1364/JOSAA.24.001714). (Cited on pages: [73](#), [134](#))
- K. Hinnen, M. Verhaegen, and N. Doelman. A Data-Driven H_2 - Optimal Control Approach for Adaptive Optics. *IEEE Transactions on Control Systems Technology*, 16(3):381–395, May 2008. ISSN 1558-0865. doi:[10.1109/TCST.2007.903374](https://doi.org/10.1109/TCST.2007.903374). (Cited on page: [82](#))
- S. Hippler, F. Hormuth, W. Brandner, D. J. Butler, T. Henning, and S. Egner. The MPIA multipurpose laboratory atmospheric turbulence simulator MAPS. In *Advances in Adaptive Optics II*, volume 6272, pages 1635–1645. SPIE, June 2006a. doi:[10.1117/12.671362](https://doi.org/10.1117/12.671362). (Cited on page: [186](#))
- S. Hippler, F. Hormuth, D. J. Butler, W. Brandner, and T. Henning. Atmosphere-like turbulence generation with surface-etched phase-screens. *Optics Express*, 14(22):10139–10148, Oct. 2006b. ISSN 1094-4087. doi:[10.1364/OE.14.010139](https://doi.org/10.1364/OE.14.010139). (Cited on page: [186](#))
- R. H. Hudgin. Wave-front reconstruction for compensated imaging. *JOSA*, 67(3): 375–378, Mar. 1977. doi:[10.1364/JOSA.67.000375](https://doi.org/10.1364/JOSA.67.000375). (Cited on page: [36](#))
- B. R. Hunt. Matrix formulation of the reconstruction of phase values from phase differences. *Journal of the Optical Society of America*, 69(3):393, Mar. 1979. ISSN 0030-3941. doi:[10.1364/JOSA.69.000393](https://doi.org/10.1364/JOSA.69.000393). (Cited on page: [36](#))
- D. Ivanov and Z. Yakoub. Overview of Identification Methods of Autoregressive Model in Presence of Additive Noise. *Mathematics*, 11(3):607, Jan. 2023. ISSN 2227-7390. doi:[10.3390/math11030607](https://doi.org/10.3390/math11030607). (Cited on page: [86](#))
- K. Jackson, C. Correia, O. Lardière, D. Andersen, and C. Bradley. Linear prediction of atmospheric wave-fronts for tomographic adaptive optics systems: Modelling

- and robustness assessment. *Optics Letters*, 40(2):143–146, Jan. 2015. ISSN 1539-4794. doi:[10.1364/OL.40.000143](https://doi.org/10.1364/OL.40.000143). (Cited on pages: [83](#), [100](#), [112](#) et [133](#))
- L. Jolissaint. Optical Turbulence Generators for Testing Astronomical Adaptive Optics Systems: A Review and Designer Guide. *Publications of the Astronomical Society of the Pacific*, 118(847):1205, Sept. 2006. ISSN 1538-3873. doi:[10.1086/507849](https://doi.org/10.1086/507849). (Cited on page: [186](#))
- M. B. Jorgenson and G. J. Aitken. Neural network prediction of turbulence-induced wavefront degradations with applications to adaptive optics. 1706:113–121, Aug. 1992. doi:[10.1117/12.139936](https://doi.org/10.1117/12.139936). (Cited on page: [73](#))
- R. Juvenal, C. Kulcsar, H.-F. Raynaud, J.-M. Conan, C. Petit, L. Leboulleux, G. Sivo, and V. Garrel. Tip-tilt modelling and control for GeMS: A performance comparison of identification techniques. *Adaptive Optics for Extremely Large Telescopes 4 – Conference Proceedings*, 1(1), 2015a. doi:[10.20353/K3T4CP1131628](https://doi.org/10.20353/K3T4CP1131628). (Cited on page: [78](#))
- R. Juvenal, C. Kulcsar, H.-F. Raynaud, J.-M. Conan, and G. Sivo. Performance assessment for the linear control of adaptive optics systems: Noise propagation and temporal errors. eScholarship, 2015b. doi:[10.20353/K3T4CP1131623](https://doi.org/10.20353/K3T4CP1131623). (Cited on page: [135](#))
- R. Juvénal, C. Kulcsár, H.-F. Raynaud, and J.-M. Conan. LQG adaptive optics control with wind-dependent turbulent models. In E. Marchetti, L. M. Close, and J.-P. Véran, editors, *SPIE Astronomical Telescopes + Instrumentation*, page 99090M, Edinburgh, United Kingdom, July 2016. doi:[10.1117/12.2234443](https://doi.org/10.1117/12.2234443). (Cited on pages: [118](#), [136](#))
- R. Juvénal, C. Kulcsár, H.-F. Raynaud, and J.-M. Conan. Linear controller error budget assessment for classical adaptive optics systems. *JOSA A*, 35(8):1465–1476, Aug. 2018. ISSN 1520-8532. doi:[10.1364/JOSAA.35.001465](https://doi.org/10.1364/JOSAA.35.001465). (Cited on pages: [104](#), [156](#), [157](#) et [170](#))
- T. J. Kane, C. S. Gardner, and L. A. Thompson. Effects of wavefront sampling speed on the performance of adaptive astronomical telescopes. *Applied Optics*, 30(2):214–221, Jan. 1991. ISSN 2155-3165. doi:[10.1364/AO.30.000214](https://doi.org/10.1364/AO.30.000214). (Cited on page: [72](#))
- H. F. Kelemu, A. Reeves, R. M. Calvo, W. Drewelow, and T. Jeinsch. Investigation of advanced control for adaptive optics in free-space optical communication. In *Environmental Effects on Light Propagation and Adaptive Systems V*, volume 12266, pages 51–60. SPIE, Oct. 2022. doi:[10.1117/12.2636270](https://doi.org/10.1117/12.2636270). (Cited on pages: [134](#), [139](#))

- M. Keppler, M. Benisty, A. Müller, T. Henning, R. van Boekel, F. Cantalloube, C. Ginski, R. G. van Holstein, A.-L. Maire, A. Pohl, M. Samland, H. Avenhaus, J.-L. Baudino, A. Boccaletti, J. de Boer, M. Bonnefoy, G. Chauvin, S. Desidera, M. Langlois, C. Lazzoni, G.-D. Marleau, C. Mordasini, N. Pawellek, T. Stolker, A. Vigan, A. Zurlo, T. Birnstiel, W. Brandner, M. Feldt, M. Flock, J. Girard, R. Gratton, J. Hagelberg, A. Isella, M. Janson, A. Juhasz, J. Kemmer, Q. Kral, A.-M. Lagrange, R. Launhardt, A. Matter, F. Ménard, J. Milli, P. Mollière, J. Olofsson, L. Pérez, P. Pinilla, C. Pinte, S. P. Quanz, T. Schmidt, S. Udry, Z. Wahhaj, J. P. Williams, E. Buenzli, M. Cudel, C. Dominik, R. Galicher, M. Kasper, J. Lannier, D. Mesa, D. Mouillet, S. Peretti, C. Perrot, G. Salter, E. Sissa, F. Wildi, L. Abe, J. Antichi, J.-C. Augereau, A. Baruffolo, P. Baudoz, A. Bazzon, J.-L. Beuzit, P. Blanchard, S. S. Brems, T. Buey, V. D. Caprio, M. Carillet, M. Carle, E. Cascone, A. Cheetham, R. Claudi, A. Costille, A. Delboulbé, K. Dohlen, D. Fantinel, P. Feautrier, T. Fusco, E. Giro, L. Gluck, C. Gry, N. Hubin, E. Hugot, M. Jaquet, D. L. Mignant, M. Llored, F. Madec, Y. Magnard, P. Martinez, D. Maurel, M. Meyer, O. Möller-Nilsson, T. Moulin, L. Mugnier, A. Origné, A. Pavlov, D. Perret, C. Petit, J. Pragt, P. Puget, P. Rabou, J. Ramos, F. Rigal, S. Rochat, R. Roelfsema, G. Rousset, A. Roux, B. Salasnich, J.-F. Sauvage, A. Sevin, C. Soenke, E. Stadler, M. Suarez, M. Turatto, and L. Weber. Discovery of a planetary-mass companion within the gap of the transition disk around PDS 70. *Astronomy & Astrophysics*, 617:A44, Sept. 2018. ISSN 0004-6361, 1432-0746. doi:[10.1051/0004-6361/201832957](https://doi.org/10.1051/0004-6361/201832957). (Cited on page: 73)
- O. Keskin, L. Jolissaint, and C. Bradley. Hot-air optical turbulence generator for the testing of adaptive optics systems: Principles and characterization. *Applied Optics*, 45(20):4888–4897, July 2006. ISSN 2155-3165. doi:[10.1364/AO.45.004888](https://doi.org/10.1364/AO.45.004888). (Cited on page: 187)
- A. Kolmogorov. The Local Structure of Turbulence in Incompressible Viscous Fluid for Very Large Reynolds' Numbers. *Akademiia Nauk SSSR Doklady*, 30:301–305, Jan. 1941. ISSN 0002-3264. (Cited on page: 7)
- K. Kudielka, E. Fischer, and T. Dreischer. Numerical prediction and experimental validation of irradiance fluctuations in a pre-compensated optical feeder link. In *International Conference on Space Optics — ICSSO 2018*, volume 11180, page 111805N. International Society for Optics and Photonics, July 2019. doi:[10.1117/12.2536122](https://doi.org/10.1117/12.2536122). (Cited on pages: 185, 187)
- C. Kulcsár, H.-F. Raynaud, C. Petit, J.-M. Conan, and P. V. de Lesegno. Optimal control, observers and integrators in adaptive optics. *Optics Express*, 14(17):7464, Aug. 2006. ISSN 1094-4087. doi:[10.1364/OE.14.007464](https://doi.org/10.1364/OE.14.007464). (Cited on pages: 71, 88)
- C. Kulcsár, H.-F. Raynaud, C. Petit, and J.-M. Conan. Minimum variance prediction and control for adaptive optics. *Automatica*, 48(9):1939–1954, Sept. 2012.

- ISSN 0005-1098. doi:[10.1016/j.automtica.2012.03.030](https://doi.org/10.1016/j.automtica.2012.03.030). (Cited on pages: [73](#), [88](#), [95](#) et [156](#))
- C. Kulcsár, H.-F. Raynaud, J.-M. Conan, R. JuvÃ©nal, and C. Correia. Towards minimum-variance control of ELTs AO systems. In *Proceedings of the Adaptive Optics for Extremely Large Telescopes 5*. Instituto de Astrofísica de Canarias (IAC), 2017. doi:[10.26698/AO4ELT5.0175](https://doi.org/10.26698/AO4ELT5.0175). (Cited on page: [95](#))
- O. Lai, J. K. Withington, R. Laugier, and M. Chun. Direct measure of dome seeing with a localized optical turbulence sensor. *Monthly Notices of the Royal Astronomical Society*, 484(4):5568–5577, Apr. 2019. ISSN 0035-8711. doi:[10.1093/mnras/stz396](https://doi.org/10.1093/mnras/stz396). (Cited on page: [33](#))
- D. J. Laidlaw, J. Osborn, T. J. Morris, A. G. Basden, E. Gendron, G. Rousset, M. J. Townson, and R. W. Wilson. Automated wind velocity profiling from adaptive optics telemetry. *Monthly Notices of the Royal Astronomical Society*, 491(1):1287–1294, Jan. 2020. ISSN 0035-8711. doi:[10.1093/mnras/stz3062](https://doi.org/10.1093/mnras/stz3062). (Cited on page: [143](#))
- D. J. Laidlaw, A. P. Reeves, H. Singhal, H. Singhal, and R. M. Calvo. Characterizing turbulence profile layers through celestial single-source observations. *Applied Optics*, 61(2):498–504, Jan. 2022. ISSN 2155-3165. doi:[10.1364/AO.443698](https://doi.org/10.1364/AO.443698). (Cited on page: [143](#))
- R. Landman, S. Y. Haffert, V. M. Radhakrishnan, and C. U. Keller. Self-optimizing adaptive optics control with reinforcement learning for high-contrast imaging. *Journal of Astronomical Telescopes, Instruments, and Systems*, 7(3):039002, Aug. 2021. ISSN 2329-4124, 2329-4221. doi:[10.1117/1.JATIS.7.3.039002](https://doi.org/10.1117/1.JATIS.7.3.039002). (Cited on page: [73](#))
- S. Le Clainche and J. M. Vega. Higher Order Dynamic Mode Decomposition. *SIAM Journal on Applied Dynamical Systems*, 16(2):882–925, Jan. 2017. doi:[10.1137/15M1054924](https://doi.org/10.1137/15M1054924). (Cited on page: [144](#))
- B. Le Roux, J.-M. Conan, C. Kulcsar, H.-F. Raynaud, L. M. Mugnier, and T. Fusco. Optimal control law for multiconjugate adaptive optics. In P. L. Wizinowich and D. Bonaccini, editors, *Astronomical Telescopes and Instrumentation*, page 878, Waikoloa, Hawai'i, United States, Feb. 2003. doi:[10.1117/12.459704](https://doi.org/10.1117/12.459704). (Cited on pages: [73](#), [134](#))
- B. Le Roux, J.-M. Conan, C. Kulcsár, H.-F. Raynaud, L. M. Mugnier, and T. Fusco. Optimal control law for classical and multiconjugate adaptive optics. *JOSA A*, 21(7):1261–1276, July 2004. ISSN 1520-8532. doi:[10.1364/JOSAA.21.001261](https://doi.org/10.1364/JOSAA.21.001261). (Cited on page: [95](#))

- C. B. Lim, C. Petit, K. Saab, B. Fleury, F. Mendez, J. Montri, N. Vedrenne, and V. Michau. Single-Mode Fiber Coupling for Satellite-To-Ground Telecommunication Links Corrected by Adaptive Optics. 2018. (Cited on pages: [63](#), [212](#), [217](#) et [218](#))
- X. Liu, T. Morris, C. Saunter, F. J. de Cos Juez, C. González-Gutiérrez, and L. Bardou. Wavefront prediction using artificial neural networks for open-loop adaptive optics. *Monthly Notices of the Royal Astronomical Society*, 496(1): 456–464, July 2020. ISSN 0035-8711. doi:[10.1093/mnras/staa1558](#). (Cited on page: [73](#))
- M. Lloyd-Hart and P. McGuire. Spatio-temporal prediction for adaptive optics wavefront reconstructors. 54:95, Jan. 1996. (Cited on page: [73](#))
- M. Lloyd-Hart, C. Baranec, N. M. Milton, M. Snyder, T. Stalcup, J. Roger, and P. Angel. Experimental results of ground-layer and tomographic wavefront reconstruction from multiple laser guide stars. *Optics Express*, 14(17):7541–7551, Aug. 2006. ISSN 1094-4087. doi:[10.1364/OE.14.007541](#). (Cited on page: [73](#))
- J. Lochard, N. de Guembecker, P. Chéoux-Damas, X. Calmet, E. Giraud, A. Jullien, M. Ghezal, L. Barthe, J.-F. Chouteau, L. Coret, G. Artaud, L. Perret, P. Viallefont, and E. Cazala-Hourcade. LASIN optical link on-board CO3D constellation. In *International Conference on Space Optics — ICSO 2022*, volume 12777, pages 375–383. SPIE, July 2023. doi:[10.1117/12.2689018](#). (Cited on page: [47](#))
- P. Lognone, A. M. Bonnefois, J.-M. Conan, L. Paillier, C. Petit, C. B. Lim, S. Meimon, J. Montri, J.-F. Sauvage, and N. Vedrenne. New Results From the 2021 FEEDELIO Experiment - a Focus on Reciprocity. In *2022 IEEE International Conference on Space Optical Systems and Applications (ICSOS)*, pages 261–266, Kyoto City, Japan, Mar. 2022. IEEE. ISBN 978-1-66543-439-3. doi:[10.1109/ICSOS53063.2022.9749723](#). (Cited on page: [41](#))
- P. Lognoné, J.-M. Conan, G. Rekaya, and N. Vedrenne. Phase Estimation at Point-Ahead Angle for AO Pre-Compensated Ground to GEO Satellite Telecoms. *Optics Express*, Dec. 2022. ISSN 1094-4087. doi:[10.1364/OE.476328](#). (Cited on pages: [xiv](#), [25](#), [41](#), [143](#), [187](#) et [226](#))
- D. P. Looze. Discrete-time model of an adaptive optics systems. *Journal of the Optical Society of America A*, 24(9):2850, 2007. ISSN 1084-7529, 1520-8532. doi:[10.1364/JOSAA.24.002850](#). (Cited on page: [71](#))
- D. P. Looze. Linear-quadratic-Gaussian control for adaptive optics systems using a hybrid model. *JOSA A*, 26(1):1–9, Jan. 2009. ISSN 1520-8532. doi:[10.1364/JOSAA.26.000001](#). (Cited on page: [71](#))

- J. S. Luo and A. Johnson. Stability robustness of the continuous-time LQG system under plant perturbation and noise uncertainty. *Automatica*, 29(2):485–489, Mar. 1993. ISSN 0005-1098. doi:[10.1016/0005-1098\(93\)90143-H](https://doi.org/10.1016/0005-1098(93)90143-H). (Cited on page: [130](#))
- H. Lütkepohl. *New Introduction to Multiple Time Series Analysis*. New York : Springer, Berlin, 2005. ISBN 978-3-540-40172-8. (Cited on pages: [75](#), [76](#), [77](#), [78](#) et [79](#))
- B. Macintosh. Extreme AO: The future of high-contrast imaging with adaptive optics. 198:83.04, May 2001. (Cited on page: [73](#))
- P.-Y. Madec. Overview of deformable mirror technologies for adaptive optics and astronomy. In B. L. Ellerbroek, E. Marchetti, and J.-P. Véran, editors, *SPIE Astronomical Telescopes + Instrumentation*, pages 844705–844705–18, Amsterdam, , Netherlands, Sept. 2012. doi:[10.1117/12.924892](https://doi.org/10.1117/12.924892). (Cited on page: [32](#))
- F. Mahe, V. Michau, G. Rousset, and J.-M. Conan. Scintillation effects on wavefront sensing in the Rytov regime. In *Propagation and Imaging through the Atmosphere IV*, volume 4125, pages 77–86. International Society for Optics and Photonics, Nov. 2000. doi:[10.1117/12.409307](https://doi.org/10.1117/12.409307). (Cited on pages: [30](#), [40](#))
- S. V. Mantravadi, T. A. Rhoadarmer, and R. S. Glas. Simple laboratory system for generating well-controlled atmospheric-like turbulence. In *Advanced Wavefront Control: Methods, Devices, and Applications II*, volume 5553, pages 290–300. SPIE, Oct. 2004. doi:[10.1117/12.559933](https://doi.org/10.1117/12.559933). (Cited on page: [186](#))
- O. Martin, É. Gendron, G. Rousset, and F. Vidal. Temporal convergence of phase spatial covariance matrix measurements in tomographic adaptive optics. In *Adaptive Optics Systems III*, volume 8447, pages 855–868. SPIE, Sept. 2012. doi:[10.1117/12.924845](https://doi.org/10.1117/12.924845). (Cited on pages: [86](#), [142](#))
- O. A. Martin, C. M. Correia, E. Gendron, G. Rousset, F. Vidal, T. J. Morris, A. G. Basden, R. M. Myers, Y. H. Ono, B. Neichel, and T. Fusco. William Herschel Telescope site characterization using the MOAO pathfinder CANARY on-sky data. In *Adaptive Optics Systems V*, volume 9909, pages 1143–1157. SPIE, July 2016. doi:[10.1117/12.2231437](https://doi.org/10.1117/12.2231437). (Cited on page: [143](#))
- P. Massioni, C. Kulcsár, H.-F. Raynaud, and J.-M. Conan. Fast computation of an optimal controller for large-scale adaptive optics. *JOSA A*, 28(11):2298–2309, Nov. 2011. ISSN 1520-8532. doi:[10.1364/JOSAA.28.002298](https://doi.org/10.1364/JOSAA.28.002298). (Cited on pages: [95](#), [135](#) et [136](#))
- S. Meimon, C. Petit, T. Fusco, and C. Kulcsar. Tip-tilt disturbance model identification for Kalman-based control scheme: Application to XAO and ELT systems. *Journal of the Optical Society of America A*, 27(11):A122, Nov. 2010. ISSN 1084-7529, 1520-8532. doi:[10.1364/JOSAA.27.00A122](https://doi.org/10.1364/JOSAA.27.00A122). (Cited on page: [78](#))

- E. Mieda, J.-P. Véran, M. Rosensteiner, P. Turri, D. R. Andersen, G. Herriot, O. Lardière, and P. Spanò. Multiconjugate adaptive optics simulator for the Thirty Meter Telescope: Design, implementation, and results. *Journal of Astronomical Telescopes, Instruments, and Systems*, 4(4):49002, Sept. 2018. ISSN 23294124. doi:[10.1117/1.jatis.4.4.049002](https://doi.org/10.1117/1.jatis.4.4.049002). (Cited on page: 186)
- G. Monchen, B. Siquin, and M. Verhaegen. Recursive Kronecker-Based Vector Autoregressive Identification for Large-Scale Adaptive Optics. *IEEE Transactions on Control Systems Technology*, 27(4):1677–1684, July 2019. ISSN 1558-0865. doi:[10.1109/TCST.2018.2834521](https://doi.org/10.1109/TCST.2018.2834521). (Cited on page: 78)
- B. Neichel. *Etude Des Galaxies Lointaines et Optiques Adaptatives Tomographiques Pour ELTs*. These de doctorat, Paris 7, Jan. 2008. (Cited on page: 42)
- M. Nicolle. *Analyse de front d'onde pour les optiques adaptatives de nouvelle generation*. PhD thesis, Université Paris Sud - Paris XI, Dec. 2006. (Cited on page: 42)
- M. Nicolle, T. Fusco, G. Rousset, and V. Michau. Improvement of Shack–Hartmann wave-front sensor measurement for extreme adaptive optics. *Optics Letters*, 29(23):2743–2745, Dec. 2004. ISSN 1539-4794. doi:[10.1364/OL.29.002743](https://doi.org/10.1364/OL.29.002743). (Cited on page: 30)
- R. J. Noll. Zernike polynomials and atmospheric turbulence. *JOSA*, 66(3):207–211, Mar. 1976. doi:[10.1364/JOSA.66.000207](https://doi.org/10.1364/JOSA.66.000207). (Cited on pages: 21, 22 et 23)
- R. J. Noll. Phase estimates from slope-type wave-front sensors. *Journal of the Optical Society of America*, 68(1):139, Jan. 1978. ISSN 0030-3941. doi:[10.1364/JOSA.68.000139](https://doi.org/10.1364/JOSA.68.000139). (Cited on page: 36)
- J. Nousiainen, C. Rajani, M. Kasper, T. Helin, S. Y. Haffert, C. Vérinaud, J. R. Males, K. V. Gorkom, L. M. Close, J. D. Long, A. D. Hedglen, O. Guyon, L. Schatz, M. Kautz, J. Lumbres, A. Rodack, J. M. Knight, and K. Miller. Toward on-sky adaptive optics control using reinforcement learning - Model-based policy optimization for adaptive optics. *Astronomy & Astrophysics*, 664:A71, Aug. 2022. ISSN 0004-6361, 1432-0746. doi:[10.1051/0004-6361/202243311](https://doi.org/10.1051/0004-6361/202243311). (Cited on page: 73)
- S. Oberti, F. Quirós-Pacheco, S. Esposito, R. Muradore, R. Arsenault, E. Fedrigo, M. Kasper, J. Kolb, E. Marchetti, A. Riccardi, C. Soenke, and S. Stroebele. Large DM AO systems: Synthetic IM or calibration on sky? In *Advances in Adaptive Optics II*, volume 6272, pages 652–663. SPIE, June 2006. doi:[10.1117/12.671709](https://doi.org/10.1117/12.671709). (Cited on pages: 35, 43 et 128)
- A. M. Obukhov. Structure of the Temperature Field in Turbulent Flow. *Izvestiya Akademia Nauk SSSR, Series Geograficheskaya i Geograficheskaya*, 13(6):58–69, 1949. (Cited on page: 8)

- E. Ollila and A. Breloy. Regularized tapered sample covariance matrix, Sept. 2021. (Cited on page: [143](#))
- Y. H. Ono, C. Correia, R. Conan, L. Blanco, B. Neichel, and T. Fusco. Fast iterative tomographic wavefront estimation with recursive Toeplitz reconstructor structure for large-scale systems. *JOSA A*, 35(8):1330–1345, Aug. 2018. ISSN 1520-8532. doi:[10.1364/JOSAA.35.001330](#). (Cited on pages: [83](#), [136](#))
- J. Osborn and M. Sarazin. Atmospheric turbulence forecasting with a general circulation model for Cerro Paranal. *Monthly Notices of the Royal Astronomical Society*, 480(1):1278–1299, Oct. 2018. ISSN 0035-8711. doi:[10.1093/mnras/sty1898](#). (Cited on page: [51](#))
- J. Osborn, R. W. Wilson, M. Sarazin, T. Butterley, A. Chacón, F. Derie, O. J. D. Farley, X. Haubois, D. Laidlaw, M. LeLouarn, E. Masciadri, J. Milli, J. Navarrete, and M. J. Townson. Optical turbulence profiling with Stereo-SCIDAR for VLT and ELT. *Monthly Notices of the Royal Astronomical Society*, 478(1):825–834, July 2018. ISSN 0035-8711. doi:[10.1093/mnras/sty1070](#). (Cited on page: [51](#))
- A. Parisot, C. Petit, T. Fusco, and J.-M. Conan. Experimental comparison of tomographic control schemes using the ONERA WFAO facility. In *Adaptive Optics Systems III*, volume 8447, pages 691–702. SPIE, Sept. 2012. doi:[10.1117/12.926309](#). (Cited on page: [95](#))
- R. N. Paschall and D. J. Anderson. Linear quadratic Gaussian control of a deformable mirror adaptive optics system with time-delayed measurements. *Applied Optics*, 32(31):6347–6358, Nov. 1993. ISSN 2155-3165. doi:[10.1364/AO.32.006347](#). (Cited on pages: [72](#), [79](#), [94](#) et [132](#))
- D. Perret, M. Lainé, J. Bernard, D. Gratadour, and A. Sevin. Bridging FPGA and GPU technologies for AO real-time control. In *Adaptive Optics Systems V*, volume 9909, pages 1364–1374. SPIE, July 2016. doi:[10.1117/12.2232858](#). (Cited on page: [43](#))
- C. Petit. *Etude de La Commande Optimale En OA et OAMC, Validation Numérique et Expérimentale*. These de doctorat, Paris 13, Jan. 2006. (Cited on page: [35](#))
- C. Petit, J.-M. Conan, C. Kulcsár, H.-F. Raynaud, T. Fusco, J. Montri, and D. Rabaud. First laboratory demonstration of closed-loop Kalman based optimal control for vibration filtering and simplified MCAO. In *Advances in Adaptive Optics II*, volume 6272, page 62721T. International Society for Optics and Photonics, June 2006. doi:[10.1117/12.671525](#). (Cited on pages: [33](#), [92](#) et [95](#))
- C. Petit, J.-M. Conan, C. Kulcsár, H.-F. Raynaud, and T. Fusco. First laboratory validation of vibration filtering with LQG control law for Adaptive Optics. *Optics Express*, 16(1):87–97, Jan. 2008. ISSN 1094-4087. doi:[10.1364/OE.16.000087](#). (Cited on pages: [44](#), [74](#) et [134](#))

- C. Petit, J.-M. Conan, C. Kulcsár, and H.-F. Raynaud. Linear quadratic Gaussian control for adaptive optics and multiconjugate adaptive optics: Experimental and numerical analysis. *Journal of the Optical Society of America A*, 26(6):1307, June 2009. ISSN 1084-7529, 1520-8532. doi:[10.1364/JOSAA.26.001307](https://doi.org/10.1364/JOSAA.26.001307). (Cited on pages: [73](#), [95](#), [156](#) et [157](#))
- C. Petit, J.-F. Sauvage, T. Fusco, A. Sevin, M. Suarez, A. Costille, A. Vigan, C. Soenke, D. Perret, S. Rochat, A. Barrufolo, B. Salasnich, J.-L. Beuzit, K. Dohlen, D. Mouillet, P. Puget, F. Wildi, M. Kasper, J.-M. Conan, C. Kulcsár, and H.-F. Raynaud. SPHERE eXtreme AO control scheme: Final performance assessment and on sky validation of the first auto-tuned LQG based operational system. In E. Marchetti, L. M. Close, and J.-P. Véran, editors, *SPIE Astronomical Telescopes + Instrumentation*, page 91480O, Montréal, Quebec, Canada, Aug. 2014. doi:[10.1117/12.2052847](https://doi.org/10.1117/12.2052847). (Cited on pages: [73](#), [95](#))
- C. Petit, N. Védrenne, M. T. Velluet, V. Michau, G. Artaud, E. Samain, and M. Toyoshima. Investigation on adaptive optics performance from propagation channel characterization with the small optical transponder. *Optical Engineering*, 55(11):111611, Sept. 2016. ISSN 0091-3286. doi:[10.1117/1.OE.55.11.111611](https://doi.org/10.1117/1.OE.55.11.111611). (Cited on page: [185](#))
- C. Petit, L. Mugnier, A. Bonnefois, J.-M. Conan, T. Fusco, N. Levraud, S. Meimon, V. Michau, J. Montri, N. Vedrenne, M.-T. Velluet, and R. Fétick. LEO satellite imaging with adaptive optics and marginalized blind deconvolution. In *21st AMOS Advanced Maui Optical and Space Surveillance Technologies Conference*, Virtual, United States, Sept. 2020. (Cited on pages: [47](#), [63](#))
- C. Petit, B. Aurelie, C. Jean-Marc, D. Anne, G. Francois, L. Caroline, M. Joseph, P. Laurie, P. Philippe, V. Marie-Therese, V. Jean-Baptiste, and V. Nicolas. FEELINGS : The ONERA’s optical ground station for Geo Feeder links demonstration. In *2022 IEEE International Conference on Space Optical Systems and Applications (ICSOS)*, pages 255–260, Kyoto City, Japan, Mar. 2022. IEEE. ISBN 978-1-66543-439-3. doi:[10.1109/ICSOS53063.2022.9749705](https://doi.org/10.1109/ICSOS53063.2022.9749705). (Cited on pages: [63](#), [185](#), [209](#) et [210](#))
- D.-H. Phung, E. Samain, J. Chabé, C. Courde, N. Maurice, H. Mariey, G. Artaud, A. Ziad, C. Giordano, E. Aristidi, D. Giggenbach, C. Fuchs, C. Schmidt, S. Klinker, and S. Gaißer. Optical bench development for laser communication OSIRIS mission at Grasse (France) station. In *International Conference on Space Optics — ICSO 2020*, volume 11852, pages 981–994. SPIE, June 2021. doi:[10.1117/12.2599371](https://doi.org/10.1117/12.2599371). (Cited on page: [212](#))
- P. Piatrou and M. C. Roggemann. Performance study of Kalman filter controller for multiconjugate adaptive optics. *Applied Optics*, 46(9):1446–1455, Mar. 2007. ISSN 2155-3165. doi:[10.1364/AO.46.001446](https://doi.org/10.1364/AO.46.001446). (Cited on pages: [83](#), [133](#))

- P. Piscaer, O. Soloviev, and M. Verhaegen. Predictive wavefront sensorless adaptive optics for time-varying aberrations. *JOSA A*, 36(11):1810–1819, Nov. 2019. ISSN 1520-8532. doi:[10.1364/JOSAA.36.001810](https://doi.org/10.1364/JOSAA.36.001810). (Cited on page: 82)
- B. Pou, B. Pou, F. Ferreira, E. Quinones, D. Gratadour, D. Gratadour, and M. Martin. Adaptive optics control with multi-agent model-free reinforcement learning. *Optics Express*, 30(2):2991–3015, Jan. 2022. ISSN 1094-4087. doi:[10.1364/OE.444099](https://doi.org/10.1364/OE.444099). (Cited on page: 73)
- L. Poyneer and J.-P. Véran. Predictive wavefront control for adaptive optics with arbitrary control loop delays. *Journal of the Optical Society of America A*, 25(7):1486, July 2008. ISSN 1084-7529, 1520-8532. doi:[10.1364/JOSAA.25.001486](https://doi.org/10.1364/JOSAA.25.001486). (Cited on page: 72)
- L. Poyneer, M. van Dam, and J.-P. Véran. Experimental verification of the frozen flow atmospheric turbulence assumption with use of astronomical adaptive optics telemetry. *JOSA A*, 26(4):833–846, Apr. 2009. ISSN 1520-8532. doi:[10.1364/JOSAA.26.000833](https://doi.org/10.1364/JOSAA.26.000833). (Cited on pages: 10, 49)
- L. A. Poyneer and B. Macintosh. Spatially filtered wave-front sensor for high-order adaptive optics. *JOSA A*, 21(5):810–819, May 2004. ISSN 1520-8532. doi:[10.1364/JOSAA.21.000810](https://doi.org/10.1364/JOSAA.21.000810). (Cited on pages: 42, 157)
- L. A. Poyneer and J.-P. Véran. Kalman filtering to suppress spurious signals in adaptive optics control. *JOSA A*, 27(11):A223–A234, Nov. 2010. ISSN 1520-8532. doi:[10.1364/JOSAA.27.00A223](https://doi.org/10.1364/JOSAA.27.00A223). (Cited on pages: 44, 74 et 157)
- L. A. Poyneer, D. T. Gavel, and J. M. Brase. Fast wave-front reconstruction in large adaptive optics systems with use of the Fourier transform. *JOSA A*, 19(10):2100–2111, Oct. 2002. ISSN 1520-8532. doi:[10.1364/JOSAA.19.002100](https://doi.org/10.1364/JOSAA.19.002100). (Cited on page: 136)
- L. A. Poyneer, B. A. Macintosh, and J.-P. Véran. Fourier transform wavefront control with adaptive prediction of the atmosphere. *JOSA A*, 24(9):2645–2660, Sept. 2007. ISSN 1520-8532. doi:[10.1364/JOSAA.24.002645](https://doi.org/10.1364/JOSAA.24.002645). (Cited on pages: 137, 157)
- L. A. Poyneer, D. W. Palmer, B. Macintosh, D. Savransky, N. Sadakuni, S. Thomas, J.-P. Véran, K. B. Follette, A. Z. Greenbaum, S. M. Ammons, V. P. Bailey, B. Bauman, A. Cardwell, D. Dillon, D. Gavel, M. Hartung, P. Hibon, M. D. Perrin, F. T. Rantakyrö, A. Sivaramakrishnan, and J. J. Wang. Performance of the Gemini Planet Imager’s adaptive optics system. *Applied Optics*, 55(2):323–340, Jan. 2016. ISSN 2155-3165. doi:[10.1364/AO.55.000323](https://doi.org/10.1364/AO.55.000323). (Cited on pages: 42, 73 et 95)

- L. A. Poyneer, S. M. Ammons, M. K. Kim, B. Bauman, J. Terrel-Perez, A. J. Lemmer, and J. Nguyen. Laboratory demonstration of the prediction of wind-blown turbulence by adaptive optics at 8 kHz with use of LQG control. *Applied Optics*, 62(8):1871–1885, Mar. 2023. ISSN 2155-3165. doi:[10.1364/AO.474730](https://doi.org/10.1364/AO.474730). (Cited on page: [137](#))
- L. Prengère, C. Kulcsár, and H.-F. Raynaud. Zonal-based high-performance control in adaptive optics systems with application to astronomy and satellite tracking. *Journal of the Optical Society of America A*, 37(7):1083, July 2020. ISSN 1084-7529, 1520-8532. doi:[10.1364/JOSAA.391484](https://doi.org/10.1364/JOSAA.391484). (Cited on pages: [82](#), [83](#), [111](#), [133](#), [134](#), [135](#) et [170](#))
- L. Prengère, C. Kulcsár, and H.-F. Raynaud. Adaptive optics control with predictive controllers based on frozen-flow models for Low-Earth Orbit satellite tracking. In *Imaging and Applied Optics Congress (2020), Paper JW4G.5*, page JW4G.5. Optical Society of America, June 2020. doi:[10.1364/AOMS.2020.JW4G.5](https://doi.org/10.1364/AOMS.2020.JW4G.5). (Cited on pages: [149](#), [157](#) et [169](#))
- Z. Qu and I. B. Djordjevic. Approaching terabit optical transmission over strong atmospheric turbulence channels. In *2016 18th International Conference on Transparent Optical Networks (ICTON)*, pages 1–5, July 2016. doi:[10.1109/ICTON.2016.7550346](https://doi.org/10.1109/ICTON.2016.7550346). (Cited on pages: [185](#), [187](#))
- F. Quirós-Pacheco, J.-M. Conan, and C. Petit. Generalized aliasing and its implications in modal gain optimization for multi-conjugate adaptive optics. *Journal of the Optical Society of America A*, 27(11):A182, Nov. 2010. ISSN 1084-7529, 1520-8532. doi:[10.1364/JOSAA.27.00A182](https://doi.org/10.1364/JOSAA.27.00A182). (Cited on pages: [157](#), [261](#))
- R. Ragazzoni. Pupil plane wavefront sensing with an oscillating prism. *Journal of Modern Optics*, 43(2):289–293, Feb. 1996. ISSN 0950-0340. doi:[10.1080/09500349608232742](https://doi.org/10.1080/09500349608232742). (Cited on page: [29](#))
- R. Ragazzoni and J. Farinato. Sensitivity of a pyramidal Wave Front sensor in closed loop Adaptive Optics. *Astronomy and Astrophysics*, 350:L23–L26, Oct. 1999. ISSN 0004-6361. (Cited on page: [29](#))
- H. V. Ramió, J. Vernin, C. Muñoz-Tuñón, M. Sarazin, A. M. Varela, H. Trinquet, J. M. Delgado, J. J. Fuensalida, M. Reyes, A. Benhida, Z. Benkhaldoun, D. G. Lambas, Y. Hach, M. Lazrek, G. Lombardi, J. Navarrete, P. Recabarren, V. Renzi, M. Sabil, and R. Vrech. European Extremely Large Telescope Site Characterization. II. High Angular Resolution Parameters. *Publications of the Astronomical Society of the Pacific*, 124(918):868, Aug. 2012. ISSN 1538-3873. doi:[10.1086/667599](https://doi.org/10.1086/667599). (Cited on page: [51](#))

- R. Rampy, D. Gavel, D. Dillon, and S. Thomas. New method of fabricating phase screens for simulated atmospheric turbulence. In *Adaptive Optics Systems II*, volume 7736, pages 1063–1072. SPIE, July 2010. doi:[10.1117/12.856517](https://doi.org/10.1117/12.856517). (Cited on page: [186](#))
- H.-F. Raynaud, C. Correia, C. Kulcsár, and J.-M. Conan. Minimum-variance control of astronomical adaptive optic systems with actuator dynamics under synchronous and asynchronous sampling. *International Journal of Robust and Nonlinear Control*, 21(7):768–789, May 2011. ISSN 10498923. doi:[10.1002/rnc.1625](https://doi.org/10.1002/rnc.1625). (Cited on page: [72](#))
- H.-F. Raynaud, C. Kulcsár, R. Juvénal, and C. Petit. The control switching adapter: A practical way to ensure bumpless switching between controllers while AO loop is engaged. In *Adaptive Optics Systems V*, volume 9909, page 99094K. International Society for Optics and Photonics, July 2016. doi:[10.1117/12.2234266](https://doi.org/10.1117/12.2234266). (Cited on page: [145](#))
- C. Rickenstorff, J. A. Rodrigo, and T. Alieva. Programmable simulator for beam propagation in turbulent atmosphere. *Optics Express*, 24(9):10000–10012, May 2016. ISSN 1094-4087. doi:[10.1364/OE.24.010000](https://doi.org/10.1364/OE.24.010000). (Cited on page: [186](#))
- F. Rigaut and E. Gendron. Laser guide star in adaptive optics: The tilt determination problem. *Astronomy and Astrophysics*, 261:677–684, Aug. 1992. ISSN 0004-6361. (Cited on pages: [31](#), [36](#) et [150](#))
- F. J. Rigaut, J.-P. Veran, and O. Lai. Analytical model for Shack-Hartmann-based adaptive optics systems. In *Adaptive Optical System Technologies*, volume 3353, pages 1038–1048. International Society for Optics and Photonics, Sept. 1998. doi:[10.1117/12.321649](https://doi.org/10.1117/12.321649). (Cited on page: [42](#))
- M. P. Rimmer. Method for Evaluating Lateral Shearing Interferograms. *Applied Optics*, 13(3):623–629, Mar. 1974. ISSN 2155-3165. doi:[10.1364/AO.13.000623](https://doi.org/10.1364/AO.13.000623). (Cited on page: [36](#))
- L. Roberts, G. Block, S. Fregoso, H. Herzog, S. Meeker, J. Roberts, J. Tesch, T. Truong, J. Rodriguez, and A. Bechter. *First Results from the Adaptive Optics System for LCRD’s Optical Ground Station One*. Sept. 2018. (Cited on page: [186](#))
- P. Robles, C. Petit, J.-M. Conan, B. Benammar, and B. Neichel. Predictive adaptive optics for satellite tracking applications: Optical communications and satellite observation. In *Adaptive Optics Systems VIII*, volume 12185, pages 917–931. SPIE, Aug. 2022. doi:[10.1117/12.2630217](https://doi.org/10.1117/12.2630217). (Cited on pages: [151](#), [209](#))
- P. Robles, C. Petit, M.-T. Velluet, L. Le Leuch, A. Montmerle-Bonnefois, L. Paillier, J.-M. Conan, F. Cassaing, J. Montri, B. Neichel, and N. Vedrenne. Emulating and characterizing strong turbulence conditions for space-to-ground optical links: The PICOLO bench. 2023. (Cited on pages: [4](#), [182](#))

- F. Roddier. V The Effects of Atmospheric Turbulence in Optical Astronomy. In E. Wolf, editor, *Progress in Optics*, volume 19, pages 281–376. Elsevier, Jan. 1981. doi:[10.1016/S0079-6638\(08\)70204-X](https://doi.org/10.1016/S0079-6638(08)70204-X). (Cited on pages: 17, 18)
- T. S. Ross. Limitations and applicability of the Maréchal approximation. *Applied Optics*, 48(10):1812–1818, Apr. 2009. ISSN 2155-3165. doi:[10.1364/AO.48.001812](https://doi.org/10.1364/AO.48.001812). (Cited on page: 59)
- C. Ruilier and F. Cassaing. Coupling of large telescopes and single-mode waveguides: Application to stellar interferometry. *JOSA A*, 18(1):143–149, Jan. 2001. ISSN 1520-8532. doi:[10.1364/JOSAA.18.000143](https://doi.org/10.1364/JOSAA.18.000143). (Cited on page: 60)
- S. M. Rytov, Y. A. Kravtsov, and V. I. Tatarskii. *Principles of Statistical Radiophysics. 4. Wave Propagation through Random Media*. Jan. 1989. (Cited on page: 12)
- K. Saab. *Adaptive Optics for Free Space Optical Communication*. PhD thesis, Université Paris sciences et lettres, Nov. 2017. (Cited on page: 217)
- R. J. Sasiela. *Electromagnetic Wave Propagation in Turbulence*, volume 18 of *Springer Series on Wave Phenomena*. Springer, Berlin, Heidelberg, 1994. ISBN 978-3-642-85072-1 978-3-642-85070-7. doi:[10.1007/978-3-642-85070-7](https://doi.org/10.1007/978-3-642-85070-7). (Cited on page: 16)
- J.-F. Sauvage, T. Fusco, C. Petit, S. Meimon, E. Fedrigo, M. S. Valles, M. Kasper, N. Hubin, J.-L. Beuzit, J. Charton, A. Costille, R. P. D. Mouillet, P. Baudoz, T. Buey, A. Sevin, F. Wildi, and K. Dohlen. SAXO, the eXtreme Adaptive Optics System of SPHERE: Overview and calibration procedure. In *Adaptive Optics Systems II*, volume 7736, pages 175–184. SPIE, July 2010. doi:[10.1117/12.856942](https://doi.org/10.1117/12.856942). (Cited on page: 43)
- J.-F. Sauvage, T. Fusco, A. Guesalaga, P. Wizinowitch, J. O’Neal, M. N’Diaye, A. Vigan, J. Grard, G. Lesur, D. Mouillet, J.-L. Beuzit, M. Kasper, M. Le Louarn, J. Milli, K. Dohlen, B. Neichel, P. Bourget, P. Heigenauer, and D. Mawet. Low Wind Effect, the main limitation of the SPHERE instrument. *Adaptive Optics for Extremely Large Telescopes 4 – Conference Proceedings*, 1(1), 2015. doi:[10.20353/K3T4CP1131541](https://doi.org/10.20353/K3T4CP1131541). (Cited on page: 33)
- D. Saxenhuber, G. Auzinger, M. L. Louarn, and T. Helin. Comparison of methods for the reduction of reconstructed layers in atmospheric tomography. *Applied Optics*, 56(10):2621–2629, Apr. 2017. ISSN 2155-3165. doi:[10.1364/AO.56.002621](https://doi.org/10.1364/AO.56.002621). (Cited on page: 188)
- M. Schöck and E. J. Spillar. Method for a quantitative investigation of the frozen flow hypothesis. *JOSA A*, 17(9):1650–1658, Sept. 2000. ISSN 1520-8532. doi:[10.1364/JOSAA.17.001650](https://doi.org/10.1364/JOSAA.17.001650). (Cited on page: 10)

- M. Schöck, S. Els, R. Riddle, W. Skidmore, T. Travouillon, R. Blum, E. Bustos, G. Chanan, S. G. Djorgovski, P. Gillett, B. Gregory, J. Nelson, A. Otárola, J. Seguel, J. Vasquez, A. Walker, D. Walker, and L. Wang. Thirty Meter Telescope Site Testing I: Overview. *Publications of the Astronomical Society of the Pacific*, 121(878):384, May 2009. ISSN 1538-3873. doi:[10.1086/599287](https://doi.org/10.1086/599287). (Cited on page: [51](#))
- M. Sechaud, F. Mahe, T. Fusco, V. Michau, and J.-M. Conan. High-resolution imaging through atmospheric turbulence: Link between anisoplanatism and intensity fluctuations. In A. Kohnle and J. D. Gonglewski, editors, *Remote Sensing*, page 100, Florence, Italy, Dec. 1999. doi:[10.1117/12.371314](https://doi.org/10.1117/12.371314). (Cited on pages: [19](#), [202](#))
- B. D. Shaffer, A. J. McDaniel, C. C. Wilcox, and E. S. Ahn. Dynamic mode decomposition based predictive model performance on supersonic and transonic aero-optical wavefront measurements. *Applied Optics*, 60(25):G170–G180, Sept. 2021. ISSN 2155-3165. doi:[10.1364/AO.426031](https://doi.org/10.1364/AO.426031). (Cited on page: [144](#))
- S. Shaklan and F. Roddier. Coupling starlight into single-mode fiber optics. *Applied Optics*, 27(11):2334–2338, June 1988. ISSN 2155-3165. doi:[10.1364/AO.27.002334](https://doi.org/10.1364/AO.27.002334). (Cited on pages: [59](#), [184](#) et [216](#))
- J. H. Shapiro. Point-ahead limitation on reciprocity tracking*. *JOSA*, 65(1):65–68, Jan. 1975. doi:[10.1364/JOSA.65.000065](https://doi.org/10.1364/JOSA.65.000065). (Cited on page: [41](#))
- H. W. Shepherd, J. Osborn, R. W. Wilson, T. Butterley, R. Avila, V. S. Dhillon, and T. J. Morris. Stereo-SCIDAR: Optical turbulence profiling with high sensitivity using a modified SCIDAR instrument. *Monthly Notices of the Royal Astronomical Society*, 437(4):3568–3577, Feb. 2014. ISSN 0035-8711. doi:[10.1093/mnras/stt2150](https://doi.org/10.1093/mnras/stt2150). (Cited on page: [49](#))
- D. Simon. *Optimal State Estimation: Kalman, H [Infinity] and Nonlinear Approaches*. Wiley-Interscience, Hoboken, N.J, 2006. ISBN 978-0-471-70858-2. (Cited on page: [90](#))
- B. Sinquin, L. Prengère, C. Kulcsár, H.-F. Raynaud, E. Gendron, J. Osborn, A. Basden, J.-M. Conan, N. Bharmal, L. Bardou, L. Staykov, T. Morris, T. Buey, F. Chemla, and M. Cohen. On-sky results for adaptive optics control with data-driven models on low-order modes. *Monthly Notices of the Royal Astronomical Society*, 498(1):3228–3240, July 2020. ISSN 1365-2966. doi:[10.1093/mnras/staa2562](https://doi.org/10.1093/mnras/staa2562). (Cited on pages: [73](#), [78](#), [82](#), [134](#), [144](#) et [170](#))
- G. Sivo, H.-F. Raynaud, J.-M. Conan, C. Kulcsár, E. Gendron, F. Vidal, and A. Basden. First laboratory validation of LQG control with the CANARY MOAO pathfinder. In *Adaptive Optics Systems III*, volume 8447, page 84472Y.

- International Society for Optics and Photonics, Sept. 2012. doi:[10.1117/12.926257](https://doi.org/10.1117/12.926257). (Cited on pages: [95](#), [134](#))
- G. Sivo, C. Kulcsár, J.-M. Conan, H.-F. Raynaud, É. Gendron, A. Basden, F. Vidal, T. Morris, S. Meimon, C. Petit, D. Gratadour, O. Martin, Z. Hubert, A. Sevin, D. Perret, F. Chemla, G. Rousset, N. Dipper, G. Talbot, E. Younger, R. Myers, D. Henry, S. Todd, D. Atkinson, C. Dickson, and A. Longmore. First on-sky SCAO validation of full LQG control with vibration mitigation on the CANARY pathfinder. *Optics Express*, 22(19):23565–23591, Sept. 2014. ISSN 1094-4087. doi:[10.1364/OE.22.023565](https://doi.org/10.1364/OE.22.023565). (Cited on pages: [74](#), [95](#) et [134](#))
- W. H. Southwell. Wave-front estimation from wave-front slope measurements. *JOSA*, 70(8):998–1006, Aug. 1980. doi:[10.1364/JOSA.70.000998](https://doi.org/10.1364/JOSA.70.000998). (Cited on page: [36](#))
- D. Sprung and E. Sucher. Characterization of optical turbulence at the solar observatory at the Mount Teide, Tenerife. In *Remote Sensing of Clouds and the Atmosphere XVIII; and Optics in Atmospheric Propagation and Adaptive Systems XVI*, volume 8890, pages 321–329. SPIE, Oct. 2013. doi:[10.1117/12.2032744](https://doi.org/10.1117/12.2032744). (Cited on page: [51](#))
- J. W. Strohbehn, S. Amelinkcx, V. P. Chebotayev, R. Gomer, H. Ibach, V. S. Letokhov, H. K. V. Lotsch, H. J. Queisser, F. P. Schäfer, A. Seeger, K. Shimoda, T. Tamir, W. T. Welford, and H. P. J. Wijn, editors. *Laser Beam Propagation in the Atmosphere*, volume 25 of *Topics in Applied Physics*. Springer, Berlin, Heidelberg, 1978. ISBN 978-3-540-08812-7 978-3-540-35826-8. doi:[10.1007/3-540-08812-1](https://doi.org/10.1007/3-540-08812-1). (Cited on page: [11](#))
- R. Swanson, M. Lamb, C. Correia, S. Sivanandam, and K. Kutulakos. Wave-front reconstruction and prediction with convolutional neural networks. In *Adaptive Optics Systems VI*, volume 10703, pages 481–490. SPIE, July 2018. doi:[10.1117/12.2312590](https://doi.org/10.1117/12.2312590). (Cited on page: [73](#))
- V. I. Tatarskii. *Wave Propagation in Turbulent Medium*. Jan. 1961. (Cited on pages: [8](#), [9](#), [11](#), [14](#), [15](#) et [16](#))
- J. Tesch, T. Truong, R. Burruss, and S. Gibson. On-sky demonstration of optimal control for adaptive optics at Palomar Observatory. *Optics Letters*, 40(7):1575–1578, Apr. 2015. ISSN 1539-4794. doi:[10.1364/OL.40.001575](https://doi.org/10.1364/OL.40.001575). (Cited on page: [78](#))
- E. Thiébaud and M. Tallon. Fast minimum variance wavefront reconstruction for extremely large telescopes. *JOSA A*, 27(5):1046–1059, May 2010. ISSN 1520-8532. doi:[10.1364/JOSAA.27.001046](https://doi.org/10.1364/JOSAA.27.001046). (Cited on page: [38](#))
- S. Thomas. A simple turbulence simulator for adaptive optics. In *SPIE Astronomical Telescopes + Instrumentation*, page 766, USA, Oct. 2004. doi:[10.1117/12.549858](https://doi.org/10.1117/12.549858). (Cited on page: [186](#))

- S. Thomas, T. Fusco, A. Tokovinin, M. Nicolle, V. Michau, and G. Rousset. Comparison of centroid computation algorithms in a Shack–Hartmann sensor. *Monthly Notices of the Royal Astronomical Society*, 371(1):323–336, Sept. 2006. ISSN 0035-8711. doi:[10.1111/j.1365-2966.2006.10661.x](https://doi.org/10.1111/j.1365-2966.2006.10661.x). (Cited on pages: 30, 31)
- A. Tokovinin. From Differential Image Motion to Seeing. *Publications of the Astronomical Society of the Pacific*, 114(800):1156, Oct. 2002. ISSN 1538-3873. doi:[10.1086/342683](https://doi.org/10.1086/342683). (Cited on page: 195)
- A. Tokovinin and V. Kornilov. Accurate seeing measurements with MASS and DIMM. *Monthly Notices of the Royal Astronomical Society*, 381(3):1179–1189, Nov. 2007. ISSN 0035-8711. doi:[10.1111/j.1365-2966.2007.12307.x](https://doi.org/10.1111/j.1365-2966.2007.12307.x). (Cited on page: 143)
- R. K. Tyson. Adaptive optics and ground-to-space laser communications. *Applied Optics*, 35(19):3640, July 1996. ISSN 0003-6935, 1539-4522. doi:[10.1364/AO.35.003640](https://doi.org/10.1364/AO.35.003640). (Cited on page: 41)
- R. K. Tyson and B. W. Frazier. Microelectromechanical system programmable aberration generator for adaptive optics. *Applied Optics*, 40(13):2063–2067, May 2001. ISSN 2155-3165. doi:[10.1364/AO.40.002063](https://doi.org/10.1364/AO.40.002063). (Cited on page: 187)
- USC. Satellite Database — Union of Concerned Scientists, 2023. (Cited on pages: xxiii, 47 et 48)
- G. C. Valley. Isoplanatic degradation of tilt correction and short-term imaging systems. *Applied Optics*, 19(4):574, Feb. 1980. ISSN 0003-6935, 1539-4522. doi:[10.1364/AO.19.000574](https://doi.org/10.1364/AO.19.000574). (Cited on pages: 51, 188)
- M. van Kooten, N. Doelman, and M. Kenworthy. Impact of time-variant turbulence behavior on prediction for adaptive optics systems. *JOSA A*, 36(5):731–740, May 2019. ISSN 1520-8532. doi:[10.1364/JOSAA.36.000731](https://doi.org/10.1364/JOSAA.36.000731). (Cited on pages: 143, 145)
- M. A. M. van Kooten, N. Doelman, and M. Kenworthy. Robustness of prediction for extreme adaptive optics systems under various observing conditions: An analysis using VLT/SPHERE adaptive optics data. *Astronomy & Astrophysics*, 636:A81, Apr. 2020. ISSN 0004-6361, 1432-0746. doi:[10.1051/0004-6361/201937076](https://doi.org/10.1051/0004-6361/201937076). (Cited on page: 145)
- M. A. M. van Kooten, R. M. Jensen-Clem, S. Cetre, S. Ragland, C. Z. Bond, J. Fowler, and P. L. Wizinowich. Predictive wavefront control on Keck II adaptive optics bench: On-sky coronagraphic results. *Journal of Astronomical Telescopes, Instruments, and Systems*, 8(2):029006, June 2022. ISSN 2329-4124, 2329-4221. doi:[10.1117/1.JATIS.8.2.029006](https://doi.org/10.1117/1.JATIS.8.2.029006). (Cited on pages: 36, 73, 143 et 145)

- N. Védrenne. *Propagation Optique et Correction En Forte Turbulence*. These de doctorat, Nice, Jan. 2008. (Cited on page: 20)
- N. Védrenne, V. Michau, C. Robert, and J.-M. Conan. C_n^2 profile measurement from Shack-Hartmann data. *Optics Letters*, 32(18):2659–2661, Sept. 2007. ISSN 1539-4794. doi:[10.1364/OL.32.002659](https://doi.org/10.1364/OL.32.002659). (Cited on page: 143)
- N. Vedrenne, M.-T. Velluet, M. Sechaud, J.-M. Conan, M. Toyoshima, H. Takenada, A. Guerin, and F. Lacoste. Turbulence effects on bi-directional ground-to-satellite laser communication systems. page 6, 2012. (Cited on pages: 14, 185 et 195)
- N. Vedrenne, J.-M. Conan, A. Bonnefois, C. Petit, M.-T. Velluet, and V. Michau. Adaptive optics pre-compensation for GEO feeder links: Towards an experimental demonstration. In *2017 IEEE International Conference on Space Optical Systems and Applications (ICSOS)*, pages 77–81, Naha, Nov. 2017. IEEE. ISBN 978-1-5090-6511-0. doi:[10.1109/ICSOS.2017.8357215](https://doi.org/10.1109/ICSOS.2017.8357215). (Cited on page: 209)
- N. Védrenne, C. Petit, A. Montmerle-Bonnefois, C. B. Lim, J.-M. Conan, L. Paillier, M.-T. Velluet, K. Caillault, F. Gustave, A. Durecu, V. Michau, F. Cassaing, S. Meimon, and J. Montri. Performance analysis of an adaptive optics based optical feeder link ground station. In Z. Sodnik, B. Cugny, and N. Karafolas, editors, *International Conference on Space Optics — ICSO 2020*, page 45, Online Only, France, June 2021. SPIE. ISBN 978-1-5106-4548-6 978-1-5106-4549-3. doi:[10.1117/12.2599232](https://doi.org/10.1117/12.2599232). (Cited on pages: 51, 52)
- M.-T. Velluet, C. Petit, L. Le Leuch, A. Bonnefois, J.-M. Conan, F. Cassaing, and N. Védrenne. PICOLO: Turbulence simulator for adaptive optics systems assessment in the context of ground-satellite optical links. In K. Stein and S. Gladysz, editors, *Environmental Effects on Light Propagation and Adaptive Systems III*, page 5, Online Only, United Kingdom, Oct. 2020. SPIE. ISBN 978-1-5106-3877-8 978-1-5106-3878-5. doi:[10.1117/12.2573954](https://doi.org/10.1117/12.2573954). (Cited on pages: 182, 185 et 189)
- F. Vidal, E. Gendron, and G. Rousset. Tomography approach for multi-object adaptive optics. *JOSA A*, 27(11):A253–A264, Nov. 2010. ISSN 1520-8532. doi:[10.1364/JOSAA.27.00A253](https://doi.org/10.1364/JOSAA.27.00A253). (Cited on pages: 82, 86, 133 et 141)
- C. R. Vogel, G. A. Tyler, and D. J. Wittich. Spatial–temporal-covariance-based modeling, analysis, and simulation of aero-optics wavefront aberrations. *Journal of the Optical Society of America A*, 31(7):1666, July 2014. ISSN 1084-7529, 1520-8532. doi:[10.1364/JOSAA.31.001666](https://doi.org/10.1364/JOSAA.31.001666). (Cited on pages: 85, 100)
- C. Volland, Z. Sodnik, J. M. Perdignes-Armengol, D. Alaluf, N. Vedrenne, and K. Nicklaus. Towards optical data highways through the atmosphere. In *Free-Space Laser Communications XXXI*, volume 10910, pages 296–305. SPIE, Mar. 2019. doi:[10.1117/12.2509648](https://doi.org/10.1117/12.2509648). (Cited on page: 184)

- E. P. Wallner. Optimal wave-front correction using slope measurements. *JOSA*, 73(12):1771–1776, Dec. 1983. doi:[10.1364/JOSA.73.001771](https://doi.org/10.1364/JOSA.73.001771). (Cited on pages: [38](#), [94](#), [95](#) et [139](#))
- M. R. Whiteley, M. C. Roggemann, and B. M. Welsh. Optimal beam steering using time-delayed wavefront measurements in airborne laser target engagements. In T. D. Steiner and P. H. Merritt, editors, *Aerospace/Defense Sensing and Controls*, pages 98–109, Orlando, FL, Sept. 1998a. doi:[10.1117/12.323929](https://doi.org/10.1117/12.323929). (Cited on pages: [84](#), [100](#), [125](#) et [133](#))
- M. R. Whiteley, B. M. Welsh, and M. C. Roggemann. Optimal modal wave-front compensation for anisoplanatism in adaptive optics. *Journal of the Optical Society of America A*, 15(8):2097, Aug. 1998b. ISSN 1084-7529, 1520-8532. doi:[10.1364/JOSAA.15.002097](https://doi.org/10.1364/JOSAA.15.002097). (Cited on page: [139](#))
- W. J. Wild. Innovative wavefront estimators for zonal adaptive optics systems. In *Adaptive Optics and Applications*, volume 3126, pages 278–287. SPIE, Oct. 1997. doi:[10.1117/12.290154](https://doi.org/10.1117/12.290154). (Cited on page: [74](#))
- R. W. Wilson. SLODAR: Measuring optical turbulence altitude with a Shack–Hartmann wavefront sensor. *Monthly Notices of the Royal Astronomical Society*, 337(1):103–108, Nov. 2002. ISSN 0035-8711. doi:[10.1046/j.1365-8711.2002.05847.x](https://doi.org/10.1046/j.1365-8711.2002.05847.x). (Cited on page: [143](#))
- A. M. Yaglom. On the local structure of a temperature field in a turbulent flow. *Dokl. akad. nauk sssr.*, 69(6):743–746, 1949. (Cited on page: [8](#))
- K. Yang, P. Yang, S. Chen, S. Wang, L. Wen, L. Dong, X. He, B. Lai, X. Yu, and B. Xu. Vibration identification based on Levenberg–Marquardt optimization for mitigation in adaptive optics systems. *Applied Optics*, 57(11):2820–2826, Apr. 2018. ISSN 2155-3165. doi:[10.1364/AO.57.002820](https://doi.org/10.1364/AO.57.002820). (Cited on page: [78](#))
- H. T. Yura and W. G. McKinley. Optical scintillation statistics for IR ground-to-space laser communication systems. *Applied Optics*, 22(21):3353, Nov. 1983. ISSN 0003-6935, 1539-4522. doi:[10.1364/AO.22.003353](https://doi.org/10.1364/AO.22.003353). (Cited on page: [185](#))
- L. Zhou, Y. Tian, R. Wang, T. Wang, T. Sun, C. Wang, and X. Yang. Mitigating effect on turbulent scintillation using non-coherent multi-beam overlapped illumination. *Optics & Laser Technology*, 97:97–105, Dec. 2017. ISSN 0030-3992. doi:[10.1016/j.optlastec.2017.06.013](https://doi.org/10.1016/j.optlastec.2017.06.013). (Cited on page: [186](#))
- V. E. Zuev and V. P. Lukin. Dynamic characteristics of optical adaptive systems. *Applied Optics*, 26(1):139–144, Jan. 1987. ISSN 2155-3165. doi:[10.1364/AO.26.000139](https://doi.org/10.1364/AO.26.000139). (Cited on page: [72](#))

Appendices

A. Mathematical Notation

A.1. Covariance and Cross-covariance Matrices

We define the covariance matrix of a vector of random variables \mathbf{X} as:

$$\Sigma_{\mathbf{X}} = \mathbb{E}\left\{(\mathbf{X} - \boldsymbol{\mu}_{\mathbf{X}})(\mathbf{X} - \boldsymbol{\mu}_{\mathbf{X}})^{\top}\right\}. \quad (\text{A.1})$$

where $\boldsymbol{\mu}_{\mathbf{X}} = \mathbb{E}\{\mathbf{X}\}$ is the vector containing the expected value of \mathbf{X} .

We define the cross-covariance matrix of two vectors of random variables \mathbf{X} and \mathbf{Y} as:

$$\Sigma_{\mathbf{XY}} = \mathbb{E}\left\{(\mathbf{X} - \boldsymbol{\mu}_{\mathbf{X}})(\mathbf{Y} - \boldsymbol{\mu}_{\mathbf{Y}})^{\top}\right\}, \quad (\text{A.2})$$

where $\boldsymbol{\mu}_{\mathbf{X}} = \mathbb{E}\{\mathbf{X}\}$ and $\boldsymbol{\mu}_{\mathbf{Y}} = \mathbb{E}\{\mathbf{Y}\}$ are the vectors that contain the expected values of \mathbf{X} and \mathbf{Y} .

We usually work with zero-mean random variables, such as turbulence. Therefore, the previous expressions can be simplified to:

$$\Sigma_{\mathbf{X}} = \mathbb{E}\{\mathbf{X}\mathbf{X}^{\top}\} \quad (\text{A.3})$$

and

$$\Sigma_{\mathbf{XY}} = \mathbb{E}\{\mathbf{X}\mathbf{Y}^{\top}\}. \quad (\text{A.4})$$

The covariance matrix is symmetric, since:

$$\Sigma_{\mathbf{X}}^{\top} = \mathbb{E}\{\mathbf{X}\mathbf{X}^{\top}\}^{\top} = \mathbb{E}\left\{(\mathbf{X}\mathbf{X}^{\top})^{\top}\right\} = \mathbb{E}\{\mathbf{X}\mathbf{X}^{\top}\} = \Sigma_{\mathbf{X}} \quad (\text{A.5})$$

The cross-covariance matrix transpose gives:

$$\Sigma_{\mathbf{XY}}^{\top} = \mathbb{E}\{\mathbf{X}\mathbf{Y}^{\top}\}^{\top} = \mathbb{E}\left\{(\mathbf{X}\mathbf{Y}^{\top})^{\top}\right\} = \mathbb{E}\{\mathbf{Y}\mathbf{X}^{\top}\} = \Sigma_{\mathbf{YX}} \quad (\text{A.6})$$

A.2. Auto-covariance Matrix

Consider a vectorial stochastic process where each entry of the vector

$$\mathbf{X} = (X_1, X_2, \dots, X_n)^{\top} \quad (\text{A.7})$$

is a stochastic process $\{X\}_t$. We define its autocovariance as the covariance of the process with itself at different past points.

$$\mathbf{\Gamma}_{\mathbf{X}}(\tau) = \mathbb{E}\left\{(\mathbf{X}_t - \boldsymbol{\mu}_t)(\mathbf{X}_{t-\tau} - \boldsymbol{\mu}_{t-\tau})^\top\right\}, \quad (\text{A.8})$$

where τ is the lag time.

In the case of zero-mean processes such as piston-removed atmospheric turbulence we can write:

$$\mathbf{\Gamma}_{\mathbf{X}}(\tau) = \mathbb{E}\{\mathbf{X}_t \mathbf{X}_{t-\tau}^\top\}, \quad (\text{A.9})$$

The negative auto-covariances can be computed with the transpose of the auto-covariance matrix:

$$\mathbf{\Gamma}_{\mathbf{X}}(\tau)^\top = \mathbb{E}\{\mathbf{X}_t \mathbf{X}_{t-\tau}^\top\}^\top = \mathbb{E}\left\{(\mathbf{X}_t \mathbf{X}_{t-\tau}^\top)^\top\right\} = \mathbb{E}\{\mathbf{X}_{t-\tau} \mathbf{X}_t^\top\}^\top = \mathbf{\Gamma}_{\mathbf{X}}(-\tau) \quad (\text{A.10})$$

B. Derivation of the Minimum Mean Square Error Estimator

Contents

B.1. Derivation of the MMSE Estimator without Measurement Noise . . .	258
B.2. Derivation of the MMSE Estimator with Measurement Noise	259

B.1. Derivation of the MMSE Estimator without Measurement Noise

We recover the definition of the minimum square error from Equation 5.4:

$$MSE = \text{Tr}(\mathbb{E}\{\tilde{\mathbf{x}}\tilde{\mathbf{x}}^\top\}) = \text{Tr}\left(\mathbb{E}\left\{(\mathbf{x} - \hat{\mathbf{x}})(\mathbf{x} - \hat{\mathbf{x}})^\top\right\}\right) \quad (\text{B.1})$$

We search the linear estimator \mathbf{R}_{MMSE} that minimizes the MSE of the estimate:

$$\hat{\mathbf{x}} = \mathbf{R}_{\text{MMSE}}\mathbf{y} \quad (\text{B.2})$$

so that

$$\min_{\mathbf{R}_{\text{MMSE}}} MSE(\mathbf{R}_{\text{MMSE}}). \quad (\text{B.3})$$

We compute the MSE associated to the estimate to then minimize it and solve for \mathbf{R}_{MMSE} , the optimal estimator:

$$MSE(\mathbf{R}_{\text{MMSE}}) = \text{Tr}\left(\mathbb{E}\left\{(\mathbf{x} - \mathbf{R}\mathbf{y})(\mathbf{x} - \mathbf{R}\mathbf{y})^\top\right\}\right) \quad (\text{B.4})$$

$$MSE(\mathbf{R}_{\text{MMSE}}) = \text{Tr}\left(\mathbb{E}\left\{\mathbf{x}\mathbf{x}^\top - \mathbf{R}\mathbf{y}\mathbf{x}^\top - \mathbf{x}\mathbf{y}^\top\mathbf{R}^\top + \mathbf{R}\mathbf{y}\mathbf{y}^\top\mathbf{R}^\top\right\}\right) \quad (\text{B.5})$$

$$MSE(\mathbf{R}_{\text{MMSE}}) = \text{Tr}\left(\Sigma_{\mathbf{x}\mathbf{x}} - \mathbf{R}\Sigma_{\mathbf{y}\mathbf{x}} - \Sigma_{\mathbf{x}\mathbf{y}}\mathbf{R}^\top + \mathbf{R}\Sigma_{\mathbf{y}\mathbf{y}}\mathbf{R}^\top\right) \quad (\text{B.6})$$

$$\frac{\partial MSE(\mathbf{R}_{\text{MMSE}})}{\partial \mathbf{R}_{\text{MMSE}}} = 0 \quad (\text{B.7})$$

B. Derivation of the Minimum Mean Square Error Estimator
B.2. Derivation of the MMSE Estimator with Measurement Noise

We remind the following properties related to the matrices \mathbf{A} , \mathbf{B} , and \mathbf{C} , the vector \mathbf{x} , and the derivatives of their trace:

1. $\partial \mathbf{A} / \partial \mathbf{B}^\top = (\partial \mathbf{A}^\top / \partial \mathbf{B})^\top$
2. $(\partial / \partial \mathbf{B}) [\text{Tr}(\mathbf{B}\mathbf{A})] = (\partial / \partial \mathbf{B}) [\text{Tr}(\mathbf{A}^\top \mathbf{B})] = (\partial / \partial \mathbf{B}) [\text{Tr}(\mathbf{A}\mathbf{B})] = \mathbf{A}^\top$
3. $(\partial / \partial \mathbf{B}) [\text{Tr}(\mathbf{B}^\top \mathbf{A})] = (\partial / \partial \mathbf{B}) [\text{Tr}(\mathbf{B}\mathbf{A}^\top)] = \mathbf{A}$
4. $(\partial / \partial \mathbf{B}) [\text{Tr}(\mathbf{A}\mathbf{B}\mathbf{C})] = \mathbf{A}^\top \mathbf{C}^\top$
5. $(\partial / \partial \mathbf{B}) [\text{Tr}(\mathbf{B}\mathbf{A}\mathbf{B}^\top)] = 2\mathbf{B}\mathbf{A}$

Compute the derivative of each term:

- $(\partial / \partial \mathbf{R}) [\text{Tr}(\boldsymbol{\Sigma}_{\mathbf{x}\mathbf{x}})] = 0$
- $(\partial / \partial \mathbf{R}) [\text{Tr}(-\boldsymbol{\Sigma}_{\mathbf{x}\mathbf{y}}\mathbf{R})] = -\boldsymbol{\Sigma}_{\mathbf{x}\mathbf{y}}$, using rule 2.
- $(\partial / \partial \mathbf{R}) [\text{Tr}(-\mathbf{R}\boldsymbol{\Sigma}_{\mathbf{y}\mathbf{x}})] = -\boldsymbol{\Sigma}_{\mathbf{y}\mathbf{x}}^\top = -\boldsymbol{\Sigma}_{\mathbf{x}\mathbf{y}}$, using rule 2.
- $(\partial / \partial \mathbf{R}) [\text{Tr}(\mathbf{R}\boldsymbol{\Sigma}_{\mathbf{y}\mathbf{y}}\mathbf{R}^\top)] = 2\mathbf{R}\boldsymbol{\Sigma}_{\mathbf{y}\mathbf{y}}$, using rule 5.

Writing all together:

$$\frac{\partial \text{MSE}(\mathbf{R})}{\partial \mathbf{R}} = 2\mathbf{R}\boldsymbol{\Sigma}_{\mathbf{y}\mathbf{y}} - 2\boldsymbol{\Sigma}_{\mathbf{x}\mathbf{y}} = 0 \quad (\text{B.8})$$

Solving for \mathbf{R} :

$$\boxed{\mathbf{R} = \boldsymbol{\Sigma}_{\mathbf{x}\mathbf{y}} (\boldsymbol{\Sigma}_{\mathbf{y}\mathbf{y}})^{-1}} \quad (\text{B.9})$$

B.2. Derivation of the MMSE Estimator with Measurement Noise

We can extend the method to the case of measurement noise in the measurement vector, \mathbf{y} , used for the estimation. The measurement equation is:

$$\mathbf{y} = \mathbf{D}\mathbf{x} + \mathbf{w} \quad (\text{B.10})$$

where \mathbf{D} is the linear measurement model and \mathbf{w} is a Gaussian white noise vector with zero mean and covariance matrix \mathbf{C}_w . In this case, the estimate will be:

$$\hat{\mathbf{x}} = \mathbf{R}\mathbf{y} = \mathbf{R}(\mathbf{D}\mathbf{x} + \mathbf{w}) \quad (\text{B.11})$$

This gives an estimation error:

B. Derivation of the Minimum Mean Square Error Estimator
B.2. Derivation of the MMSE Estimator with Measurement Noise

$$\tilde{\mathbf{x}} = \mathbf{x} - \mathbf{R}(\mathbf{D}\mathbf{x} + \mathbf{w}) \quad (\text{B.12})$$

Computing the covariance matrix of the estimation error:

$$\mathbb{E}\{\tilde{\mathbf{x}}\tilde{\mathbf{x}}^\top\} = \mathbb{E}\left\{(\mathbf{x} - \mathbf{R}\mathbf{D}\mathbf{x} - \mathbf{R}\mathbf{w})(\mathbf{x} - \mathbf{R}\mathbf{D}\mathbf{x} - \mathbf{R}\mathbf{w})^\top\right\} \quad (\text{B.13})$$

$$= \mathbb{E}\left\{(\mathbf{x} - \mathbf{R}\mathbf{D}\mathbf{x} - \mathbf{R}\mathbf{w})(\mathbf{x}^\top - \mathbf{x}^\top\mathbf{D}^\top\mathbf{R}^\top - \mathbf{w}^\top\mathbf{R}^\top)\right\} \quad (\text{B.14})$$

Expanding the previous expression:

$$\begin{aligned} \mathbb{E}\{\tilde{\mathbf{x}}\tilde{\mathbf{x}}^\top\} &= \mathbb{E}\{\mathbf{x}\mathbf{x}^\top\} - \mathbb{E}\{\mathbf{x}\mathbf{x}^\top\}\mathbf{D}^\top\mathbf{R}^\top - \mathbb{E}\{\mathbf{x}\mathbf{w}^\top\}\mathbf{R}^\top \\ &\quad - \mathbf{R}\mathbf{D}\mathbb{E}\{\mathbf{x}\mathbf{x}^\top\} + \mathbf{R}\mathbf{D}\mathbb{E}\{\mathbf{x}\mathbf{x}^\top\}\mathbf{D}^\top\mathbf{R}^\top + \mathbf{R}\mathbf{D}\mathbb{E}\{\mathbf{x}\mathbf{w}^\top\}\mathbf{R}^\top \\ &\quad - \mathbf{R}\mathbb{E}\{\mathbf{w}\mathbf{x}^\top\} + \mathbf{R}\mathbb{E}\{\mathbf{w}\mathbf{x}^\top\}\mathbf{D}^\top\mathbf{R}^\top + \mathbf{R}\mathbb{E}\{\mathbf{w}\mathbf{w}^\top\}\mathbf{R}^\top \end{aligned} \quad (\text{B.15})$$

Eliminating the cross-covariances between \mathbf{x} and \mathbf{w} , since they are statistically independent:

$$\begin{aligned} \mathbb{E}\{\tilde{\mathbf{x}}\tilde{\mathbf{x}}^\top\} &= \mathbb{E}\{\mathbf{x}\mathbf{x}^\top\} - \mathbb{E}\{\mathbf{x}\mathbf{x}^\top\}\mathbf{D}^\top\mathbf{R}^\top \\ &\quad - \mathbf{R}\mathbf{D}\mathbb{E}\{\mathbf{x}\mathbf{x}^\top\} + \mathbf{R}\mathbf{D}\mathbb{E}\{\mathbf{x}\mathbf{x}^\top\}\mathbf{D}^\top\mathbf{R}^\top \\ &\quad + \mathbf{R}\mathbb{E}\{\mathbf{w}\mathbf{w}^\top\}\mathbf{R}^\top \end{aligned} \quad (\text{B.16})$$

We now minimize each of the terms of the sum:

- $(\partial/\partial\mathbf{R}) [\text{Tr}(\mathbb{E}\{\mathbf{x}\mathbf{x}^\top\})] = 0$, since it does not depend on \mathbf{R} .
- $(\partial/\partial\mathbf{R}) [\text{Tr}(-\mathbb{E}\{\mathbf{x}\mathbf{x}^\top\}\mathbf{D}^\top\mathbf{R}^\top)] = -\mathbb{E}\{\mathbf{x}\mathbf{x}^\top\}\mathbf{D}^\top$, using rule 2.
- $(\partial/\partial\mathbf{R}) [\text{Tr}(-\mathbf{R}\mathbf{D}\mathbb{E}\{\mathbf{x}\mathbf{x}^\top\})] = -\mathbb{E}\{\mathbf{x}\mathbf{x}^\top\}\mathbf{D}^\top$, using rule 2.
- $(\partial/\partial\mathbf{R}) [\text{Tr}(\mathbf{R}\mathbf{D}\mathbb{E}\{\mathbf{x}\mathbf{x}^\top\}\mathbf{D}^\top\mathbf{R}^\top)] = 2\mathbf{R}\mathbf{D}\mathbb{E}\{\mathbf{x}\mathbf{x}^\top\}\mathbf{D}^\top$, using rule 5.
- $(\partial/\partial\mathbf{R}) [\text{Tr}(\mathbf{R}\mathbb{E}\{\mathbf{w}\mathbf{w}^\top\}\mathbf{R}^\top)] = 2\mathbf{R}\mathbb{E}\{\mathbf{w}\mathbf{w}^\top\}$, using rule 5.

Writing all together:

$$\frac{\partial \text{MSE}(\mathbf{R})}{\partial \mathbf{R}} = 2\mathbf{R}\mathbf{D}\mathbb{E}\{\mathbf{x}\mathbf{x}^\top\}\mathbf{D}^\top + 2\mathbf{R}\mathbb{E}\{\mathbf{w}\mathbf{w}^\top\} - 2\mathbb{E}\{\mathbf{x}\mathbf{x}^\top\}\mathbf{D}^\top = 0 \quad (\text{B.17})$$

Solving for \mathbf{R} :

$$\boxed{\mathbf{R}_{\text{MMSE}} = \mathbb{E}\{\mathbf{x}\mathbf{x}^\top\}\mathbf{D}^\top (\mathbf{D}\mathbb{E}\{\mathbf{x}\mathbf{x}^\top\}\mathbf{D}^\top + \mathbb{E}\{\mathbf{w}\mathbf{w}^\top\})^{-1}} \quad (\text{B.18})$$

B. Derivation of the Minimum Mean Square Error Estimator
B.2. Derivation of the MMSE Estimator with Measurement Noise

Remark

The *minimum mean square error (MMSE)* estimator is here equivalent to the *maximum a posteriori (MAP)* estimator since for Gaussian random variables the mean and the mode are equivalent. [Quirós-Pacheco et al. \(2010\)](#) extended this analysis for the study of aliasing propagation in the reconstruction of *Shack-Hartmann (SH)* measurements.

The estimation error of the estimator presented in Equation [B.18](#) can be computed by substituting into Equation [B.16](#) and it is equal to:

$$\mathbb{E}\left\{(\mathbf{x} - \hat{\mathbf{x}}_{\text{MMSE}})(\mathbf{x} - \hat{\mathbf{x}}_{\text{MMSE}})^\top\right\} = (\mathbf{D}^\top \boldsymbol{\Sigma}_w^{-1} \mathbf{D} + \boldsymbol{\Sigma}_x^{-1})^{-1} \quad (\text{B.19})$$

C. Frequency Coverage of Zernike Polynomials vs. Zonal Basis

We want to compare the number of variables that are necessary for both bases to represent the same frequency coverage. We start by defining the frequency coverage of the Shack-Hartmann wavefront sensor. The maximum spatial sampling frequency is given by:

$$\kappa_{\text{SH}} = \frac{1}{2d_{\text{sp}}}, \quad (\text{C.1})$$

where d_{sp} is the subpupil pitch. The subpupil pitch is computed in terms of the number of subpupils N_{sp} and the telescope diameter D as:

$$d_{\text{sp}} = \frac{D}{N_{\text{sp}}}. \quad (\text{C.2})$$

The number of phase points that can be computed per subpupil is 4, assuming Fried geometry, the number of unique phase points for a grid of $N_{\text{sp}} \times N_{\text{sp}}$ subpupils is:

$$N_{\text{SH}} = (N_{\text{sp}} + 1)^2, \quad (\text{C.3})$$

As a result, the spatial sampling frequency as a function of the number of subpupils is:

$$\kappa_{\text{SH}} = \frac{N_{\text{sp}}}{2D}. \quad (\text{C.4})$$

which is also the number of variables related to the number of subpupils used. Note, this does not count for not illuminated subpupils due to the telescope aperture shape and its obscuration.

For the Zernike polynomials, their equivalent spatial frequency is defined in terms of their radial order n :

$$\kappa_{\text{Z}} \approx 0.37 \frac{(n + 1)}{D}. \quad (\text{C.5})$$

For a given maximum radial order n_{max} in a Zernike polynomial basis, the Noll index $j_{\text{Noll,max}}$ of the last polynomial is:

C. Frequency Coverage of Zernike Polynomials vs. Zonal Basis

$$j_{\text{Noll,max}} = \frac{n_{\text{max}}(n_{\text{max}} + 3)}{2} + 1. \quad (\text{C.6})$$

Therefore, the number of modes (piston mode removed) is given by:

$$N_Z = \frac{n_{\text{max}}(n_{\text{max}} + 3)}{2}, \quad (\text{C.7})$$

which is also the number of variables related to the maximum radial order used.

We search for the number of Zernike polynomials equivalent to a given number of Shack-Hartmann subpupils. For this we set $\kappa_Z = \kappa_{\text{SH}}$ and solve for n :

$$n \approx \frac{N_{\text{sp}}/2}{0.37} - 1. \quad (\text{C.8})$$

Finally, we consider for our comparison the case of a *SH* wavefront sensor with N_{sp} subpupils. Normally, the sampling of the sensor allows reconstruction of four points per subpupil, but an oversampling of the reconstruction modal basis is possible if a regularized reconstructor such as the *MAP* is used. In this case, it is possible to reconstruct phase points equivalent to the stencil given by a virtual subpupil grid of $N_{\text{oversamp}} \cdot N_{\text{sp}}$, so the number of oversampled phase points can be computed by substituting this "number of virtual subpupils" in Equation C.3. Oversampling in the Zernike modal basis allows for more flexibility since it can be done for any additional Zernike polynomials desired.

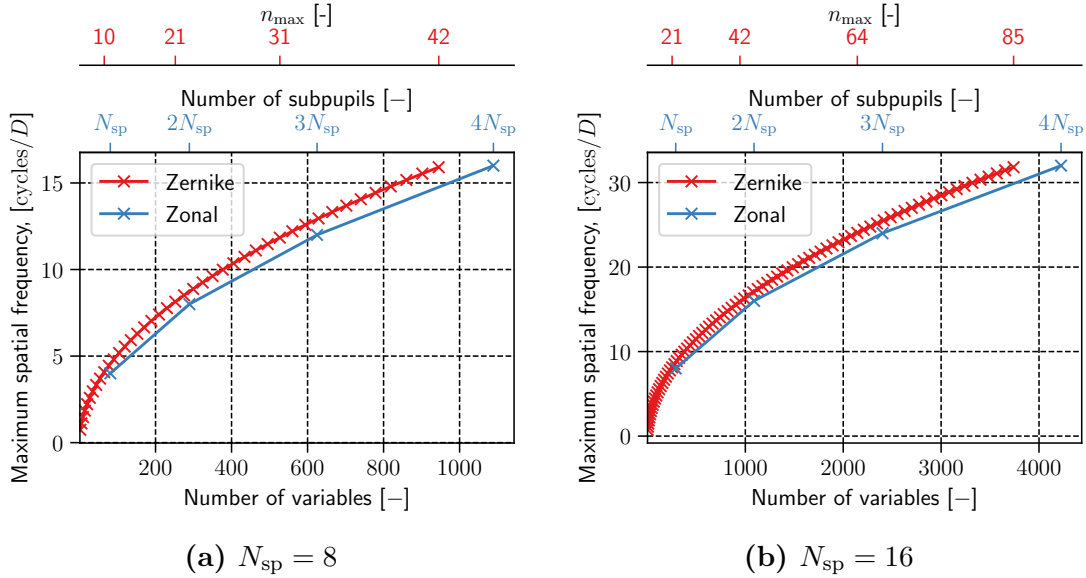


Figure C.1.: Comparison of the spatial frequency coverage vs. the number of required variables for a zonal and a Zernike polynomial basis. The zonal basis is oversampled as a multiple of the number of subpupils in the system, N_{sp} , or an equivalent number of radial orders, n_{max} .

C. Frequency Coverage of Zernike Polynomials vs. Zonal Basis

Conclusions:

- Both zonal and Zernike basis require a similar number of variables for covering the same range of spatial frequencies.
- The modal representation provides a finer control of the number of variables (all crosses in the plot are one possible option). This allows for example an intermediate number of variables w.r.t. to the zonal options.

D. Turbulence temporal prediction performance assessment for adaptive optics: application to LEO satellite observation and communication links

Turbulence temporal prediction performance assessment for adaptive optics: application to LEO satellite observation and communication links.

JEAN-MARC CONAN^{1*}, CYRIL PETIT¹, PABLO ROBLES^{1,2}, PERRINE LOGNONÉ^{1,3}

¹ONERA, DOTA, Paris Saclay University, 92322 Châtillon, FRANCE

²Aix-Marseille Univ., CNRS, CNES, LAM, Marseille, France, 13013

³Télécom Paris, 91120 Palaiseau, FRANCE

*conan@onera.fr

Abstract: Adaptive optics temporal error is a key contributor to the overall system error budget. In the framework of adaptive optics design, this term sets constraints on the choice of the loop sampling frequency. This is of particular concern for applications aiming at moving targets which are more stringent in terms of temporal error due to the strong apparent winds induced by the target motion. A question then arises: can we use turbulence temporal prediction to alleviate the temporal error? We present here a simple theoretical formalism that allows estimating the standard temporal error, meaning the error obtained without temporal prediction, as well as the error reduction brought by optimal linear prediction based on turbulence priors. This formalism allows quantifying the temporal error ahead of the development of dedicated control laws, and the analysis brings a better insight on the prediction efficiency. These developments are then illustrated on two scenarios involving scrolling satellites: the observation of a LEO satellite and LEO to ground optical links.

© 2023 Optical Society of America under the terms of the [OSA Open Access Publishing Agreement](#)

1. Introduction

Adaptive optics is now a well spread technique for applications that require a real time mitigation of turbulence. Among these applications one can cite: ground based astronomy, space surveillance, free space optical links for telecom, quantum communication and frequency dissemination . Establishing models of the various contributors that limit the performance, that is the so-called adaptive optics error budget, is a key aspect for the design of such systems . The temporal error is the limitation induced by the temporal evolution of the turbulent phase during the loop delay, that is the time difference between the sensing of the perturbation and its correction. The temporal error is often an important contributor to the overall error budget. It even becomes a critical issue in conditions involving a fast evolution of the turbulent phase, such as in the case of satellite tracking scenarios that are associated to strong apparent winds .

The characterization of the turbulence temporal dynamics and of the related temporal error, in the frozen flow hypothesis, goes back to late 70s with the pioneering work of Greenwood (Greenwood-1977) later revisited in [Fried-1990] and to the progressive definition of the turbulence coherence time τ_0 (RoddierGilliLund-1982, Fried-1990). These seminal works however do not consider a correction on a finite number of modes defined on a finite aperture..

There have been parallel developments based on modal description (see for instance (Hogge and Butts, 1976), (Roddier et al., 1993), (Conan et al., 1995)). These references clearly show that, in the frozen flow hypothesis, the temporal statistics, correlation or power spectral density (PSD), can directly be inferred from the spatial statistics (Kolmogorov or Von Kármán spectrum) and spatial correlations described in (Valley and Wandzura, 1979). (Roddier et al., 1993) underlines

the similarity between temporal and angular correlations, the latter corresponding to the so-called anisoplanatism effect (Valley, 1980) (Chassat, 1989) (+ thèse Chassat en 1992). Indeed, both temporal and angular correlations are derived from the same basic equations describing the spatial correlations in a given turbulent layer. These works have then been developed and extended based on the three above mentioned points of view: spatial aspects (Takato and Yamaguchi, 1995), temporal aspects (Whiteley et al., 1998b) and (Pachter and Oppenheimer, 2002) that accounts for the motion of both aperture and source, or anisoplanatism aspects (Whiteley et al., 1998c). Beyond the statistical characterization, the aim is to use correlations to estimate AO error terms and eventually to reduce these error terms based on the use of such prior information. (Roddier et al., 1993) and (Conan et al., 1995) estimate the temporal error in the presence of loop delay with a standard control modeled respectively by a mere finite difference in time and an approximation of the rejection transfer function of an integrator. Among the first publications suggesting exploiting priors to improve correction we can cite (Olivier and Gavel, 1994) that analyses the capacity to reduce tilt anisoplanatism, and (Ellerbroek, 1994) that presents optimal control for wide field AO. We now restrict our analysis to publications that have exploited these original ideas through a modal MMSE formalism. Several publications of this vein have developed and applied such a modal MMSE formalism, in the absence of temporal considerations, in the context of optimal multi-mode AO correction in the presence of anisoplanatism (Whiteley et al., 1998c), for TT estimation issues with NGS and LGS (Whiteley et al., 1998d), for wide field AO (Fusco et al., 2001) and later (Neichel et al., 2009) (Vidal et al., 2010). We stress the fact that we have recently presented an extension of the modal MMSE approach (based on phase and scintillation measurements) that allows a strong reduction of the impact of point ahead angle anisoplanatism on ground-satellite uplinks (Lognoné et al. 2023). The same MMSE approach has also been applied to temporal prediction so as to reduce tilt temporal error in the presence of loop delay (Whiteley et al., 1998a) (Whiteley, 1999), these publications however consider a prediction based only on the last available measurement. One finds a similar MMSE approach in the performance analysis of complex tomographic AO configurations (Ono et al., 2016) including both priors on anisoplanatism as well as temporal effects, this time with an account of several past measurements and not only of the last one. This paper also inherits from (Correia et al., 2014) and (Correia et al., 2015) that address tomographic AO from a more general control perspective based on LQG approaches.

Our article focuses on multi-mode single conjugate AO and more precisely aims at providing a simple analytical formalism able to estimate the temporal error without and with prediction. Prediction is based on the MMSE formalism of the previously cited articles and includes the use of multiple past measurements. Following previous references the system is simplified: no account of a specific wavefront sensor device, 2 frame delay loop (although formalism could be easily extended to other values), standard control modeled by finite difference in time, priors assumed to be known with no error, etc... Given the approximations made, our formalism aims at giving a lower bound of the temporal error. It also provides insights on the gains brought by temporal prediction. These are key elements to guide the system and control developments.

The formalism is then applied to two LEO satellite tracking scenarios involving a ground telescope equipped with AO: optical telecommunication on downlink between the satellite and the ground, and observation of the satellite from ground. These cases have the interest to represent two major applications with active developments and important strategic stakes. Besides, the question of temporal prediction is very critical in these cases due to the fast slewrate with LEO satellites. They are therefore perfect candidates to illustrate the assets of the present analysis.

The outline is as follows: Sect. 2 describes the theoretical formalism used to assess the temporal error and gives a first illustration on a tutorial scalar case; Sect. 3 defines the telecom and satellite observation scenarios retained; Sect. 4 presents the prediction error results with static and MMSE prediction and Sect. 5 analyses the results obtained.

2. Turbulence temporal prediction formalism

This section describes the theoretical formalism and the associated hypotheses. Section 2.1 gives the problem statement and defines the notion of temporal prediction. Section 2.2 introduces the notion of static and MMSE prediction while the expression of the associated prediction errors are given in Sect. 2.3. So as to obtain straightaway a good insight on the formalism and its potentiality, it is applied in Sect. 2.4 to a conceptual scalar case tutorial. Section 2.5 finally describes the vectorial model used to describe the turbulent phase and explains how the statistical priors can be obtained.

2.1. Phase prediction: problem statement

We first start with the problem statement as well as the description of the main hypothesis. The main physical quantity at stake here is the turbulent phase in the pupil plane. A discrete-time description is used as in most AO modeling publications [JMC][cite few articles]. The pupil plane turbulent phase at time step k , denoted ϕ_k , is described here by a vector of N components corresponding for instance to the coefficients of a modal expansion. The detailed physical description of the turbulent phase is the object of Sect. 2.5. The sampling time is denoted t_{samp} .

This article aims at giving a quantitative assessment of the ability to predict the turbulent phase ahead of time. Although the formalism could be easily extended, we particularize to the question of a 2 step ahead prediction, representative of a typical 2 frame AO loop delay. The question is therefore the prediction of ϕ_{k+2} knowing current and past phases $\{\phi_k, \phi_{k-1}, \phi_{k-2} \dots\}$, and the evaluation of the associated prediction error. This question may seem rather conceptual, however, as already explained in the introduction, this analysis is analogous to the evaluation of the temporal error of a 2 frame delay AO system in the ideal case of a direct measurement of the phase (no explicit wavefront sensor, no noise), of a direct correction of the phase (no explicit DM geometry) and without explicit feedback loop and control. We indeed seek for an estimation of this ultimate temporal error so as to obtain a lower bound of the temporal error achievable with practical control laws on practical systems, and to provide tools allowing a better understanding of the temporal prediction efficiency for specific scenarios.

2.2. Static and optimal prediction

Again the aim is to assess the performance when predicting ϕ_{k+2} from past phase data that are assumed to be available. Two prediction estimators are considered hereafter: a plain static prediction and an optimal prediction based on physical priors.

We call static prediction the estimation given simply by the last available data ϕ_k , hence with the implicit assumption that the turbulent phase is static (no temporal evolution). The estimate therefore simply reads:

$$\hat{\phi}_{k+2}^{static} = R_{static} y_k^{data} = \phi_k. \quad (1)$$

which is a particular linear estimation with $R_{static} = Id$ (identity) and $y_k^{data} = \phi_k$. We choose the wording "static prediction" since this indeed can be seen as a prediction with a simplistic static prior, we admit, though, that it could also be referred to as "no prediction".

The optimal prediction is the prediction that minimizes the variance of the prediction error defined as the difference between the true value and its estimate: $\tilde{\phi}_{k+2} = \phi_{k+2} - \hat{\phi}_{k+2}$. It therefore minimizes the quadratic criterion $E(\|\tilde{\phi}_{k+2}\|^2)$, where $E()$ denotes the mathematical expectation. This optimal estimation is given by the so-called MMSE estimator. In the following we consider an MMSE estimation based on a finite number K of known current and past phase steps. The vector of K known data then reads:

$$y_k^{data} = (\phi_k, \phi_{k-1}, \phi_{k-2}, \dots, \phi_{k-(K-1)})^T. \quad (2)$$

Influence of the value chosen for K will be investigated in Sect. 4.2. Assuming joint zero-mean Gaussian statistics for the variable to be estimated ϕ_{k+2} and the data vector y_k^{data} leads to an MMSE estimate that is linear in the data in the form:

$$\hat{\phi}_{k+2}^{mmse} = R_{mmse} y_k^{data} = \Gamma (C_{data})^{-1} y_k^{data} , \quad (3)$$

where $\Gamma = E \left(\phi_{k+2} (y_k^{data})^T \right)$ and $C_{data} = E \left(y_k^{data} (y_k^{data})^T \right)$. The MMSE prediction matrix R_{mmse} therefore builds on supposedly known statistical priors: namely the covariance matrices of ϕ_{k+2} with y_k^{data} and y_k^{data} with y_k^{data} respectively. Note that this MMSE formalism is identical to the original temporal prediction approach proposed in (Whiteley1998a, Whiteley1999). The equations are also identical even though the data vector is extended here to include K time steps instead of a single one, a feature that is shown to be essential to obtain efficient temporal prediction (see Sect. 2.4 and 4).

We also stress that the MMSE estimation of Eq. 3 does not take a recursive form, an asset that would be intrinsic of LQG control that can be seen as a natural extension of MMSE prediction in the context of AO real time control. The present MMSE expression is however perfectly satisfactory for the prediction efficiency analysis performed in the present paper, in which we recall that control issues are left aside.

2.3. Prediction error

As introduced in the previous paragraph, the prediction error $\tilde{\phi}_{k+2}$ is by definition the difference between the true value and its estimate: $\tilde{\phi}_{k+2} = \phi_{k+2} - \hat{\phi}_{k+2}$. It is statistically characterized by the prediction error covariance matrix $C_{err} = E \left(\tilde{\phi}_{k+2} (\tilde{\phi}_{k+2})^T \right)$ from which one can deduce the prediction error variance for each phase component (diagonal elements of C_{err}) or the overall prediction error variance (trace of C_{err} that is the sum of its diagonal elements).

Before considering the specific static and MMSE prediction estimators, we consider the general case of a linear estimator of the form $\tilde{\phi}_{k+2} = R y_k^{data}$. It is straightforward to show that general form of the prediction error covariance matrix for estimators of this class reads:

$$C_{err} = C_\phi - R \Gamma^T - \Gamma R^T + R C_{data} R^T . \quad (4)$$

From Eqs. 4 and 1 one can then easily derive the prediction covariance matrix for the static prediction:

$$C_{err}^{static} = 2C_\phi - \Gamma - \Gamma^T . \quad (5)$$

While for the optimal prediction the prediction, when exploiting its specific form given in Eq. 3, the error covariance matrix can be simplified in the form:

$$C_{err}^{mmse} = C_\phi - R_{mmse} \Gamma^T . \quad (6)$$

The questions raised here are the following: can the prediction error be significantly reduced by applying an optimal prediction instead of a static one? If so, what is the influence of the number of time steps K in the data vector? We show, in the next section, through a simple scalar tutorial, that the answer to these questions depends on the signal temporal dynamics. We then precise in Section 2.5 how the temporal dynamics of the turbulent phase can be deduced from physical models.

2.4. Scalar tutorial

Before addressing the issue of turbulence prediction, we present a brief scalar case tutorial for a better insight into the formalism developed here. Besides, although they may seem naive, these

scalar case results will be very valuable for the interpretation of the turbulent prediction results that are discussed in Sect. 5.

The prediction is then applied to a simple scalar signal with temporal dynamics described by a second order autoregressive model (AR2). We express the dynamical AR2 model following the harmonic form described in (CyrilPetitOptExpr2008):

$$\phi_k = a_1\phi_{k-1} + a_2\phi_{k-2} + v_k \quad (7)$$

$$a_1 = 2 \exp(-2\pi\xi f_0/f_{samp}) \cos\left(2\pi\sqrt{1-\xi^2}f_0/f_{samp}\right) \quad (8)$$

$$a_2 = -\exp(-4\pi\xi f_0/f_{samp}), \quad (9)$$

where v is a white zero mean Gaussian noise of variance σ_v^2 , ξ is the damping coefficient, f_0 is the natural frequency and $f_{samp} = 1/t_{samp}$ is the sampling frequency. The interest of the harmonic form is to introduce the notion of natural frequency, and in turn of relative natural frequency f_0/f_{samp} , a parameter that is shown hereafter to play a key role. Besides, as we will see in Sect. 5, this notion will have its counterpart for turbulence prediction.

Such an AR2 process is characterized by three parameters: either $\{\sigma_v^2, a_1, a_2\}$ or equivalently by $\{\sigma_v^2, \xi, f_0\}$. For a given set of such parameters it is straightforward to compute the signal variance $\sigma_\phi^2 = E(\phi_k^2)$ as well as its correlation function $\gamma(q) = E(\phi_k\phi_{k+q})$. The correlation function is for instance given by:

$$\gamma(0) = \sigma_\phi^2; \quad (10)$$

$$\gamma(1) = \frac{a_1}{1-a_2}\sigma_\phi^2; \quad (11)$$

$$\gamma(q) = a_1\gamma(q-1) + a_2\gamma(q-2) \text{ for } q \geq 2. \quad (12)$$

These temporal correlations are the only ingredients needed in Eqs. 3, 5 and 6 to obtain the prediction error covariance matrices that are simply here a scalar error variance. For instance the static prediction error variance simply reads $C_{err}^{static} = 2(\sigma_\phi^2 - \gamma(2))$. Its is worth underlying that the static prediction error only depends on the signal variance and the 2 step correlation, hence only two parameters while the AR2 process is characterized by three. In the meantime the MMSE prediction, that can use several time steps of data, can be shown to exploit more broadly the signal temporal dynamics. Conversely, we expect that MMSE performance shall depend intimately on this dynamics.

Based on this latter observation, we construct the following test cases: we consider a well damped system with $\xi = 0.8$, and we compute the MMSE prediction error variance (for different number of time steps K in the data vector) as a function of the relative natural frequency f_0/f_{samp} , while adjusting σ_ϕ^2 so as to maintain the static error variance constant to an arbitrary value, set to 0.01. The results are summarized in Table 1.

f_0/f_{samp}	0.001	0.004	0.016	0.064	
Signal variance σ_ϕ^2	63.6	4.04	0.269	0.0221	
$C_{err}^{static}/C_{err}^{mmse}$ for $K = 1$	1.00004	1.00062	1.00939	1.12756	max/min=1.13
$C_{err}^{static}/C_{err}^{mmse}$ for $K \geq 2$	40.3	10.5	3.06	1.41	max/min=28.5

Table 1. Signal variance σ_ϕ^2 and MMSE prediction gain $C_{err}^{static}/C_{err}^{mmse}$ for various relative natural frequencies f_0/f_{samp} while static prediction error is kept constant to an arbitrary value set to 0.01.

Firstly, we observe that MMSE prediction with a single time step data ($K = 1$) gives poor gains. Secondly, the optimal gain is reached with $K = 2$ time steps: using more time steps does not provide any additional benefit. It can indeed be shown theoretically that for any autoregressive signal of order n the optimal prediction is reached for $K = n$ (H. Lütkepohl, New introduction to multiple time series analysis. Berlin: New York: Springer, 2005). This means that, for an AR2 signal, MMSE prediction based on $K = 2$ time step data captures, and exploits, the whole temporal dynamics. In this particular case, it can even be shown that the optimal prediction comes down to iterating the deterministic part of the AR expression, iterating here twice for the two step ahead prediction.

Besides, the results obtained on the large variety of scenarios that we have, somewhat artificially, constructed are in the end rather intuitive. On the one hand, a signal that is strong (large signal variance) and slow (small relative natural frequency) can logically lead to the same static prediction error as a weaker but faster signal. On the second hand, these scenarios are shown to lead to very diverse performance in terms of optimal prediction (MMSE with $K = 2$): the prediction gain spans values between 1.41 and more than 40. Although this result may seem astonishing at first sight, it appears, as might have been suspected, that slow signals, with respect to sampling time, that is having a small relative natural frequency, and hence strong temporal correlations, can be much more efficiently predicted few steps ahead than fast signals. At the limit, a white noise is "infinitely fast" and has no temporal correlation, hence a very poor prediction that merely comes down to the signal mean value.

An intermediate conclusion is therefore that the formalism presented here easily allows to estimate the gain brought by optimal prediction. Obviously the predictability of a signal is inherently related to its temporal dynamics. The objective of Sect. 2.5 is to describe the priors available to describe such dynamics for the turbulent phase, while the rest of the paper exploits these priors to assess prediction performance for observation of, as well as for ground-space optical links with, slewing LEO satellites.

2.5. Turbulent phase description and priors

As mentioned in Sect. 2.1, the turbulent phase in the ground-station pupil at time step k , is described by a vector of N components: $\phi_k = (\phi_{k;1}, \phi_{k;2}, \dots, \phi_{k;N})^T$. Moreover, we particularize here to the case where these components are the coefficients of a modal expansion on the Zernike basis (Noll-1976). We recall that this resultant phase observed in the reception aperture is the sum of individual contributions coming from turbulent layers in the volume along the line of sight. Taking the usual description in statistically independent discrete individual layers one can write in the case of L layers and in the geometrical optics approximation :

$$\phi_k = \sum_{l=1}^L \varphi_{k,l} \quad (13)$$

where $\varphi_{k,l}$ is the phase at step k and in the layer l in the form of a vector of N Zernike coefficients defined on a support corresponding to the foot-print given by the on-axis projection onto the layer l of the ground aperture support. Based on this model, the computation of the temporal correlation matrices of the type $E(\phi_k (\phi_{k+q})^T)$ can be deduced from individual layer contributions of the type $E(\varphi_k (\varphi_{k+q})^T)$ which in turn correspond to the correlation between the Zernike coefficients in an on-axis aperture foot-print and those obtained in a foot-print shifted by $q t_{samp} \mathbf{V}_l$ where \mathbf{V}_l is the wind vector at layer l (see Fig. 1).

The wind vector is either the natural wind at layer l or the composition of the natural wind plus an apparent wind induced by the satellite tracking. The apparent wind depends on the distance z_l between the ground aperture and the layer l . Its norm is simply given the product of the slewrate $\dot{\theta}$ (in rad/s) by z_l .

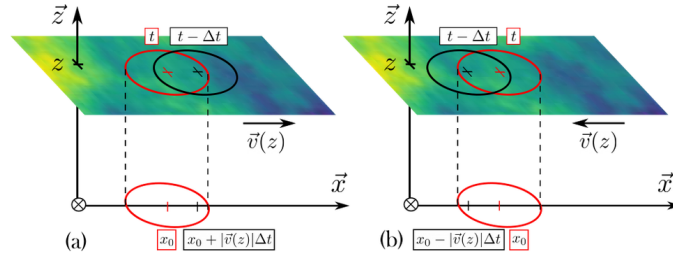


Fig. 1. Principle sketch describing the geometry used to express the temporal priors.
 [Figure To Be Updated for better consistency with notations in the paragraph]

The temporal priors described here are similar to those used in the seminal work by Whiteley, although these articles were only focused on tip-tilt prediction without using higher orders.

Incidentally we see from the above considerations and from the general MMSE formalism described in Sect. 2.2 and 2.3 that the prediction estimator and associated error can be expressed solely from the statistics of the resultant phase in the telescope aperture that can be easily described on the Zernike basis.

3. Application scenarios: description and rationale

In this section, we describe the application scenarios. The rationale is to define two scenarios involving satellite scrolling with some diversity, as well as some commonalities, so as to compare temporal errors and gains brought by MMSE prediction. We now motivate the choice of the observation scenarios and discuss the associated turbulence conditions.

Two applications of strong interest for the community are, on one hand, LEO-to-ground optical telecommunications with typical sub-meter telescopes and, on the other hand, LEO satellite observation from earth, using meter size telescopes. Besides, since turbulent phase temporal dynamics is driven by wind speed but also by the telescope diameter (Roddier-1993, Conan-1995), these two configurations seem favorable to explore temporal error and prediction aspects in diverse circumstances.

Of course, operational and turbulence conditions are specific to each of the two applications. Satellite observation is mostly performed at night, in the visible, using typically sunlight back-scattered by the target, generally with ground telescopes located in astronomical sites. While optical telecommunication is performed in the near infrared and has to face stronger turbulence conditions due to night and day operation, in locations not necessarily being astronomical sites.

More precisely, we consider, on the one hand, a LEO satellite observation system, with a 1.5 m telescope, operating in nighttime in a good site. Imaging is performed at 850 nm, based on back-scattered sunlight. The Onera ODISSEE system is considered as a baseline for this system. On the second hand, we consider a LEO-to-ground optical telecommunication system, with a 0.4 m telescope, working in daytime, at 1550 nm. The LISA AO system can be considered as a typical case.

We choose similar satellite parameters: a LEO satellite evolving at a 700 km altitude, with a culmination at an elevation of 60°. Observations are however considered at two different elevations: the satellite observation is performed at an elevation of 40°, as usually one shall await favorable conditions such as reduced distance to the target (for higher resolution and return flux) and improved turbulence conditions, while the telecommunication case is considered at an elevation of 20° elevation. This lower value of the latter elevation is motivated by the need to extend the time range of communication, considering in the meantime that flux is less an issue in this framework.

Again, we do not claim that the two selected scenarios are representative of all possible systems and observation conditions. They are however inspired from actual configurations and they will be shown to provide a good illustration of the diversity in terms of temporal predictability.

Let us first recall the definition of the integrated parameters used here to characterize the turbulence conditions: the Fried parameter r_0 , which characterizes the overall turbulence strength integrated along the line of sight, the coherence time τ_0 , which characterizes the temporal evolution of the wavefront, the isoplanatic angle θ_0 , which characterizes the angular evolution of the wavefront.

Considering the long distance to the satellite one can take the expressions of these quantities for a descending plane wave propagation. The Fried parameter (Fried-1966) then reads:

$$r_0 = \left[0.423 \left(\frac{2\pi}{\lambda} \right)^2 \int_0^{z_{max}} C_n^2(z) dz \right]^{-3/5}, \quad (14)$$

where $C_n^2(z)$ is the refractive index structure constant that characterizes the distribution of the turbulence strength along the line of sight, z being the distance to the ground aperture, and z_{max} the distance beyond which turbulence is assumed to be negligible. The coherence time (RoddiGilliLund-1982,Fried-1990) is given by:

$$\tau_0 = \left[2.91 \left(\frac{2\pi}{\lambda} \right)^2 \int_0^{z_{max}} V(z)^{5/3} C_n^2(z) dz \right]^{-3/5}, \quad (15)$$

where $V(z)$ is the norm of the wind speed projected in a plane perpendicular to the line of sight. The coherence time can also be expressed (RoddiGilliLund-1982) as $\tau_0 = 0.314 r_0 / \bar{V}$ where \bar{V} is the mean wind speed defined as follows:

$$\bar{V} = \left[\frac{\int_0^{z_{max}} V(z)^{5/3} C_n^2(z) dz}{\int_0^{z_{max}} C_n^2(z) dz} \right]^{3/5}, \quad (16)$$

While the isoplanatic angle (Fried-1982) is given by:

$$\theta_0 = \left[2.91 \left(\frac{2\pi}{\lambda} \right)^2 \int_0^{z_{max}} z^{5/3} C_n^2(z) dz \right]^{-3/5}. \quad (17)$$

We first consider hereafter the limiting case referred to as "slew rate only" that corresponds to a wind equal to the apparent wind induced by the satellite tracking, in the absence of natural wind contributions. In this limiting case $V(z) = \dot{\theta}z$ where $\dot{\theta}$ is the slewrate (in rad/s) that corresponds to the satellite apparent motion in the sky. Consequently it is obvious from the above equations that the coherence time, in this particular case, reads: $\tau_0 = \theta_0 / \dot{\theta}$. Hence a particular interest for θ_0 for the satellite tracking scenarios even without any considerations of anisoplanatism effects. This limiting case allows us to compare the two scenarios with temporal dynamics exclusively induced by the satellite tracking. The influence of an additional natural wind is considered in a second step. For the sake of simplicity apparent wind and natural wind, when present, are considered hereafter colinear and along the x -axis. Note also that the present analysis focuses on phase effects, scintillation is therefore not considered.

Despite the specificities of these two scenarios, we have tried to preserve key parameters so as to simplify the interpretation of the results.

We pay a particular attention to the following quantities:

- Ratio diameter over Fried parameter D/r_0 : conserving this ratio allows to compare the two scenarios with a similar turbulence level. In practice, one can indeed justify relevant

observation conditions that ensure the same D/r_0 in both scenarios exploiting the fact that the scenarios differ in terms of telescope diameter, wavelength, elevation and day/night conditions (see discussion hereafter on the C_n^2 profile selection).

- Ratio diameter over turbulence outer scale D/L_0 : conserving this ratio, together with D/r_0 , allows to ensure an identical low order mode variance for the two test cases, despite the change in diameter. The outer-scale L_0 is therefore adjusted accordingly.
- Sampling time t_{samp} : this is of course a key parameter for temporal error assessment; we decided, as a baseline, to compare systems with the same sampling frequency; possibility to relax t_{samp} thanks to MMSE prediction is discussed in a second step.

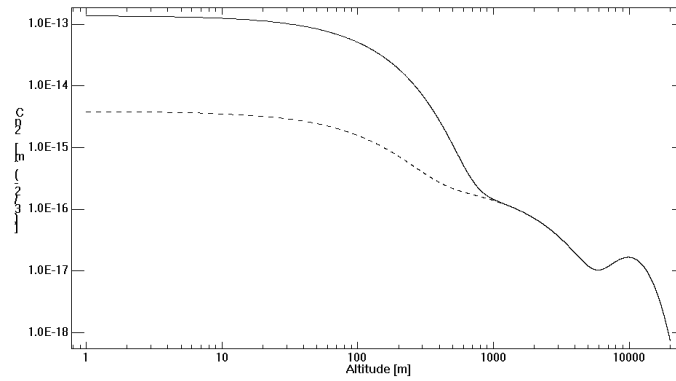


Fig. 2. Vertical Hufnagel-Valley turbulence profiles taken from the recommendation ITU-RP.1621-1: C_n^2 as a function of altitude for telecom (solid line) and satellite observation (dashed line) scenarios.

Concerning the choice of the turbulence profile that is the distribution of the C_n^2 in altitude, from which is in turn deduced the distribution along the line of sight, we use the Hufnagel-Valley profile (Valley-1980) taken from the ITU recommendation ITU-RP.1621-1. This model is parameterized by the value of the C_n^2 at the ground level C_0 and the so-called "high-altitude root-mean-square wind speed", denoted v_{RMS} , that allows to adjust the high altitude strength. The latter term v_{RMS} is set here to the standard value 21 m/s. While C_0 is set to $1.38 \cdot 10^{-13}$ and $3.59 \cdot 10^{-15}$ respectively for the telecom and satellite observation scenarios. The values of C_0 ensure the conservation of D/r_0 (found equal to 12) in both scenarios. Having a higher value of C_0 for the telecom case is consistent with the daytime observation. The two selected profiles are displayed in Fig. 2. One can note that the free atmosphere turbulence, corresponding here to altitudes above 1 km, is identical for the two scenarios.

Table 2 summarizes the main parameters of the two scenarios.

4. Prediction performance assessment

We now apply the formalism of Sect. 2 to the two application scenarios described in Sect. 3 so as to assess the temporal error with static and MMSE prediction. The analysis is performed on 90 Zernike polynomials (radial orders 1 to 12 included, Zernike mode 2 to 91). The slew rate only case is addressed in Sect. 4.1 and 4.2 and the impact of a natural wind, in addition to the apparent wind induced by slew rate, is studied in Sect. 4.3.

Parameter	Telecommunication	Observation
diameter D (m)	0.4	1.5
wavelength (nm)	1550	850
satellite distance (km)	1583	1021
elevation ($^{\circ}$)	20	40
slew rate $\dot{\theta}$ (mrad/s)	2.8	5.9
r_0 (cm)	3.3	12.5
L_0 (m)	12	45
θ_0 (μ rad)	4.8	6.6
\bar{V} (m/s)	6	35
τ_0 (ms)	1.73	1.12
f_{samp} (Hz)	2500	2500
D/r_0	12	12
D/L_0	30	30

Table 2. Summary of the observation conditions and of the turbulence parameters for the telecommunication and satellite observation cases in the slew rate only case.

4.1. Modal variance performance

This section presents the two step ahead prediction performance in terms of variance of the prediction error as a function of the Zernike mode number. We compare the static prediction and the MMSE prediction. MMSE prediction is performed for now with a data vector that includes $K = 10$ time steps to ensure a certain convergence. The convergence with K is discussed in detail in Sect. 4.2. Results are presented in Fig. 3.

MMSE prediction is shown to provide a significant variance reduction. In the telecom case, the tip-tilt variance (averaged over the two modes) is divided by a factor 6.7, while the overall variance (summed over the 90 modes) is divided by 13. The gain is even more impressive for the satellite observation case, factors 35 and 210 respectively.

Note that unlike Von Kármán turbulence variance that depends solely on the Zernike radial order, the prediction error variance is specific to each mode. For instance, the first two points (Zernike number 2 and 3) correspond to tip and tilt modes. The prediction error variance is larger for tip (pointing mode along the apparent wind direction) than for tilt (pointing mode orthogonal to the wind direction). This is a direct consequence of the well known property that the mode along the wind has more energy in the high frequencies of its temporal spectrum (Roddier-JOSAA1993) hence a faster evolution. The tip variance remains larger also with MMSE prediction. The variances of higher order modes are also impacted by the relative orientation of the mode with respect to the wind direction.

4.2. Impact of the number of data time steps

We now study the MMSE prediction convergence with respect to the number of data time steps K . The results are given in Fig. 4. We observe huge step when moving from 1 data sample to 2 data samples. Minor improvements are still obtained when increasing further K . The convergence is

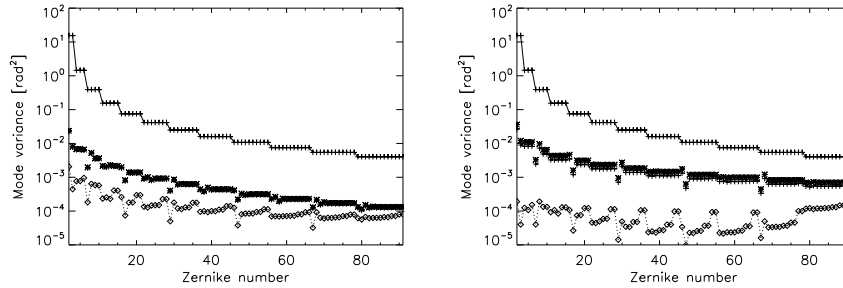


Fig. 3. Modal variance versus Zernike number: Von Kárman turbulence variance [crosses], static prediction [stars] and MMSE prediction error [diamonds]. Slewing rate only case with two step ahead prediction. Left graph corresponds to the telecom scenario, and right graph to the satellite observation scenario.

slightly slower for the telecom scenario. In any case convergence is clearly reached with $K = 10$ the value selected in the previous section.

These curves clearly show that the turbulence dynamics is not strictly equivalent to a second order autoregressive process, otherwise convergence would be strictly obtained for $K = 2$ (see Sect. 2.4). It still appears that an AR2 model could be an acceptable approximation. Of course the main effect noticeable on this curves is the fact that, even at convergence, MMSE prediction is much more efficient in the satellite observation scenario, which was already observed in the previous section. This difference in behavior is discussed in Sect. 5.

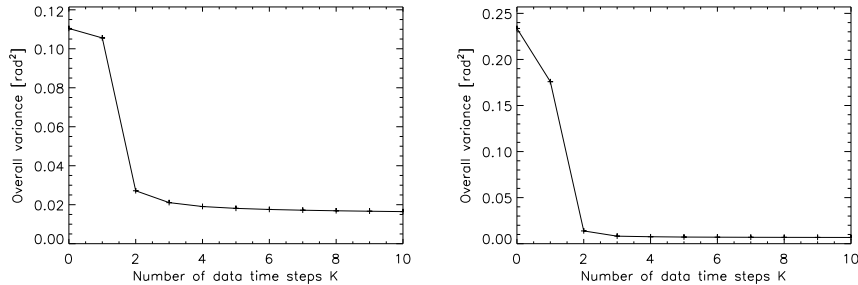


Fig. 4. Overall phase variance (sum over the 90 Zernike modes) with MMSE prediction versus the number of data time steps. For comparison, the variance obtained with static prediction is indicated arbitrarily at $K = 0$. Slewing rate only case with two step ahead prediction. Left graph corresponds to the telecom scenario, and right graph to the satellite observation scenario.

4.3. Impact of the natural wind

Previous results have been obtained in the limiting case said "slew rate only" in the absence of natural wind. To confirm the previous results in a more realistic scenario we have also estimated the prediction performance with natural wind added to the slew rate induced apparent wind. For the sake of simplicity we have taken a constant 10 m/s natural wind in the same direction as the apparent wind.

The results are displayed in Fig. 5. MMSE prediction again provides a significant variance reduction. In the telecom case, the tip-tilt variance (averaged over the two modes) is divided

by a factor 16, while the overall variance (summed over the 90 modes) is divided by 24. The gain is again more impressive for the satellite observation case, factors 34 and 212 respectively. Compared to the slew rate only case, gains are increased for telecom case, while they remain almost unchanged for satellite observation scenario. Convergence is still almost reached with two time steps, and is slightly faster, for the telecom scenario, than in the slew rate only case.

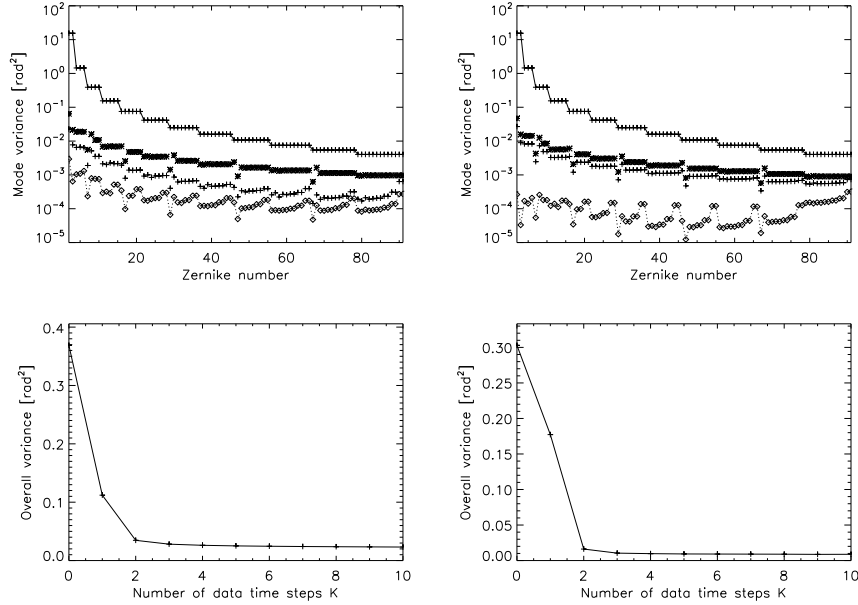


Fig. 5. Top row: Modal variance versus Zernike number (see symbol description in Fig. 3). Overall phase variance (sum over the 90 Zernike modes) with MMSE prediction versus the number of data time steps. For comparison, the variance obtained with static prediction is indicated arbitrarily at $K = 0$. Case of slewing rate plus 10 m/s natural wind, with two step ahead prediction. Left column corresponds to the telecom scenario, and right column to the satellite observation scenario.

4.4. Relaxation of the sampling frequency

As demonstrated in the previous sections, for a given sampling frequency, MMSE prediction provides a large reduction of the temporal error. Conversely MMSE prediction can allow to alleviate the sampling frequency while preserving performance. So as to illustrate this point, we have used our analytical tool to find, for each case considered in this section, the sampling frequency that provides an MMSE prediction temporal error equal to that of static prediction at the original sampling frequency of 2500 Hz. In the absence of natural wind, respectively for the telecom and satellite observation scenario, we obtain 1150 and 650 Hz, hence a reduction by a factor 2.2 and 3.8. In the case of a 10 m/s natural wind the relaxed sampling frequencies become 750 and 600 Hz. Prediction therefore allows a very significant relaxation of the sampling frequency. As might have been expected, relaxation is more important for the satellite observation cases for which prediction efficiency is better. The final choice of the sampling frequency is of course a complex system trade-off. One can however say that for satellite observation where flux is limited, the high potential of prediction in terms of reduction sampling frequency reduction is a very valuable asset that should alleviate the wavefront sensing constraints. In the telecom case,

flux is less an issue but a relaxed sampling frequency can reduce system complexity, hardware constraints (DM dynamics...) and eventually cost.

5. Discussion

In order to go beyond the simple assessment of the prediction performance, we now give here an interpretation of the results, and explain the difference in terms of predictability between the two scenarios considered. This analysis will be supported by parallels made with the scalar tutorial of the Sect. 2.4.

Hereafter, when giving numerical values we always give sequentially the value for the telecom scenario and then for the satellite observation scenario, separated by the word "respectively". We first discuss the limiting case with slew rate only and later broaden the discussion to the case with an additional natural wind.

Firstly, we stress the fact that for the two scenarios selected the temporal error with static prediction is of the same order: 0.11 respectively 0.23 rad². Besides, these two values are approximately in the ratio of the respective τ_0 to the $5/3$ which confirms that the modal temporal error evaluated here still follows, for a given loop sampling frequency, the dependency in $1/\tau_0^{5/3}$ given by Fried (Fried-1990). However as already underlined in Sect. 2.4, the static prediction error only depends on the variance and 2 step correlation. Balancing these two terms can therefore lead to similar temporal error for very different signal dynamics and does not presume the prediction ability of the MMSE estimator.

Secondly, we recall that in the slew rate only case $\tau_0 = \theta_0/\dot{\theta}$, we can therefore deduce that this quantity is, similarly to the isoplanatic angle θ_0 , essentially driven by the free atmosphere. From Eq. 15 one can compute that the contribution to the term $1/\tau_0^{5/3}$ of the layers above 1 km in altitude. We indeed find that they represent a very large proportion, found here equal to 94% respectively 99%.

Thirdly, if we then focus on these main contributors, that is the turbulence contributions above 1 km in altitude, we can compute that the D/r_0 associated to this high altitude slab is respectively XXX and YYY for the two scenarios accounting for their specific elevation, wavelength and diameter. Hence a high altitude D/r_0 multiplied by about 5 when going from the telecom to the satellite observation case.

Fourthly, one can estimate the apparent wind speed for instance at this 1 km altitude corresponding to a distance to the ground aperture of 2900 respectively 1555 m owing to the respective elevation. We find 8, respectively 9 m/s. Moreover it is of interest to compare the ratio V/D that is related to the cut-off frequency of the modal temporal PSD (Roddier-1993, Conan-1995). We obtain 20, respectively 6 Hz. Of course, all these values are multiplied by 10 when considering the jet stream layer at an altitude of 10 km rather than the preceding altitude of 1 km. For instance the ratio V/D now reaches 200 Hz in the telecom scenario. This ratio V/D drives the intrinsic turbulent temporal dynamics and can be seen as the counterpart of the natural frequency f_0 of Sect. 2.4. The fact that V/D , and hence $V/D/f_{samp}$, is larger for the telecom case than for the satellite observation case therefore denotes faster temporal decorrelation similarly to the cases with larger f_0/f_{samp} in Sect. 2.4.

Lastly, all things considered, and still for the high altitude layers that are, in the slew rate only case, the major contributors to the temporal error, we can state that: the satellite observation dynamics corresponds, relatively to the telecom case, to a turbulence that is stronger (high altitude D/r_0 multiplied by 5) but also much slower (ratio $V/D/f_{samp}$ reduced by factor ≈ 3). We are therefore exactly in the conditions described in Sect. 2.4 where, indeed, much larger MMSE prediction gains were obtained with strong and slow signals, that is with large variance and small relative natural frequency.

This analysis now leads us to formulate a number of warnings. For what concerns temporal dynamics and hence MMSE predictability, the integrated parameters given in Table 2 are far

from sufficient and can sometimes be misleading. The mean wind speed could for instance give the impression that the satellite observation turbulence is fast and difficult to predict. It is actually easy to show that the adjustment of the ground C_n^2 modifies strongly the mean wind speed while having little effect on the turbulence dynamics and predictability since wind speed, in the slew only case, is nearly zero near the ground. Similarly, the value of D/r_0 for the whole profile gives the overall strength of the turbulence but gives no information on the energy of the layers that contribute significantly to the prediction error.

Concerning the results with slew rate together with natural wind (see Sect. 4.3), obviously it adds near ground contributions to the prediction error since the wind speed is dominated by the natural wind in this region. For the telecom case it therefore adds a strong turbulence component (daytime conditions correspond to strong ground C_n^2) with a reasonable wind (10 m/s), and in turn a rather small $V/D/f_{smp}$, hence a strong and relatively slow component that is favorable to MMSE prediction. And indeed the prediction gain is increased compared to slew rate only. For the satellite observation case, predictability was already quite high and the gains are little affected by the presence of this near ground component, limited anyway in strength since the ground C_n^2 is smaller in this scenario.

6. Conclusion

Temporal error is a key contributor to the AO error budget and is often a major issue for applications involving moving targets. We present a simple theoretical formalism that allows to estimate the temporal error for any linear prediction. This analytical formalism is based on a modal expansion of the resulting phase in the ground aperture and on its associated modal temporal correlations that are easily deduced from Von Kármán statistics and assumptions on the wind. This formalism allows to assess both temporal error with static prediction, sometimes referred to as no prediction at all, and with an MMSE prediction based on an adjustable number K of past data.

The formalism is applied to two application scenarios: a LEO to ground telecom link, with a ground aperture of a few decimeters, and the observation of a LEO from the ground with a metric telescope. Prediction performance is shown to quickly converge with K (2 time steps nearly reaches convergence). Gains brought by MMSE temporal prediction are large and also shown to be very dependent of the configuration: gains of about a decade are obtained in the telecom case while it reaches several decades for the satellite observation.

This therefore gives a perfect illustration that with scenarios having a similar static prediction error, one can obtain very different prediction capacities with optimal methods that exploit the temporal dynamics of the perturbation. Thanks to a didactic scalar tutorial and to a refined analysis of the selected scenarios, the difference in behavior is shown to be related to the balance between the signal strength and speed of evolution with respect to the sampling time. A balance in which the telescope diameter plays an essential role.

The formalism therefore allows, for given observation scenarios, to quickly grasp perspectives of gain brought by temporal prediction. Considering the simplifying approximations made, our approach also gives an estimation of the lower bound of the temporal error one may expect. These elements can guide the control developments and help the performance validation. We have also shown that important gains brought by prediction can also be exploited to relax the sampling time while maintaining good performance. Such trade-offs are essential even in early stage of system design. For satellite observation, reducing the AO loop frequency means a larger wavefront sensor exposure time which is a strong asset when flux is limited. For the telecom case it means reduced complexity and relaxed constraints on the components (DM dynamics...).

We stress the fact that for ground to satellite optical uplinks another major contributor to the AO error budget is related to point-ahead anisoplanatism. To limit this effect, we have recently proposed (Lognoné-OptExpr-2023) an innovative strategy, based again on an MMSE estimator,

so as to obtain an efficient angular prediction at point ahead. We plan to combine angular and temporal prediction in future developments.

7. Bibliography

- Basu, S., Voelz, D., 2008. Tracking in a ground-to-satellite optical link: effects due to lead-ahead and aperture mismatch, including temporal tracking response. *J. Opt. Soc. Am. A* 25, 1594. <https://doi.org/10.1364/JOSAA.25.001594>
- Basu, S., Voelz, D., Borah, D.K., 2009. Fade statistics of a ground-to-satellite optical link in the presence of lead-ahead and aperture mismatch. *Appl. Opt.* 48, 1274. <https://doi.org/10.1364/AO.48.001274>
- Chassat, F., 1989. Theoretical evaluation of the isoplanatic patch of an adaptive optics system working through the atmospheric turbulence. *J. Opt.* 20, 13–23. <https://doi.org/10.1088/0150-536X/20/1/002>
- Conan, J.-M., Rousset, G., Madec, P.-Y., 1995. Wave-front temporal spectra in high-resolution imaging through turbulence. *J. Opt. Soc. Am. A* 12, 1559. <https://doi.org/10.1364/JOSAA.12.001559>
- Correia, C., Jackson, K., Véran, J.-P., Andersen, D., Lardière, O., Bradley, C., 2014. Static and predictive tomographic reconstruction for wide-field multi-object adaptive optics systems. *J. Opt. Soc. Am. A* 31, 101. <https://doi.org/10.1364/JOSAA.31.000101>
- Correia, C.M., Jackson, K., Véran, J.-P., Andersen, D., Lardière, O., Bradley, C., 2015. Spatio-angular minimum-variance tomographic controller for multi-object adaptive-optics systems. *Appl. Opt.* 54, 5281. <https://doi.org/10.1364/AO.54.005281>
- Ellerbroek, B.L., 1994. First-order performance evaluation of adaptive-optics systems for atmospheric-turbulence compensation in extended-field-of-view astronomical telescopes. *J. Opt. Soc. Am. A* 11, 783. <https://doi.org/10.1364/JOSAA.11.000783>
- Fusco, T., Conan, J.-M., Rousset, G., Mugnier, L.M., Michau, V., 2001. Optimal wave-front reconstruction strategies for multiconjugate adaptive optics. *J. Opt. Soc. Am. A* 18, 2527. <https://doi.org/10.1364/JOSAA.18.002527>
- Hogge, C., Butts, R., 1976. Frequency spectra for the geometric representation of wavefront distortions due to atmospheric turbulence. *IEEE Trans. Antennas Propag.* 24, 144–154. <https://doi.org/10.1109/TAP.1976.1141310>
- Johnson, L.C., Gavel, D.T., Wiberg, D.M., 2011. Bulk wind estimation and prediction for adaptive optics control systems. *J. Opt. Soc. Am. A* 28, 1566. <https://doi.org/10.1364/JOSAA.28.001566>
- Neichel, B., Fusco, T., Conan, J.-M., 2009. Tomographic reconstruction for wide-field adaptive optics systems: Fourier domain analysis and fundamental limitations. *J. Opt. Soc. Am. A* 26, 219. <https://doi.org/10.1364/JOSAA.26.000219>
- Olivier, S.S., Gavel, D.T., 1994. Tip–tilt compensation for astronomical imaging. *J. Opt. Soc. Am. A* 11, 368. <https://doi.org/10.1364/JOSAA.11.000368>
- Ono, Y.H., Akiyama, M., Oya, S., Lardière, O., Andersen, D.R., Correia, C., Jackson, K., Bradley, C., 2016. Multi time-step wavefront reconstruction for tomographic adaptive-optics systems. *J. Opt. Soc. Am. A* 33, 726. <https://doi.org/10.1364/JOSAA.33.000726>

- Pachter, M., Oppenheimer, M.W., 2002. Adaptive optics for airborne platforms—Part 1: modeling. *Opt. Laser Technol.* 34, 143–158. [https://doi.org/10.1016/S0030-3992\(01\)00104-9](https://doi.org/10.1016/S0030-3992(01)00104-9)
- Roddier, F., Roddier, D., Northcott, M.J., Graves, J.E., McKenna, D.L., 1993. One-dimensional spectra of turbulence-induced Zernike aberrations: time-delay and isoplanicity error in partial adaptive compensation. *J. Opt. Soc. Am. A* 10, 957. <https://doi.org/10.1364/JOSAA.10.000957>
- Takato, N., Yamaguchi, I., 1995. Spatial correlation of Zernike phase-expansion coefficients for atmospheric turbulence with finite outer scale. *J. Opt. Soc. Am. A* 12, 958. <https://doi.org/10.1364/JOSAA.12.000958>
- Tyler, G.A., 1984. Turbulence-induced adaptive-optics performance degradation: evaluation in the time domain. *JOSA A* 12.
- Valley, G.C., 1980. Isoplanatic degradation of tilt correction and short-term imaging systems. *Appl. Opt.* 19, 574–577. <https://doi.org/10.1364/AO.19.000574>
- Valley, G.C., Wandzura, S.M., 1979. Spatial correlation of phase-expansion coefficients for propagation through atmospheric turbulence. *J. Opt. Soc. Am.* 69, 712. <https://doi.org/10.1364/JOSA.69.000712>
- Vidal, F., Gendron, E., Rousset, G., 2010. Tomography approach for multi-object adaptive optics. *J. Opt. Soc. Am. A* 27, A253. <https://doi.org/10.1364/JOSAA.27.00A253>
- Vogel, C.R., Tyler, G.A., Wittich, D.J., 2014. Spatial–temporal-covariance-based modeling, analysis, and simulation of aero-optics wavefront aberrations. *J. Opt. Soc. Am. A* 31, 1666. <https://doi.org/10.1364/JOSAA.31.001666>
- Whiteley, M.R., 1999. Finite outer scale considerations for beam-steering optimization, in: Steiner, T.D., Merritt, P.H. (Eds.), . Presented at the AeroSense '99, Orlando, FL, pp. 338–348. <https://doi.org/10.1117/12.356974>
- Whiteley, M.R., Roggemann, M.C., Welsh, B.M., 1998a. Optimal beam steering using time-delayed wavefront measurements in airborne laser target engagements, in: Steiner, T.D., Merritt, P.H. (Eds.), . Presented at the Aerospace/Defense Sensing and Controls, Orlando, FL, pp. 98–109. <https://doi.org/10.1117/12.323929>
- Whiteley, M.R., Roggemann, M.C., Welsh, B.M., 1998b. Temporal properties of the Zernike expansion coefficients of turbulence-induced phase aberrations for aperture and source motion. *J. Opt. Soc. Am. A* 15, 993. <https://doi.org/10.1364/JOSAA.15.000993>
- Whiteley, M.R., Welsh, B.M., Roggemann, M.C., 1998c. Optimal modal wave-front compensation for anisoplanatism in adaptive optics. *J. Opt. Soc. Am. A* 15, 2097. <https://doi.org/10.1364/JOSAA.15.002097>
- Whiteley, M.R., Welsh, B.M., Roggemann, M.C., 1998d. Incorporating higher-order modal measurements in tilt estimation: natural and laser guide star applications. *Appl. Opt.* 37, 8287. <https://doi.org/10.1364/AO.37.008287>